7-1-2016

An Evaluation of p-Phenylene Ethynylenes and their Interactions with Pathogenic Microbes

Harry Pappas

Harry Craig Pappas
Candidate

Nanoscience & Microsystems Engineering
Department

This dissertation is approved, and it is acceptable, in quality and form for publication:

Approved by the Dissertation Committee:

David G. Whitten , Chairperson

Aaron K. Neumann

Linnea K. Ista

David J. Keller

An Evaluation of *p*-Phenylene Ethynylenes and their Interactions with Pathogenic Microbes

by

Harry Craig Pappas
B.S. Mechanical Engineering, University of Massachusetts Amherst, 2010
M.S. Nanoscience & Microsystems Engineering, University of New Mexico, 2012

DISSERTATION

Submitted in Partial Fulfillment of the
Requirements for the Degree of

Doctor of Philosophy
Nanoscience & Microsystems Engineering

The University of New Mexico
Albuquerque, New Mexico

June 2016

Acknowledgements

It all starts with my parents, who have always put me in position to succeed. Thanks to the Hopkinton Public School system, for exposing me to so many opportunities. Thanks to the FIRST Robotics program, which gave me my first true exposure to creativity, design, engineering, and team work. Thanks to Caliper Life Sciences, who provided me my first internship position while I was still in high school. I certainly wish to acknowledge the School of Engineering at UMass Amherst, and particularly the engineering writing course that showing me the value of interdisciplinary education. Thank you to John Stoffolano, who gave me my first lab experience.

Thank you to the University of New Mexico, and, in particular, the Nanoscience & Microsystems degree program, for giving me a chance when others turned me away. Thank you to the NSF and the Professional Science Master's program for opening the door to entrepreneurship. Thank you to David Whitten, for mentoring me both as a student and as a person; again, thank you. Thank you to the Defense Threat Reduction Agency for sponsoring my position for four years. Thank you to my committee members, Aaron Neumann, Linnea Ista, and David Keller for your invaluable advice and guidance. Thanks to Julie Lovchik for your collaborative contributions. Thank you the American Heart Association for one year of sponsorship. Lastly, thanks to all my friends (you know who you are) for your unconditional support.

An Evaluation of *p*-Phenylene Ethynylenes and their Interactions with Pathogenic Microbes

by

Harry Craig Pappas

B.S. Mechanical Engineering, University of Massachusetts Amherst, 2010

M.S. Nanoscience & Microsystems Engineering, University of New Mexico, 2012

Antibiotics are critical to the welfare of humans domestically and abroad, and their importance cannot be overlooked. However, over the past century, the rise of antibiotic-resistant bacteria and fungi has warranted the investigation of alternative antimicrobials and decontamination strategies. Recently, a new class of antimicrobial has come into view and appears to offer promise in our ongoing defense against pathogenic microbes. These compounds, known as *p*-phenylene ethynylenes, fundamentally differ from traditional antibiotics in that they are "light-activated" and deal broad-spectrum damage in a detergent-like manner. Despite the promise of these compounds, there was—up until recently—good reason to believe that they were simply not suitable for use outside of the laboratory. A series of studies, described herein, was conducted to address these legitimate concerns. First, the compatibility of oligomers with surfactant was investigated, and found to confer numerous biocidal benefits. Similar oligomers were found to be sporicidal and fungicidal. Polymers were also investigated, and were found to be well-suited for attachment onto glass surfaces. The culmination of these studies foreshadows the use of these compounds as anti-biowarfare agents, and at the point-of-care.

Table of Contents

Chapter 1: Introduction

1.1 Antibiotic Resistance Contributes Greatly to Healthcare Costs and Mortality

Hospitals in the United States have seen a drastic increase in cases of patients acquiring infections of antibiotic-resistant bacteria such as Gram-negative *Klebsiella pneumonia* and *Acinetobacter baumannii*, as well as Gram-positive *Staphylococcus aureus*, to the extent of 1.7 million hospital-acquired infections, annually [1]. Controlling these pathogens is, therefore, a major challenge in the clinical setting—one that was thought to be alleviated upon the widespread introduction of antibiotics in the 1940s [2–4].

Additionally, the problem of antibiotic-resistant bacteria has become a substantial burden for healthcare providers in the last few decades. A large number of nosocomial (hospital-acquired) infections are caused by a methicillin-resistant strain of *S. aureus*, which can survive most conventional antibiotic treatments. Several large-scale studies have shown that exposure to antibiotics can increase the chances of acquiring such an infection in a hospital environment, as the antibiotics kill most of the natural flora of the body while allowing the antibiotic-resistant bacteria to thrive [5–7]. The development of novel antibiotics or bactericides that do not induce resistance in targeted pathogens is essential for effective treatment of many types of nosocomial infections [8,9].

1.2 Broad-Spectrum Strategies may circumvent the Development of Antibiotic Resistance

In the U.S., greater numbers of hospital-acquired infections from antibiotic-resistant strains of bacteria have led to an increased need for broad-spectrum antimicrobial compounds which are capable of eliminating bacteria on surfaces and medical tools [1,5–9],

especially those frequently implicated in catheter-related infections [10,11]. One useful method of sterilization is the use of a light-activated biocide in combination with ultraviolet or visible light [12–14]. Examples of tested photosensitizers include porphyrins, C_{60} derivatives[15], phthalocyanines [16], gold nanoparticles [17], and conjugated polyelectrolyte derivatives [18,19].

In 2005, Lu *et al.* demonstrated nearly two log reduction (98.9% viability decrease) of *Bacillus anthracis* Sterne spores using a cationic conjugated polyelectrolyte in the presence of yellow light [12]. These initial results stimulated a research program that has included not only "iteration" and "improvement" efforts but also a significant amount of "discovery" focused research. A key theme in this dissertation is that the "discovery" focused research efforts have themselves led to important consequences and potential applications that are driven by new ideas and, above all, curiosity.

1.3 *p*-Phenylene Ethynylenes

The antimicrobial properties and reactivity of these compounds have been investigated by a number of researchers in laboratories at the Universities of Florida and New Mexico

since 2005. As indicated above, the research was initiated by an exploratory investigation of a cationic CPE with two representative bacterial species [12].

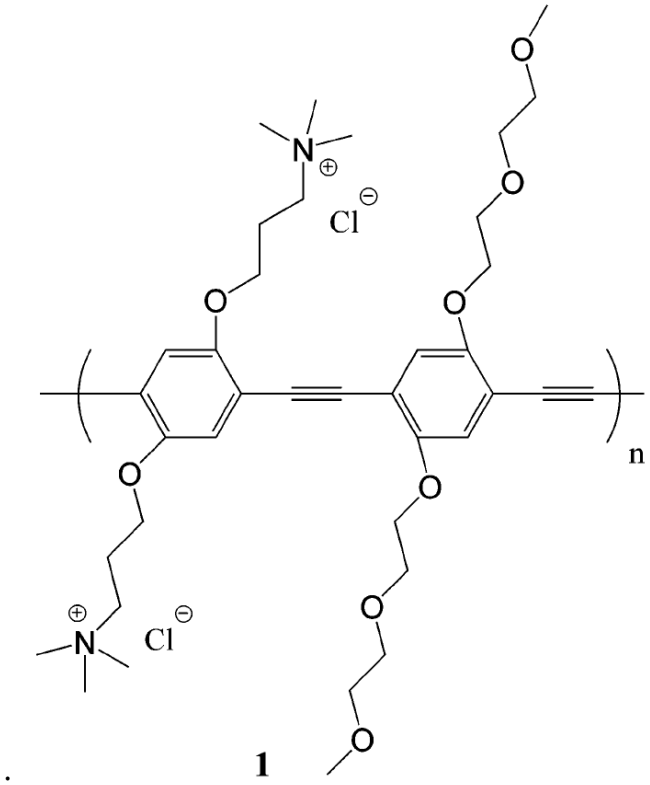

1

Figure 1.1*:* Structure of PPE-1.

In particular, a cationic compound (PPE-1, shown above in Figure 1.1) with a *p*-phenylene ethynylene backbone and pendant charged groups, known as conjugated polyelectrolytes, was tested in aqueous solution against *E. coli* and *B. anthracis* Sterne spores [12]. In these experiments, it was observed that brief exposure of either bacterium to PPE-1 in the dark did not cause much harm, but on irradiation of the suspensions with visible light absorbed by PPE-1 there was efficient killing of both strains of bacteria. It was also observed through fluorescence microscopy that both bacteria contained a uniform coating of PPE-1 upon recovery of the treated bacteria by centrifugation [12].

In subsequent studies at UNM and UF, we carried out experiments to determine the mechanism of the light-activated biocidal activity of the cationic PPE. Two likely mechanisms were initially considered. The simplest seemed to be an activation of oxygen to its excited singlet electronic state followed by subsequent reaction and generation of other reactive oxygen intermediates. An alternative mechanism could be a photoinduced electron transfer whereby the excited PPE could abstract an electron from a halide counterion, leading to a reactive halide atom and an ion-radical from reduced PPE. Studies at UF demonstrated that irradiation of PPE-1 in aerated solutions (water or methanol) results in formation of $^1O_2$* detected by chemical trapping or near-IR emission from the excited state [20]. Studies at UNM showed that deaeration of aqueous suspensions of PPE with Gram-negative *Pseudomonas aeruginosa* attenuated the biocidal effect of irradiation [20]. Thus it appears clear that generation of singlet oxygen and subsequent generation of other reactive oxygen species can account for much of the light activated bactericidal effect [20–22].

It was also found that, in addition to the light-activated biocidal activity, there is a dark biocidal activity of the PPE against bacteria, predicated on the interaction of the cationic quaternary ammonium groups with net-anionic membranes and cell walls; this interaction facilitates contact with microbes, leading to membrane perturbation, pore formation, and the leakage of cell contents [23]. A series of investigations demonstrated that envelope damage by the PPEs is the driver for dark killing [23–26]. Experimental evidence [27] and computational modeling [28,29] suggest that OPEs disrupt membranes by a similar manner to that of detergents, via a mechanism known as the carpet model. Briefly, the carpet model describes a scenario by which amphiphilic antimicrobials orient

parallel to the lipid bilayer surface of the cell membrane and, upon reaching a threshold concentration, promote membrane destruction and solubilization [30,31].

All in all, oligomeric and polymeric *p*-phenylene ethynylenes have been demonstrated to kill Gram-negative and Gram-positive bacteria (including spores) [12,18,27,32,33] biofilms, viruses, and fungi [32,34,35]. Both mechanisms of biocidal action are broad-spectrum, and kill bacteria with similar effectiveness regardless of antibiotic resistance. In addition, it is unlikely that bacteria would evolve a resistance to these compounds due to the non-specific nature of the killing mechanisms. PEs are versatile in their application, as they have been demonstrated to kill bacteria in liquid solution [12], on fabrics [36], and on glass [37].

1.4 PEs have other properties that make them promising

The polymers exhibit a number of interesting properties in that, while they are polyelectrolytes and water-soluble, they are also moderately to strongly hydrophobic. The first conjugated polyelectrolyte that our research group worked with was an anionic poly(phenylene vinylene) derivative. It was found that this material is fluorescent in aqueous solution and that its fluorescence is quenched by very low concentrations of neutral or cationic electron acceptors [38]. Thus, these compounds were further developed as sensors and in energy conversion [38–45].

The ionic side chains attached to the conjugated polymer backbone render CPEs water-soluble, while the materials retain the optical and electronic properties characteristic of π-conjugated polymers [41,46,47]. The presence of both hydrophilic side chains and the hydrophobic backbone makes CPEs amphiphilic, giving the materials the

propensity to self-assemble into aggregates and other supramolecular structures depending on the solvent environment [41,48,49]. A compelling property of fluorescent CPEs is related to the "amplified quenching effect". In particular, fluorescent CPEs are efficiently quenched by ultralow concentrations of oppositely charged quencher ions [38,50]. The amplified quenching effect is attributed to the spatial delocalization and rapid diffusion of excitons along the polymer backbone: a process often referred to as the "molecular wire effect" [50]. It has also been shown that CPE aggregation enhances the amplified quenching effect by enabling exciton transport between polymer chains. Researchers have exploited the amplified quenching property to develop ultrasensitive chemical and biological sensors that are based on the quenched fluorescence of CPEs [38,41,45,51].

Our research group has explored the properties of poly-(phenylene ethynylene) (PPE)-based CPEs [41,52]. During the course of this work, a variety of PPE-backbone CPEs have been synthesized that are functionalized with anionic solubilizing groups, including sulfonate ($-SO_3^-$) [48], phosphonate ($-PO_3^{2-}$) [53], and carboxylate ($-CO_2^-$) [54]. The properties of CPEs with various cationic solubilizing groups have also been investigated, mostly based on tetraakylammonium salts ($-NR_3^+$) [52]. These cationic CPEs have been studied as fluorescent sensors for anions, and some have been shown to display interesting selectivity for di- and triphosphate ions (e.g., pyrophosphate, PPi) [55–57]. In subsequent investigations it was found that these materials also could easily coat oppositely charged supports including planar surfaces and microspheres.

1.4.1 Fluorescent Detection of Amyloid Protein Aggregates

The fortuitous discovery of the ethyl ester-terminated OPEs led to another sensor application: their development as dyes for amyloid fibrils and oligomers [58]. Amyloid protein aggregates are fibrillar protein conformers with unusually high thermodynamic stability, mechanical integrity and resistance to proteolysis, formed of many protein monomers arranged with intermolecular beta-sheets perpendicular to the fibril axis [59,60]. Understanding the biology and biochemistry of amyloid formation is critical to developing knowledge and therapies for Alzheimer's disease [61], type II diabetes [62], transmissible spongiform encephalopathies and other diseases, as well as structural and chemical properties of bacterial extracellular matrix [63]. Unique to amyloid is their ability to bind certain linear organic dyes with high specificity [64], which has led to the development of various small molecules as optical sensors for amyloid in solution and in tissue. The benzothiazinium salt thioflavin T and its derivatives are the most widely used amyloid dyes. Experimental and computational studies of amyloid dyes has identified a rigid, linear, highly conjugated backbone as a key shared element [65], which led to the hypothesis that OPEs, which have a rigid, linear, pi-conjugated phenylene ethynylene backbone, might be suitable amyloid dyes.

Using hen egg white lysozyme model amyloids formed *in vitro* [66,67], it was found that many OPEs bind selectively and strongly to amyloid, with the COOEt-terminated OPEs showing an especially large increase in fluorescence signal upon amyloid binding. Preliminary work shows that OPEs are also effective in dyeing intraneuronal tau amyloid aggregates in brain tissue from mouse models of tau diseases, using both one- and two-photon microscopy. We hope to see OPEs further exploited as tool compounds for

detection of amyloids in many arenas. Crucial to the development of this application, like the others in this report, was the unexpected discovery of the photophysical properties imparted to OPEs by ethyl ester end groups.

1.5 Motivation

Clearly, a substantial amount of research was conducted in the study of *p*-phenylene ethynylenes. The basis for the research described in this dissertation is an extension of the in-depth studies conducted by the Whitten and Schanze research groups at UNM and UFL, respectively. In particular, the eight-year span, from 2005-2012, served as a critical point by which the fundamental mechanisms of biocidal activity were investigated. During this time period, oligomeric and polymeric phenylene ethynylenes were investigated. While phenylene ethynylenes were indeed promising for their biocidal capacity, significant questions remained: could these compounds actually be used to help mitigate microbial infection in humans?

As discussed, cationic *p*-phenylene ethynylenes are highly effective light-activated biocides that deal broad-spectrum damage to a variety of pathogens, including bacteria. However, the capacity to absorb light is a double edged sword, in that this characteristic also means that the compounds are prone to photodegradation. This poses a major barrier to entry for these compounds, for their use in either clinical settings, or as a defense against biowarfare agents. As things stood in 2012, we had no way of granting phenylene ethynylenes long-term biocidal activity, as their susceptibility to photodegradation in water limited their usefulness outside of the laboratory, where lighting conditions are often sporadic and uncontrollable. We were able to show that

these molecules complex with oppositely-charged surfactants, and that the resulting complexes are protected from photodegradation. These findings helped us to develop a simple, yet robust, strategy to mitigate photodegradation (Chapter 2.2).

These results were extremely enlightening, and allowed us to address yet another major concern: the inability of anionic phenylene ethynylenes to kill bacteria. Since microbes generally have a net-negative charge of the cell wall, anionic phenylene ethynylenes are ineffective at accessing and penetrating the plasma membranes of bacteria, thereby exhibiting a far lower degree of killing relative to their cationic counterparts. By modifying the strategy detailed in Chapter 2.2, we were able to grant anionic OPEs a respectable degree of biocidal activity (results shown in Chapter 2.3). Even though it's unclear whether this strategy is also applicable to PPEs, this allows synthetic chemists a greater degree of choice as to how conjugated polyelectrolyte is designed. These studies are crucial in demonstrating the fact that phenylene ethynylenes are still capable of exhibiting biocidal effects in the presence of surfactants, such as SDS and TTAB. Surfactants of this nature are commonly found in disinfecting wipes and similar products, meaning their compatibility with phenylene ethynylenes is significant.

Mitigation of bacterial adhesion and subsequent biofilm formation is quickly becoming a strategy for the prevention of hospital-acquired infections. While phenylene ethynylenes have never been tested in the format of a disinfecting wipe per se, they were tested on a cotton-based textile [36]. This was probably the best example of a PE-based antimicrobial application at the onset of the research described in this dissertation. This study was critical, as it demonstrated, along with the roach motel studies [21], that PEs could still exhibit biocidal effects upon being bound to a substrate; in particular, $MnCO_3$.

Recently, the Whitten and Schanze groups collaborated to advance this concept; this time on a different material, and with a slightly different aim. Rather than just being interested in bacterial cell death, we set out to characterize a material that integrated PEs with temperature-sensitive PNIPAAm. As disclosed in Chapter 3, we demonstrate a basic strategy for surface modification that combines the ability to control attachment by microbes with the ability to inactivate microbes.

While this was a very important study for us, we were quick to learn that, in this format, our PPE was unable to kill Gram-positive *S. aureus* or Gram-negative *E. coli*, unless favorable lighting conditions were present. We hypothesized that this limitation was, for the most part, a result of our selected PPE, which, despite its high fluorescence yield, is often undesirable to work with, due to its hydrophobic nature and poor solubility in water. Thus, we hypothesized that a compound with prolific dark-killing would be well-suited for a format such as a self-cleaning CPE/PNIPAAm surface. In Chapter 4, we disclose the synthesis of two polymers featuring the same PPE-type backbone, but differing in the frequency of imidazoliums on the chains: PIM-4 features two imidazolium units on every phenylene repeat, whereas PIM-2 contains two imidazolium units on every other phenylene unit. The results of this study show that this class of compound is among the best in terms of its biocidal characteristics, efficiently killing *S. aureus* and *E. coli* in light and dark conditions, making it an ideal candidate for implementation in textiles and solid substrates. These studies also provide insight into the impact of hydrophilicity and, in particular, its effect on aggregation and biocidal activity.

The rapid generation of research conducted by the Whitten and Schanze research groups since 2005 is largely attributed to funding by the Defense Threat Reduction Agency for the purpose of addressing bacterial biowarfare agents. The most notorious bacterial biowarfare agent is *Bacillus anthracis*, infection by which causes the Anthrax disease in humans. Addressing this bacterium is complex, not because of the disease it causes, but because of the manner in which it happens. Unlike most bacteria, this organism is capable of assuming a state of dormancy, which coincides with increased aerosolization and, therefore, infection (usually through cutaneous or respiratory means). A PE had previously been tested against *Bacillus*, but in a limited fashion, as little attention was paid to exactly how PEs impacted the organism's ability to abandon its state of dormancy. We conducted a comprehensive study with *B. atrophaeus* and *B. anthracis* Sterne, not only demonstrating biocidal capabilities, but also a technique that allows for rapid identification and monitoring of the aforementioned dormant state. In theory, these findings could allow diagnosticians and pathologists to rapidly determine the time of infection, and could even mitigate infection entirely, if employed correctly.

The final study disclosed in this dissertation deals with bacteria's partner in crime: *Candida* yeast. Candida species are the cause of many bloodstream infections through contamination of indwelling medical devices. These infections account for a 40% mortality rate, posing a significant risk to immunocompromised patients. Traditional treatments against *Candida* infections include amphotericin B and various azole treatments. Unfortunately, these treatments are associated with high toxicity, and resistant strains have become more prevalent. As a new frontier, light-activated phenylene ethynylenes have shown promising biocidal activity against Gram-positive and -negative

bacterial pathogens, as well as the environmental yeast, *Saccharomyces cerevisia*e. In this study, we monitored the viability of *Candida* species after treatment with a cationic conjugated polymer (PPE) or oligomer (OPE) by flow cytometry in order to explore the antifungal properties of these compounds. The oligomer was found to disrupt *Candida albicans* yeast membrane integrity independent of light-activation, while the PPE is only able to do so in the presence of light, allowing for some control as to the manner in which cytotoxic effects are induced. The contrast in killing efficacy between the two compounds is likely related to their size difference and their intrinsic abilities to penetrate the fungal cell wall. Unlike EO-OPE-DABCO, PPE-DABCO displayed a strong propensity to associate with soluble β-glucan, which is expected to inhibit its ability to access and perturb the inner cell membrane of Candida yeast. Furthermore, treatment with PPE-DABCO unmasked *Candida albicans* β-glucan, and increased phagocytosis by Dectin-1-expressing HEK-293 cells. In summary, cationic phenylene ethynylenes show promising biocidal activity against pathogenic *Candida* yeast cells, while also exhibiting immunostimulatory effects. While many questions were answered, many more remain to be investigated.

Chapter 2: Complexation of Oligo p-*Phenylene Ethynylenes with Oppositely-Charged Surfactants*

2.1 Introduction

One class of small molecules synthesized by Zhou and coworkers was shown to be biocidally active against both Gram-negative and Gram-positive strains of bacteria [18]. However, these compounds, composed of a phenylene ethynylene monomer with cationic end-groups, also suffer from efficient photodegradation under UVA irradiation [68].

These compounds can be grafted onto substrates [36] for use in settings where long-term biocidal applications, such as surfaces and clothing, may be desirable. Recent studies have shown that the OPEs are susceptible to photodegradation in water and air, which foreshadows the possible problem of loss of biocidal activity in long-term usage [68,69]. These "end-only" OPEs are particularly susceptible to photodegradation, with quantum yields of disappearance approaching 1% in water. The mechanism of photoreactivity is the addition of water or oxygen across one of the ethynyl groups. Our group's recent study of the photochemistry of these compounds focused on the photo-protective effect observed upon complexation of the OPEs with sodium dodecyl sulfate (SDS), an anionic surfactant [68]. The complex was formed with SDS either at the critical micelle concentration (8.3 mM) or below it at 0.33 mM, and in both cases a profound decrease in photoreactivity was observed. With the assistance of classical Molecular Dynamics calculations, this decrease in photoreactivity could be attributed to the desolvation of interfacial water from the OPE backbone. The OPE used in this study, EO-OPE (C2), is shown below in Figure 2.1.

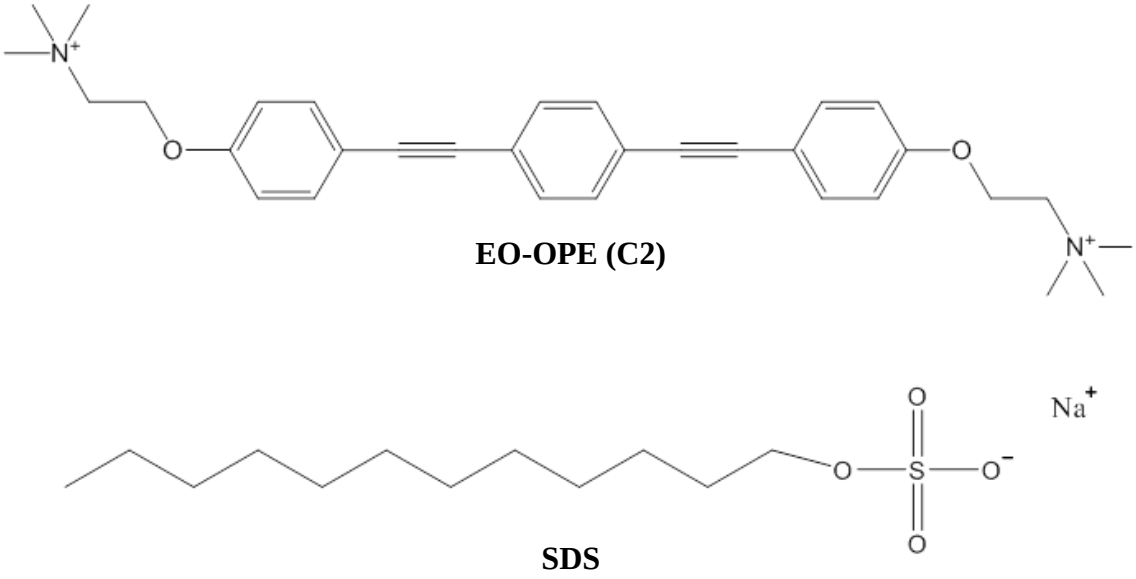

Figure 2.1: Compounds used in this study

The mixing of EO-OPE (C2) with SDS led to a highly photostable complex [68], but the biocidal activity of this complex was not known, nor was it clear what effects the surfactant would have on the biocidal activity of the OPE. In this study we explored the biocidal activity of the complex formed with EO-OPE (C2) and SDS against both Gram-negative and Gram-positive bacteria using flow cytometry and confocal fluorescence microscopy, focusing on the changes in biocidal activity incurred with prolonged irradiation. The results of this study revealed that these complexes can protect the OPE from prolonged damage by UVA light, while still maintaining a high light-induced biocidal activity against *Escherichia coli* and *Staphylococcus aureus*.

2.2 Gauging bacterial cell viability using dual-fluorescence flow cytometry

Flow cytometry gating and analysis were carried out as performed in previous studies of biocidal activity of OPEs [70]. Flow cytometry was utilized to determine the cell concentration of *S. aureus* or *E. coli* in the 0.85% NaCl-suspended bacterial stock solutions. The Accuri C6 (Becton Dickinson, Franklin Lakes, New Jersey) used was equipped with a blue laser that excites at 488 nm, as well as two filters: a green fluorescence filter (FL-1: 530 nm) and a red fluorescence filter (FL-3: 670 nm long-pass). A primary threshold ensured that only events exhibiting 40,000 FSC-A scatter units were included in the data, while a secondary threshold ensured that only events exhibiting 250 FL-1 fluorescence units (live stain fluorescence channel) were included. The core size of the flow cytometer was set to 10 μm, with a flow rate of 14 μL/min. 100,000 events were recorded in each sample. Cells were stained with 5 mM SYTO 21 (live stain; Life Technologies, Grand Island, NY) and 1.5 mM propidium iodide (dead stain; Life Technologies, Grand Island, NY) for 15 min prior to flow cytometry analysis. Flow cytometry gating schemes are shown for *S. aureus* and *E. coli* in Figure 2.2 and Figure 2.3, respectively.

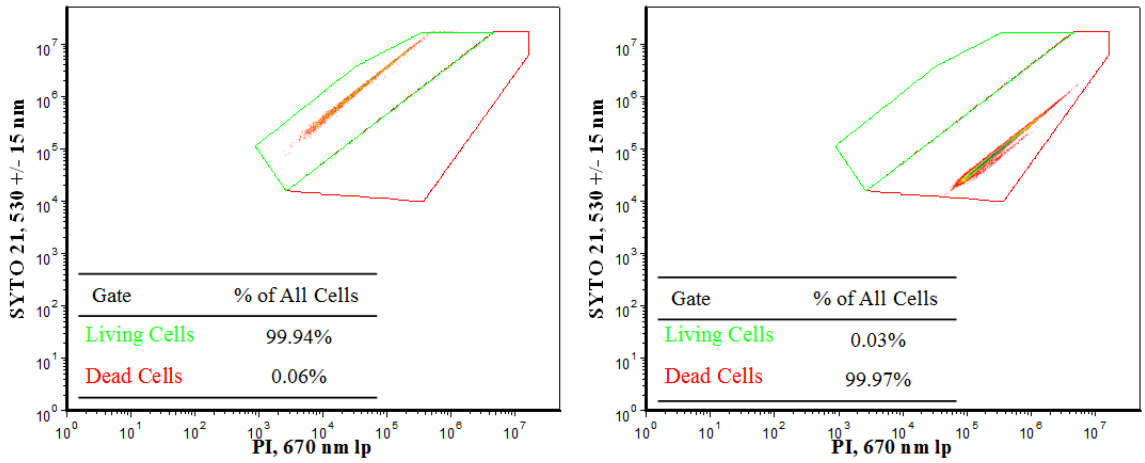

Figure 2.2: Example of flow cytometry gating scheme used for biocidal analysis of *S. aureus*, with a dark negative control in the left panel and a 70% EtOH positive control in the right panel.

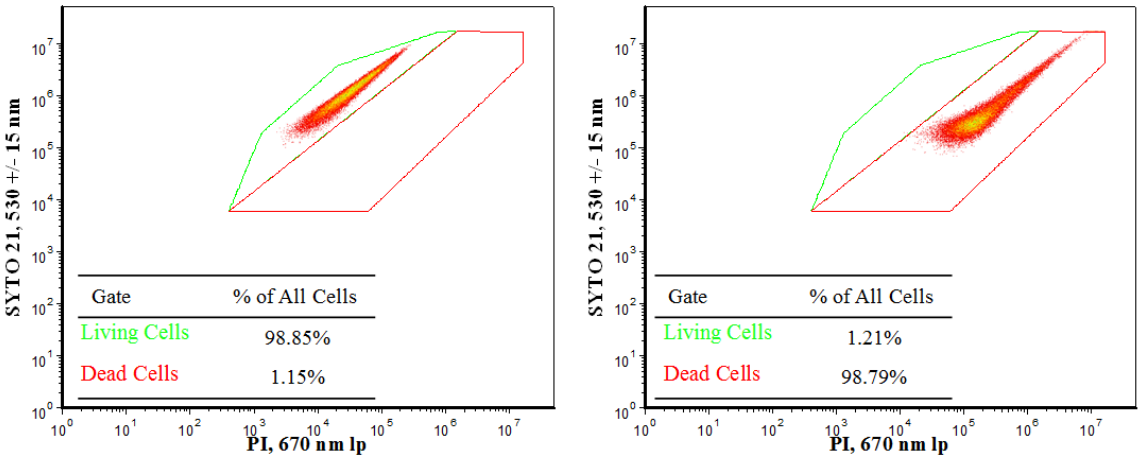

Figure 2.3: Example of flow cytometry gating scheme used for biocidal analysis of *E. coli*, with a dark negative control in the left panel and a 70% EtOH positive control in the right panel.

2.3 Cationic oligo-*p*-phenylene ethynylenes form complexes with surfactants for long-term light-activated biocidal applications

2.3.1 Effects of prolonged irradiation on biocidal activity of OPE

The bacterial killing of *E. coli* by EO-OPE (C2) as a function of pre-irradiation time is shown below in Figure 2.4, and the killing of *S. aureus* is shown in Figure 2.5.

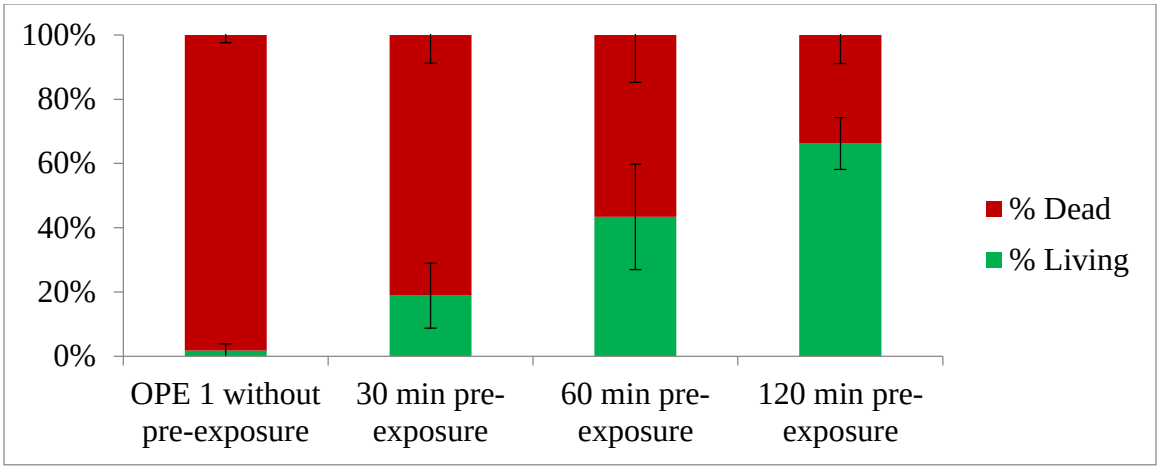

Figure 2.4: Biocidal activity of EO-OPE (C2) vs. *E. coli* with samples irradiated for 0, 30, 60, or 120 minutes prior to bacterial exposure.

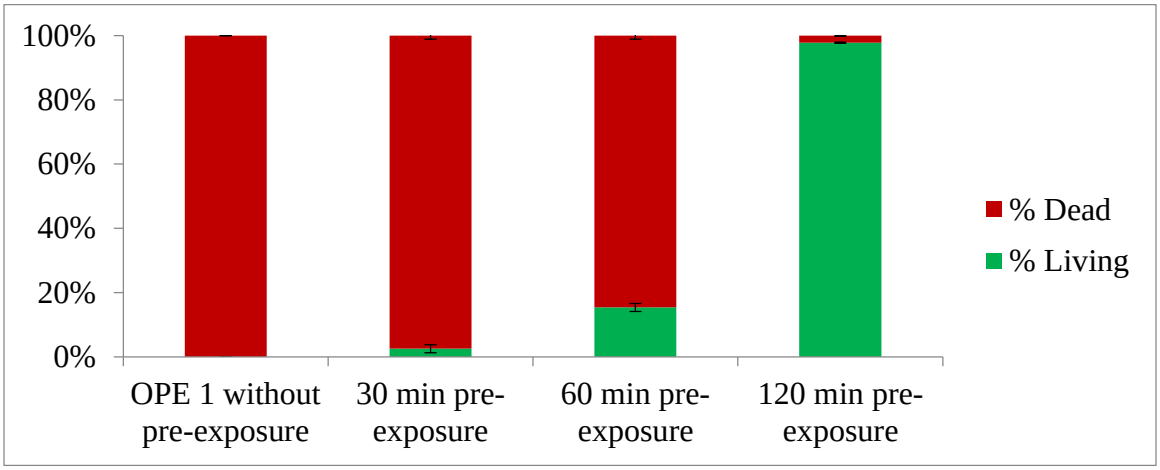

Figure 2.5: Biocidal activity of EO-OPE (C2) vs. *S. aureus* with samples irradiated for 0, 30, 60, or 120 minutes prior to bacterial exposure.

The results of the live/dead assay carried out using flow cytometry reveal a significant drop in biocidal activity of EO-OPE (C2), even after only 30 minutes of UVA irradiation prior to bacterial exposure. While this drop in biocidal activity is significant, there is a much quicker decrease in absorbance and fluorescence upon irradiation. It was reported that within 2 minutes of photolysis under the same conditions, the absorbance of the compound was observed to diminish and the fluorescence was completely quenched [68]. However, as shown in Figure 2.4 and Figure 2.5, there was still some biocidal activity at 30 minutes and beyond. This suggests that the initial photoproducts may still be biocidal, and may continue to function for a time, albeit less efficiently. However, by 2 hours of pre-exposure the biocidal activity is nearly lost for *E. coli*, and entirely lost for *S. aureus*. This result confirms that these compounds can be rendered harmless against bacteria with prolonged exposure to UVA light.

2.3.2 Effects of prolonged irradiation on biocidal activity of OPE-SDS complex

The bacterial killing of *E. coli* by OPE-SDS as a function of pre-irradiation time is shown below in Figure 2.6, and the killing of *S. aureus* is shown in Figure 2.7.

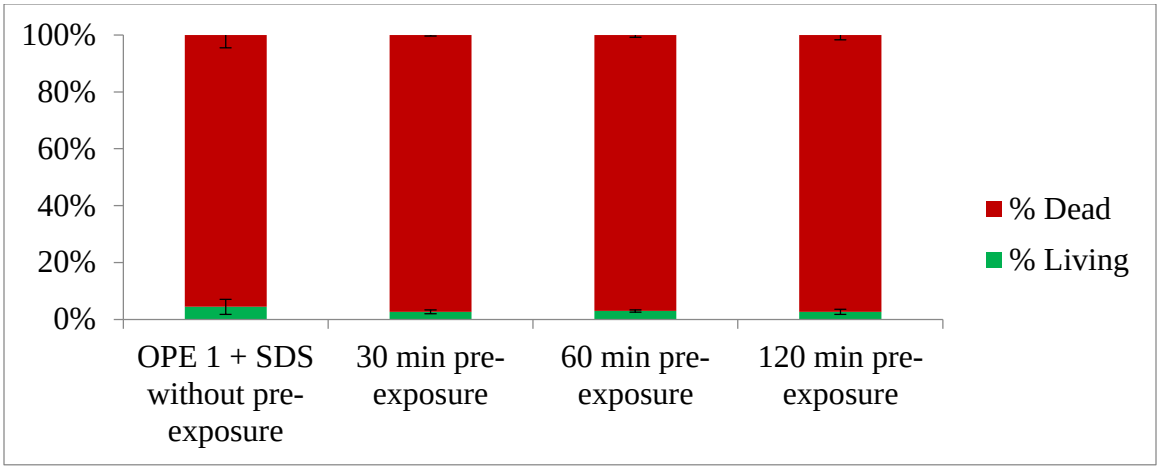

Figure 2.6: Biocidal activity of OPE-SDS vs. *E.coli* with samples irradiated for 0, 30, 60, or 120 minutes prior to bacterial exposure.

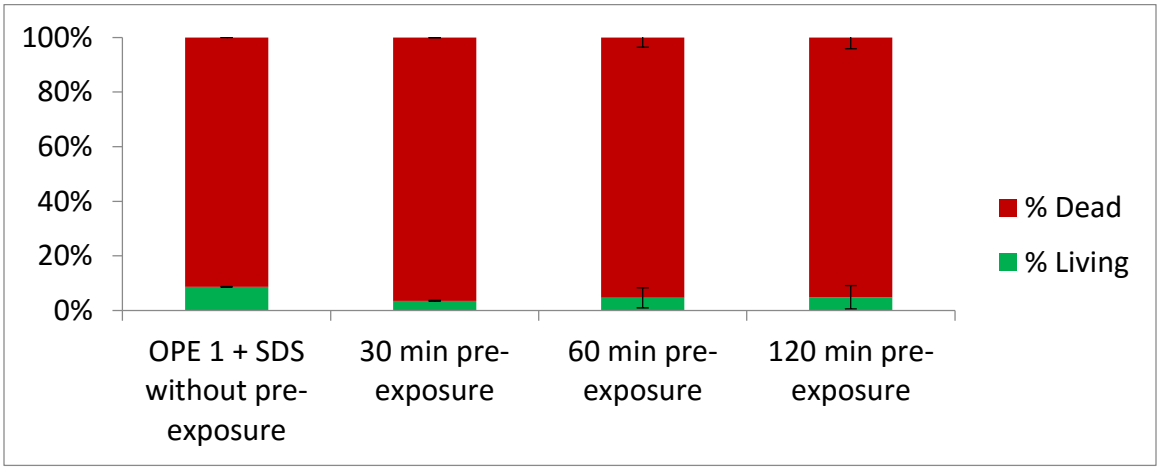

Figure 2.7: Biocidal activity of OPE-SDS vs. *S. aureus* with samples irradiated for 0, 30, 60, or 120 minutes prior to bacterial exposure.

The results shown in Figure 2.6 and Figure 2.7 reveal that the OPE-SDS complex is able to effectively kill both *S. aureus* and *E. coli* despite prolonged UVA irradiation prior to bacterial exposure. The killing effectiveness of both *E. coli* and *S. aureus* was maintained at more than 95%, even after two hours of irradiation. This result is significant, as it

supports the use of molecular self-assembly of surfactants onto OPEs to confer resistance to photodegradation. The structure of the aggregate is likely an H-aggregate with interfacial water removed by the interaction with the hydrocarbon tails of SDS, as was reported in a previous study [68]. SDS does not absorb light in the UVA region, nor should it react with singlet oxygen that is produced. Thus, complexation with SDS allows the OPEs to maintain their biocidal activity while being protected from photolysis.

It should be noted that while SDS itself is bactericidal to both *E. coli* and *S. aureus* at the critical micelle concentration (~8.3 mM [71]), a low level of killing is observed at the 40 µM concentrations used for complex formation. In addition, it was observed in the control experiments that the two bacteria exhibit different levels of resistance to SDS. As shown in Figure 2.8, below, *S. aureus* was observed to be viable in the presence of 0.33 mM SDS, yet this concentration was sufficient to achieve significant killing of *E. coli*. 40 µM SDS killed ~40% of the *E. coli* cells. In order to avoid this loss of viability in future studies, it may be useful to assess the performance of a surfactant with less innate biocidal activity, such as a phospholipid. When comparing *S. aureus* and *E. coli*, it is clear that *S. aureus* is much more resistant of the effects of SDS. In light of this fact and the close relation of Rosenbach *S. aureus* to methicillin-resistant *S. aureus* (MRSA), *S. aureus* serves as a useful model organism for this study as it reveals the biocidal activity of the OPE-SDS complex without any bias from killing by SDS.

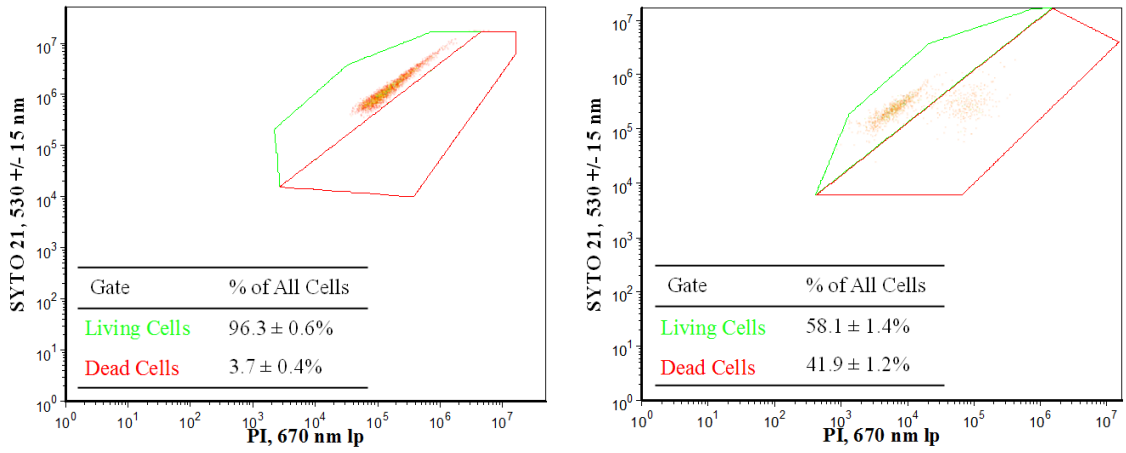

Figure 2.8: Flow Cytometry Analysis of *S. aureus* with 0.33 mM SDS Control (left) and *E. coli* with 40 µM SDS Control (right).

Overall, both strains of bacteria undergo ~5-10% less killing with the OPE-SDS complex compared with EO-OPE (C2) alone. In the case of *E. coli*, EO-OPE (C2) has 99% killing, while the OPE-SDS complex exhibits just 95% killing. Against *S. aureus* the results are similar, with >99% killing for EO-OPE (C2) and 95% for the OPE-SDS complex. With longer irradiations, the total killing will increase, as the *E. coli* and *S. aureus* were only irradiated with the samples for 30 and 15 minutes, respectively. However, it is difficult to determine whether this reduction in killing is simply due to a remainder of healthy bacteria or whether different phases of cell growth that are induced by stress contribute to this total.

2.3.3 Stress-induced Filament formation is observed with E. coli *and OPE*

While the analysis of *S. aureus* was relatively straightforward, confocal fluorescence microscopy revealed that *E. coli* cells exposed to EO-OPE (C2) or OPE-SDS were more

likely to undergo filamentous growth than untreated cells, as is shown in Figure 2.9, below.

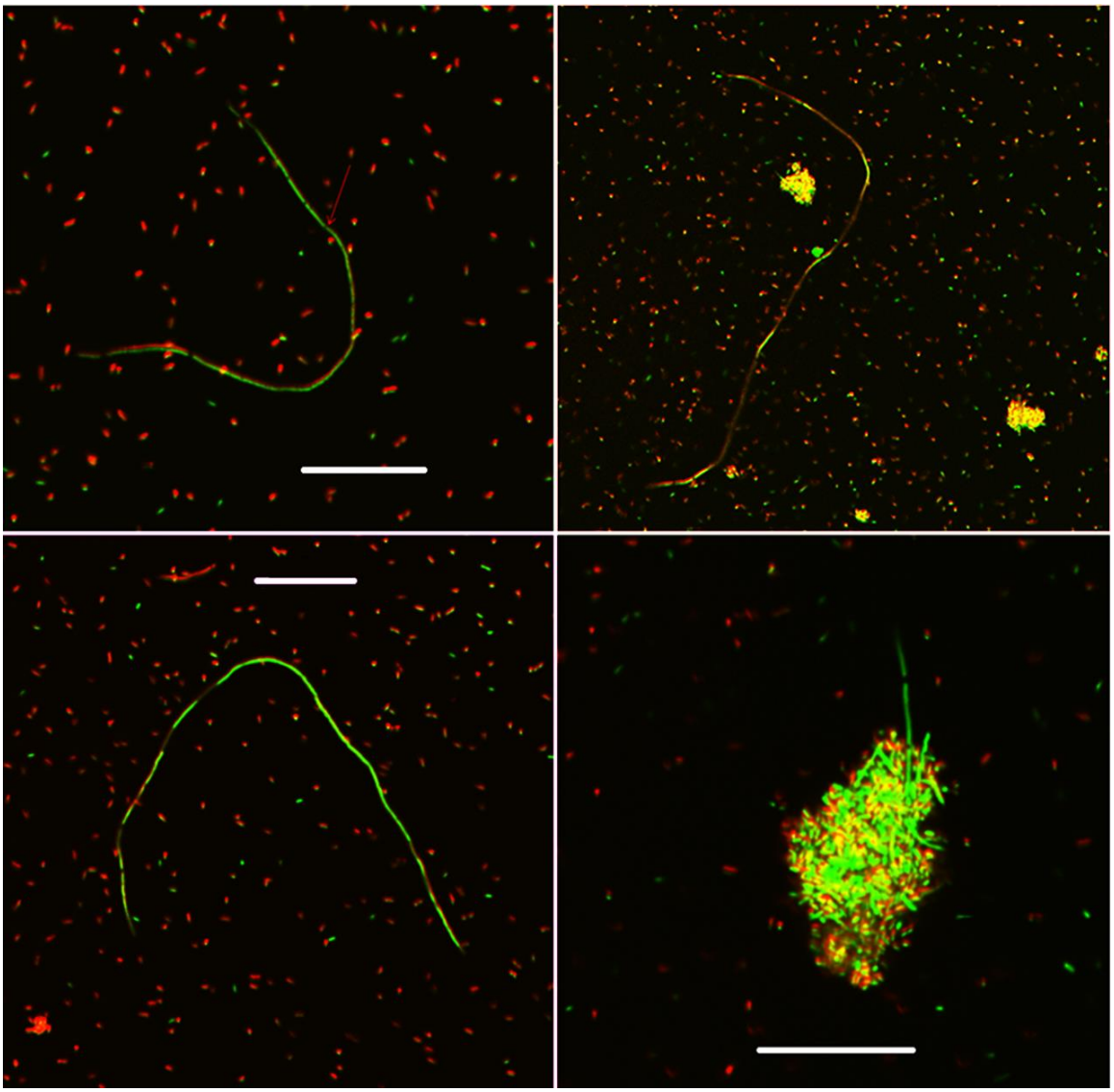

Figure 2.9: Filamentous *E. coli* observed upon exposure to EO-OPE (C2) or OPE-SDS; the white line is 20 µM. Samples were irradiated in UVA light for 30 min.

Cell elongation (or filamentation) is a known stress response that *E. coli* is prone to exhibit upon exposure to high heat [72], antibiotics [73], and UV irradiation [74]. Due to the lack of frequent occurrence of these filaments in a UVA-treated *E. coli* control (Figure 2.10),

such behavior is attributable to the presence of EO-OPE (C2) or OPE-SDS. While the mechanism by which these biocides elicit such behavior is not well understood, it is reasonable that the damage caused by the OPE causes a significant level of oxidative stress and degradation of DNA and proteins, since this has been demonstrated in previous work [27]. Filament growth does not appear to be mitigated by the complexation of EO-OPE (C2) with SDS. There are several likely possibilities for the cause of filamentation upon exposure to the biocides, concerning DNA and protein damage caused by reactive oxygen species (ROS) [75,76]. Oxidative stress is known to occur in *E. coli* when the ROS exposure exceeds the capacity of the cell to repair membrane and DNA damage, while still producing proteins to counteract ROS [77].

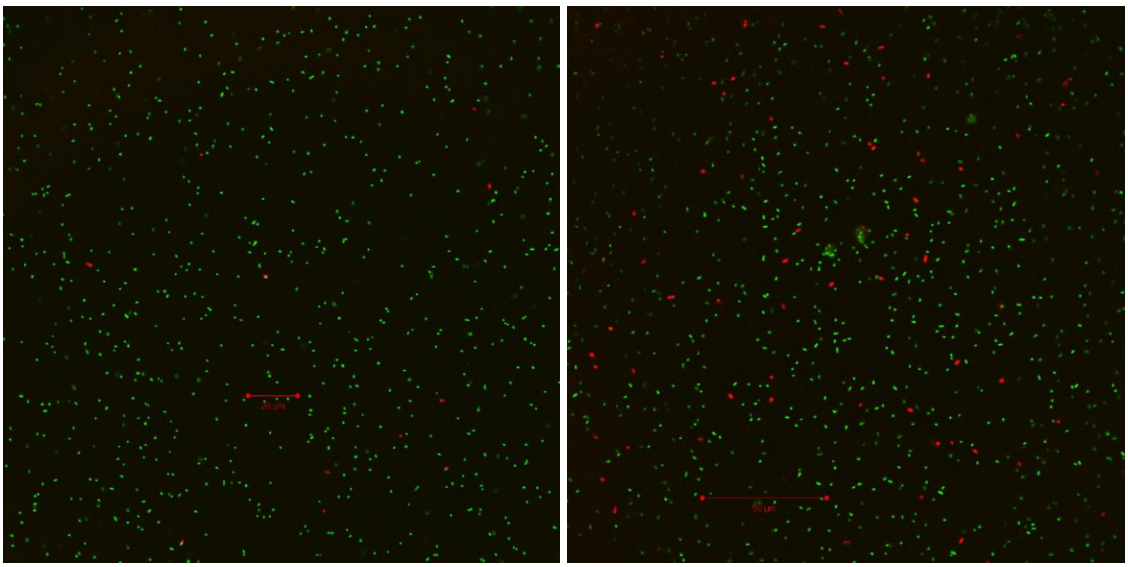

Figure 2.10: Confocal Fluorescence Microscopy images of *E. coli* Negative Control (left) and in 40 µM SDS (right).

Inspection of Figure 2.9 reveals several features that may indicate specific cellular structures formed by stress responses. The reduced amount of red fluorescence emitting

from the filaments suggests that the filaments have taken up less propidium iodide (dead stain) than the surrounding dead cells. It is important to note that the darker regions of the filament in the top-right image occur as a result of the filaments twisting conformation, causing it to leave the confocal plane. Evidence suggests that the short, dim sections of the filament, such as that indicated by the red arrow in the top-left image, arise from the "Z-ring" formed by FtsZ: an essential division protein that mediates septation [78–84]. FtsZ generally occupies regions of septation, where cell division is to occur. Due to its importance in bacterial cell division, FtsZ serves as a target for broad-spectrum antimicrobials, largely due to a lack of homology with human proteins [78]. Oxidative stress incurred by the presence of EO-OPE (C2) may be sufficient to elicit a depletion of guanosine-5'-triphosphate (GTP), which in turn would reduce the amount of active FtsZ. A lack of FtsZ has been attributed to the formation of filamentous cells [77]. An interesting feature that has been observed in several filaments is the occurrence of helical-shaped patterns within the filament that are brightly-stained with SYTO 21. Two images of these structures are shown below, in Figure 2.11.

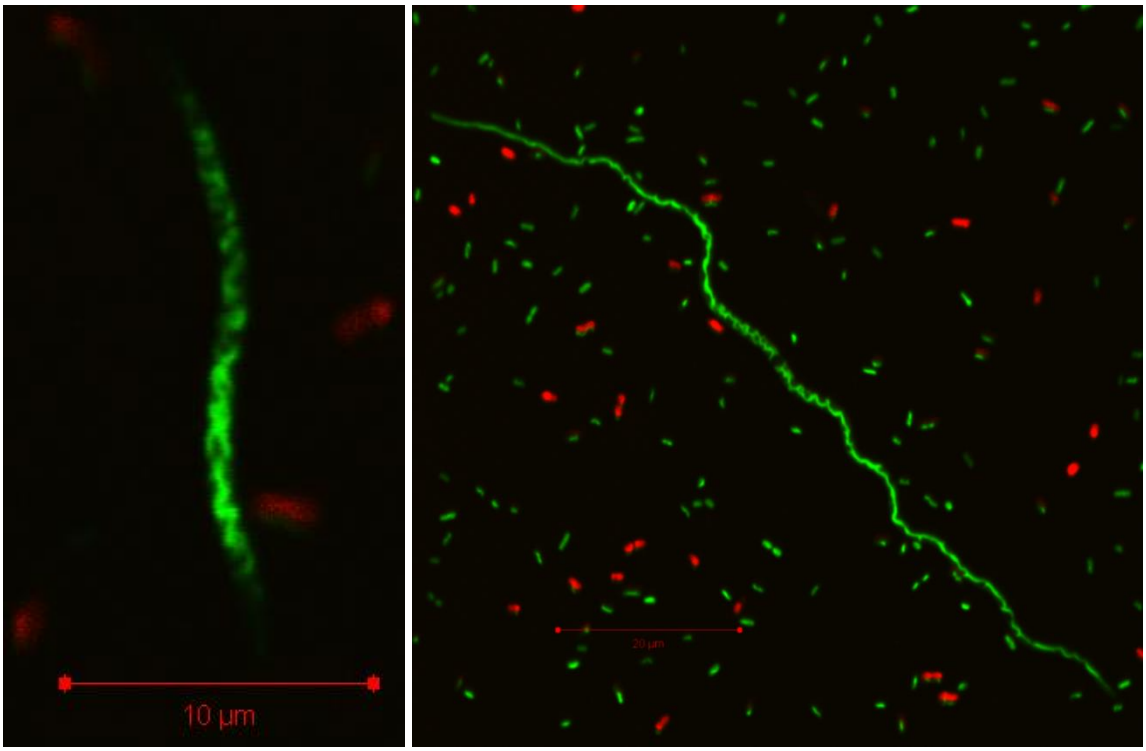

Figure 2.11: Helical structures within filamentous *E. coli.*

Though both SYTO 21 and propidium iodide are nucleic acid stains, the helical structures shown above, in Figure 2.11**,** resemble several previously observed structures of different cell-division proteins. In one study, helical GFP-tagged FtsZ structures were observed when FtsZ levels were greatly elevated [85]. MreB (an actin homolog) also maintains a helical structure similar to that seen in the left panel of Figure 2.11, and damage of this protein has been shown to induce filamentation [86].

In recent work, it has been shown that specific genetic mutations can give rise to elongated cells [87]. Filament formation may also be induced by oxidative DNA damage resulting in the SOS response, in which the protein SulA prevents cell division and further chromosome damage [83]. Boeneman *et al*. observed similar helical structures to those in the left panel of Figure 2.11 in *E. coli* by tracking GFP-labeled DnaA protein,

which is responsible for initiating chromosomal replication during a filamentous phase of growth [88]. Another protein that may induce DNA into a helical structure, RecA, is responsible for DNA repair during the SOS response and has a strong tendency to bind with ssDNA in a filament formation. As it has been shown in previous *in vitro* experiments [27], broad-spectrum damage caused by EO-OPE (C2) damages DNA and many of the mentioned proteins whose dysfunction may be responsible for filament formation. As the complex with SDS does significant killing and induces the same signs of stress as the OPE alone, it must only benefit from the photo-protection offered by the SDS.

2.3.4 Cell Clumping is observed with S. aureus *and OPE*

The damage caused by irradiation of *S. aureus* in the presence of EO-OPE (C2) leads to clusters of large numbers of cells. Confocal microscopy images of *S. aureus* irradiated with UVA light for 15 minutes in the presence of EO-OPE (C2) are shown below, in Figure 2.12.

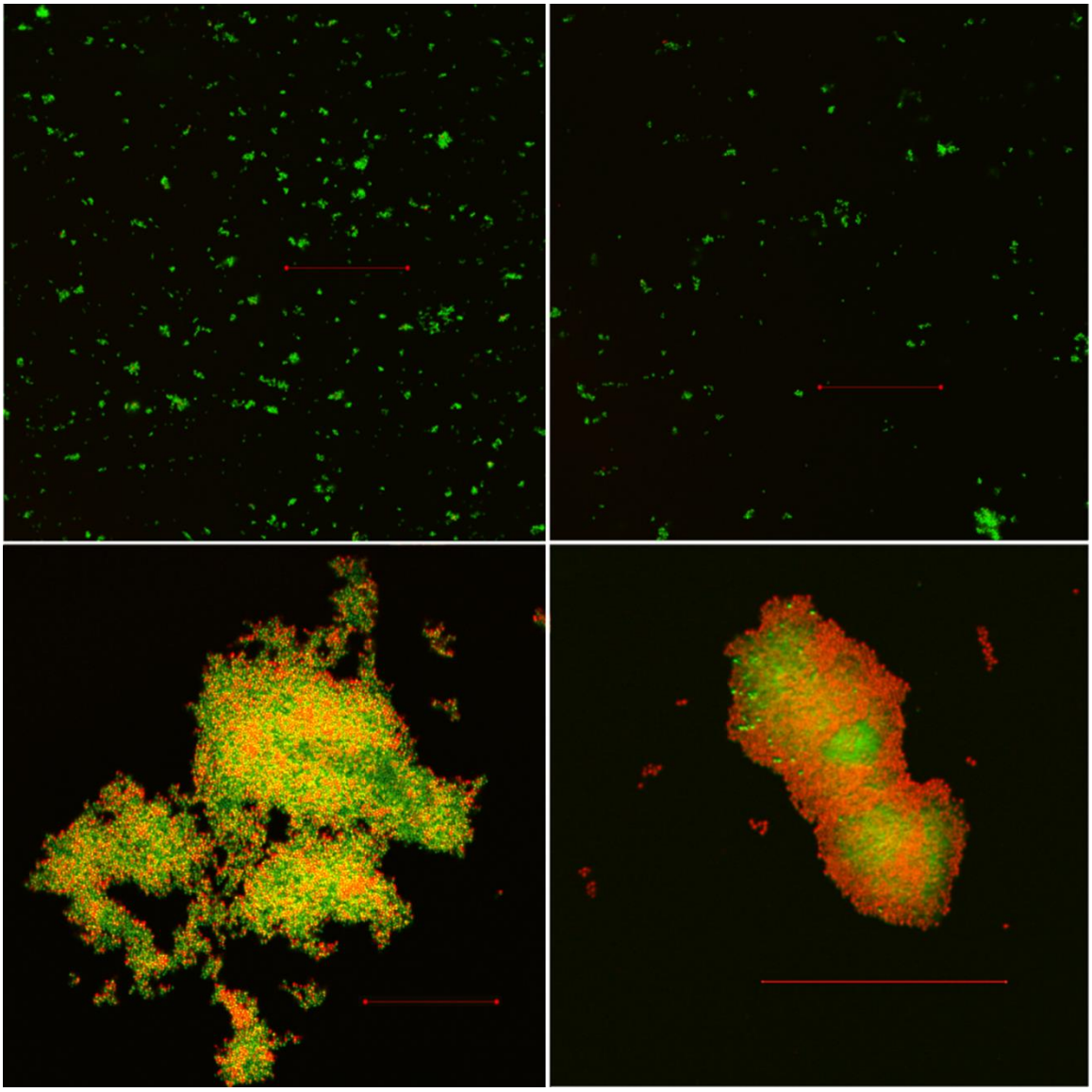

Figure 2.12: Confocal Microscopy images of *S. aureus*, where red and yellow indicate dead bacteria and green indicates live bacteria. The red line indicates 50 µM. Top-left: Negative control; Top-right: SDS control; Bottom-left: EO-OPE (C2) without SDS; Bottom-right: EO-OPE (C2) with SDS. Samples were irradiated in UVA light for 15 min.

In Figure 2.12, we can clearly see in the top row of images that *S. aureus* that was irradiated without EO-OPE (C2) formed clusters of ~10 bacteria. In the bottom panel we observe that large numbers of dead bacteria have agglomerated to form massive clusters, some larger than 100 μM in diameter. These clusters may be indicative of the initial stages of biofilm formation. Biofilm formation in *S. aureus* is a response to environmental stress and has been shown to be caused by UV exposure, metal toxicity [89], acid exposure [90], dehydration and salinity [91], phagocytosis [92], and several antibiotics and antimicrobial agents [93–95]. Previous studies reveal images of *S. aureus* biofilms that are remarkably similar to what we observe in the bottom row of Figure 2.12 [92,96–99].

Biofilm formation is both a stress-response and a result of released cell contents inducing adhesion between cells. The formation of *S. aureus* biofilms has been shown to be dependent on cell-lysis, so it stands to reason that the light-activated damage caused by EO-OPE (C2) could induce such a response [98–100]. It has also been suggested that DNA, proteins, and other cell contents play an important role in the initial aggregation of the cells [101]. It has been previously shown by Ying Wang and coworkers that the cells can be emptied as a result of the damage inflicted on the cell membrane [27]. It is likely that the DNA and proteins emptied from the cells induce the initial aggregation between cells that leads to these large clusters. We also observe in the bottom-right panel and the top of the bottom-left panel of Figure 2.12 that some of the clusters observed have an abundance of dead bacteria on the periphery of the cluster, while fewer dead bacteria are found in the center of the cluster. This is consistent with results observed in previous studies of *S. aureus* biofilms [98].

2.4 Activating the antimicrobial activity of an anionic singlet-oxygen sensitizer through surfactant complexation

Recent studies by the Whitten and Schanze groups have focused on cationic biocides based on the *p*-phenylene ethynylene repeat unit. Studies have shown that polymers based on this backbone are highly effective light-activated biocides at low concentrations [102]. The mechanism of their biocidal activity was shown to be the result of both membrane disruption and singlet oxygen generation upon irradiation to UV or visible light [102].

While the cationic small molecules and polymers are highly biocidal, the anionic analogs of these compounds do not exhibit significant antimicrobial killing in the light or dark. Malik and coworkers reported in 1990 that a singlet-oxygen sensitizing porphyrin can effectively kill bacteria, but that this effect is dependent on close association with the membrane [103].

A recent study used the surfactant sodium dodecyl sulfate to form a complex with a cationic OPE, protecting it from photodegradation over long irradiations due to the removal of interfacial water [68]. This complexation allowed for the retention of antimicrobial activity despite high doses of UVA prior to bacterial exposure, where the compound alone is completely photodegraded [70]. Additionally, it was previously observed that anionic and cationic OPEs from this series form similar complexes with oppositely charged surfactants through spectroscopic measurements [104]. In light of these results, the biocidal activity of an anionic OPE was compared with that of an OPE-surfactant complex. The anionic OPE, EO-OPE-SO3, and cationic surfactant, tetradecyl trimethylammonium bromide (TTAB), are shown below, in Figure 2.13.

EO-OPE-SO3

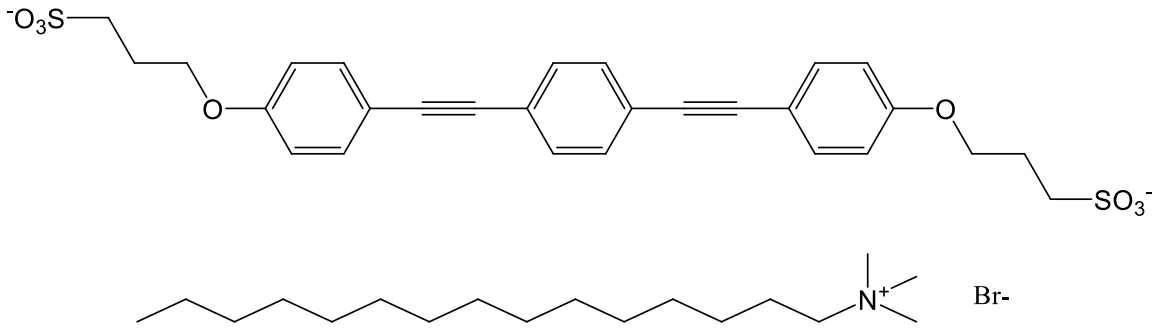

TTAB

Figure 2.13: Structures of compounds used in this study.

The biocidal activity of EO-OPE-SO3, TTAB, and a 1:4 complex between the OPE and TTAB were compared for both Gram-positive *S. aureus* and Gram-negative *E. coli* by flow cytometry, standard plating techniques, and confocal fluorescence microscopy. This study describes the influence that complexation with an oppositely-charged surfactant has on the biocidal activity of an anionic OPE. EO-OPE-SO3 and TTAB both have a low level of biocidal activity on their own at the micromolar range of concentrations used. Striking results indicate that the complexation of the OPE with the surfactant TTAB allows it to elicit strong antimicrobial activity, particularly under UVA irradiation. It is possibly that the cationic TTAB allows EO-OPE-SO3 to be transported into the cell, resulting in the strong biocidal response when exposed to light.

The results of biocidal testing using standard plating techniques is shown below for *S. aureus* and *E. coli*, in Figure 2.14 and Figure 2.15. Flow cytometry results were obtained as support for the plating and are shown in Figure 9.3 and Figure 9.4 (appendix) for *S. aureus* and *E. coli*, respectively. In addition, confocal fluorescence microscopy was used as described in the methods section to visualize and verify the biocidal measurements,

and images are shown in Figure 9.5 and Figure 9.6 (appendix).

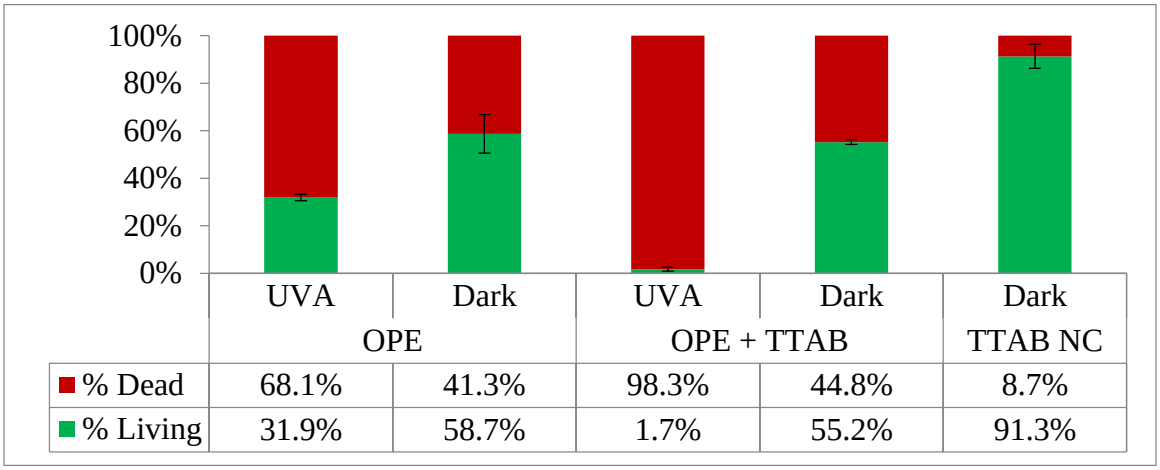

Figure 2.14: Viability of *S. aureus* after one hour of exposure to EO-OPE-SO3, OPE-TTAB complex, or TTAB alone. Biocidal activity is relative to that observed in a negative control exposed to UVA light for 1 hour.

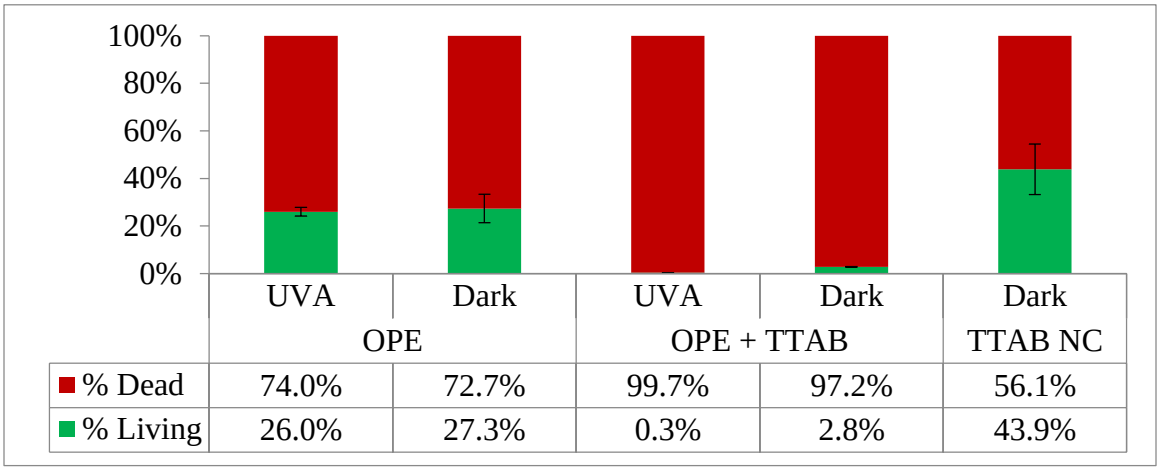

Figure 2.15: Viability of *E. coli* after one hour of exposure to OPE, OPE-TTAB complex, or TTAB. Biocidal activity is relative to that observed in a negative control exposed to UVA light for 1 hour.

The OPE-to-TTAB ratio was kept at 1:4 so that complex formation is assured and the concentration of TTAB (40 µM) is mostly non-biocidal. This concentration is far below the reported values (5 mM) for the minimum inhibitory concentration of TTAB against both *S. aureus* and *E. coli* [105]. In Figure 2.14 it is shown that only 8.7% of *S. aureus* was killed by TTAB alone. Higher killing is observed with *E. coli* (Figure 2.15, 56.1%) than with *S. aureus*. This differences between killing of Gram-positive and Gram-negative bacteria by surfactant has been observed previously with SDS [70]. As the concentration of TTAB used (40 µM) is far below the critical micelle concentration (4.3 mM [106]), the biocidal activity is relatively low and allows study of the effect of complexation of OPEs without a significant bias due to killing by TTAB.

The anionic OPE alone did exhibit modest biocidal activity against both strains of bacteria in both light and dark. As shown in Figure 2.14, 10 µM EO-OPE-SO3 killed 68.1% of *S. aureus* in the light and 41.3% in the dark. It is worth noting that immediate killing observed by flow cytometry showed lower killing than standard plating techniques, with 35.1% killed under UVA irradiation and 23.2% in the dark. Interestingly, the biocidal activity of OPE alone was higher against *E. coli,* with 74% killed under UVA and 72.7% killed in the dark. It is reasonable that the biocidal activity of this compound is low, as this has been previously shown for anionic OPEs [18]. It has been also shown with *in vitro* studies of model membranes that the anionic biocides do not affect the integrity of the membrane [102]. This is likely the result of unfavorable electrostatic interactions between EO-OPE-SO3 and the net-anionic bacterial membrane, which would result in the repulsion of the OPE sulfonates from the negatively-charged lipids.

The complex between the OPE and TTAB showed significant enhancement of biocidal activity under UVA irradiation compared to either EO-OPE-SO3 or TTAB alone. As shown in Figure 2.14, 98.3% of *S. aureus* were killed by the OPE-TTAB complex in the light. The killing in the dark was significantly lower (44.8%), with little change from the dark killing observed with the OPE alone. Against Gram-negative *E. coli*, the complexation with TTAB resulted in significant enhancement of both light and dark killing, as shown in Figure 2.15. Under UVA irradiation, the OPE-TTAB complex resulted in a 3 log reduction of bacteria, with 99.7% dead. Even in the dark, significant enhancement was observed, with 97.2% of *E. coli* killed by the OPE-TTAB complex. The concentration of 10 μM EO-OPE-SO3 is low compared to the concentrations that have been reported for 4-6 log killing for this class of compounds, and these levels could easily be reached with a doubling of the OPE concentration.

These results suggest that the surfactant enhances the ability of the anionic OPE to associate with the cell membrane, particularly in the case of Gram-negative *E. coli*. Since the primary mechanism of light-induced biocidal activity is singlet-oxygen generation leading to reactive oxygen species (ROS), and singlet-oxygen has a very short lifetime in water, close proximity to the cell is essential [107]. Bacterial cell membranes are net-anionic, and it is likely that the reason the anionic compound is not an effective biocide is that it cannot get close enough to affect the cell membrane with ROS [108–110]. Based on the results of this study one can predict that a layer of cationic surfactant surrounding the OPE provides the electrostatic attraction needed to bring the complex into close proximity of the membrane. The increased killing of *E. coli* (56%) by the TTAB alone compared to *S. aureus* (9%) suggests that the interactions between TTAB

and the Gram-negative bacterial membranes are greater. This is reasonable, as the structure of the Gram-positive cell wall is more complex, and the thick peptidoglycan outer layer may serve as a greater barrier to entry to the plasma membrane [111]. The outer membrane of the Gram-negative cell wall is known to contain negatively-charged lipids such as glycerophospholipids, and these would readily associate with the quaternary ammonium headgroup of TTAB. In addition, it is likely that the TTAB is involved in a cation exchange process with the lipids in the Gram-negative bacterial membrane.

While close proximity is enough to significantly enhance biocidal activity in the light, there may be additional mechanisms for the biocidal enhancement in both light and dark. *In vitro* studies of bacterial membrane mimics also show that the anionic OPEs do not induce membrane damage. It has been suggested that the structure of the OPE-TTAB complex consists of the aliphatic backbone of several TTAB molecules solvating the backbone of the OPE, while the quaternary ammoniums of the TTAB are associated with the sulfonate groups of the OPE [70]. With this structure, it is likely that TTAB molecules are able to associate on the periphery of the complex without electrostatic association with EO-OPE-SO3 sulfonates, due to favorable hydrophobic interactions between the hydrocarbon tails of the TTAB. This net-cationic complex would strongly interact with the net-negative bacterial membrane.

If incorporation of the OPE-TTAB complex into the membrane occurs, it would be likely that the TTAB would "dissolve" into the fluid environment of lipids in the membrane. Once disassociated from its "shield" of TTAB, the OPEs would repel the negative lipids in the membrane. There are two mechanisms by which this could enhance biocidal activity. First, the repulsion of lipids in the membrane may cause instabilities

that lead to membrane disruption or leakage, ultimately causing cell death. As the OPE is repelled, it may be ejected from the membrane into the cytoplasm, where it would then be able to easily damage cytoplasmic contents with ROS when irradiated. This will be explored in a future study by Langmuir monolayer insertion studies and classical molecular dynamics. The results of this study suggest that this method of surfactant complexation could be applied to many useful anionic singlet-oxygen sensitizers. Molecules such as tetraphenylporphyrin sulfonate could be viable candidates for a similar approach, and many different surfactants including lipids would be applicable.

Besides the implications for biocidal applications, this methodology may be useful for developing applications for transport across cell membranes and *in vitro* studies such as delivering cargo into vesicles. The enhanced ability of the OPE-TTAB complex to kill both Gram-negative and Gram-positive bacteria over either OPE or TTAB alone suggests that the TTAB plays a role in transporting EO-OPE-SO3 to a site where it can induce damage. The development of colloidal particles or vesicles to transport compounds has been well-studied for the purpose of enhanced drug-loading for drug delivery [112,113]. Many delivery strategies are developed to generally enhance uptake of drugs through different routes, such as oral or topical [114–116]. The use of surfactants to enable transport across biological membranes has been recently studied for delivery of cargo to specific regions, such as the brain [117]. These studies highlight the importance of colloidal effects for modifying the interactions between small molecules of interest and biological barriers such as membranes. This study shows through the enhancement of biocidal activity of a singlet-oxygen sensitizer with a simple bacterial model that ionic

surfactants and the resulting colloidal particles formed could be used for transmembrane delivery of ionic compounds.

2.5 Conclusions and Outlook

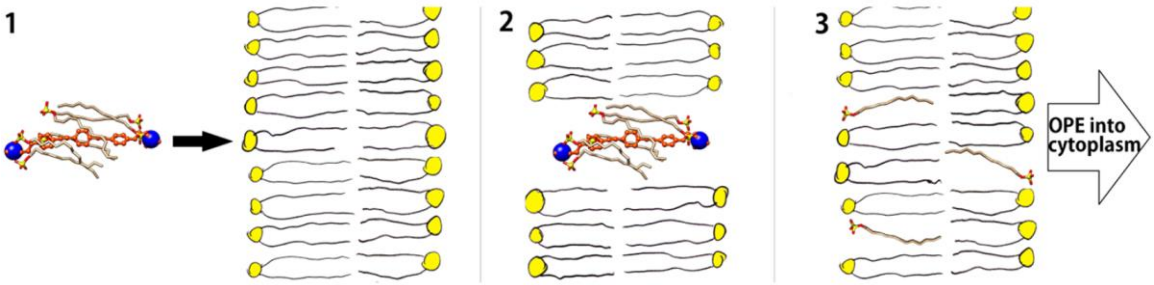

Figure 2.16: Schematic of the proposed mechanism behind the enhancement of light-activated biocidal activity. (1) The OPE−TTAB complex is formed and added to the bilayer (lipids shown with yellow headgroups). (2) The OPE−TTAB complex, with net positive charge, intercalates with the anionic lipid bilayer. (3) The TTAB from the complex dissociates into the bilayer and associates with anionic lipids; this results in a repulsive electrostatic force between the OPE and the bilayer, ejecting it from the membrane into either the periplasmic space (for Gram-negative bacterial outer membranes) or the cytoplasm.

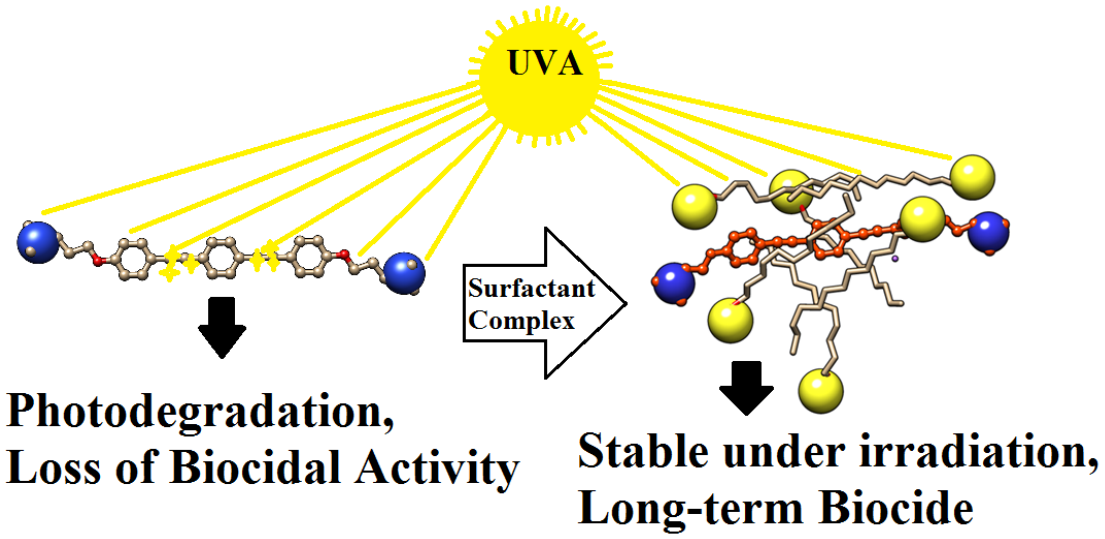

Figure 2.17: The formation of a surfactant complex leads to reduced photochemistry with water, allowing a *p*-phenylene ethynylene oligomer to have light-activated biocidal activity against both Gram-positive and Gram-negative bacteria despite prolonged irradiation.

The cationic "end-only" OPE, EO-OPE (C2), was shown to lose biocidal activity with prolonged exposure to UVA light, leading to an ineffective composition of non-biocidal photoproducts. The evidence of biocidal activity of EO-OPE (C2) after 30 minutes' irradiation, despite the complete loss of fluorescence and absorbance of the OPE, suggests that the early photoproducts are biocidal. The mixing of "end-only" cationic oligo-p-phenylene ethynylenes with the anionic surfactant sodium dodecyl sulfate forms a complex which has drastically reduced photoreactivity, but retains high light-activated biocidal activity against both Gram-negative and Gram-positive bacteria. Confocal microscopy revealed evidence of *E. coli* filamentation, which was attributed to oxidative stress or protein damage caused by the OPE. A different type of stress response was seen

in *S. aureus*, where large clusters of bacteria resembling the initial formation of a biofilm occurred with UVA exposure in the presence of EO-OPE (C2). This work will increase the capability for applications where protection of broad-spectrum biocides from sunlight for long periods of time is necessary. In addition to enhancing the lifetime of biocides, the same approach could possibly be applied to enhance the lifetime of sensors, dyes, and organic LEDs.

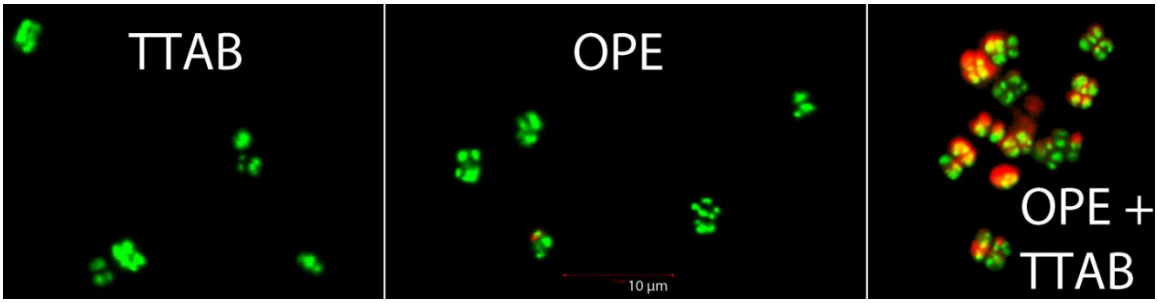

Figure 2.18: Activating the antimicrobial activity of an anionic singlet-oxygen sensitizer through surfactant complexation.

The biocidal activity of an anionic OPE was studied, and the effects of complexation with TTAB were studied by flow cytometry and confocal microscopy. EO-OPE-SO3 and TTAB separately had a marginal amount of biocidal activity in both the light and the dark for *S. aureus*, but *E. coli* was killed 50% by TTAB and 75% by the OPE. The complex formed between the two at a 1:4 OPE:TTAB ratio exhibited high light-activated biocidal activity, with 3 logs killing against Gram-negative *E. coli* and 2 logs killing against Gram-positive *S. aureus*. This study reveals an effective and inexpensive method for activating the biocidal activity of a non-biocidal singlet-oxygen sensitizing compound. In addition to providing a general method for enhancing interactions of anionic molecules

with bacterial cell membranes, this study also has implications for membrane transport and vesicle loading.

Chapter 3: *Biocidal Surfaces for Controlled Killing and Release of Bacteria*

3.1 Introduction

The ability to inactivate or "kill" bacteria on contact using an inherently biocidal surface is at the core of many strategies for reducing the risk of bacterial infections (especially nosocomial infections) in the healthcare sector [118–121] or for reducing bacterial biofouling and corrosion problems in industrial and other settings. One way biocidal activity has been achieved is by incorporating natural[122–126] or synthetic[127,128] antimicrobials such as quaternary ammoniums[129–131] and cationic conjugated polyelectrolytes into surface coatings.[52,132]

The control of the bacterial adhesion to solid surfaces, through control of surface free energy or "hydrophobicity", represents a second approach to preventing or controlling bacterial biofilms. Control of surface properties is also useful in applications for detecting harmful bacteria and for decontaminating e.g., air and water supplies. One particularly promising class of approaches uses dynamic manipulation of surface properties, for example, in surfaces that can undergo a hydrophobic-to-hydrophilic phase transition, and so switch from adhesive to non-adhesive states.[133–137]

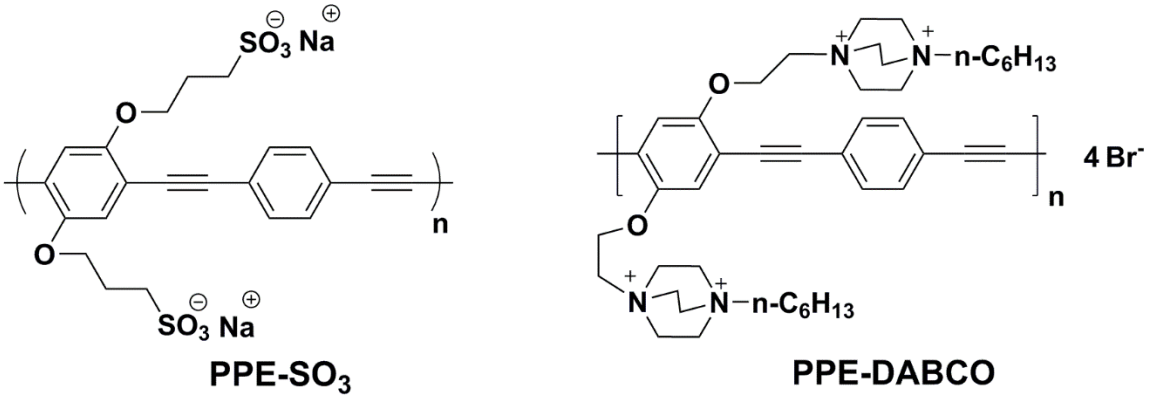

Figure 3.1: Structures of antimicrobial polymers used in this study: anionic PPE-SO_3 (left) and cationic PPE-DABCO (right).

Here we describe the fabrication, characterization and preliminary testing of an active, nanostructured surface that is functionalized with both biocidal CPEs (Figure 3.1) and temperature-switchable PNIPAAm. The surface was prepared by a combined approach involving layer-by-layer polyelectrolyte deposition and surface-initiated atom transfer radical polymerization (ATRP). The resulting surface exhibits both characteristics of the biocidal CPEs and temperature-switchable PNIPAAm. CPEs have been studied in great detail while suspended in aqueous medium,[12] or even on fabrics.[36] It is only recently that CPEs or OPEs have been studied on rigid substrates.[138] A layer of temperature-sensitive PNIPAAm was incorporated—the hydrophobicity of which varies as a function of temperature.[139–142] Bacterial cells, which were deposited onto the surfaces, were stained with nucleic acid stains to interpret membrane integrity, and thus, viability. These studies show that the added presence of PNIPAAm allows for controlled release of ~80% of all surface-adhered bacteria. Furthermore, moderate levels of cell death (between 60 and 70%) are observed following just a 1 hr exposure in the light. Cell viability and surface

concentration were quantified following imaging by confocal microscopy.

3.2 Self-Sterilizing, Self-Cleaning Mixed Polymeric Multifunctional Antimicrobial Surfaces

*3.2.1 Fabrication and Characterization of poly(*p*-phenylene ethynylene) Polyelectrolyte Films*

Earlier work [136] has shown that thin films of CPEs can be formed using a layer-by-layer (LbL) strategy, in which an initial layer of a CPE polycation (PPE-DABCO) is first physisorbed to a (negatively charged) glass substrate, then a second layer of a CPE polyanion (PPE-SO_3) is physisorbed on top, followed by a third layer of a CPE polycation (Figure 9.7). A higher degree of surface roughness is achieved by introducing a multilayer film, rather than just a single layer of cationic polymer, which is optimal for the binding of bacteria. Moreover, since polyelectrolyte complexes are insoluble in the presence of organic solvent, we speculate that a multilayer film confers an increased level of stability, relative to that of a single layer of cationic polymer. Additional layers of alternating charged polyelectrolytes could be built up if desired. Each pair of positive and negative layers is referred to as a CPE bilayer. For example, a layer of positive PPE-DABCO, a layer of negative PPE-SO_3, and then another layer of positive PPE-DABCO constitute 1.5 bilayers. Figure 3.2a shows such an LbL CPE film imaged by AFM (1.5 bilayers, substrate//PPE-DABCO//PPE-SO_3//PPE-DABCO, on a glass coverslip) on a wide scale (main image, 5 µm x 5 µm) and on a 10x magnified scale (inset, 500 nm x 500 nm). On the wide scale the film appears quite smooth, with only sub-nanometer

roughness. By scratching the film with the AFM tip, it was possible to show that the overall film is about 5 nm thick.

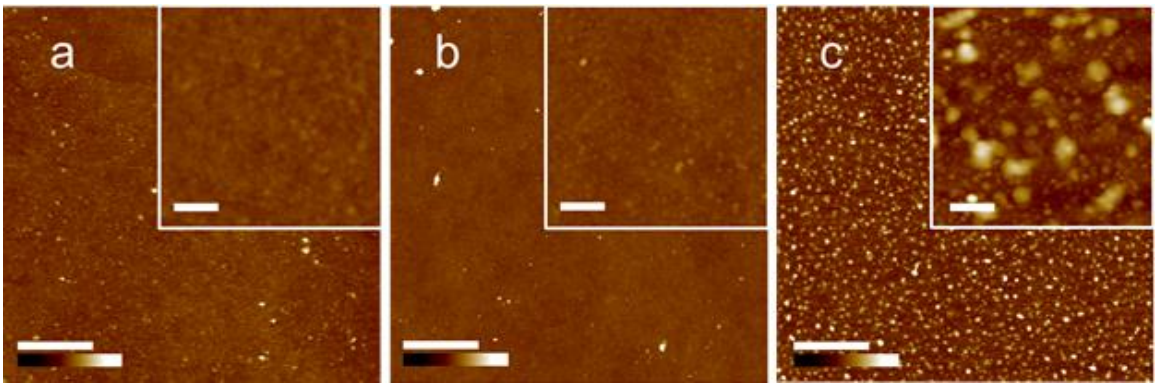

Figure 3.2: AFM tapping mode height images of active films on borosilicate glass substrates: a) LbL CPE film with the structure: substrate//PPE-DABCO//PPE-SO_3//PPE-DABCO. The main image is 5 µm x 5 µm (scale bar 1 µm). The inset image is 500 nm x 500 nm (scale bar 100 nm). Height scale color bar is 25 nm from black to white. b) Surface-polymerized film of PNIPAAm alone. Scale and color bars as in (a). c) Mixed CPE/PNIPAAm film created by forming the LbL layers in (a), followed by surface polymerization of PNIPAAm as in (b). Scale and color bars as in (a).

A higher resolution AFM image of the CPE film is shown in the inset of Figure 3.2a. Here, it can be seen that the surface is populated by distinct nodular structures averaging about 10-20 nm in size. The nodules are presumably due to aggregated CPE chains, either with themselves or with the polymer of opposite charge. It is also apparent that the top layer of PPE-DABCO may not be completely continuous; some regions of the surface descend by about 1.5 nm from the average height of the top layer, which is enough to reach down to the PPE-SO_3 layer below. Statistically, such regions of deficiency may extend to the glass substrate. Overall, the structure of the CPE LbL film as seen by AFM

is consistent with the model shown in Figure 9.7 (appendix), where regions with 1.5 bilayers are mixed with regions with fewer layers, including some regions of bare glass. The relatively low receding contact angles measured (Figure 9.8, appendix) for CPE glass substrates indicate a high degree of hydrophilicity, suggesting that the polymer swells in the presence of water.

3.2.2 Surface Polymerized PNIPAAm Films

Surface-polymerized PNIPAAm films have often been fabricated in the two-step process shown in Figure 8.5.[139] In this case, a free radical polymerization initiator is first attached to a glass substrate using a silane linkage; then PNIPAAm is grown from these initiator sites using atom transfer radical polymerization (ATRP) in alcoholic solution. Figure 3.2b shows an AFM image of a PNIPAAm film grown in this way. The main image shows the film on a wide scale, and the inset shows a higher resolution image. On both scales the film appears smooth and continuous, with a grain structure of about 10 nm visible at high resolution. It was not possible to measure the PNIPAAm film thickness directly in this case. The film could not be scratched, consistent with covalent grafting of the polymer chains to the glass. Films made under similar conditions were reported to have thickness of less than 10 nm.[132]

From images like those in Figure 3.2a, it was expected that thin LbL films of CPEs (especially films with only 1.5 bilayers) on glass might be discontinuous, having small regions of uncoated, solvent-exposed glass substrate surrounded by CPE. If so, a combined CPE/PNIPAAm film could be created by first depositing a thin LbL film, then attaching ATRP initiators in these exposed regions. Control experiments in which CPE

LbL films were exposed to the polymerization conditions for ATRP (toluene solvent overnight and alcohol solvent) showed no damage to the CPE LbL films.

Figure 3.2c shows a mixed CPE/PNIPAAm film fabricated by first doing a 1.5 BL deposition, followed by surface grafting of PNIPAAm, in accordance with the sequence shown in Figure 8.5. Both the wide scale main image and the high-resolution inset image now show a pattern of relatively large raised features on a smoother background. The size of these raised features varies widely, from about 5 nm to more than 50 nm in lateral dimension, and from less than 1 nm to about 5 nm in height. Overall this structure is consistent with the model shown in Figure 9.7 (appendix), where plumes of PNIPAAm have grown from a set of discrete sites where ATRP initiators where located originally. In Figure 2c the fractional surface coverage by PNIPAAm appears to be about 50%. In other samples with longer growth times, much higher surface coverage was seen, including some large areas (~1 μm) of nearly continuous PNIPAAm overgrowth of the CPE film. Overall, AFM shows that the 1.5 BL CPE film remains intact following exposure to acetone and methanol.

3.2.3 Biocidal Activity and Temperature-Switchable Release of Bacteria

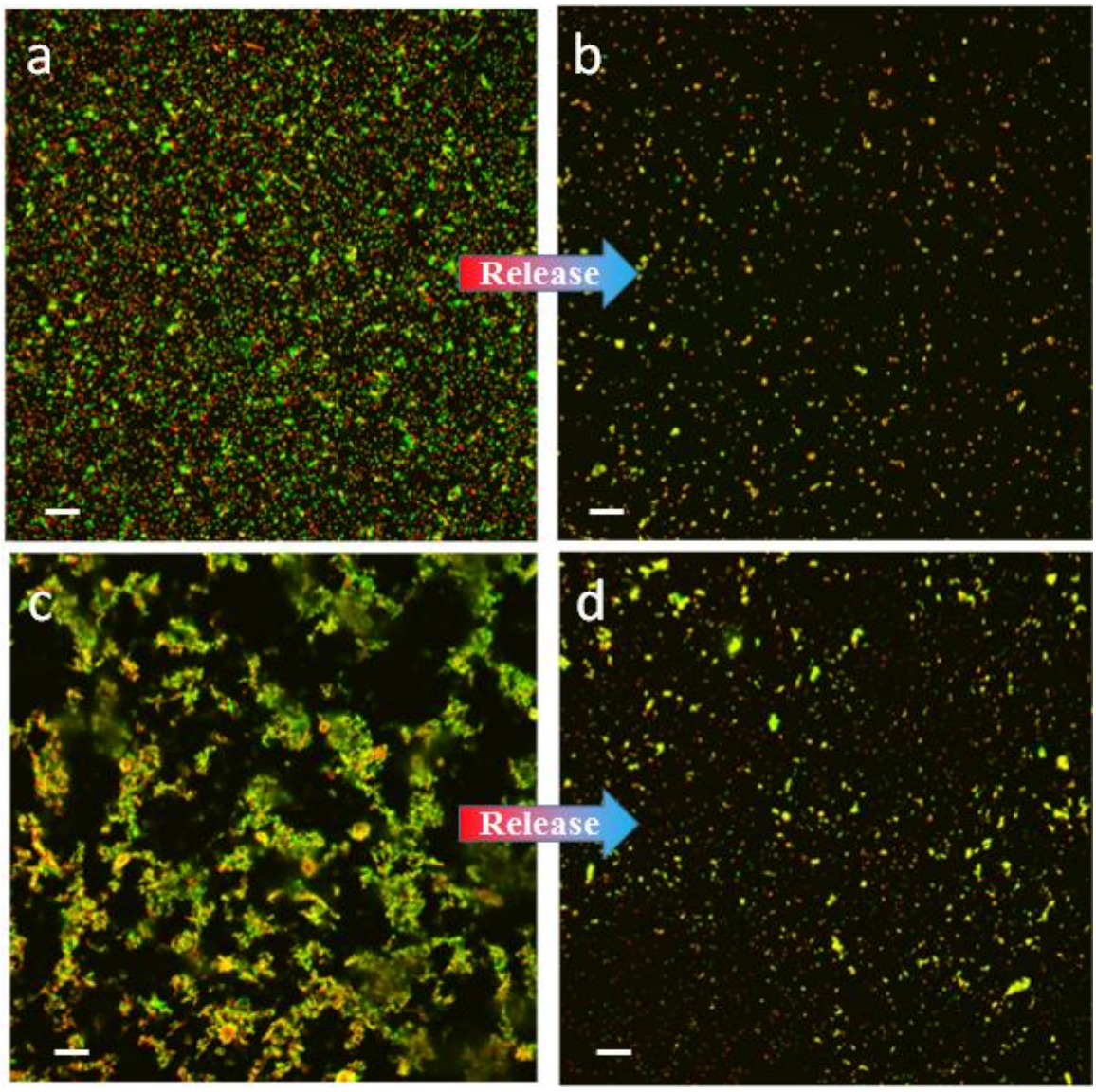

Figure 3.3: Fluorescence images of bacteria on combined CPE/PNIPAAm surfaces. Bacteria were adsorbed from suspension at a concentration of 1 x 10^7 cells/mL. a) *E. coli* after adsorption for 1 hr at 37 °C and 1 hr exposure to 420 nm light. Green cells are living; yellow or red cells are dead. b) *E. coli* substrate, shown in (a), following rinsing with 5 mL of 4 °C water. c) *S. aureus* after adsorption for 1 hr at 37 °C and 1 hr

exposure to 420 nm light. d) *S. aureus* substrate shown in (c) following rinsing with 5 mL of 4 °C water. Scale bars denote 20 μm in all images.

The ability of mixed CPE/PNIPAAm surfaces to inactivate bacterial cells and then release them was tested by a) depositing cells on the surface at high temperature (37 °C), b) exposing the adsorbed bacteria to visible light for a fixed length of time, c) staining the cells with "live" and "dead" fluorescent stains and imaging by confocal fluorescence microscopy, and finally d) releasing the cells with a cold-buffer rinse (4 °C). The fluorescent stains are propidium iodide (PI), a membrane-impermeable nucleic acid stain, and either SYTO 9 (for *E. coli*) or SYTO 21 (for *S. aureus*). Both SYTO 9 and SYTO 21 are membrane-permeable, so by this assay a "live" cell is one that stains only with SYTO 9 (or SYTO 21) and a "dead" cell is one that stains with both SYTO 9 (or SYTO 21) and PI. Live and dead cells were counted by capturing fluorescence images for each type of stain from a single field of view and then either counting cells by hand or computing total pixels above a minimum brightness threshold. Figure 3.3 shows confocal fluorescence images of several mixed CPE/PNIPAAm films similar to those in Figure 3.2c after adsorption of bacteria and then exposure to light. These are false color images: green corresponds to fluorescence emission from SYTO 9 (Figure 3.3a,b) or SYTO 21 (Figure 3.3c,d) alone, and hence identifies a live cell. Red or yellow (colocalized green and red) corresponds to emission from PI or both PI and a STYO dye, and hence to a dead cell. The top two images show the CPE/PNIPAAm surface after adsorption of *E. coli* (Gram-negative) at high temperature (37 °C), where the PNIPAAm is in its condensed, more hydrophobic state (Figure 3.3a), and after a gentle rise at low temperature (4 °C), where

PNIPAAm is in its polymer-brush, expanded hydrophilic state (Figure 3.3b).[143] The first image (Figure 3.3a) shows that many of the bacteria are dead (red or yellow). Figure 3.4 shows that about 70% of both *E. coli* and *S. aureus* bound to the mixed CPE/PNIPAAm film are killed after one hour of exposure to light. Films of pure CPE show slightly higher levels of killing, but a control surface with no film (bare glass) shows only about 20% killing under the same conditions. Figure 3.3c shows the results for Gram-positive *S. aureus* under conditions similar to those used for *E. coli*. Figure 3.4 shows that, in all cases—bare glass, CPE alone, or CPE/PNIPAAm —rod-like *E. coli* incurred slightly more damage than spherical *S. aureus*, which may be attributed to *E. coli*'s larger surface area-to-volume ratio[144,145] or the large differences in cell envelope between Gram-negative and Gram-positive bacteria. Importantly, for both bacteria, the addition of PNIPAAm only slightly decreases the killing capacity of the substrates, indicating that its presence does not interfere with the biocidal activity of the CPE film. The level of killing observed in cells attached to blank glass is higher than reported in traditional experiments by which bacteria are suspended in an aqueous buffer; this may be due to the fact that our cover slips were freshly piranha-cleaned. The surface is, therefore, chemically reactive due to the presence of hydroxyl groups, promoting an acidic environment that may damage bacterial cell walls.

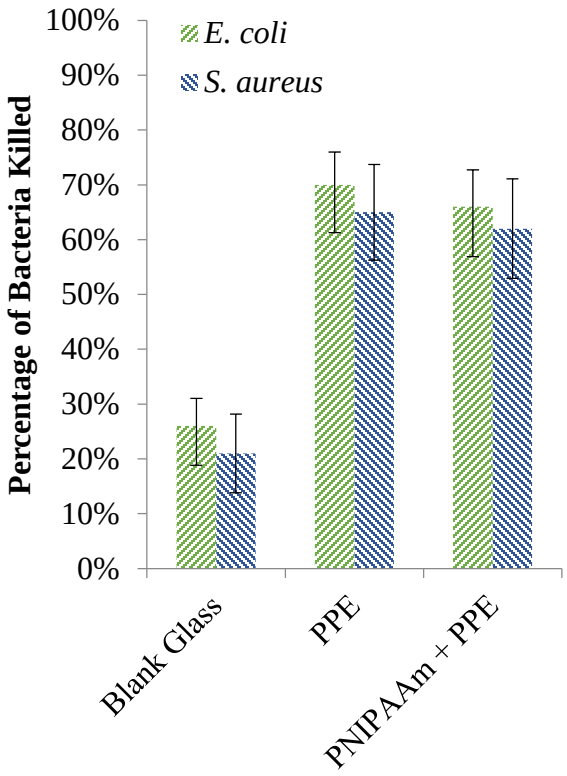

Figure 3.4: Cell viability following exposure to substrates following a 1-hour exposure 420 nm light. Viability determined by a cell's capacity to take up membrane-impermeable PI relative to membrane-permeable SYTO. Fluorescence of individual bacteria was examined by confocal microscopy and subsequently underwent image processing. Cell concentrations used to seed the surfaces were set to 1 x 10^5 cells/mL, according to flow cytometry.

The images in Figure 3.3b and Figure 3.3d show a pronounced release of bacteria, and Figure 3.5 quantifies the capacity of PNIPAAm and CPE-grafted cover slips to release bacteria from the surface upon being rinsed with cold water. After being exposed to the glass cover slips for a total of 2 hr—1 hr at 37 °C and 1 hr in 420 nm light—both Gram-negative *E. coli* and Gram-positive *S. aureus* exhibit significant attachment. At high cell

concentrations (Figure 3.3), clusters of *E. coli* on the surface rarely exceed 10 bacteria; conversely, *S. aureus* clusters approach 100 bacteria in nearly every case (clustering data not shown). Far less clustering is observed at low cell concentrations (Figure 3.7, appendix).

After confocal microscopy images were taken, substrates were rinsed with cold water (4 °C) to eject cells from the surface by altering the thermodynamic state of temperature-sensitive PNIPAAm. PNIPAAm undergoes a phase transition from a hydrophobic, collapsed state above about 32 °C (lower critical solution temperature, LCST) to a hydrophilic expanded state at low temperature. Exposure to cold water should therefore induce a change in surface chemistry and physical swelling of the PNIPAAm. The advancing contact angle of the CPE/PNIPAAm film exhibits a dependence on water temperature (Figure 9.8, appendix), albeit to a slight degree. We suspect that discontinuous PNIPAAm formation on the micron length scale fails to elicit a macroscopic change in hydrophobicity, resulting in only minute changes to the advancing contact angle. As can be seen in Figure 3.3, cold-water exposure strongly induces bacterial release of both *E. coli* and *S. aureus*, while not appearing to have an effect on cell viability. Larger clusters of *S. aureus* appeared more prone to temperature-directed release than smaller clusters. At least 75% of cells were ejected from the surface.

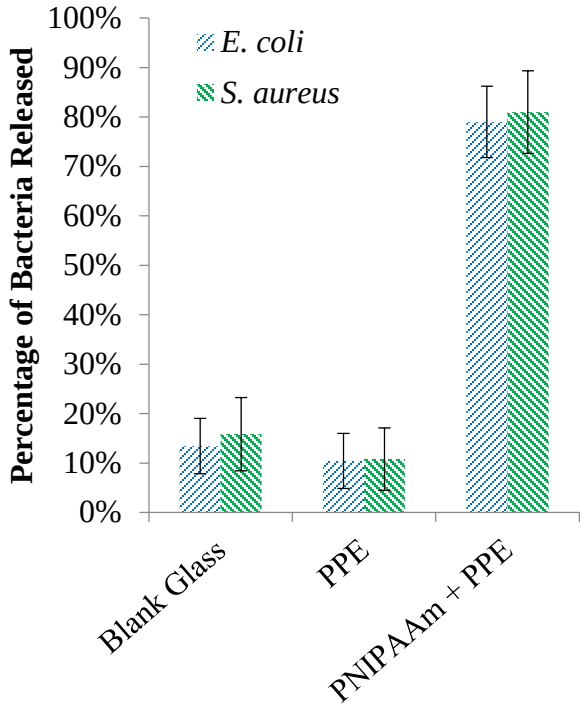

Figure 3.5: Release of surface-bound bacteria following rinsing with cold water. Bacteria were adsorbed at a concentration of 1 x 10^7 cells/mL. Cell release was quantified as the fraction of pixels occupied by bacteria following the rinse relative to that before rinsing.

While some degree of shear stress is necessary to cause bacterial release, Figure 9.9 (appendix) shows that release is not a solely due the shear stresses induced by the 5 mL rinse. When the rinse occurred at 37 °C, above the LCST of PNIPAAm, most bacteria remain attached, indicating that cell release is contingent on the PNIPAAm's transition into a hydrophilic expanded state. Relative to the blank glass substrate, slightly less bacterial release is observed with the CPE substrates, suggesting that the cationic nature of the polymer can, to some extent, prevent release caused by shear stresses. Using an anionic polymer as the uppermost layer would likely enhance the percentage of cells released, albeit at the expense of reduced absolute attachment and killing.

Recent work conducted by Yu *et al.*[138] elegantly demonstrates a technique by which OPE/PNIPAAm films are deposited by resonant infrared, matrix-assisted pulsed laser evaporation (RIR-MAPLE). Unlike the relatively simplistic dip-coating method described herein, the RIR-MAPLE technique allows for precise control of OPE-to-PNIPAAm ratios during film deposition. Despite this disparity, both films demonstrate a similar degree of biocidal activity and bacterial release. In particular, both films are able to kill 70% of *E. coli* in the presence of light, with release rates exceeding 60% in both cases. Both films fail to exhibit biocidal activity in the dark (data not shown), suggesting that all observed biocidal activity is predicated on the light-induced production of singlet oxygen and other ROS. Furthermore, in both cases, films absent of PNIPAAm failed to induce cell release upon being rinsed with cold water (Figure 9.10 and Figure 9.11, appendix). It is hereby hypothesized that the dip-coating deposition technique demonstrated herein could be improved using phenylene ethynylenes with a higher degree of biocidal activity.[146] It is likely that the fabrication process used in this study could be applied to surfaces other than glass, especially metal oxides. Polymer substrates such as polypropylene, polystyrene, or polyacrylates may also be used, assuming the polymer surface is primed for CPE and PNIPAAm deposition through a process such as oxygen plasma treatment.

3.3 Conclusions and Outlook

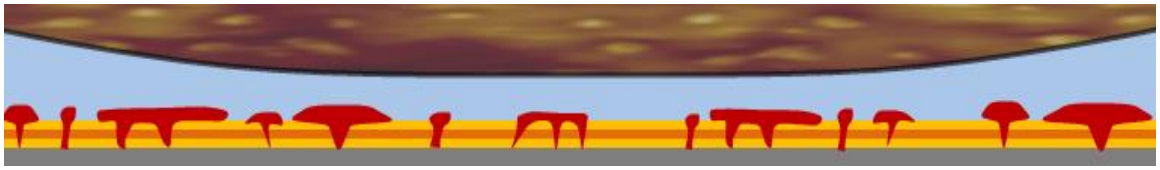

Figure 3.6: Large-scale structure of the random mixed CPE and PNIPAAm surface. Three layers of the CPE film are PPE-DABCO (light brown) and PPE-SO_3 (orange) on a glass surface (gray). The PNIPAAm (red) extends beyond the CPE layers to create islands of coverage. An incoming bacterium (brown) will be exposed to multiple PNIPAAm islands along with the CPE film.

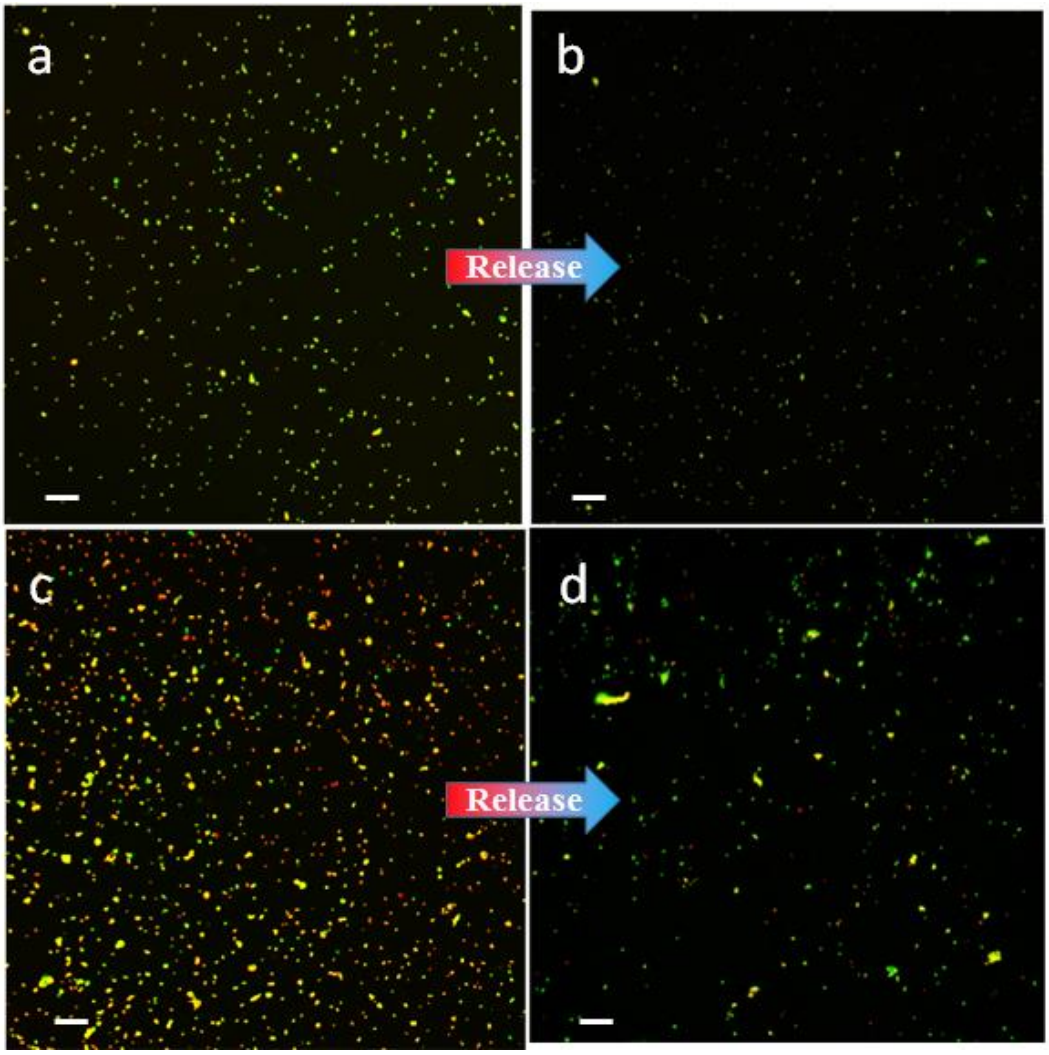

Figure 3.7: Fluorescence images of bacteria on CPE/PNIPAAm surfaces. Bacteria were adsorbed from suspension at a concentration of 1 x 10^5 cells/mL. a) *E. coli* after adsorption for 1 hr at 37 °C and 1 hr exposure to near-visible light. Green cells are living; yellow or red cells are dead. b) *E. coli* substrate, shown in (a), following rinsing with 5 mL of 4° C water. c) *S. aureus* after adsorption for 1 hr at 37 °C and 1 hr exposure to near-visible light. d) *S. aureus* substrate shown in (c) following rinsing with 5 mL of 4° C water. Scale bars denote 20 µm in all images.

A biocidal, temperature-responsive polymeric surface has been developed with two active materials: light-activated, biocidal CPE and temperature-switchable PNIPAAm. Despite the fact that the fabrication described herein is remarkably simple, levels of induced release and cell death are very similar to recently reported studies incorporating phenylene ethynylene-based materials with PNIPAAm [138]. Using a rapid and inexpensive dip-coating technique, 1.5 bilayers of CPE are applied to a glass cover slip and subsequently evaluated for biocidal activity. 65% of Gram-positive *S. aureus* were killed following an hour's exposure to 420 nm light, with 70% of Gram-negative *E. coli* being killed under identical conditions. Temperature-sensitive PNIPAAm was then incorporated to elicit bacterial release as a function of temperature. The addition of PNIPAAm only reduces biocidal efficacy to a small degree, yet grants the capacity for ~80% bacterial release with a simple cold water rinse (5 mL; 4 °C). This research suggests that such a surface could be incorporated to prevent biofouling and therefore, retain antimicrobial characteristics for prolonged periods of time.

Chapter 4: *A new class of* p-*Phenylene Ethynylene*

4.1 Introduction

Wudl and co-workers were among the first to report the synthesis and properties of conjugated polymers that feature ionic solubilizing groups (conjugated polyelectrolytes, CPEs) [147,148]. In another line of work, we have shown that cationic CPEs exhibit profound, light-activated, and dark broad spectral biocidal activity against Gram-negative and -positive bacteria, viruses, and biofilms [22].

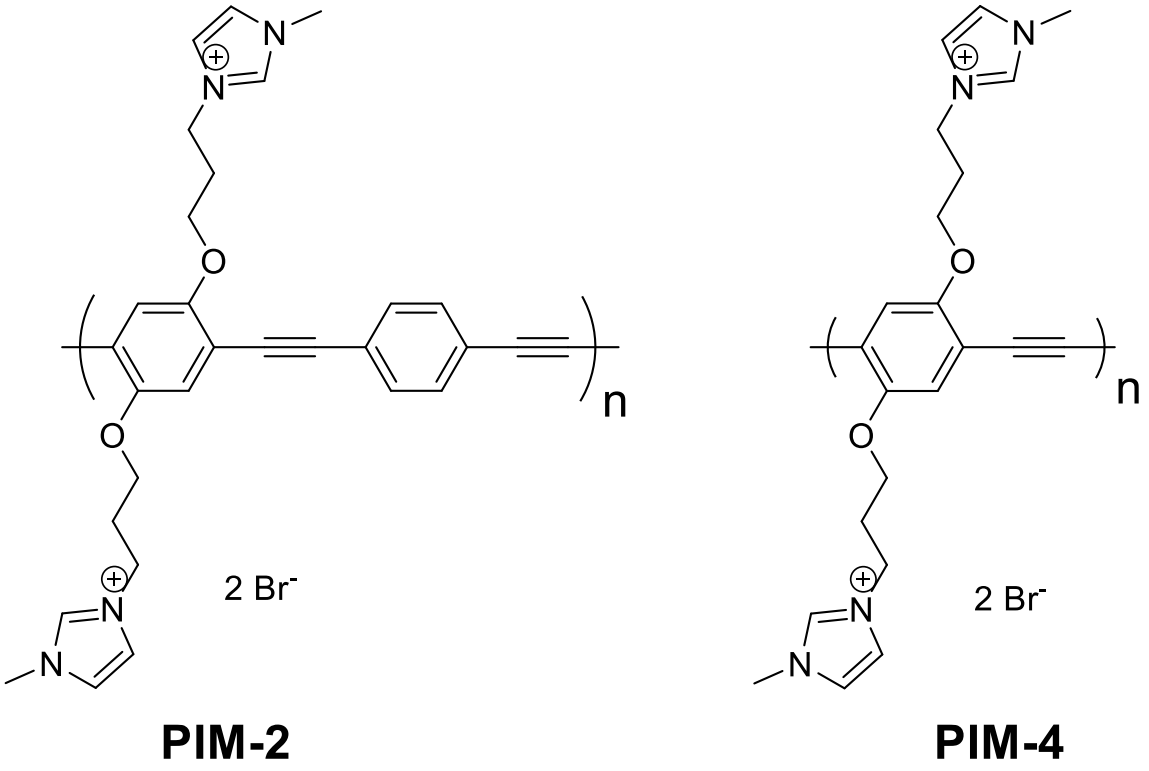

Figure 4.1: Structures of PIM-2 and PIM-4

As an extension of our previous work on cationic CPEs, here we report the synthesis and characterization of a pair of PPE-type polyelectrolytes (PIM-2 and PIM-4; Figure 4.1) that feature imidazolium solubilizing groups. As part of this investigation, we have

characterized the solution properties of the imidazolium CPEs, including assessing their tendency to aggregate, as well as their fluorescence quenching by anions. The quenching results show that the CPEs exhibit an amplified quenching effect, and they are quenched efficiently by PPi in a methanol solution and less strongly in water. The results are in accordance with the few previous studies that have explored the interaction of imidazole and imidazolium CPEs with anions [149,150]. In addition, a survey was carried out to assess the biocidal activity of the imidazolium CPEs versus *Escherichia coli* and *Staphylococcus aureus* as model Gram-negative and -positive bacteria. These results indicate that the imidazole CPEs exhibit pronounced light-activated biocidal activity at low concentration ($\leq$5 μg mL^{-1}) and activity in the dark at higher concentrations ($\geq$10 μg mL^{-1}).

4.2 Conjugated Polyelectrolytes with Imidazolium Solubilizing Groups: Properties and Application to Photodynamic Inactivation of Bacteria

4.2.1 Synthesis and Characterization of the Conjugated Polyelectrolytes

The studies described herein were conducted with the following objectives in mind. Our primary goal was to establish a synthetic route to incorporate the imidazolium moiety in the PPE backbone as pendant, cationic solubilizing groups for biocidal evaluation against varying bacterial strains in both light and dark conditions. Secondly, we were interested in investigating the photophysical properties of these polymers and their response to different fluorescence quenchers, as doing so would provide an understanding as to how the imidazolium moieties interact with the surrounding environment and quenching species. In light of such objectives, PIM-2 and PIM-4 were prepared following approach

and methods summarized in Figure 8.6. Additionally, both polymers were structurally characterized by ^{1}H NMR spectroscopy (Figure 8.7 and Figure 8.8).

4.2.2 Absorption and Fluorescence Spectra

Our previous work with CPEs has demonstrated that these polymers are soluble in water, as well in as polar organic solvents such as methanol. In addition, methanol was found to be a "good solvent" in which CPEs exist as individual chains (less aggregated), whereas water is a "poor" solvent due to its tendency to drive the formation of inter-chain aggregates [47]. As such, in this investigation we compared the properties of the imidazole polymers in water and methanol.

Figure 1 illustrates the absorption and fluorescence spectra of PIM-2 and PIM-4 in methanol and water, and the photophysical properties are summarized in Table 1. Both polymers feature a strong absorption band ($\lambda \sim 410 – 430$ nm) that is due to the π,π^* (HOMO-LUMO) transition of the poly(phenylene ethynylene) backbone. For both polymers, the band is slightly red-shifted in water compared to methanol. In addition, overall the band is red-shifted for PIM-4 compared to PIM-2. The latter effect is due to the increased frequency of –O-R substituents on the backbone of PIM-4 which raises the energy of the HOMO slightly [54]. The fluorescence of PIM-2 appears as a well-defined 0-0 band with $\lambda_{max} = 410$ nm along with a well resolved vibrational progression at lower energy that is characteristic of the PPE backbone. On the basis of previous work on PPE-type conjugated polyelectrolytes [48,52,54], we infer that the fluorescence shape indicates that PIM-2 exists in a mostly unaggregated state in methanol. Interestingly, in water the fluorescence of PIM-2 is significantly red-shifted and appears as a broad unstructured band. Similar emission spectra for PPE-type conjugated polyelectrolytes in water have

been observed [48,52], and effect is attributed to aggregation of the chains, with the emission arising from interchain aggregate states. In contrast to the properties of PIM-2, the fluorescence of PIM-4 appears as a broad, structured band with a small Stokes shift in both methanol and water. This behavior strongly suggests that PIM-4 is not aggregated in either solvent medium. The different behavior of this CPE in water may stem from the higher charge density on the polymer backbone, which renders the polymer with a higher degree of hydrophilic character, and also increases the inter-chain charge repulsion. Additional insight regarding the effect of solvent on the fluorescence of PIM-2 and PIM-4 comes from comparing the spectra in a series of methanol-water mixtures (Figure 8.9).

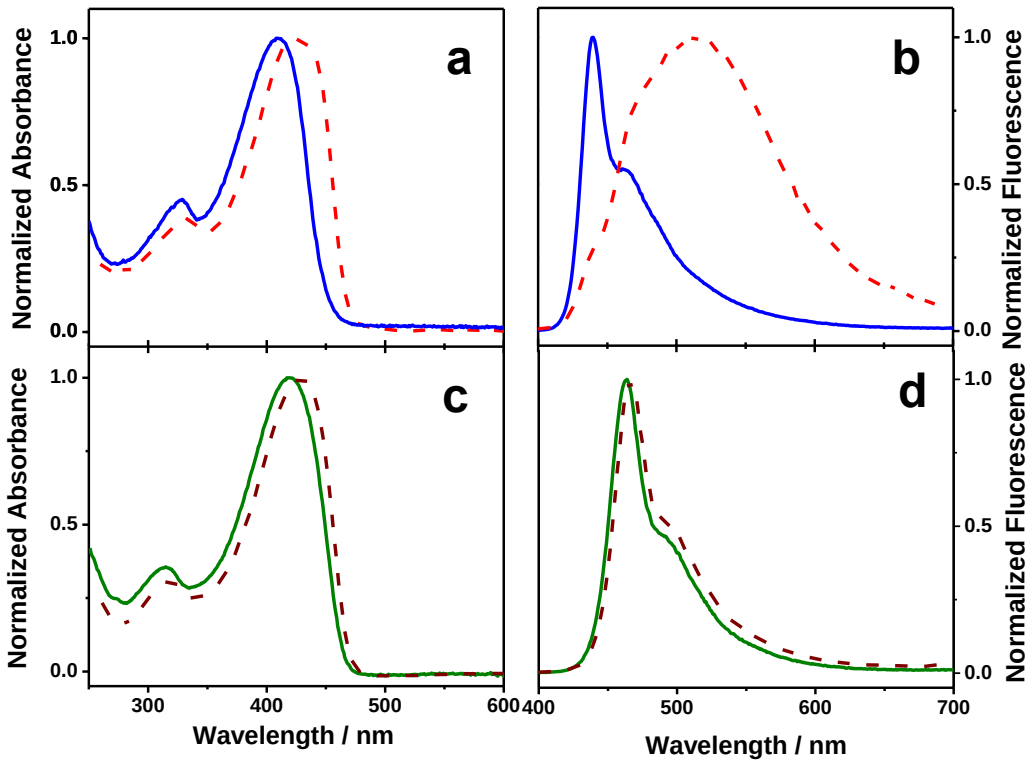

Figure 4.2: Normalized absorption (a) and fluorescence (b) of PIM-2 in methanol (blue solid lines) and in water (red dotted lines). Normalized absorption (c) and fluorescence (d) of PIM-4 in methanol (green solid lines) and in water (maroon dotted lines).

4.2.3 Biocidal Activity Studies

Testing of the light- and dark-biocidal activity was carried out by mixing bacterial suspensions with various concentrations of the CPEs and incubating under illumination (blue-violet light, λ = 420 nm) or in the dark for defined periods. Bacterial viability was assessed by using fluorescent live-dead stains with read-out using flow cytometry and/or confocal fluorescence microscopy, or by using standard plating techniques (Figure 8.15 and Figure 8.16). The results indicate that biocidal activity of both PIM-2 and PIM-4 is comparatively high in the presence of blue-violet light, and modest in the dark.

Figure 4.3 summarizes the results of the biocidal activity investigation of PIM-2 and PIM-4 against Gram-negative *E. coli*. As shown in Figure 4.3a, at a concentration of just 5 µg/mL, PIM-2 is able to kill approximately 90% of *E. coli* in the presence of blue-violet light, with somewhat higher efficiency at higher concentration. In the dark, however, a higher concentration of PIM-2 is needed (20 µg/mL) to exceed 90% killing. Similarly, as illustrated in Figure 4.3b, PIM-4 is relatively ineffective at low concentrations in the dark. However, unlike PIM-2, PIM-4 at 5 µg/mL was found to induce 2-log kill of *E. coli* under blue-violet light with 60 min exposure time, and it approaches 3-log kill with 30 min light exposure at 10 µg/mL concentration.

The difference between the kill effectiveness of PIM-2 and PIM-4 is less apparent with Gram-positive *S. aureus*. As seen in Figure 4.4, at 5 µg/mL concentration, both CPEs give ~96% killing with 1 h of illumination. When the concentration is increased to 10 µg/mL, both polymers exceed 3-logs of killing with only 30 min of irradiation. Both PIM-2 and PIM-4 appear to be very effective against Gram-positive *S. aureus* in the light.

Interestingly, the results show that, while PIM-2 is able to kill in the dark at concentration > 10 µg/mL, the same does not apply to PIM-4, which, even at an elevated concentration of 20 µg/mL, fails to elicit *S. aureus* killing. PIM-4 may be too hydrophilic to effectively perturb the peptidoglycan-dense cell wall of Gram-positive *S. aureus*, which may account for a lack of biocidal activity in the dark. Ion exchange with lipopolysaccharides in Gram-negative *E. coli* may contribute to Gram-negative cell damage.

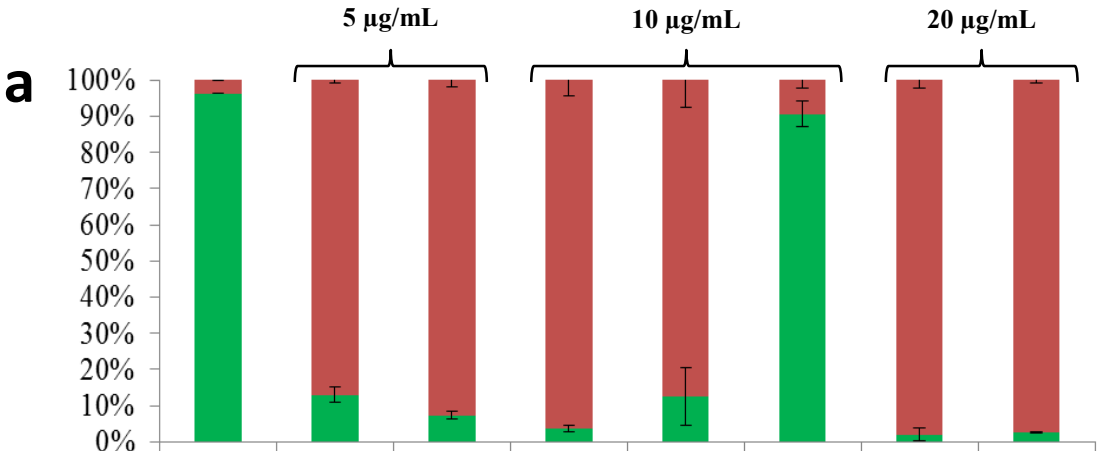

	420 nm NC	30 min; 420 nm	60 min; 420 nm	30 min; 420 nm	60 min; 420 nm	60 min; Dark	60 min; 420 nm	60 min; Dark
% Dead	3.63	87.09	92.77	96.44	87.49	9.31	97.98	97.49
% Living	96.37	12.91	7.23	3.56	12.51	90.69	2.02	2.51

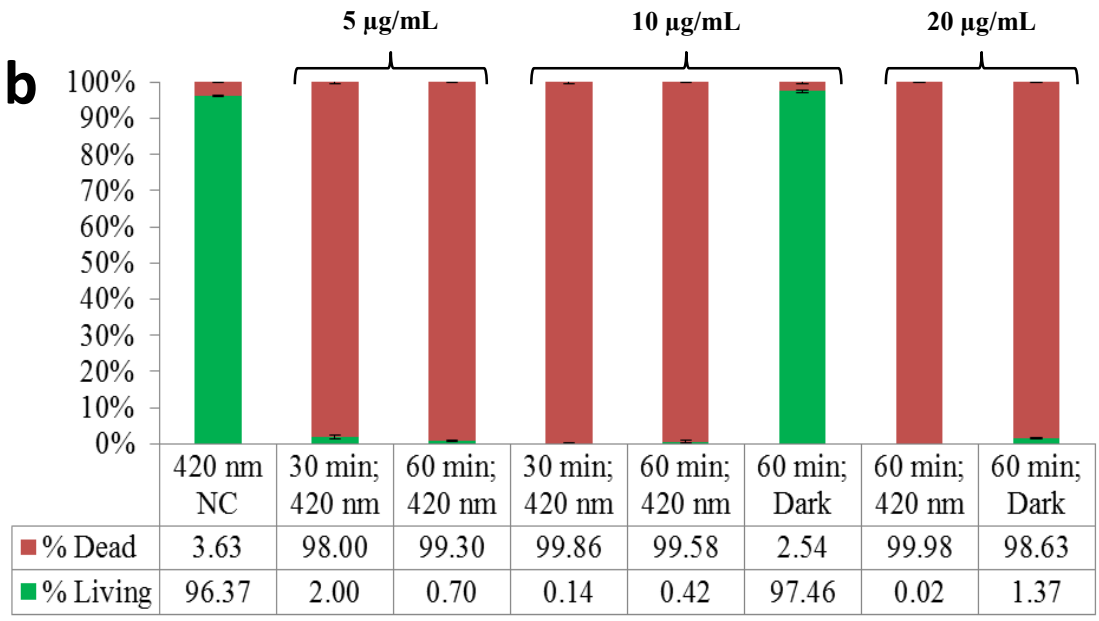

	420 nm NC	30 min; 420 nm	60 min; 420 nm	30 min; 420 nm	60 min; 420 nm	60 min; Dark	60 min; 420 nm	60 min; Dark
% Dead	3.63	98.00	99.30	99.86	99.58	2.54	99.98	98.63
% Living	96.37	2.00	0.70	0.14	0.42	97.46	0.02	1.37

Figure 4.3: *E. coli* viability against PIM-2 and PIM-4 upon exposure to visible light for various time intervals. In all cases, NC refers to the negative control, which did not contain biocidal polymer. In the bar graphs, red indicates % dead and green indicates % alive, as assessed by flow cytometry. (a) PIM-2 and (b) PIM-4.

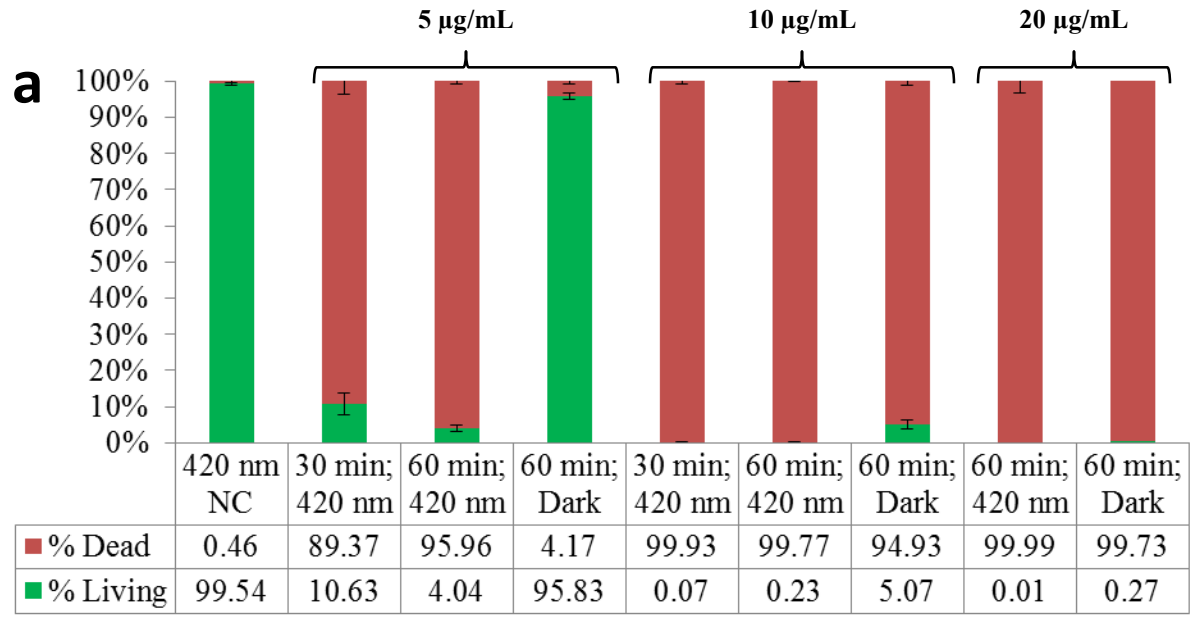

	420 nm NC	30 min; 420 nm	60 min; 420 nm	60 min; Dark	30 min; 420 nm	60 min; 420 nm	60 min; Dark	60 min; 420 nm	60 min; Dark
% Dead	0.46	89.37	95.96	4.17	99.93	99.77	94.93	99.99	99.73
% Living	99.54	10.63	4.04	95.83	0.07	0.23	5.07	0.01	0.27

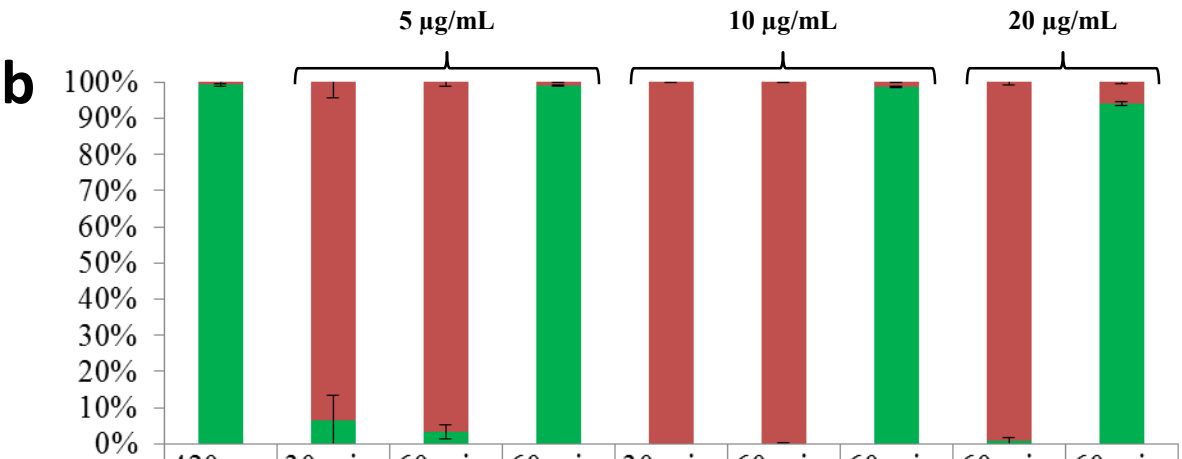

	420 nm NC	30 min; 420 nm	60 min; 420 nm	60 min; Dark	30 min; 420 nm	60 min; 420 nm	60 min; Dark	60 min; 420 nm	60 min; Dark
% Dead	0.46	93.56	96.71	1.03	99.99	99.87	1.25	99.11	5.96
% Living	99.54	6.44	3.29	98.97	0.01	0.13	98.75	0.89	94.04

Figure 4.4: *S. aureus* viability against PIM-2 and PIM-4 upon exposure to visible light for various time intervals. In all cases, NC refers to the negative control, which did not contain biocidal polymer. In the bar graphs, red indicates % dead and green indicates % alive, as assessed by flow cytometry. (a) PIM-2 and (b) PIM-4.

The biocidal activity of both of the imidazolium substituted polymers in the light is high as compared to other cationic CPEs based on the *p*-phenylene ethynylene backbone. To test the efficacy of PIM polymers, we compared them with biocidal activity of a cationic CPE with quaternized diazabicyclo[2,2,2]octane (DABCO) functionalized side chains (PPE-DABCO) that has been recently studied against *E. coli* [24]. We find that the biocidal activity of PPE-DABCO is only 43% at 5 µg/mL and 63% at 10 µg/mL after 1 h of 420 nm irradiation (Figure 8.17 and Figure 8.18). This suggests that the imidazolium functionality imparts a greater biocidal activity to the PPE motif compared to the DABCO moiety. The efficient light-activated bacterial killing of PIM polymers against

both Gram-negative and Gram-positive strains at low concentrations shows the potential of imidazolium functionalized PPEs as effective biocides.

Several recent studies have shown that imidazolium small molecules and polymers exhibit biocidal activity vs. Gram-negative and -positive bacteria [151,152]. Minimum inhibitory concentrations (MIC) for these materials vary widely, but they are generally less for Gram-positive bacterial strains, with values typically less than 100 μg/mL and in some cases as low as seen for PIM-2 and PIM-4 in the dark (≤ 20 μg/mL) [152]. The mode of action of the imidazolium molecules and polymers is suggested to be membrane disruption by interaction of the cationic imidazolium groups with the negatively charged phospholipid bacterial membrane. This hypothesis is supported by electron microscopy analysis of bacteria treated with the compounds, which provide evidence for membrane disruption [151]. We believe that the dark biocidal activity of the imidazole CPEs studied herein arises via a similar mechanism; however, it is quite clear that the biocidal activity of PIM-2 and PIM-4 is increased substantially in the light, likely due to a mechanism involving the sensitization of singlet oxygen and/or other reactive oxygen species (ROS) which give rise to rapid degradation of the bacterial membrane and other intracellular components.

4.3 Conclusions and Outlook

This study examined the photophysical properties, fluorescence quenching and light- and dark-activated biocidal activity of a pair of PPE-type conjugated polyelectrolytes that are substituted with cationic imidazolium groups. The polymers differ by the frequency of the imidazolium units, with PIM-2 having a pair of imidazolium units on every other

repeat, and PIM-4 having two on every repeat. Both CPEs are soluble in water and polar organic solvents. Fluorescence studies in water and methanol suggest that PIM-4 is molecularly dissolved in both media, whereas PIM-2 is molecularly dissolved in methanol, but exists in an aggregated state in water. The difference in the solution behavior of the two polymers is likely due to the difference in charge density on the backbones. PIM-4 exhibits a very high fluorescence quantum efficiency in both methanol and water, while that of PIM-2 is high in methanol, but somewhat less in water, again due to aggregation. Fluorescence quenching studies show that the polymers are efficiently quenched by the anionic electron acceptor anthraquinone disulfonate, with $K_{SV} \sim 10^6\ M^{-1}$, which is consistent with the typical "amplified quenching" effect seen for anionic CPEs when quenched by cationic electron acceptors such as methyl viologen [54]. The imidazolium CPEs are also quenched by PPi, with somewhat lower efficiency than that seen for anthraquinone sulfonate, but relatively efficiently nonetheless. The quenching by the diphosphate anion is believed to arise due to ion-induced aggregation [56], and this premise is supported by the fact that shifts in the absorption and fluorescence spectra are observed concomitant with addition of PPi.

The biocidal activity of PIM-2 and PIM-4 vs. *E. coli* and *S. aureus* was examined and compared to the previously studied cationic PPE-DABCO. The results find that both of the imidazolium CPEs exhibit pronounced light-activated biocidal activity, at concentrations as low as 5 μg/mL with 30 to 60 mins of exposure to blue violet light. Less pronounced biocidal activity is observed in the dark, yet the CPEs are still effective, with pronounced kill observed with 60 min dark exposure at 20 μg/mL concentration.

In conclusion, we have developed a pair of poly(phenylene ethynylene) based CPEs with cationic imidazolium side chains as cationic solubilizing groups. These CPEs exhibit strong light-activated biocidal activity. We also demonstrated that the photophysical properties could be manipulated to some extent by controlling the frequency of the imidazolium solubilizing groups on the CPE backbone. The preliminary results presented herein suggest that imidazolium substituted CPEs have promise for application as light-activated biocides and in fluorescent or optical biosensors.

Chapter 5: *Defending against Spore-forming Bacteria: Notorious Biowarfare Agents*

5.1I Introduction

Despite not always being differentiated from metabolically active individuals in early molecular studies, certain bacterial genera are actually capable of assuming a state of dormancy[153,154]. *Bacillus* species are unique, however, in that quiescence coincides with extreme core dehydration[155], thereby conferring profound resistance to stressful or extreme environmental conditions[154]. The process by which a bacterium changes its morphology into that of a dormant spore is referred to as sporulation. Sporulation can be triggered by numerous factors; most commonly, nutrient-deficiencies in the environment. Conversely, the process by which a spore resumes metabolic activity is known as germination, which physiologically occurs upon the introduction of nutrients and inhabitable temperatures. Unlike spores, which are robust and capable of host-independent survival for decades[156,157], vegetative bacilli undergo symmetric division and are highly vulnerable in the absence of a host[156,158,159]. It is through successful germination that spore-forming bacteria cause food spoilage and disease[160], which is why spores are often the focal point of decontamination regimens[161]. It is reasonable to believe that $^1O_2$ and any subsequently formed reactive oxygen species (ROS) were largely responsible for the damage inflicted upon *B. anthracis* Sterne spores, as reported by Lu and coworkers in 2005.

In this study, a novel class of oligo-*p*-phenylene ethynylene (OPE) is tested against *B. atrophaeus* and *B. anthracis* Sterne. Capped by cationic quaternary ammonium groups, these OPEs are linear structures that effectively kill numerous strains

of Gram-positive bacteria (*Staphylococcus epidermidis*, *Staphylococcus aureus*), antibiotic-resistant Gram-negative *Escherichia coli,* bacterial biofilms, fungi, and viruses[18,162–165]. OPEs strongly absorb light in the ultraviolet A (UVA) region[166], which ranges from 316-400 nm. UVA irradiation, therefore, confers OPEs with exceptional light-induced biocidal activity—which positively correlates with their high singlet oxygen quantum yield ($\Phi_{^1O_2}$) of 0.45±0.03[18], exceeding that of the PPE previously shown to kill *B. anthracis* Sterne spores[12].

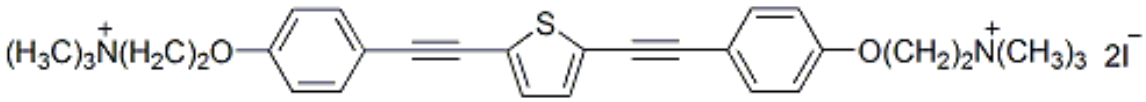

Figure 5.1: Structure of EO-OPE (Th,C2).

One particular OPE, referred to as EO-OPE (Th,C2), was synthesized with alkylammonium ends, and exhibits a lower rate of photobleaching than its OPE counterparts[18]. The presence of sulfur atoms in the chromophore increases intersystem crossing (ISC) from the excited singlet to triplet states, resulting in more efficient sensitization of singlet oxygen[18]. The studies described herein demonstrate the capacity of EO-OPE (Th,C2) to efficiently kill *B. atrophaeus* and *B. anthracis* Sterne vegetative cells in the presence of UVA light, while also exhibiting a lower degree of biocidal activity against spores. Furthermore, this compound was found to induce rapid germination of spores into colony-forming vegetative cells in the dark—a process monitored by scanning electron microscopy (SEM), standard plating techniques on tryptic soy agar, and flow cytometry.

5.2 Assessing the Sporicidal Activity of Oligo(*p*-Phenylene Ethynylenes) and their role as *Bacillus* Germinants

Preliminary experiments focused on appraising the biocidal efficacy of cationic EO-OPE (Th,C2) based on its ability to deactivate *Bacillus atrophaeus*: a nonpathogenic surrogate of *Bacillus anthracis*.[167,168] OPE-induced cell death was inferred using a complementary set of nucleic acid stains such that bacteria with intact cell membranes exhibit uptake of SYTO 21, while only cells with compromised membranes exhibit uptake of PI. In these studies, flow cytometry was utilized to gauge cell viability by rapid interrogation of dual-stain fluorescence[22]. Figure 5.2 illustrates flow cytometry-reported fluorescence of stained *B. atrophaeus* vegetative cells following various treatment conditions.

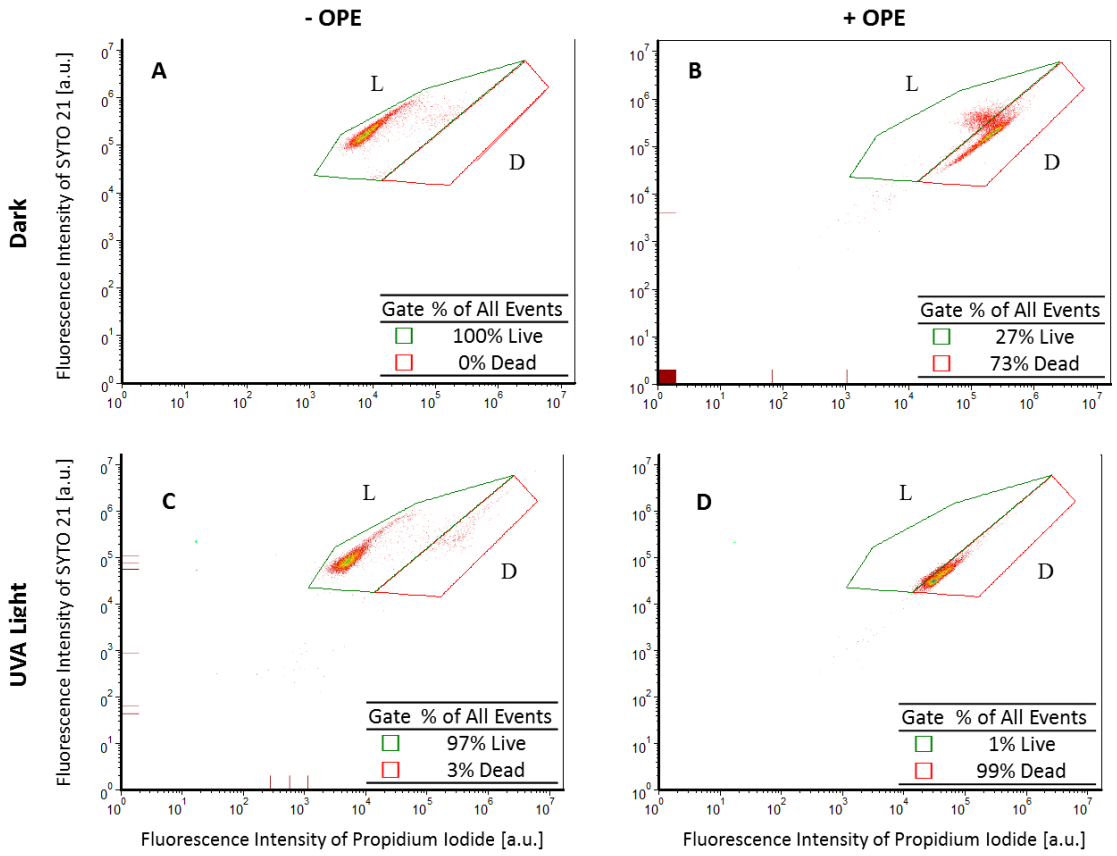

Figure 5.2: Flow cytometry-reported viability of 10,000 *B. atrophaeus* vegetative cells determined by changes in PI (X-axis) and SYTO 21 (Y-axis) fluorescence. The L Gate represents the live vegetative cells and the D gate represents the dead vegetative cells. *B. atrophaeus* vegetative were cells suspended in physiological saline solution for 1 hr. A: Negative control (0 µg/mL OPE); B: 10 µg/mL OPE in the dark; C: Negative control (0 µg/mL) in UVA light; D: 10 µg/mL OPE in UVA light.

Figure 5.2A illustrates fluorescence emitted from untreated *B. atrophaeus* vegetative cells: 1 hr in physiological saline solution at a temperature of 28.5 °C. Under these conditions, 100% of untreated *B. atrophaeus* vegetative cells retained their ability to form colonies and exhibit greater uptake of SYTO 21 (~10^5 arbitrary fluorescence units) than

PI (~10^4 arbitrary fluorescence units). In this case, cellular membranes remained intact, limiting propidium iodide uptake. As one might expect, the addition of a known membrane-disrupting agent, such as EO-OPE (Th,C2), results in a noticeable fluorescence shift (Figure 5.2B). Following an hour's exposure to this OPE at a concentration of 10 μg/mL, *B. atrophaeus* cells appear to exhibit uptake of SYTO 21 with the same propensity as untreated cells (Figure 5.2A); however, the uptake of PI has increased tenfold, indicating that OPEs induce moderate membrane damage to the extent that 73% of cells are killed in the absence of light. Figure 5.2C shows that *B. atrophaeus* vegetative cells are somewhat vulnerable to UVA irradiation, with 3% of bacilli killed in an hour. Significant killing of *B. atrophaeus* vegetative cells was only achieved upon exposure to light-activated OPE; an exposure duration of 1 hour causes 99% cell death (Figure 2D). It is important to note that membrane damage to vegetative bacilli rarely results in non-specific uptake of both stains; that is, the uptake of one stain appears to occur independently of the other.

Having defined regions of fluorescence characteristic of viable and non-viable *B.* atrophaeus vegetative cells, flow cytometry was then utilized to determine the extent by which EO-OPE (Th,C2) can inflict damage on *B. atrophaeus* spores. Spores were treated under the same conditions as the aforementioned vegetative cells (depicted in Figure 5.2); however, spores were stained with SYTO 21 and PI for 45 minutes, whereas vegetative cells needed just 15 minutes to stain.

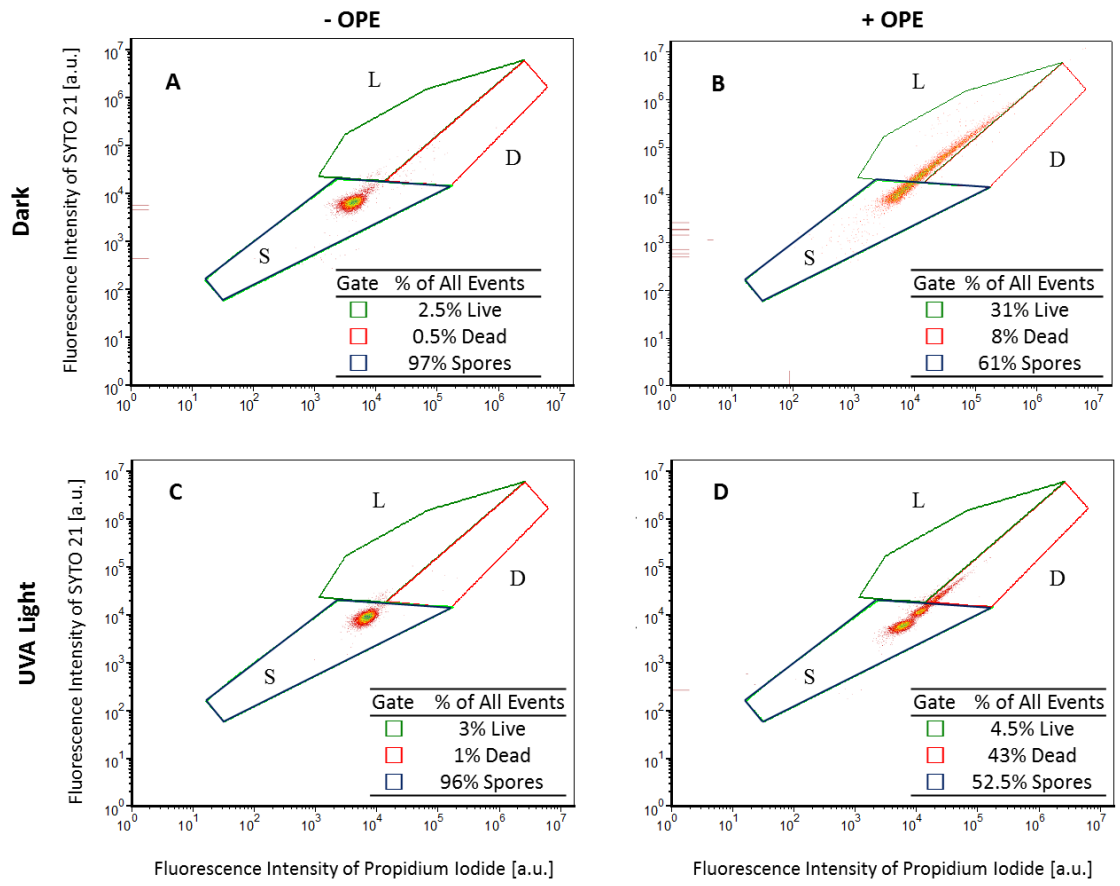

Figure 5.3: Flow cytometry-reported germination of 10,000 *B. atrophaeus* spores determined by changes in PI (X-axis) and SYTO 21 (Y-axis) fluorescence. The S gate represents spores, the L Gate represents viable germinating spores, and the D gate represents cells that have died during germination. *B. atrophaeus* spores were suspended in physiological saline solution for 1 hr. A: Negative control (0 µg/mL OPE) in the dark; B: 20 µg/mL OPE in the dark; C: Negative control (0 µg/mL OPE) in UVA light; D: 20 µg/mL OPE in UVA light.

Despite a prolonged staining period, the untreated *B. atrophaeus* spores depicted in Figure 5.3A exhibit decreased uptake of both stains relative to the untreated vegetative cells shown in Figure 5.2A. Decreased nucleic acid staining in *Bacillus* spores is

attributed to their low water content, relatively small volume, and limited access of stains to centralized supercoiled DNA resulting from an intact inner spore membrane[158]. The S gate is therefore included in Figure 5.3 to indicate regions of fluorescence characteristic of untreated *B. atrophaeus* spores. As can be seen in Figure 5.3B, the addition of EO-OPE (Th,C2) affects spores' stain uptake in a different manner than was observed with *B. atrophaeus* vegetative cells in Figure 5.2B. While exposure to OPEs in the dark selectively enhanced uptake of PI in vegetative cells, the uptake of SYTO 21 is also significantly enhanced in spores following OPE exposure in the dark. This non-specific fluorescent enhancement is characteristic of *Bacillus* spore germination: within 10 minutes of induced germination, spore coat porosity rapidly increases, leading to a water influx event, and thus, increased cell volume and increased uptake of stains[169,170].

This method of interrogation suggests that the water influx event sufficiently progressed in 39% of spores to the point where the magnitude of stain uptake matched that of *B. atrophaeus* vegetative cells. Figure 5.3B shows that 61% of spores still fluoresce in a manner characteristic of that of untreated spores (the S gate), which suggests these spores either underwent delayed germination or were not induced to germinate at all. In the absence of light, OPE-exposed spores were found to germinate into viable vegetative cells—meaning they were capable of forming colonies on TSA, while also exhibiting fluorescence characteristic of late-log-phase vegetative cells.

Irradiating *B. atrophaeus* spores with UVA light, alone, does not affect stain uptake, as is shown in Figure 5.3C. Figure 5.3D shows that exposing spores to light-activated OPE also results in non-specific stain uptake; however, in this case, the uptake ratio of membrane impermeable stain (PI) to membrane permeable stain (SYTO 21) is

increased, resulting in failed germination and inability to form colonies. Therefore, light-activated OPE promptly kills most germinating spores—not surprising, given the susceptibility of *Bacillus* vegetative cells to light-activated OPE (Figure 5.2D). Increasing the OPE concentration to 50 or 100 μg/mL was found to have no increased effect on the death or germination of *B. atrophaeus* spores, presumably to the inner filter effect.

The presence of UVA light is significant in achieving significant biocidal activity with cationic OPEs, as light-induced inactivation of *B. anthracis* Sterne is believed to involve three steps. First, the OPE is excited from the ground state, S_0, to its excited singlet state, S_1. Second, via intersystem crossing, S_1 decays to a longer-lived, albeit lower energy, triplet state, S_3; in turn, S_3 transfers its energy to molecular triplet oxygen, subsequently generating singlet oxygen ($^1O_2$) and ROS via a type I and type II photoreactions, respectively. Thirdly, ROS and $^1O_2$ can locally oxidize lipids, proteins, and nucleic acids[18]. It is evident that the additional level of OPE-inflicted damage conferred by the presence of UVA light plays a major role in viability of germinating *B. atrophaeus* spores. We hypothesize that the additional damage inflicted by light activation of OPE (as opposed to OPE in the dark) stunts germination by limiting the progression of one or both water influx events, as both fluorescence magnitudes (Figure 5.3D) and forward scatter values (Figure 9.18, appendix) are mitigated in this scenario.

The ability of OPEs to induce germination of *B. atrophaeus* spores was confirmed with scanning electron microscopy (SEM). As shown in Figure 5.4, SEM imaging illustrates an increased quantity of germinating cells following their exposure to OPE in the dark, as evidenced by their increased volume, rod-like morphology, and spore coat

remnants. Vegetative cells were present in the negative control, although they were far outnumbered by spores (the gating scheme used in Figure 5.3A suggests that spores represent 97% of all bacteria, in this instance). The observed dimensions of the rod-like vegetative cells (diameter: 0.8 μm; length: 2-3 μm)[171] and spores (width: 0.7 μm; length: 1.8 μm)[172] both match previously reported records. Arrows are included (Figure 5.4B and Figure 5.4D) to highlight the presence of spore coat remnants—the presence of which generally coincides with one of the last stages of spore germination. In the case of many bacilli, however, there is no sign of a spore coat remnant, signifying that there is a large degree of disparity concerning germination progress across the sample population—corroborating the heterogeneous fluorescence exhibited by germinating *B. atrophaeus* spores seen via flow cytometry. While germination is still observed in the presence of light-activated OPE, the majority of cells exhibit significant morphological damage that is too severe for the bacterium to overcome (Figure 5.4D and Figure 5.4E).

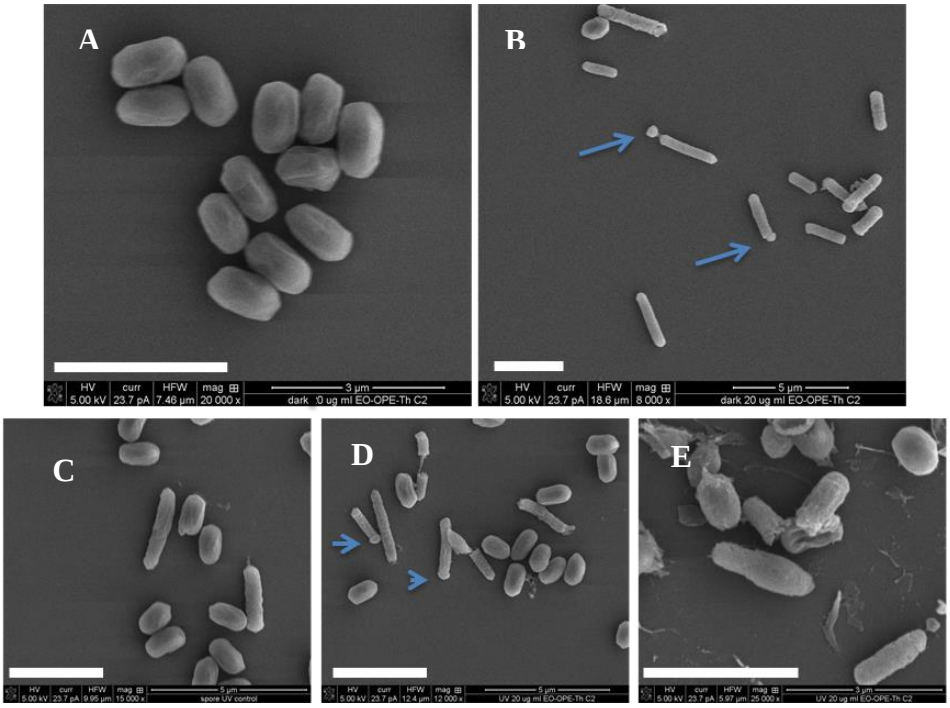

Figure 5.4: *B. atrophaeus* spores visualized via SEM. A: Spores suspended in physiological saline solution for 5 hrs in the dark; B; Spores exposed to 20 µg/mL OPE for 5 hrs in the dark; C: Spores suspended in physiological saline solution for 5 hrs in UVA light; D and E: Spores exposed to 20 µg/mL OPE for 5 hrs in UVA light. Scale bars spanning 3 µm are included. Arrows indicate spore coat remnants.

While flow cytometry is utilized to gauge the percentage of spores that germinate into viable or non-viable vegetative cells, there is no accurate way to determine viability of non-germinated spores (those that fluoresce within the S gate) with the aforementioned gating scheme. Determining direct death of spores in the absence of germination would require a fourth gate; the current gating scheme cannot be used to monitor death of a spore that does not germinate. In order to accurately determine the viability of *Bacillus* spores and subsequently germinated vegetative cells with accuracy, *Bacillus anthracis* Sterne was evaluated by standard plating techniques. Figure 5.5 illustrates the profound

killing of *B. anthracis* Sterne vegetative cells in the presence of light-activated OPE, thereby corroborating the rapid death of germinating spores observed in Figure 5.6B. Once again, standard plating techniques are implemented, with colony growth being used as the determining factor in viability. Nearly 4 log reduction of *B. anthracis* Sterne vegetative cells is observed within 30 minutes; within 90 minutes, 5 log reduction is observed.

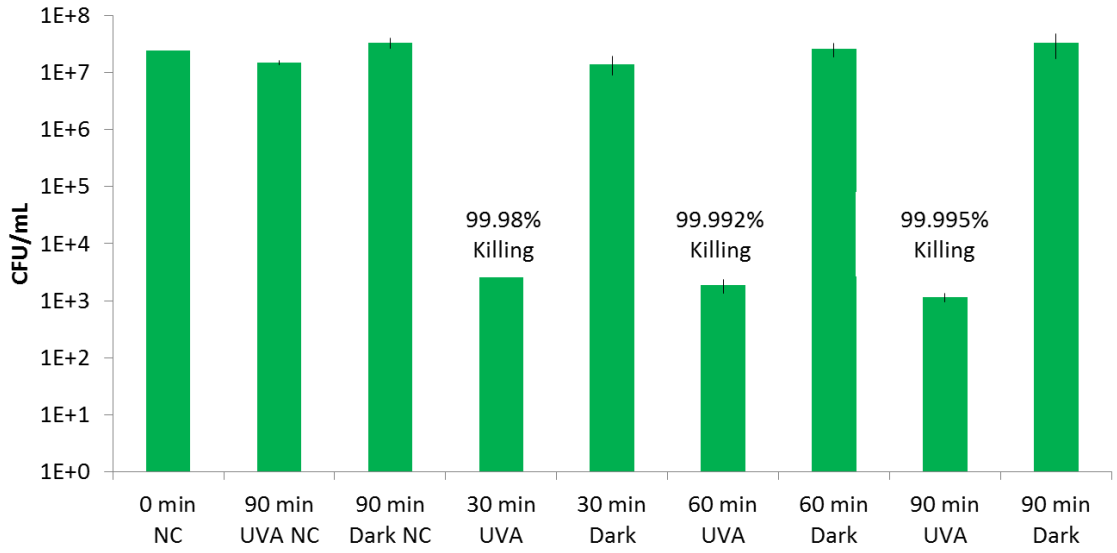

Figure 5.5: *B. anthracis* Sterne vegetative cell viability following exposure to 10 μg/mL OPE. NC denotes Negative Controls, where OPE was not used.

Even though *B. atrophaeus* spores to OPE in the dark facilitates germination within 30 minutes, longer exposure times (Figure 9.19, appendix) only marginally increases the percentage of spores that are induced to germinate. Increasing the exposure time beyond 90 minutes does not increase the percentage of spores that are induced to germinate—presumably due to OPE photodegradation and loss of biocidal efficacy.[70] In the presence of light-activated OPE, just 15% of spores will successfully germinate. Furthermore, in

the case of both *B. atrophaeus* and *B. anthracis* Sterne spores, 20 μg/mL OPE was insufficient to induce complete germination. In effort to induce complete spore germination, the starting concentration of spores was diminished, with the OPE concentration held constant at 20 μg/mL.

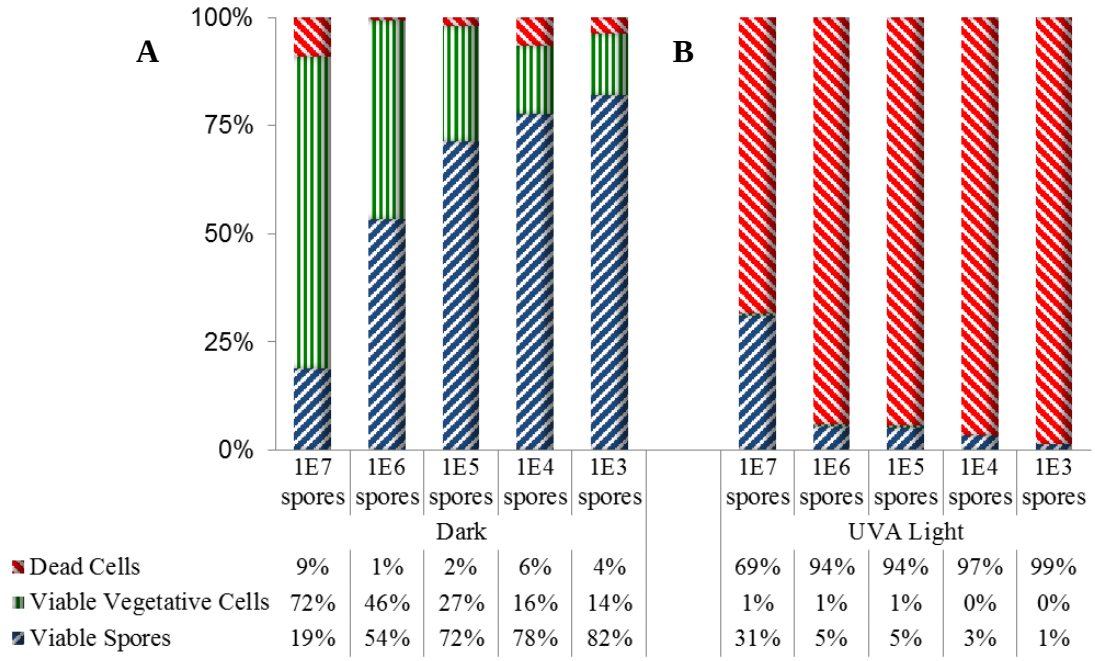

Figure 5.6: *B. anthracis* Sterne spore and germinated vegetative cell viability as a function of starting concentration. OPE exposed to varying spore concentrations for 90-min durations in the absence (A) and presence (B) of UVA light. Viability was inferred based on the spore's capacity to grow colonies on TSA before and after heat treatment, as described by Equations 1-3 (appendix).

Figure 5.6 illustrates that, within 90 minutes, 81% of spores were induced to germinate, even though the large majority (72% of all spores) are not killed and thus achieve successful germination into a viable, colony-forming vegetative cell. The percentage of spores able to germinate into viable vegetative cells actually decreased when the starting

concentration of spores was lessened. Germination still occurs in the presence of UVA light; however, the resulting viability of germinated vegetative cells is severely compromised in this case. It appears that 90 minutes is a sufficient amount of time for light-activated OPEs to induce germination in *B. anthracis* Sterne spores and subsequently damage resulting vegetative cells to the point where they are incapable of colony growth. Exposing *B. anthracis* Sterne spores at a relatively high OPE-to-spore ratio (20 ng OPE/spore) resulted in 99% killing within just 90 minutes.

5.2.1 Discussion

While the intent of this work was to study the interactions of an OPE with *Bacillus* spores and vegetative cells, we were surprised to find that spores were rapidly germinated into viable vegetative cells in the dark and in the absence of nutrients. Generally speaking, germination of dormant *Bacillus* spores into a growing cell can be induced by nutrients and non-nutrient agents, alike[160]. Researchers have recently begun to "kill" spores by first germinating them into a more susceptible state, where they can more easily be killed**,** thus mitigating the need for toxic compounds. Many of these techniques take advantage of known germinants, delaying sporulation and ensuring the cells remain in a vulnerable vegetative state[19,165,173]. Commonly used germinants include amino acids, sugars, purine nucleosides, glucose, and AGFK (a mixture of asparagine, glucose, fructose, and K^+), such as that found in the blood or tissues of a mammalian or human host[174,175]. Nutrients are, however, not mandatory in inducing spore germination; lysozyme, salts, high pressures, Ca^{2+}-DPA and cationic surfactants such as dodecylamine have all been demonstrated to germinate *Bacillus* spores in the absence of nutrients[158]. In some cases,

the germinant used is detrimental to vegetative cells—heat stress, for example, can induce spore germination, but is also harmful to vegetative cells.

Interestingly enough, select oxidizing agents have previously been shown to facilitate the germination of *Bacillus* spores into non-viable vegetative cells. Peroxynitrite[176] and Sterilox[177] (Sterilox Technologies Inc.; Radnor, PA) were found to kill germinating spores by inflicting profound damage on the inner spore membrane. Conversely, hydrogen peroxide leaves the inner spore membrane intact, yet leads to severe metabolic defects that mitigate a bacterium's capacity to accumulate and retain high-energy compounds necessary for successful germination[178].

There is, therefore, at least one possible mechanism by which EO-OPE (Th,C2) is able to induce rapid germination of *Bacillus* spores into nonviable vegetative cells. Direct inactivation of spores—that is, independent of their germination—was achieved by lowering the spore concentration. The percentage of spores induced to germinate actually decreased with lesser spore concentrations, which suggests that germination is, to an extent, facilitated by quorum sensing. Since Ca^{2+}–DPA released from one spore may stimulate the germination of other neighboring spores[160], lowering the spore concentration most likely decreased the likelihood of germination resulting from the Ca^{2+}–DPA release of a neighboring spore[179]. This suggests that EO-OPE (Th,C2) induced germination in the dark via perturbation of the inner spore membrane, facilitating the release of Ca^{2+}–DPA and subsequently inducing the germination of neighboring spores.

Inspection of Figure 5.3B shows that, in the dark, spores induced to germinate in the presence of EO-OPE (Th,C2) do so succesfully, as indicated by their ability to on-

specifically uptake both nucleic acid stains. This is corroborated in Figure 5.4B, which shows vegetative cells of an apporpriate morphology and spore coat remnants. Conversely, Figure 5.3D, Figure 5.4D, and Figure 5.4E show that spores induced to germinate by OPE in UVA light are, for the most part, unable to complete germination. Relative to OPE exposure in the dark, the presence of UVA light fails to result in a major non-specific stain uptake (Figure 5.3D) and germination appears greatly stunted (Figure 5.4D and Figure 5.4E). This data that the germinating spores in the light may be running out of high-energy adenosine triphosphate (ATP), since the germination process is short-lived. It is likely that interactions between EO-OPE (Th,C2) and proteins of the germination apparatus (which may include germinant receptors and cortex lytic enzymes) are hindering the spore's capacity to accumulate high energy ATP.[178]

In summary, a low OPE-to-spore ratio (2 pg OPE/spore) facilitates the germination of *Bacillus* spores in the dark, but fails to elicit significant levels of killing in the presence of UVA light. In this case, the OPE-to-spore ratio is not high enough to severely perturb spores, and thus their deactivation is contingent on the extent of germination into a vulnerable state. It is therefore likely that more extensive deactivation would be observed if germination rates were higher, albeit at low OPE-to-spore ratios. High OPE-to-spore ratios (20 ng OPE/spore), on the other hand, result in inefficient spore germination in the dark, with profound spore death observed upon the inclusion of UVA light. Here, the OPE-to-spore ratio is high enough to directly perturb spores independent of their germination status.

One potential issue with the experiments described herein is the possibility that the exact mechanism of spore death and germination is unknown. For example, while the

most likely scenario for germination by OPE may be spore-cortex interactions, it is also possible that the OPE is affecting spore germinant receptors in such a way that germination is induced. Furthermore, in the case of the *B. anthracis* Sterne experiments by which colony-growth on TSA is utilized to quantify germination and cell death, it is possible that the OPE is interfering with cell-division proteins such as FtsZ (filamenting temperature-sensitive mutant Z)—thereby limiting colony growth and providing the illusion of viability loss[79,180]. One potential issue with the flow cytometry gating scheme is the inability to identify non-viable spores that are killed without being induced to germinate. This particular point is highlighted in Figure 5.3D, which clearly shows a population of spores that exhibits a minor fluorescence enhancement. Another issue is that there is a large gap (in terms of fluorescence) between untreated *B. atrophaeus* vegetative cells and those that are viable (capable of colony growth) following induced germination. The monitoring of germination—and in particular, direct spore death without germination—could be improved with the creation of a fourth gate. Furthermore, the gates that are in place could most likely be improved upon with further experimentation. The gates shown in in this study are specific to *B. atrophaeus*, SYTO 21 and PI, and the Accuri C6 flow cytometer. Using a different strain of *Bacillus*, different viability indicating stains, or a different flow cytometer would warrant gate-modifications and calibration. It is also possible that the gating could be improved by modifying the thresholds. Additional testing is needed to clarify the mechanism of OPE-induced germination. In particular, monitoring the capacity of germinating spores to accumulate ATP will shed light as to whether light-activated EO-OPE (Th,C2) kills

germinating *Bacillus* spores via severe inner membrane perturbation or through disruption of germination apparatuses.

5.3 Conclusions and Outlook

In ultraviolet A light, an end-only oligo (*p*-phenylene ethynylene) was found to exhibit over 4 log kill against *B. anthracis* Sterne vegetative cells and 2 log kill against low concentrations of *B. anthracis* Sterne spores. The highly effective nature of this OPE stems from its ability to rapidly induce germination of *Bacillus* spores, rendering the bacteria highly vulnerable to reactive oxygen species and ultraviolet irradiation. Furthermore, flow cytometry was utilized to monitor spore germination, and subsequently quantify the fraction of germinated vegetative cells that were either viable or nonviable. Monitoring germination via dual fluorescence flow cytometry is feasible due to the fact that *Bacillus* spore germination entails two water influx events[160] that result in increased stain uptake and thus, simultaneous increase of both nucleic acid stains. It is important to note that the water influx events cause non-specific, uniform fluorescence enhancement. Three gates are hereby used to track germination in *Bacillus* spores based on the simultaneous quantification of two nucleic acid stains. As can be seen in Figure 5.3B and Figure 5.3D, the degree which germinated spores fluoresce varies; the degree of non-uniformity observed in spore germination has previously been described, as heterogeneity is generally greatest at the onset of germination[159,181]. Further experimentation is required to isolate the mechanism by which this OPE efficiently induces germination in *Bacillus* spores.

Chapter 6: *The Unique Antifungal properties of OPEs and PPEs*

6.1 Introduction

Bloodstream infections affect a huge patient population in the United States, with more than 250,000 cases reported each year [182]. Patients with indwelling medical devices, such as central venous catheters (CVCs), are most at risk for these infections [183]. Frequently, various microorganisms from the skin of the patient, or respective healthcare professional, can gain access through the catheter wound as a result of non-sterile conditions [184–187]. Of these resulting bloodstream infections, *Candida* species account for 9% of all instances and are associated with a ~40% mortality rate [183,188]. The most commonly isolated fungal pathogen from bloodstream infections is *Candida albicans*, but the prevalence of other species, such as *C. parapsilosis, C. glabrata*, and *C. tropicalis*, is increasing [189,190].

An important determinant of pathogenicity among *Candida* spp. is the outer cell wall. The cell wall is primarily composed of carbohydrates and, structurally, is separated into two layers. The outer layer is composed mostly of cell wall glycoproteins with N- and O-linked mannans, and the inner layer is composed of β-glucan and chitin. The complexity of the cell wall contributes to various pathogenic factors including adherence of the fungus and establishment of cross-talk with the host known as "glycan code" [191–193]. Cell wall components, such as β-glucan and other polysaccharides, are also found in the extracellular matrix secreted by *Candida* spp. biofilms, which can contaminate the synthetic material surfaces of indwelling medical devices. β-glucan in the extracellular matrix of *Candida* biofilms has been shown to sequester antifungal drugs, which contributes to decreased drug susceptibility of biofilms [194–196].

Various antimicrobial impregnation approaches have been devised to prevent catheter infections. Catheter materials coated with chlorhexidine-silver sulfadiazine and minocycline/rifampin have shown trends in reduced infection rates, but their clinical effectiveness remains questionable [197,198]. Other treatments, including the use of silver-impregnated subcutaneous collagen cuffs, have also shown to be ineffective in recent trials [199,200]. CVC contamination generally requires device removal and replacement, in addition to a prolonged course of antifungal drug therapy, which raises concerns regarding drug toxicity and the development of antifungal resistance. Antifungal chemotherapy is also problematic, as many antifungal drugs are either toxic to the host (amphotericin B), or result in drug-resistant strains (triazoles) [201]. Due to the high morbidity and mortality rate of catheter-related *Candida* spp. bloodstream infections, strategies for preventing medical device contamination by fungal pathogens remain a top priority for infection control.

In this study, we sought to elucidate the antimicrobial effectiveness of two *p*-phenylene ethynylene (PE) compounds against *Candida* species. A subset of conjugated polyelectrolyte, phenylene ethynylenes have shown promising biocidal activity against Gram-positive and -negative bacterial pathogens, as well as the environmental yeast, *Saccharomyces cerevisiae* [18,162,202]. The chemical structure of these compounds renders them capable of inducing broad-spectrum cell damage. The phenylene ethynylenes

studied consist of alternating phenyl and acetylenic groups with appended cationic groups, as seen in Figure 6.1, below.

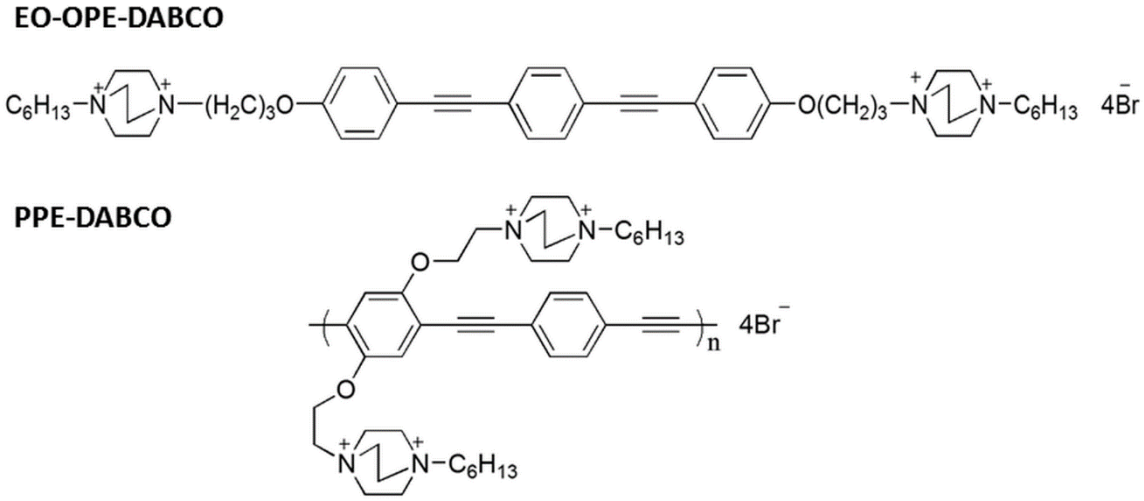

Figure 6.1: Molecular structures of oligomeric EO-OPE-DABCO (top) and polymeric PPE-DABCO (bottom).

In previous studies, the oligomeric and polymeric molecular size of PE compounds has played an important role in their mechanisms of killing. The antimicrobial activity of these compounds is dependent on various factors that include molecular conformation, size, functional groups, and, of course, membrane composition of the target pathogen [162]. The studies described herein serve as a preliminary investigation into the utility of a cationic conjugated polymer, poly(*p*-phenylene ethynylene), and oligomer, "end-only" oligo(*p*-phenylene ethynylene), as antifungals. After treatment with the compounds—hereby referred to as PPE-DABCO and EO-OPE-DABCO—the viability of *Candida* spp. was monitored using flow cytometry. This novel class of compounds may provide an innovative approach to preventing catheter-related bloodstream infections caused by *C. albicans* and other *Candida* species.

6.2 The Antifungal Properties of Cationic *p*-Phenylene Ethynylenes and their Impact on β-Glucan Exposure

A series of biocidal studies were carried out to gain insight to the light-activated effects of EO-OPE-DABCO and PPE-DABCO on *Candida* species pathogens. Phenylene ethynylenes are unique in that their mechanism of action differs, depending on the presence of light; in particular, light intensity, emission wavelength, and duration [35]. In the studies described herein, duration of light exposure was the primary variable being studied. Light intensity was kept constant using a photoreactor with 14 interchangeable lamps. Lamps were chosen to have an emission wavelength overlapping the excitation spectrum of the phenylene ethynylene being used. 350 nm-centered UVA lamps were implemented for OPE testing, while 420 nm-centered lamps were used in PPE tests. With light intensity and spectrum being held constant for a given phenylene ethynylene, we focused on light exposure duration as the major focal point in an effort to discern *C. albicans'* susceptibility to phenylene ethynylenes in the light vs. dark. Even though all samples were exposed to one of the two compounds for a total of 60 min, the duration of light exposure was varied by 4 min intervals and the balance of 60 min exposure was in the dark.

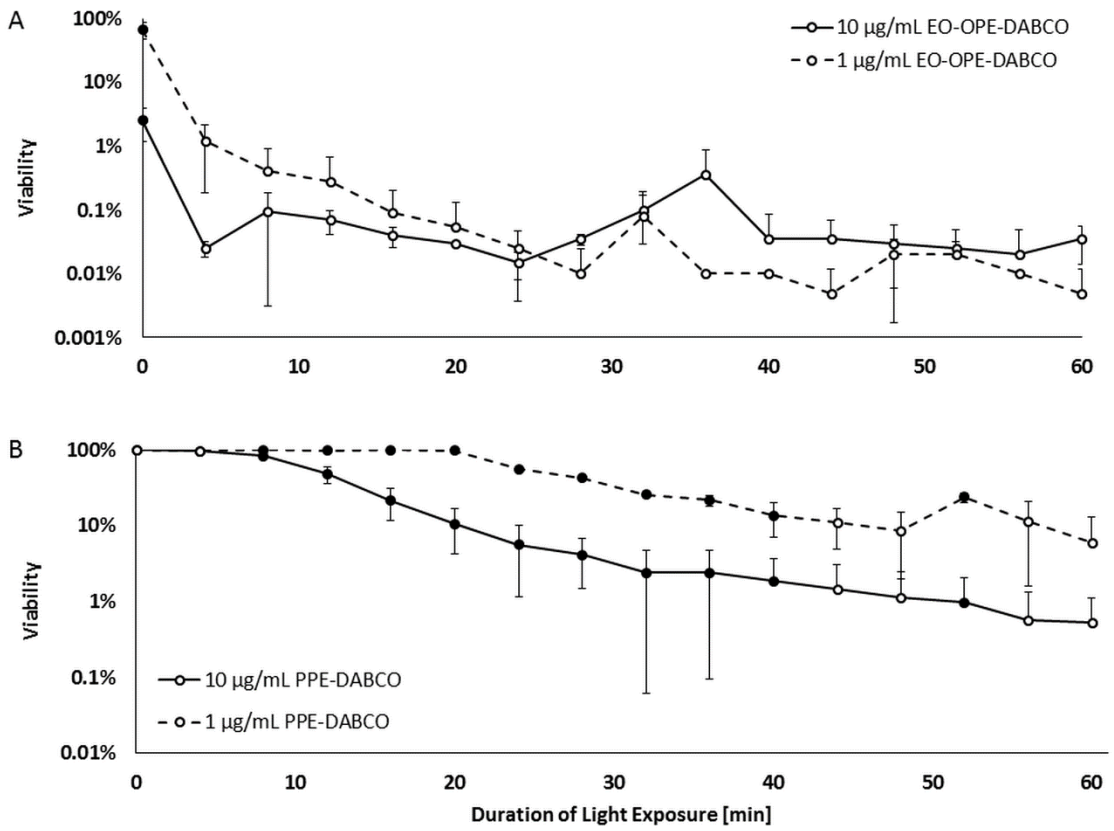

Figure 6.2: *C. albicans* yeast viability as a function of light exposure duration and antimicrobial concentration. Viability is shown on a logarithmic scale for EO-OPE-DABCO (A) or PPE-DABCO (B) at 1 µg/ml (dashed lines) or 10 µg/ml (solid lines). Significant differences in viability are indicated by filled data markers (P-value ≤ 0.01).

Figure 6.2A illustrates the biocidal activity of the two concentrations of EO-OPE-DABCO: 1 and 10 µg/mL. In the absence of light, a 1 µg/mL concentration of OPE killed 34% of *C. albicans* yeast cells; however, killing drastically increased with just minimal light exposure, as 2 log cell death was observed after just 8 min. Increasing the concentration to 10 µg/mL greatly improved the dark killing capacity of the OPE, resulting in 97% cell death. With minimal light exposure, 10 µg/mL EO-OPE-DABCO

exhibited a profound biocidal effect, exceeding 3 log reduction after just 4 min in UVA light. Both OPE concentrations exceeded 3 log kill (over 99.9% cell death) after 20 min of light exposure, and 4 log reduction (99.99% cell death) is nearly achieved after 60 min of light exposure. Interestingly enough, lowering the concentration of OPE to just 1 μg/mL had little effect on light-activated biocidal activity, but a far larger effect on dark killing. Some level of PE photodegradation was notable by 60 min (data not shown), which is why testing durations were limited to 1 h, as photodegradation limits $^1O_2$ generation.

Figure 6.2B illustrates the viability of *C. albicans* following exposure to PPE-DABCO. It is quite evident that, unlike EO-OPE-DABCO, its PPE counterpart is non-toxic in the absence of light; even at a relatively high concentration of 10 μg/mL, little-to-no cell death was observed even after 8 min of exposure to 420 nm light. After 52 min of continuous light exposure, 10 μg/mL PPE was able to kill 99% of all *C. albicans* yeast cells. In summary, we find the dark killing of the OPE to be concentration-dependent, while the light activity is not. Conversely, the PPE's dark killing was not dependent on concentration, since it failed to elicit membrane damage in that case. Biocidal activity of PPE-DABCO is predicated on light exposure.

PPE-DABCO's inability to kill *C. albicans* in the dark led us to question whether the polymer may bind extensively to cell wall components, which could limit its ability to access the cell membrane. We evaluated the interactions between both PEs with soluble β-(1,3)-glucan extracted from *Saccharomyces cerevisiae* yeast cell walls [203]. The structure of *S. cerevisiae* and *C. albicans* β-(1,3)-glucan is quite similar, and this polysaccharide is an important part of *Candida* drug resistance and pathogenicity,

amounting to 40% of the cell wall [204]. Size fractionated β-glucan (low MW = 11 kDa, medium MW = 150 kDa, high MW = 450 kDa) were tested (Figure 6.3 A-D; Figure 9.20 in the appendix). Excitation and emission spectra of EO-OPE-DABCO and PPE-DABCO were evaluated in the absence or presence of the soluble β-glucan.

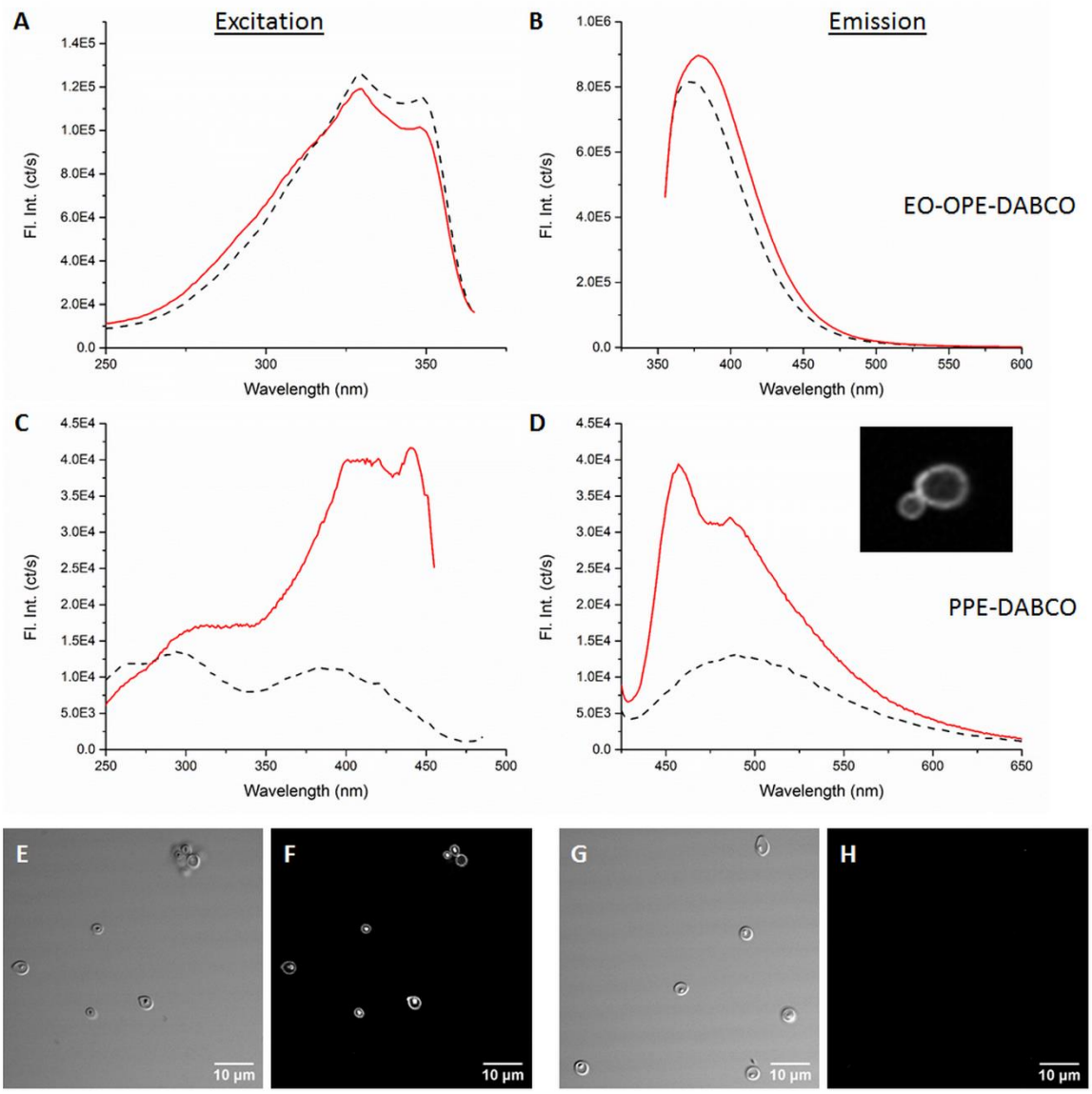

Figure 6.3: Excitation (A, C) and emission (B, D) spectra illustrating the interactions between high molecular weight soluble β-glucan and EO-OPE-DABCO (top) or PPE-DABCO (bottom). Dashed lines represent spectra of PE compounds alone, and solid lines

represent the spectra observed in PE/β-glucan mixtures. Inset illustrates fluorescent PPE-DABCO concentrated in the cell wall of a C. albicans yeast cell, as shown in Fig. S2. Additionally, confocal microscopy images illustrate PPE-DABCO bound to glucan microparticles. A transmitted light image (E) and reflected light image (F) are shown, with 405 nm excitation being used to generated fluorescence of bound PPE-DABCO. No fluorescent signal is observed in the absence of PPE-DABCO (G, H).

We observed enhanced emission of both PEs upon the introduction of the high molecular weight β-glucan, which is indicative of complexation [205]. Emission enhancement is more profound in the case of PPE-DABCO (Figure 6.3 A-D), suggesting that complexation with soluble β-glucan promotes disaggregation of the PE polymer. In addition, a small degree of red-shifting was observed, implying that rotation of the conjugated regions of the PEs is restricted due to complexation with soluble β-glucan [58]. The complexation between PPE-DABCO and β-glucan suggests that it may be largely sequestered in the cell wall; such positioning promotes interaction with components of the outer cell wall, but may limit its ability to directly disrupt the plasma membrane.

These results shed light onto the mechanisms by which EO-OPE-DABCO kills *C. albicans* yeast cells (Figure 6.2A; see discussion). With this in mind, the OPE became a focal point of this study, from a biocidal perspective. Having determined that EO-OPE-DABCO was highly effective at killing standard lab-strain *C. albicans* (SC5314), the question remained whether or not its biocidal efficacy would carry over to *C. albicans* clinical isolates.

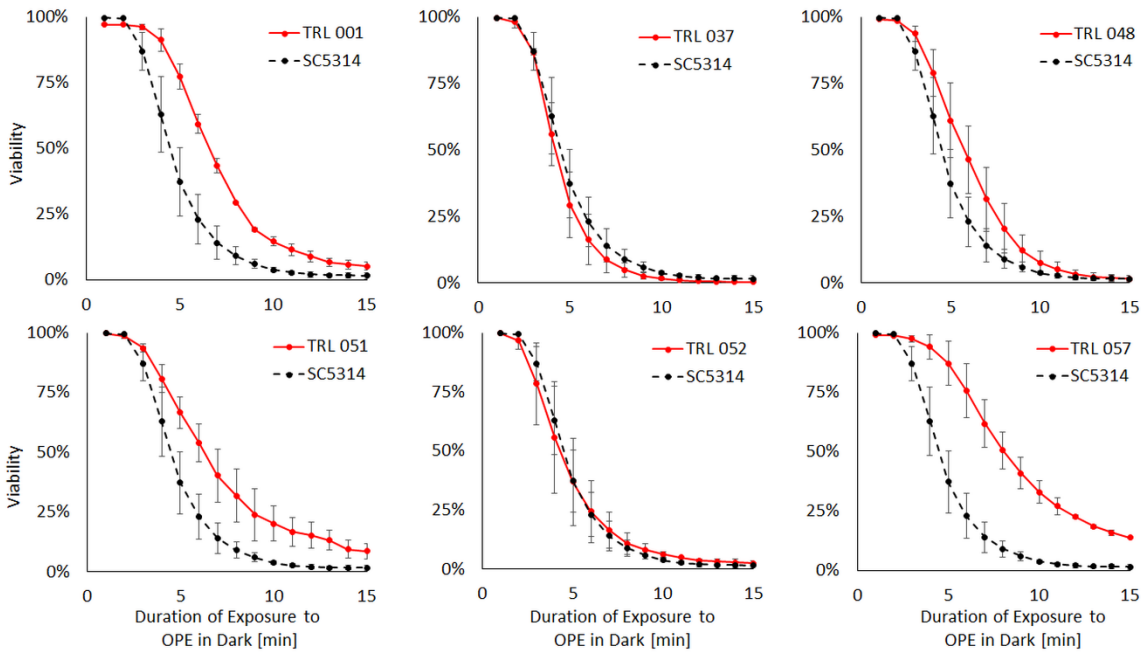

Figure 6.4: Susceptibility of various *C. albicans* clinical isolates to 10 µg/mL EO-OPE-DABCO in the dark. Lab strain SC5314 is shown for reference in all cases. Strains prefixed "TRL" are recent (circa 2015) clinical isolates obtained as described in Materials and Methods.

Using a modified biocidal assay, six *C. albicans* clinical isolates were surveyed for their susceptibility to 10 µg/mL EO-OPE-DABCO in the dark. In this instance, the cells were stained with SYTO 9 and TO-PRO-3 before the introduction of EO-OPE-DABCO. Taking a flow cytometry dual-fluorescent measurement of 10,000 events every minute allowed for real-time reporting of OPE-induced membrane perturbation. The susceptibility of clinical isolates was gauged relative to that of *C. albicans* SC5314, as shown in Figure 6.4. Three of the six isolates, TRL 001 (P-Value = 0.006), 051 (P-Value = 0.0013), and 057 (P-Value = 0.0003) showed significantly increased levels of OPE-resistance within 15 minutes' time in the form of slower kinetics of killing and higher

residual viability after 15 minutes of treatment. Conversely, no OPE-resistance was observed in TRL 037, 040, and 052.

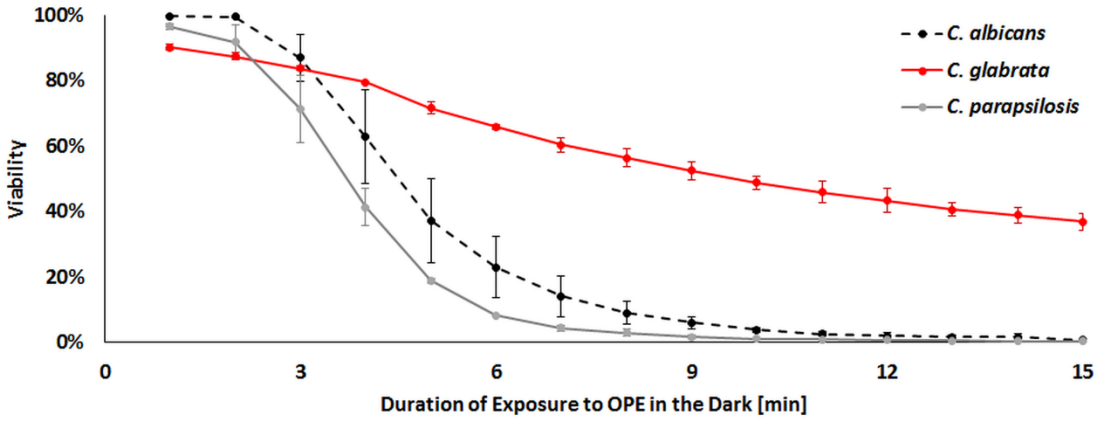

Figure 6.5: Viability of *C. albicans, C. glabrata, and C. parapsilosis* in the presence of 10 µg/mL EO-OPE-DABCO in the dark.

Variability of susceptibility to EO-OPE-DABCO amongst clinical isolates of one species (*C. albicans*) suggested that non-*albicans Candida* species pathogens might also exhibit variable sensitivity to this biocide. To test this, we revised the aforementioned 15 min flow cytometry assay to determine if EO-OPE-DABCO was more or less effective against *C. parapsilosis* and *C. glabrata* relative to *C. albicans* SC5314. Figure 6.5 shows similar degrees of biocidal activity against *C. albicans* and *C. parapsilosis*, but less activity against *C. glabrata*, with about 50% surviving through 15 min' exposure. This result is consistent with the fact that *C. albicans* and *C. parapsilosis* share a closer phylogenetic relationship than is found between *C. albicans* and *C. glabrata* [206].

β-glucan is highly immunogenic upon recognition by the innate immunoreceptors Dectin-1 or Mac-1 [207]. Several prominent genera of fungal pathogens, including *Candida*, are known to employ an innate immune evasive strategy of masking β-glucan

to restrict its exposure on the cell wall surface [208–211]. We hypothesize that PE antimicrobials bound to cell wall constituents and exposed to light will generate singlet oxygen, leading to local cell wall damage, unmasking β-glucan and increasing immunogenicity. Using an anti-β-(1,3)-glucan primary antibody in tandem with a secondary fluorescently-labeled antibody allowed for the comparison of β-glucan exposure following treatment conditions: PE in the dark, PE in the light, and a 60 min light negative control. *C. albicans* yeast treated with EO-OPE-DABCO in the dark, using conditions associated with high biocidal activity (Figure 6.2), exhibited no increase in β-glucan exposure. Likewise, we observed no β-glucan unmasking with light-activated EO-OPE-DABCO. We then treated *C. albicans* with PPE-DABCO and observed β-glucan exposure. PPE-DABCO clearly binds to the fungal cell wall as evidenced by strong PPE-DABCO emission upon 405 nm excitation using confocal imaging (Figure 9.21, appendix). In the absence of stimulation by light, PPE-DABCO treatment results in no significant increase in β-glucan exposure. After illumination, PPE-DABCO treated cell walls do show evidence of significant β-glucan unmasking (Figure 6.6). These results suggested that β-glucan masking in *Candida* cell walls is light-dependent and, presumably, mediated by $^1O_2$ and other ROS.

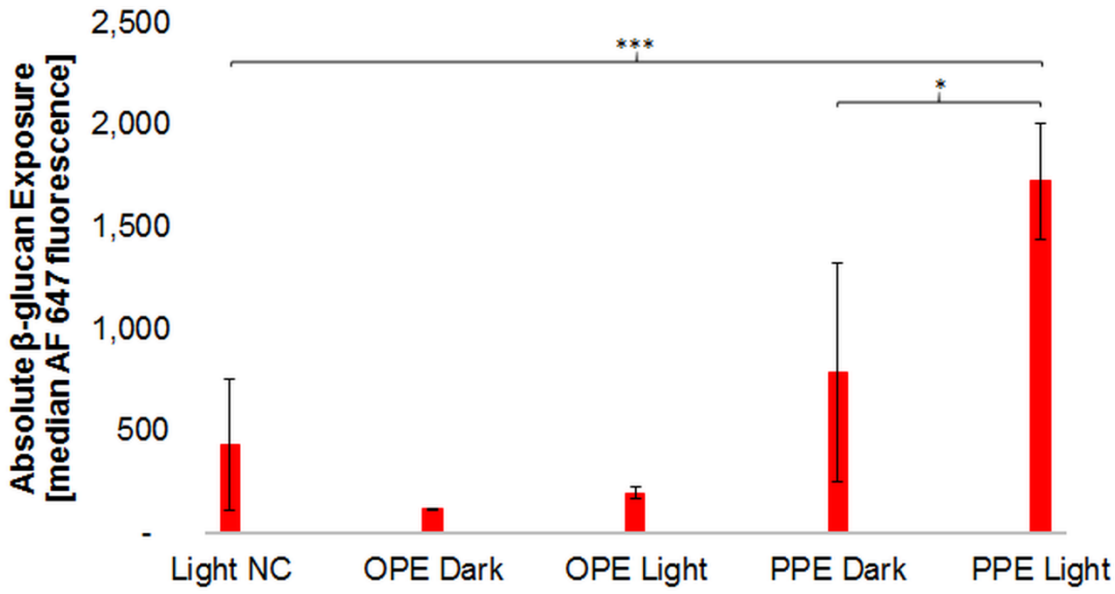

Figure 6.6: Absolute β-glucan exposure of *C. albicans* following various treatments. β-glucan exposure estimated from median fluorescence signal of AF 647. The exposure duration of all samples was 60 min, with the exception of EO-OPE-DABCO exposure in the light, for which the exposure duration was limited to 10 min.

Given the evidence that PPE-DABCO can increase β-glucan exposure on *C. albicans* yeast, we tested whether the unmasking achieved by this treatment resulted in greater recognition of yeasts through the β-glucan receptor Dectin-1. HEK-293 cells were transfected with mApple-tagged human Dectin-1a, whereby expression is sufficient to drive phagocytosis of *C. albicans* yeast cells [212]. Our transfection conditions resulted in Dectin-1^{+} HEK-293, discriminated by positive mApple signal, and non-transfected cells, which were negative for mApple and served as an internal control to assess Dectin-1 dependence of binding and phagocytosis. We employed a flow cytometric assay of yeast cell binding to and internalization by HEK-293 transfectants. Yeasts were labeled with the pH-sensitive dye CypHer 5, which increases dramatically in emission intensity after

internalization within acidic phagosomal compartments [213,214]. The Cypher 5 signal was used to measure binding and internalization of yeast. Flow cytometry data were gated on HEK-293 cell-containing events for analysis, as defined by high side scatter signal, which was significantly larger than free yeast. Yeast bound to HEK-293 cells registered a low Cypher 5 signal. If yeasts were internalized, the CypHer 5 signal was much higher. The percent of HEK-293 cells with yeast bound (for mApple-Dectin-1^{+} and mApple-Dectin-1^{-} cells) was determined by the percent of SSC-gated events having low or high CypHer 5 signal. The extent of phagocytosis was assessed by the median CypHer 5 fluorescence intensity within these populations (Figure 9.22, appendix).

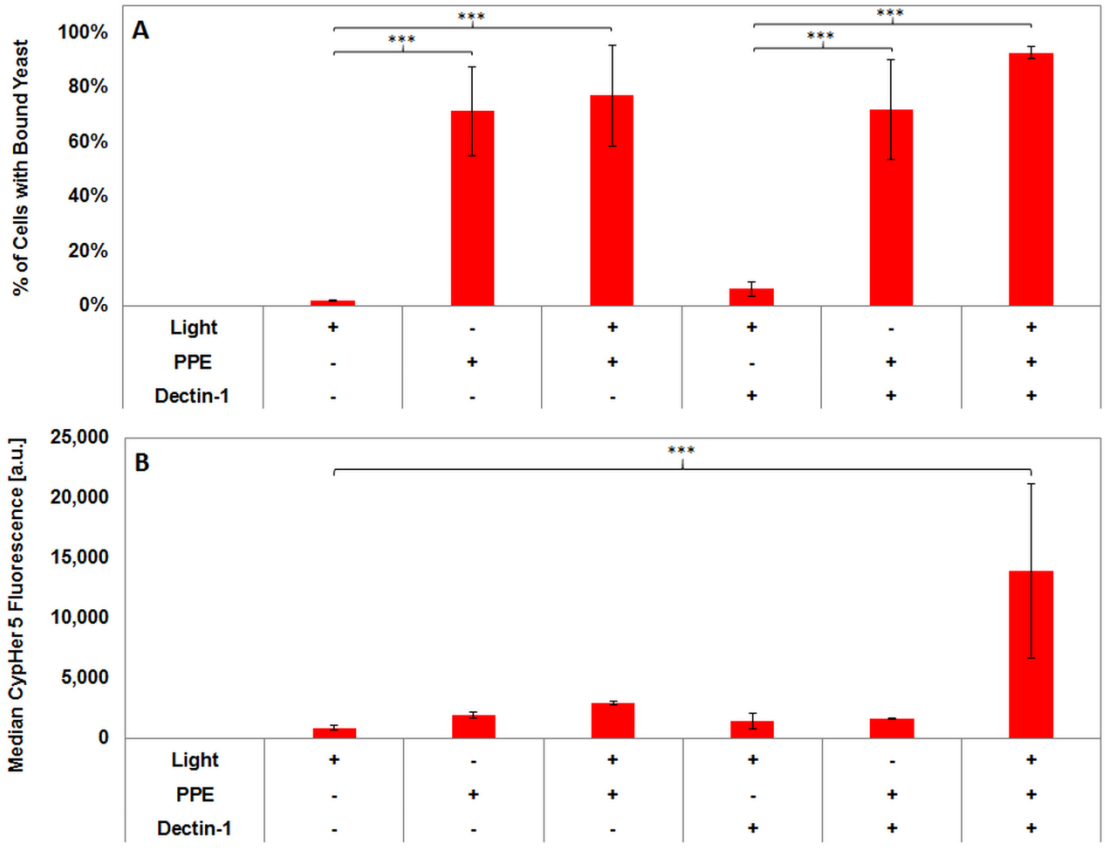

Figure 6.7: PPE-DABCO induces *C. albicans* yeast phagocytosis by HEK-293 cells in a manner that requires illumination of PPE-DABCO and expression of the β-glucan

receptor Dectin-1. Prior to the addition of HEK cells, samples were first treated with 10 μg/mL PPE-DABCO for 1 h and subsequently stained with CypHer 5 and SYTO 9. A) PPE-DABCO treatment, with or without illumination, induces increased binding of *C. albicans* to HEK-293 cells in a Dectin-1 independent fashion. B) Phagocytosis of *C. albicans* yeast bound to HEK-293 cells requires Dectin-1 expression and is induced by light treatment of PPE-DABCO.

As can be seen in Figure 6.7, we observe minimal binding between mApple-Dectin-1$^-$ HEK-293 cells and untreated *C. albicans* yeast cells. Even if the HEK-293 cell has been transfected and is expressing Dectin-1 (mApple+), β-glucan masking permits very little β-glucan to be accessible at the cell wall surface for Dectin-1 binding (as seen in Figure 6.6). Conversely, PPE-treated *C. albicans* yeast cells bind avidly to HEK-293 cells, and this binding is independent of excitation of PPE-DABCO or Dectin-1 expression by the HEK-293 (Figure 6.7A). These data suggest that the binding of PPE-DABCO to *Candida* cell walls alters their surface properties in ways that promote Dectin-1 independent adhesion to human cells, perhaps through electrostatic and/or hydrophobic mechanisms. The extent of interaction between the yeast cell and the HEK-293 cell is not dependent on the degree of incurred cell membrane damage, as *C. albicans* killed with light-activated PPE were no more likely to bind HEK-293 cells. Despite their ability to bind HEK-293, internalization of PPE-DABCO-treated *C. albicans* yeasts required Dectin-1 expression and excitation of PPE-DABCO prior to binding (Figure 6.7B). These data indicate that the β-glucan unmasking caused by light-activation of

PPE-DABCO on *C. albicans* cell walls results in the biological outcome of increased Dectin-1 dependent phagocytosis.

6.3 Conclusions and Outlook

Despite their intrinsic resistance to cationic and oxidative stresses, [215,216] *C. albicans* was highly susceptible to EO-OPE-DABCO, and to a lesser extent, PPE-DABCO. Biocidal activity of these compounds against *C. albicans* utilizes a dual mechanism combining light-independent cationic stress and light-dependent oxidative stress. These results resemble those of previous studies, which demonstrate the effectiveness of a dual-mechanism mode of biocidal action [217]. Unlike other broad-spectrum antimicrobials, PEs exhibit low levels of *in vitro* toxicity against mammalian cells [164], making them attractive candidates in numerous clinical applications.

Therefore, it is relevant to note that all clinical isolate strains exhibited significant amounts of killing during a 15 min exposure to EO-OPE-DABCO. Partial resistance of some clinical isolate strains may derive from adaptations of the pathogen to growth in the host, which may cause changes in cell wall structure and upregulation of mechanisms that permit growth under adverse conditions, such as leukocyte-derived ROS in the phagosomal environment [218,219]. Previous research has also suggested a correlation between *Candida* resistance to the antifungal drug amphotericin B and cell wall structure and composition [220,221].

While *C. parapsilosis* was found to be as susceptible to EO-OPE-DABCO in the dark as *C. albicans*, C. *glabrata* displayed an inherent resistance. *Candida* spp. experience cationic stress as they interact with innate immune defenses. For example,

cationic antimicrobial peptides, such as Histatnin-5, are deployed in host defense against *Candida* spp. and are thought to work by disrupting fungal plasma membrane integrity [222]. *C. glabrata* is noted for its resistance to killing by cationic antimicrobial peptides relative to *C. albicans* and other *Candida* spp. pathogens [223–225]. Furthermore, EO-OPE-DABCO's decreased ability to kill *C. glabrata* resembles the results of a previous study, in which a 10 μg/mL concentration of the compound failed to kill 99% of *S. cerevisiae* yeast, even after an hour in the light [202]. Although *S. cerevisiae* is benign, it is closely related to *C. glabrata* [203,206]. Finally, *C. glabrata* is also known to have robust antioxidative defenses that allow it to survive in the phagosome [226,227], and may impact its ability to resist oxidative killing by cationic phenylene ethynylenes.

An interesting result of this study is that PPE-DABCO strongly associates with soluble β-(1,3)-glucan (Figure 6.3 C-D), which is important for structural support of the cell wall of *C. albicans* [203], as well as glucan microparticles (Figure 6.3 E-F). We speculate that PPE-DABCO/β-glucan interaction may directly cause more global disruption to the cell wall, and it is likely that the targeting of polymeric phenylene ethynylenes to cell wall polysaccharides places them in an ideal position reactive oxygen-mediated damage to cell wall components after photoactivation. Using transmission electron microscopy and other techniques, Wang *et al.* demonstrated this behavior with PPE-DABCO and Gram-negative *Escherichia coli* [35]. Conversely, the OPE appears far less prone to complexation with the soluble β-(1,3)-glucan. Although this limits the OPE's ability to unmask mannoproteins and reveal more β-(1,3)-glucan (Figure 6.6), the lack of interaction with the glucan likely allows the molecule to quickly penetrate the cell wall, access and damage the cell membrane. Abundant lateral non-covalent interactions

between β-glucan and PPE-DABCO may promote PE/β-glucan complexation, analogous to the role of interpolymeric hydrogen bonding in stabilizing lateral interactions of individual β-glucan polymers in aqueous solution [228,229]. PPE-DABCO is far larger than its oligomeric counterpart, and has numerous sites where weak interactions with β-glucan polymers may form; furthermore, extensive valency of laterally-aggregated β-glucan would make this interaction very strong. Emission enhancement of the PE polymer (Figure 6.3) resembles that of a previous study, by which PPE-DABCO was shown to exhibit similar photophysical effects in methanol, as opposed to water [52]. Therefore, we suggest that abundant complexation with soluble β-glucan disaggregates PPE-DABCO in aqueous buffer.

These results help in justifying the PPE's inability to kill *C. albicans* in the dark. Exhibiting a strong propensity to interact and associate with β-glucan, it is likely that PPE-DABCO is limited in its ability to fully penetrate the cell wall and much of the compound is sequestered on β-glucan in the cell wall. Given the limited radius of destruction of singlet oxygen and the density of organic material in the cell wall capable of quenching singlet oxygen, this association may be limiting the depth of cell wall permeation of PPE-DABCO and its capacity to directly perturb the yeast's plasma membrane, relative to EO-OPE-DABCO. However, an advantage of PPE-DABCO's ability to bind β-glucan may be an increased specificity and targeting to the fungal pathogen's cell wall as opposed to host tissues, which are devoid of β-glucan. The oligomer, on the other hand, appears far less likely to interact with β-glucan, which may allow it to permeate the fungal cell wall more readily and better access the yeast's plasma membrane.

Furthermore, PPE-DABCO displays immunostimulatory attributes, particularly in the light. This polymer was found to unmask the outer cell wall of *C. albicans* yeast cells in such a way that β-(1,3)-glucan could more easily be recognized and bound by pattern recognition receptor Dectin-1. PPE-DABCO binds to yeast cell walls (Figure 9.21, appendix). The chemical basis of this binding may relate to direct interactions between PPE-DABCO and β-(1,3)-glucan, as discussed above. Additionally, PPE-DABCO may interact electrostatically with anionic moieties in the outer cell wall. Ultrastructural studies have described the presence of evenly-dispersed anionic sites on the *C. albicans* yeast surface [230]. Also, *C. albicans* N-linked mannans contain abundant oligomannose side chains attached via anionic phosphodiester linkages that could provide sites of electrostatic binding for polycations like PPE-DABCO [231,232]. In either configuration, PPE-DABCO would be ideally positioned in the outer cell wall to damage mannoproteins that are thought to provide β-glucan masking. Our results suggest that merely the binding of PPE-DABCO to *C. albicans* increases adherence of yeast to HEK-293 cells in a receptor-independent fashion, suggesting that PPE-DABCO alters cell wall surface characteristics in ways that impact interaction with host cells non-specifically (Figure 6.7A). However, increases in both β-glucan exposure and Dectin-1-dependent phagocytosis require excitation of PPE-DABCO, which probably results in direct oxidative damage to the cell wall leading to β-glucan unmasking. This is the first instance in which PEs have been demonstrated to elicit immunostimulatory attributes. Our work demonstrates that the biocidal and immunostimulatory properties of phenylene ethynylene antimicrobials make them promising candidates for novel antimicrobial

applications to improve the health outcomes of patients with life-threatening fungal infectious diseases.

Chapter 7: *Summary and Future Directions*

We are writing this at a time when the scientific enterprise is facing a challenge where, as suggested by Whitesides and others, "core disciplines have drifted more towards 'iteration' and 'improvement' and away from 'discovery.' [233]"

In both cases interfaces between these synthetic electrolytes and naturally occurring materials such as proteins, lipids, nucleic acids and cells are critical to their function or activity. We have presented a survey of several years' research, with a focus on the interactions of *p*-phenylene ethynylenes with Gram-negative bacteria (*E. coli*), Gram-positive bacteria (*S. aureus, Bacillus atrophaeus,* and *B. anthracis* Sterne), and pathogenic yeast *(Candida albicans, C. parapsilosis,* and *C. glabrata*).

First and foremost, we determined the biocidal activity of an oligomer, EO-OPE (C2) and a complex formed between it and sodium dodecyl sulfate. The complexes are able to withstand prolonged periods of irradiation, continuing to effectively kill both Gram-negative and Gram-positive bacteria, while the oligomer by itself loses its biocidal effectiveness quickly in the presence of light. In addition, damage and stress responses induced by these biocides in both *E. coli* and *S. aureus* are discussed. This work shows that complexation with surfactants is a viable method for long-term light-activated biocidal applications. In a subsequent study, we formed a complex between a weakly biocidal anionic oligomer, EO-OPE-SO3, and a cationic surfactant; the effects on their biocidal activity against Gram-negative *E. coli* and Gram-positive *S. aureus* is explored. The enhancement in biocidal activity that is observed when the complex is irradiated suggests that interfacial surfactant gives the complex a net-positive charge, allowing it to strongly associate with the bacterial membrane. The results of this study imply a method

for enhancement of biocidal activity of singlet-oxygen sensitizers, and corroborate the use of surfactants as a drug-delivery agent.

We demonstrate a basic strategy for surface modification that combines the ability to control attachment by microbes with the ability to inactivate microbes. The surface consists of two active materials: poly(*p*-phenylene ethynylene)-based polymers (cationic PPE-DABCO and anionic PPE-SO3), which can inactivate a wide range of microbes and pathogens, and poly(N-isopropylacrylamide)-based polymers, which can switch between a hydrophobic "capture" state and a hydrophilic "release" state. The combination of these materials creates a surface that can both bind microbes in a switchable way and kill surface-bound microbes efficiently. Considerable earlier work with cationic poly(*p*-phenylene ethynylene) polyelectrolytes has demonstrated and characterized their antimicrobial properties, including the ability to efficiently destroy or deactivate Gram-negative and Gram-positive bacteria, fungi, and viruses. Similarly, much work has shown that surface-polymerized films of poly(N-isopropylacrylamide) are able to switch their surface thermodynamic properties from a swollen, relatively hydrophilic state at low temperature to a condensed, relatively hydrophobic state at higher temperature, and that this switch can control the binding and/or release of microbes to poly(N-isopropylacrylamide) surfaces. The active surfaces described herein were fabricated by first creating a film of biocidal poly(*p*-phenylene ethynylene) using layer-by-layer methods, and then conferring switchable adhesion by growing poly(N-isopropylacrylamide) through the poly(*p*-phenylene ethynylene) layer, using surface-attached polymerization initiators. The resulting multi-functional, complex films were then characterized both physically and functionally. We demonstrate that such films kill

and subsequently induce widespread release of Gram-negative and Gram-positive bacteria.

We went on to investigate the photophysical properties and the light- and dark-biocidal activity of two poly(*p*-phenylene ethynylene) (PPE)-based conjugated polyelectrolytes (CPEs) bearing cationic imidazolium solubilizing groups. The two polymers feature the same PPE-type backbone, but they differ in the frequency of imidazoliums on the chains: PIM-4 features two imidazolium units on every phenylene repeat, whereas PIM-2 contains two imidazolium units on every other phenylene unit. Both polymers are very soluble in water and polar organic solvents, but their propensity to aggregate in water differs with the density of the imidazolium units. The polymers are highly fluorescent, and they exhibit the amplified quenching effect when exposed to a low concentration of anionic electron-acceptor anthraquinone disulfonate. The CPEs are also quenched by a relatively low concentration of pyrophosphate by an aggregation-induced quenching mechanism. The biocidal activity of the cationic imidazolium CPEs was studied against both Gram-negative *Escherichia coli* and Gram-positive *Staphylococcus aureus* bacteria in the dark and under blue-light illumination. Both polymers are effective biocides, exhibiting greater than 3 log kill with 30-60 min of light exposure at concentrations of $\leq$10 μg mL^{-1}.

While cell death may occur in the dark, these biocidal compounds are far more effective in the light as a result of their ability to sensitize the production of cell-damaging reactive oxygen species. In an interesting and revealing study, the interactions of a specific cationic oligo-*p*-phenylene ethynylene with spore-forming *Bacillus atrophaeus* and *Bacillus anthracis* Sterne have been investigated. Flow cytometry assays

are used to rapidly monitor cell death, as well as spore germination. EO-OPE (Th,C2) effectively killed *Bacillus anthracis* Sterne vegetative cells (over 4 log reduction), presumably by severe perturbations of the bacterial cell wall and cytoplasmic membrane, while also acting as an effective spore germinant in the dark. While 2 log reduction of *B. anthracis* Sterne spores was observed, it is hypothesized that further killing could be achieved through enhanced germination.

Finally, we monitored the viability of *Candida* species after treatment with PPE-DABCO or EO-OPE-DABCO by flow cytometry in order to explore the antifungal properties of these compounds. The oligomer was found to disrupt *Candida albicans* yeast membrane integrity independent of light-activation, while the PPE is only able to do so in the presence of light, allowing for some control as to the manner which cytotoxic effects are exhibited. The contrast in killing efficacy between the two compounds is likely related to their size difference and their intrinsic abilities to penetrate the fungal cell wall. Unlike EO-OPE-DABCO, PPE-DABCO displayed a strong propensity to associate with soluble β-glucan, which is expected to inhibit its ability to access and perturb the inner cell membrane of *Candida* yeast. Furthermore, treatment with PPE-DABCO unmasked *Candida albicans* β-glucan, and increased phagocytosis by Dectin-1-expressing HEK-293 cells. In summary, cationic phenylene ethynylenes show promising biocidal activity against pathogenic *Candida* yeast cells, while also exhibiting immunostimulatory effects.

The underlying theme of this research reveals that curiosity and application-driven directions have fed each other, generating both the discovery of several important applications for the mitigated contamination of pathogenic bacteria and fungi. The

willingness to undertake new directions and pursue new discoveries has been critical at every step of the way, requiring us to make connections between various classical fields, including organic synthesis, organic photochemistry, microbiology, colloid and interface science, materials science, computational modeling, biochemistry and neuroscience. The pursuit of useful technology for a particular application has, in our experience, many times generated as a side benefit some new knowledge, which points to another valuable purpose. Along with the scientific content of this review, we would like the reader to take away something of a case study in modern chemical research. We would like to inspire scientists to pursue the new ideas suggested to them by their research, rather than merely "iterating and improving" upon the same old ones. Furthermore, making an artificial separation between "fundamental" and "applied" research, or between "science" and "engineering", is dangerous and indeed fatal to creativity. Today's researchers must, if possible, embrace the often-unnatural interfaces between ideas, between people, and between sciences.

Chapter 8: *Experimental Methods*

8.1 Previously-Synthesized Compounds

The synthesis of EO-OPE (C2) has been reported in a previous study [27]. The synthesis of EO-OPE-SO3 has been reported in a previous study [102].

8.2 UVA Photolysis of OPE and OPE-SDS complex

The solid compound EO-OPE (C2)**,** as a dichloride salt, was dissolved in filtered water with a resistivity of 18 MΩ*cm to a final concentration of 10 μM. The solution was then exposed to UVA radiation via a Luzchem LZC-ORG photoreactor (Luzchem Research, Ontario, Canada) in a quartz tube or cuvette. This photoreactor was configured with 10 LZC-UVA lamps (>5.3 mW-cm^{-2} over 316-400 nm, Luzchem Research, Ontario, Canada) with a fan-powered exhaust to keep a stable temperature and a carousel for homogeneous irradiation of samples. Progress of the photolysis was monitored by UV-visible absorption spectroscopy with a Molecular Devices Spectramax M5 spectrophotometer (Molecular Devices, Sunnyvale, CA). Sodium dodecyl sulfate (SDS) was obtained from Sigma Aldrich. For the OPE-SDS complexes, 10 μM EO-OPE (C2) was mixed with 40 μM SDS, 0.24% of the critical micelle concentration (CMC). *S. aureus* samples were exposed to an OPE-SDS complex where the concentration of SDS was 0.33 mM, as they were much more resilient to killing caused by SDS. Samples were irradiated for 0, 30, 60, and 120 minutes prior to exposure to bacteria. Once exposed to EO-OPE (C2) or OPE-SDS, *E. coli* and *S. aureus* samples were irradiated with UVA in the photoreactor for 30 minutes and 15 minutes, respectively.

8.3 OPE-TTAB Complex Formation

The solid compound, as a sodium salt, was dissolved in filtered water with a resistivity of 18 MΩ*cm to a final concentration of 20 µM. Tetramethyl trimethylammonium Bromide was purchased from Sigma-Aldrich (St. Louis, MO), and dissolved in filtered water with a resistivity of 18 MΩ*cm to a final concentration of 80 µM. A solution of 20 µM OPE and 80 µM TTAB was prepared in a quartz cuvette, and UV-visible absorption and fluorescence spectroscopy were performed with a Molecular Devices Spectramax M5 spectrophotometer (Molecular Devices, Sunnyvale, CA). These are shown in Figure 8.1, below.

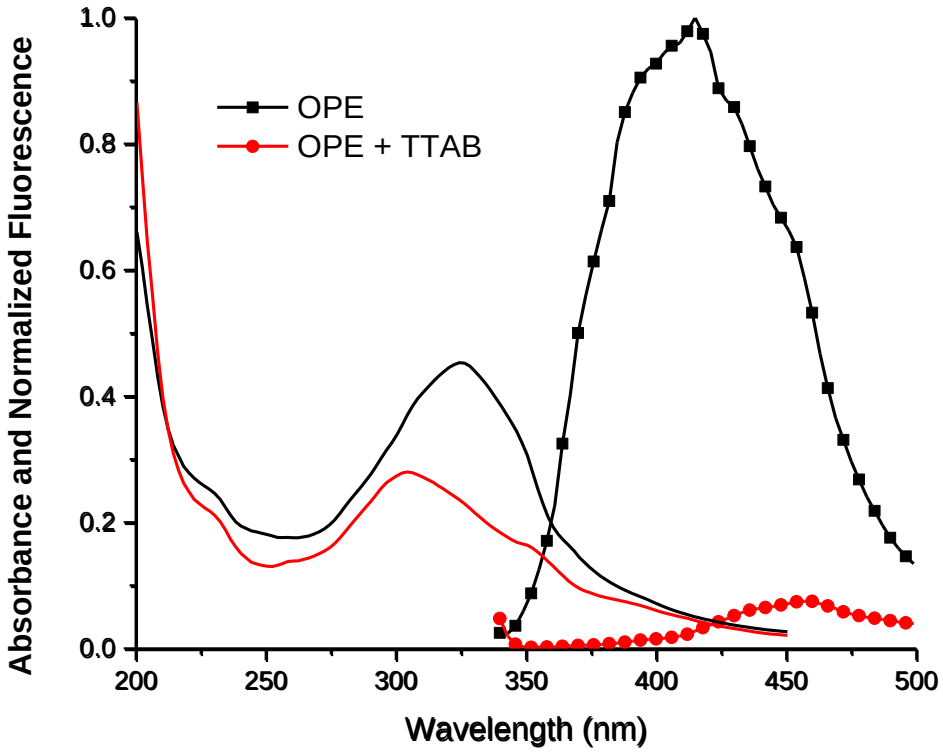

Figure 8.1: UV-Visible absorbance and fluorescence spectra (dotted) for 20 µM EO-OPE-SO3 alone and complexed with 80 µM TTAB.

8.4 Growth of non-sporulating Bacteria

All media and buffers were prepared using deionized water with a resistivity exceeding 18 MΩ*cm. Nutrient broth 234000 (Difco) was prepared according to manufacturer's instructions. Nutrient agar was prepared upon the addition of 8 g/L bacto agar (Difco). *Staphylococcus aureus* (ATCC 10832) and *Escherichia coli* (ATCC 29425) were both grown from glycerol-preserved stock which originated from first-generation cultures of original ATCC lyophilates grown in nutrient broth (containing 20% glycerol) and subsequently stored at -70 °C. Cells of the aforementioned strains were grown upon the inoculation of glycerol stock on Difco nutrient agar at 37 °C for 24 hours. Cell culture preparation for biocidal testing entailed scraping *S. aureus* or *E. coli* colonies off their agar plates and transferring them to nutrient broth for growth. Cells were then incubated in an Orbital Incubator Shaker (American Instruments, Lafayette, CA) for 18 h at 37 °C with rapid shaking (250 rpm). Following the incubation period, cells were washed by two 15 min centrifugations at 4,400 rpm; in each case, supernatant was replaced by 30 mL of 0.85% NaCl following pellet formation.

8.5 Flow Cytometry Analysis of Bacteria

Bacterial stock solutions were prepared at a concentration of 2×10^7 cells/mL^{-1}. Biocidal testing was conducted by adding 500 μL of the bacterial stock to 500 μL PIM stock, such that the final testing volume was 1 mL. After incubating in the dark or light (see below), cells were stained with 5 mM SYTO 21 (live stain; Life Technologies,

Grand Island, NY) and 1.5 mM propidium iodide (dead stain; Life Technologies, Grand Island, NY) for 15 min prior to flow cytometry analysis (see below). Flow cytometry-reported biocidal activity was validated with standard plating techniques. This entailed pipetting 50 μL of unstained, diluted sample onto petri dishes of solidified nutrient agar; the plates were allowed to incubate for 18 hours at 37ºC. Colonies were counted using ImageJ image-analysis software.

Where noted, samples were exposed to near-visible light via a Luzchem LZC-ORG photoreactor (Luzchem Research, Ontario, Canada) in translucent 0.5-dram glass vials. This photoreactor was configured with 10 LZC-420 lamps (emission wavelength range of 400-460 nm). To provide uniform light exposure to all samples, the photoreactor is equipped with a rotating carousel. Using a PM100D Optical Power Meter (Thor Labs, Newton, NJ), the incident power of this lighting configuration was measured to be 2.28 ± 0.028 mW/cm^2.

Flow cytometry was utilized to determine the cell concentration of *S. aureus* or *E. coli* in the 0.85% NaCl-suspended bacterial stock solutions [234]. The Accuri C6 (Becton Dickinson, Franklin Lakes, New Jersey) used was equipped with a blue laser that excites at 488 nm, as well as two filters: a green fluorescence filter (FL-1: 530 nm) and a red fluorescence filter (FL-3: 670 nm long-pass). A primary threshold ensured that only events exhibiting 40,000 FSC-A scatter units were included in the data, while a secondary threshold ensured that only events exhibiting 250 FL-1 fluorescence units (live stain fluorescence channel) were included. The core size of the flow cytometer was set to 10 μm, with a flow rate of 14 μL/min. 100,000 events were recorded in each sample. An example of the flow cytometry gating scheme for *E. coli* is shown below, in Figure 8.2.

The UVA-irradiated negative control is shown on the left side of the figure, and the ethanol positive control is shown on the right.

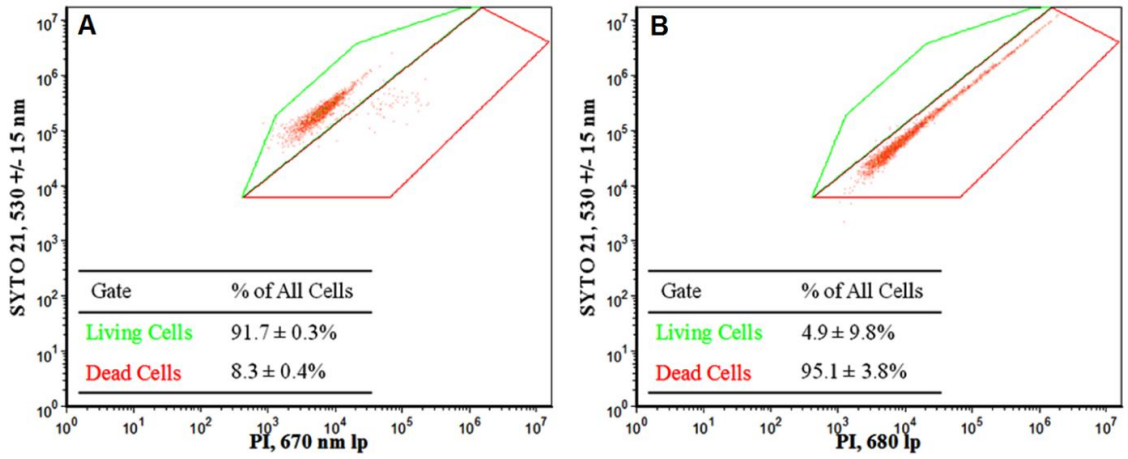

Figure 8.2: Flow cytometry gating for *E.coli;* A. UVA-irradiated negative control; B. 70% Ethanol positive control.

An example of the flow cytometry gating scheme for *S. aureus* is shown below, in Figure 8.3. The UVA-irradiated negative control is shown on the left side of the figure, and the Ethanol positive control is shown on the right. The results of the live/dead assay were verified by confocal fluorescence microscopy using a Zeiss Confocal microscope with an Ar laser (488 nm) and a HeNe laser (513 nm) as an excitation source.

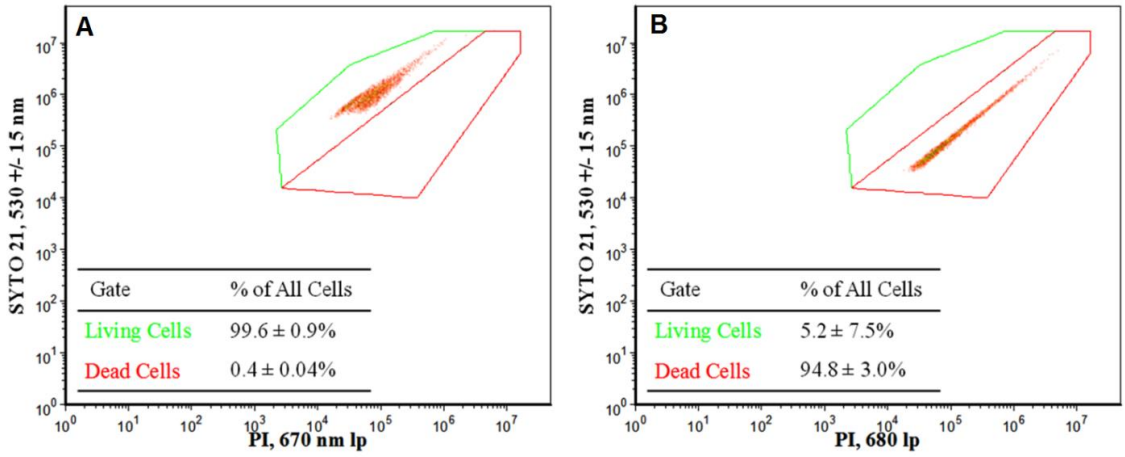

Figure 8.3: Flow cytometry gating for *S. aureus*; A. UVA-irradiated negative control; B. 70% Ethanol positive control.

8.6 Standard Plating Techniques

Standard plating techniques were utilized to validate flow cytometry data. This entailed pipetting and spreading 50 µL aliquots of diluted, unstained sample, onto nutrient agar plates. The plates were incubated at 37 °C for 18 hours to permit sufficient colony growth. Colonies were then counted and viabilities calculated relative to the UVA negative control. Exposure times matched those implemented in the aforementioned flow cytometry experiments.

8.7 Layer-by-Layer Film Deposition

Borosilicate glass slides (Corning Cover Glass No. 2, 25 mm^2; Catalogue # 2875-25) were immersed in piranha solution (3:1 mixture of H_2SO_4:H_2O_2) for 1 hr and rinsed with approximately 2 mL of high performance liquid chromatography (HPLC) water (Thermo

Fisher Scientific; Waltham, MA). The PPE-DABCO/PPE-SO_3 multilayer films were fabricated using a nanoStrata StratoSequnce IV Robot (Nanostrata; Tallahassee, FL). The formation of 1.5 bilayers involved soaking the glass substrate for 10 min in PPE-DABCO (0.1 mM PRU in Millipore water), followed by a sequence of three rinses using fresh Millipore water for 3 min, 1 min, and 1 min (3-1-1 rinse), 10 min in PPE-SO_3 (0.1 mM polymer repeat units, PRU, in Millipore water), another 3-1-1 rinse, another 10 min in PPE-DABCO, and a final 3-1-1 rinse. All Millipore water used was purified to a resistance of 18.2 MΩ using a Millipore Milli-Q system. The slides were then dried with nitrogen gas. Figure 8.4, below, illustrates the release of bacteria from glass cover slips treated with CPE and PNIPAAm. In this case, bacteria were exposed to the substrates at a concentration of 1×10^5 cells/mL. This relatively low concentration was beneficial in determining how cell attachment and viability varied as function of cell concentration.

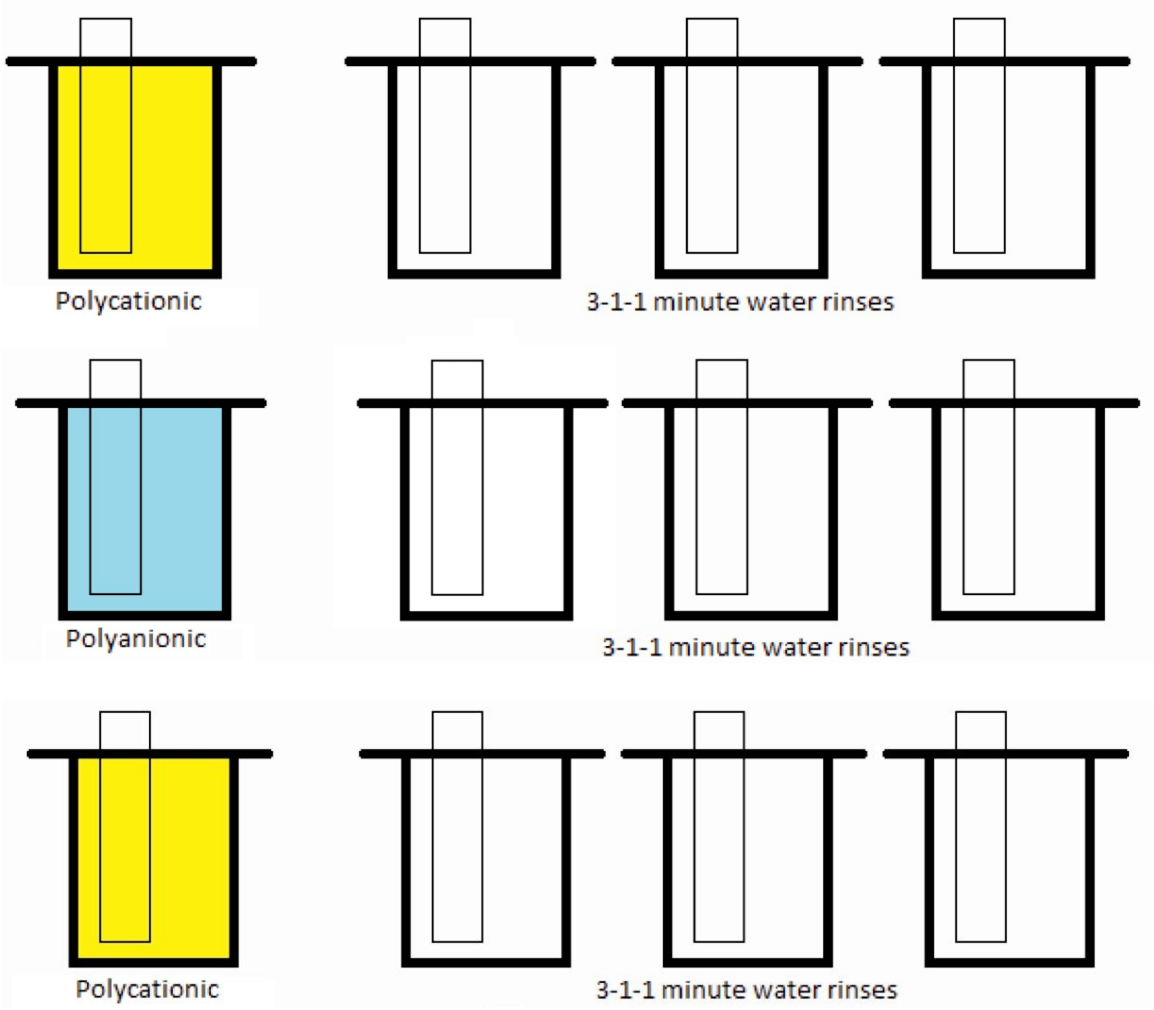

Figure 8.4: Multilayer Sequence for 1.5 bilayers of a polycationic solution (PPE-DABCO) and a polyanionic solution (PPE-SO_3).

8.8 Formation of Silane Self-Assembled Monolayers (SAMs) and Atom-Transfer-Radical-Polymerization of NIPAAm

Silane monolayer films comprised of ATRP initiators were fabricated in a manner similar to that described by Shivapooja and coworkers.[132] Briefly, the clean glass slides were placed into a jar with a lid and placed under nitrogen for 5 min. A solution of 10 mM of

(3-trimethoxysilyl) propyl 2-bromo 2-methylpropionate (ATRP initiator) in anhydrous toluene was then added to the jar, capped tightly with a lid, and sealed with Parafilm. The contents were stored at 25 °C for a minimum of 12 hr, and subsequently rinsed with acetone followed by methanol. Polymerization of NIPAAm onto borosilicate glass substrates was also carried out in a manner similar to that described by Shivapooja *et al*.[132] The glass substrates with films of ATRP initiators were placed into a jar, with a small stir bar, containing 0.75 M NIPAAm monomer, 0.4 mM Cu(II)Br, and 0.7 mM *N*,*N*,*N*′,*N*″,*N*″-pentamethyldiethylenetriamine (PMDETA) dissolved in 25 mL of water/MeOH (1:1 by volume). The polymerization reaction was initiated by addition of 8 mM ascorbic acid. The reaction was allowed to progress at room temperature for 30 min. The substrates were then rinsed with acetone (to quench the polymerization), warm methanol (to remove excess monomer), and HPLC water. The slides were then dried with nitrogen gas. Figure 8.5 provides a summary of the complete fabrication process for the CPE/PNIPAAm glass substrates.

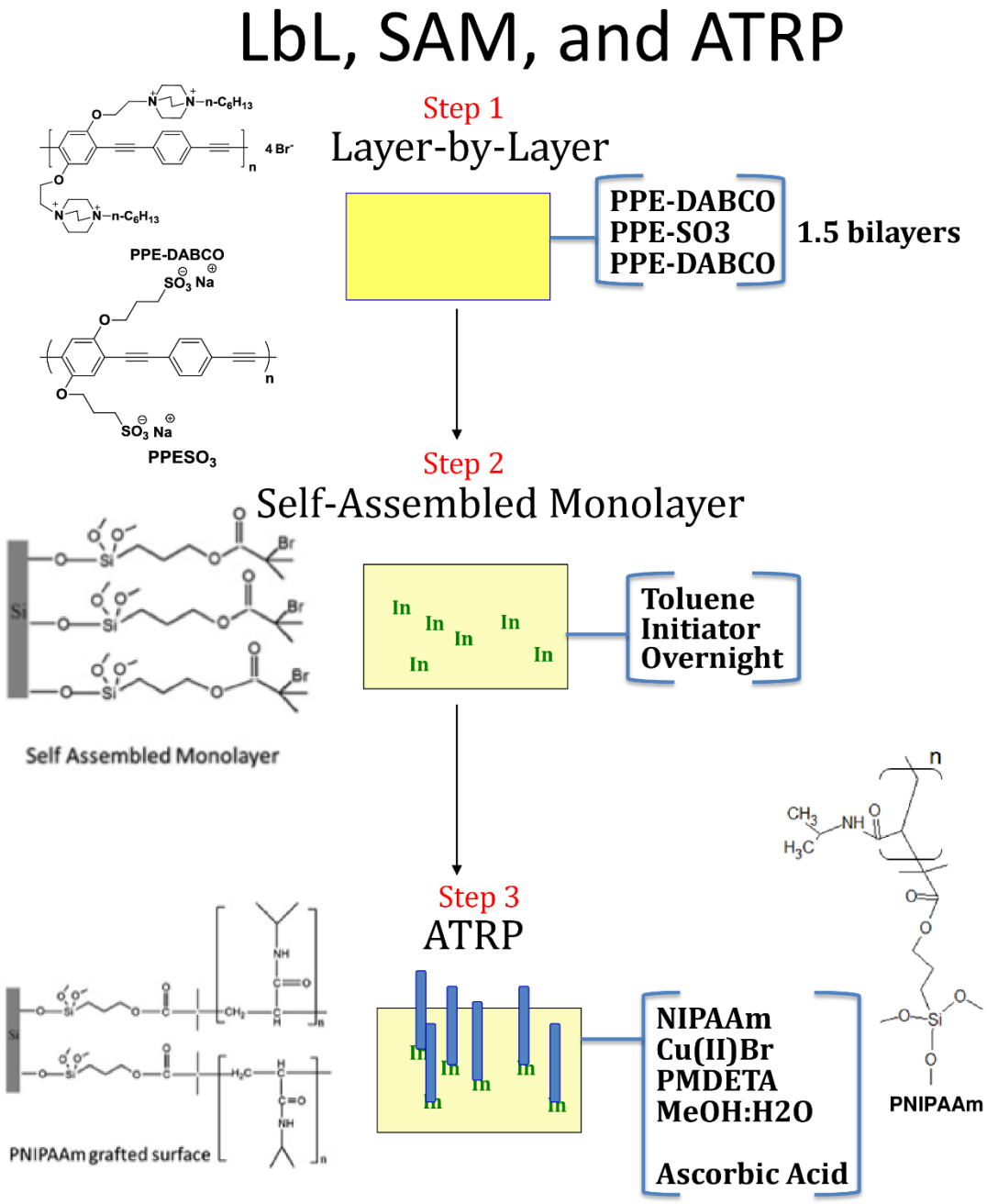

Figure 8.5: Overview of the fabrication process for the CPE/PNIPAAm glass substrates.

8.9 Atomic Force Microscopy

All samples of CPE, PNIPAAM, and CPE with PNIPAAM on coverslips were cut to a size of 1.2 cm x 1.2 cm, and thoroughly dried in flowing nitrogen gas for 30 min. AFM images were obtained in tapping mode, using a Nanoscope IIIa atomic force microscope (AFM) outfitted with a rectangular silicon cantilever (40 N/m spring constant; Veeco; RTESPAW). All captured AFM images were processed and analyzed using flatten, plane fit, and scanline erasure operations with Veeco Nanoscope V531rl imaging software.

8.10 Biocidal Testing of CPE/PNIPAAm glass substrates

A 500 μL aliquot of saline-suspended cells was added to a partitioned region of the borosilicate glass substrates, encompassing 1 in^2. Cell release was determined using initial cell concentrations of 1 x 10^7 mL^{-1}), while viability was determined using initial cell concentrations 1 x 10^5 mL^{-1}. Biocidal activity was achieved upon exposing samples to blue light in a photoreactor (Luzchem LZC-ORG; Luzchem Research; Ontario, Canada) for 1 hr. The emission spectrum of these lamps is centered at 420 nm, with a peak width of roughly 40 nm; this overlaps well with the absorption spectrum of PPE-DABCO,[52] which has a strong broad band centered at about 430 nm, with a width of 150 nm. The photoreactor was equipped with 8 lamps, which irradiated samples with an incident power density of 2.28 mW/cm^2. Samples were exposed to light for 1 hr, and subsequently incubated at 37 °C for 1 hr to permit PNIPAAm-grafted cover slips sufficient time to exceed their lower critical solution temperature (LCST) of 32°C.

8.11 Confocal Microscopy

After exposure to light, cells were stained for a period of 15 min for imaging by confocal microscopy. In the case of Gram-positive *S. aureus*, cells were stained with 5 mM SYTO 21 (live stain; Life Technologies; Grand Island, NY) and 1.5 mM propidium iodide (dead stain; Life Technologies). In the case of Gram-negative *E. coli*, SYTO 9 (Life Technologies) was utilized as the live stain, rather than SYTO 21. Both species of bacteria were stained with 1 μL live stain and 1 μL dead stain, which were combined and subsequently added to the cell-coated substrates. Following the 15-min staining period, supernatant was removed and replaced with up to 100 μL sterile 0.85% NaCl for imaging purposes. Samples were then covered with a glass slide and imaged using a Zeiss confocal microscope (Carl Zeiss AG; Jena, Germany). An Ar laser (488 nm) and a HeNe laser (513 nm) were utilized to excite the live and dead stains, respectively. A 40x oil immersion lens was utilized, providing viewing dimensions of 675 μm x 825 μm.

Cell viability was determined by evaluating confocal images of samples seeded with 1×10^5 cells/mL in ImageJ. First, the mean background intensity was subtracted from each image. Background-subtracted images were then separated into red and green channels before being binarized via a max-entropy threshold.[235] Cells exhibiting sufficient red-channel fluorescence (resulting from the dead stain, propidium iodide)—such that the threshold was exceeded—were marked as dead. Cells not marked as dead were then evaluated in the green channel; those exhibiting sufficient green-channel fluorescence (resulting from either SYTO 9 or SYTO 21) were counted as viable.

Sample viability was then determined by dividing the number of viable cells by the sum of both viable and dead cells.

Cell release was estimated in a similar manner; however, rather than manually counting cells and designating them as live or dead, the total coverage of the image was evaluated as a fraction of all pixels. Coverage percentage thus equals the fraction of pixels occupied by bacteria (whether live or dead) per image. In both cases, at least 5 images were taken per sample, with no overlap of field of view. All samples were evaluated in triplicate.

8.12 Contact Angle Measurements

Contact angles of various surfaces and surface films were obtained using a Krüss Tensiometer. Cover slips coated with each type of surface were initially submerged in either 4 °C or 37 °C Millipore water for 1 hr, then mounted onto the tensiometer's hanging clamp and the system calibrated. To measure contact angles, each cover slip was lowered into fresh water baths of either 4 °C or 37 °C at a rate of 6 mm/min, with force being recorded 6 times per mm of displacement. In total, cover slips were submerged up to 15 mm in depth. Contact angle was then computed based on the tensiometer-reported force between displacement depths of 5 and 10 mm (displacement tends to vary linearly as a function of displacement in this region). It should be noted that receding contact angle is recorded as the substrate is lifted out of the water, meaning the glass was submerged in water for ~2 min at this point.

8.13 Synthesis of PIM-2 and PIM-4

8.13.1 Materials

Triethylamine and tetrahydrofuran (THF) were purified by distillation over sodium hydride. $Pd(PPh_3)_4$ catalyst was used as received from Strem Chemical Co. Compounds 1, 2, 3, 5 and 6 (Figure 8.6) were synthesized following revised procedures reported in the literature [236,237].

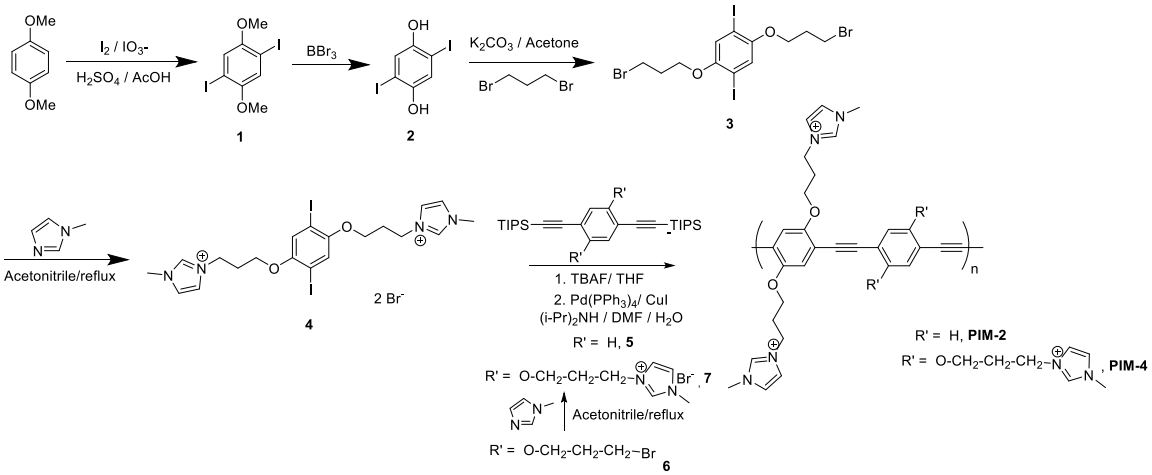

Figure 8.6: Synthesis of imidazolium-containing CPEs.

8.13.2 Synthesis of Precursor 4:

3,3'-(3,3'-(2,5-diiodo-1,4-phenylene)bis(oxy)bis(propane-3,1-diyl))bis(1-methyl-1H-imidazol-3-ium) (4)

Compound 3 (500 mg, 0.82 mmol) and 1-methylimidazole (336 mg, 4.1 mmol) were suspended in 15 ml acetonitrile and the reaction was refluxed overnight. The solvent was removed and the white solid was recrystallized from ethanol to yield 610 mg of the product. Yield (94 %). ^{1}H NMR (300 MHz, DMSO-d_6): δ 2.26 (m, 4H), 3.99 (s, 6H),

4.01 (t, 4H), 4.31 (t,4H). 7.30 (s, 2H), 7.65(m,2H), 7.75(m,2H), 9.14(s,2H). ^{13}C NMR (75 MHz, DMSO-d_6):

δ 152.7, 137.3, 124.3, 123.2, 122.969, 87.7, 67.5, 47.2, 36.6, 29.8. ESI-MS $[2M]^{2+}$ = 304.0066 (Expected: 304.0667)

8.13.3 Synthesis of Precursor 7

3,3'-(3,3'-(2,5-bis((triisopropylsilyl)ethynyl)-1,4-phenylene)bis(oxy)bis(propane-3,1-diyl))bis(1-methyl-1H-imidazol-3-ium) (7)

Compound 6 (200 mg, 0.281 mmol) and 1-methylimidazole (114 mg, 1.4 mmol) were suspended in 10 mL acetonitrile, and the reaction was refluxed overnight. The solvent was removed and the white solid was triturated with ether to yield 190 mg of the product. Yield (76 %). ^{1}H NMR (300 MHz, $CDCl_3$): δ 1.12(s, 42H), 2.48 (t, 4H) 3.95 (s, 6H), 4.05 (t, 4H), 4.61 (t,4H). 6.81 (s, 2H), 7.21(m,2H), 7.42(m,2H), 10.5(s,2H). ^{13}C NMR (75 MHz, DMSO-d_6):δ 154.09, 137.41, 124.49, 122.87, 117.66, 114.04, 103.37, 97.21, 66.23, 46.55, 36.49, 29.87, 19.14, 11.4. ESI-MS $[2M]^{2+}$ = 358.2447 (Expected: 358.2435)

8.13.4 Polymerization Reactions

All of the polymers were prepared from the corresponding monomers to a similar procedure. Representative procedure for the synthesis of cationic imidazolium polymers is provided below. For the synthesis of PIM-4, the TIPS protected monomer (7) in DMF was first deprotected with TBAF before the addition of other reagents. For the synthesis of PIM-2, a deoxygenated solution of 8.9 mg (9 μmol) of $Pd(PPh3)_4$ and 2 mg (10 μmol) of CuI in 4 mL of DMF/diisoprpylamine (1:1 mixture) was added via cannula to a deoxygenated solution of Monomers 4 (250 mg, 0.32 mmol) and 5 (40.2 mg, 0.319

mmol) in 8 mL of DMF/Water mixture in a Schlenk flask. The solution was deoxygenated with argon for 15 min and the resulting mixture was heated to 60 °C and stirred for 16 h. The obtained yellow solution was poured into acetone (100 mL), which induced the polymer to precipitate. The precipitate was collected by vacuum filtration and further purified by two repeated cycles of dissolution in minimum amount of water and precipitation into a large volume of acetone. To the aqueous solution of the polymer, 20 mg of NaCN was added and the final purification was accomplished by dialysis of an aqueous solution of the polymer against deionized water and (Millipore Simplicity water system) using a 6-8 kDa MWCO cellulose membrane (Fisher Scientific). After dialysis, the polymer solution was filtered through a 0.45 μm nylon membrane, and the concentration was adjusted to ca. 1.0 mg mL^{-1}. The polymer was stored in this format and diluted as appropriate for spectroscopic studies. The typical yield was about 75%.

8.14 Characterization of PIM-2 and PIM-4

NMR spectra were recorded using a Varian VXR-300 FT-NMR spectrometer, operating at 300 MHz for ^{1}H NMR and at 75.4 MHz for ^{13}C NMR. UV−visible spectra were recorded using a Varian Cary 100 dual-beam spectrophotometer with a scan rate of 300 nm min^{-1}. Corrected steady-state fluorescence spectra were obtained with a PTI Quanta Master spectrometer (Photon Technology International). Quartz cuvettes of 1 cm × 1 cm were used for solution spectra, and the emission was collected at 90° relative to the excitation beam. Fluorescence quantum yields are reported relative to known standards. The optical density of solutions at the excitation wavelength was ≤ 0.1, and corrections were applied for differences in the refractive index of standard and sample solutions.

Transient absorption (TA) spectra were collected using a CCD-based TA system that relies on a Nd:YAG laser for excitation, as described elsewhere [238]. Singlet oxygen yields were measured by monitoring the singlet oxygen emission at 1280 nm using a near-IR fluorescence spectrometer, as previously described [239]. The actinometer used for singlet oxygen yields was 2′-acetonaphthone (Φ_Δ = 0.79 ± 0.02) in deuterated methanol.

8.14.1 PIM-2

^{1}H NMR (300 MHz, CD_3OD): δ 2.46 (br, 4H), 3.88 (br, 6H), 4.19 (br, 4H), 4.53 (br,4H). 7.21-8.5 (br,12H).

8.14.2 PIM-4

^{1}H NMR (300 MHz, CD_3OD): δ 2.43 (br, 4H), 3.90 (br, 6H), 4.22 (br, 4H), 4.53 (br,4H). 7.29 - 8.55 (8H, aromatic).

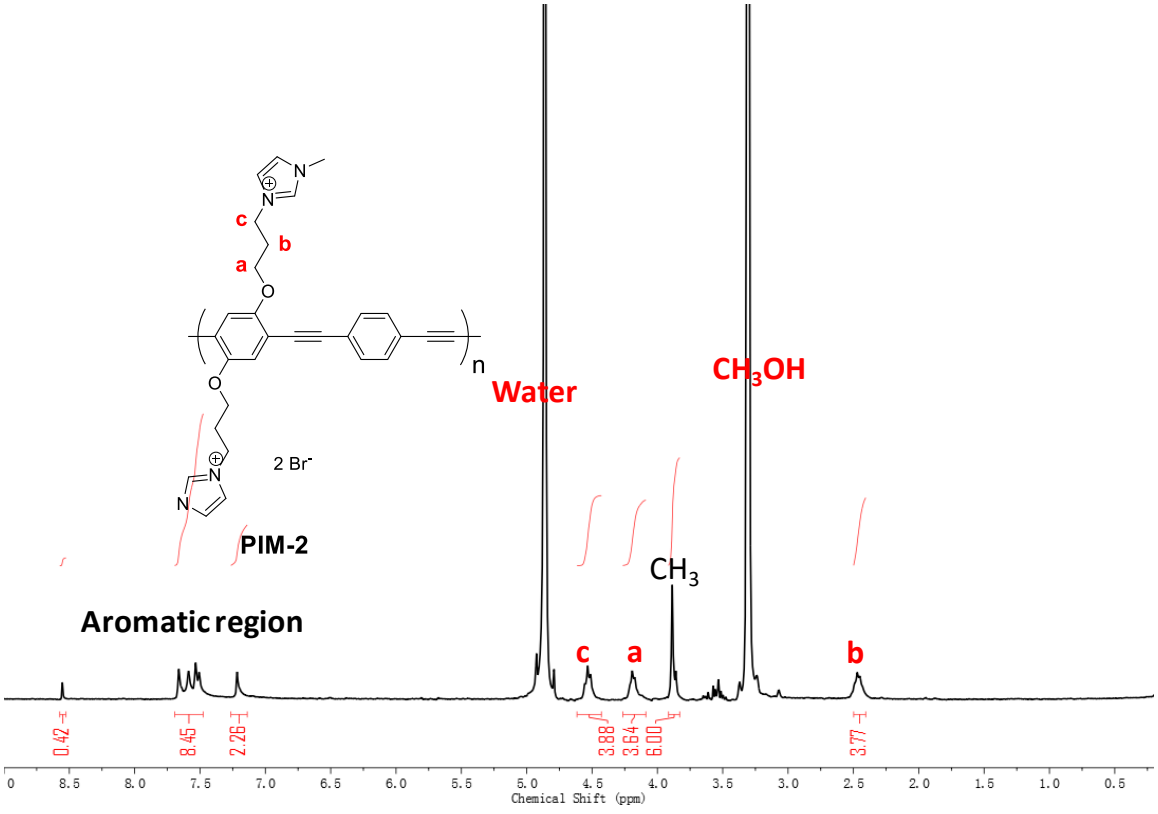

Figure 8.7: ^{1}H NMR (300 MHz) of PIM-2 in deuterated methanol.

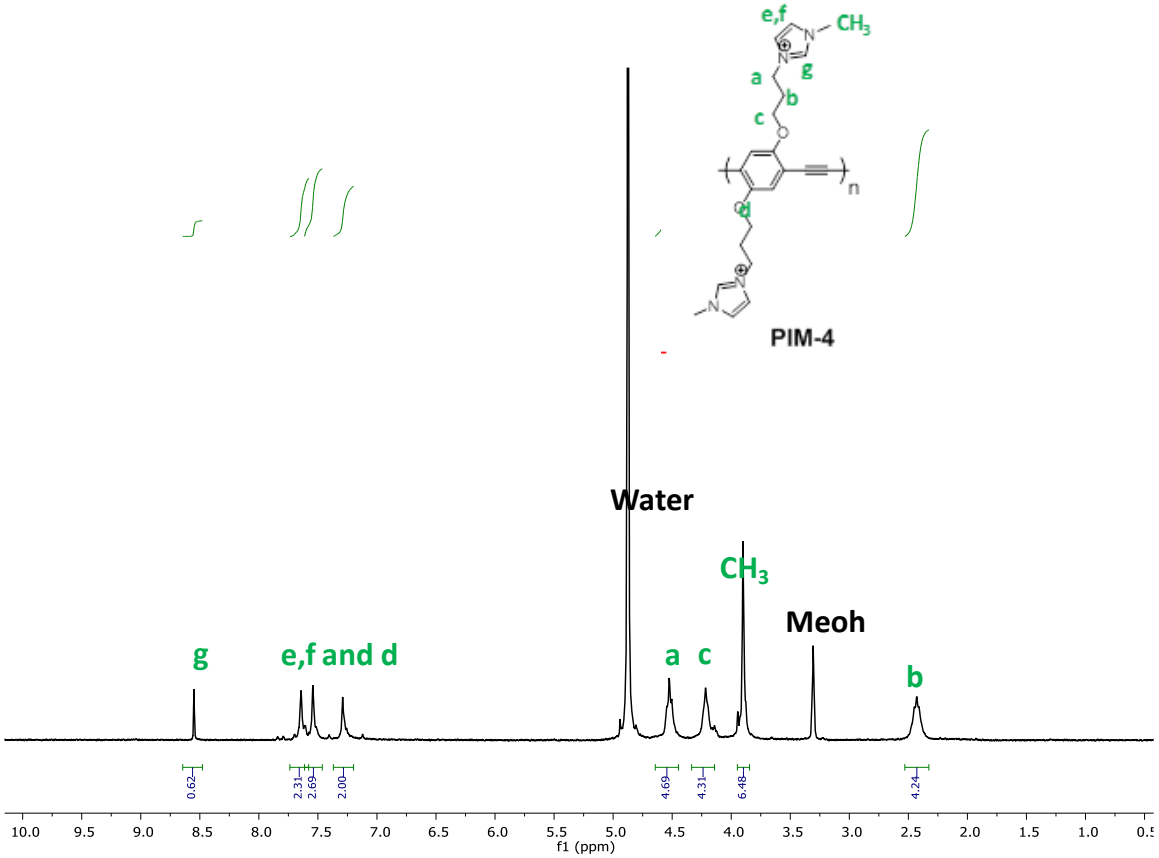

Figure 8.8: ^{1}H NMR (300 MHz) of PIM-4 in deuterated methanol.

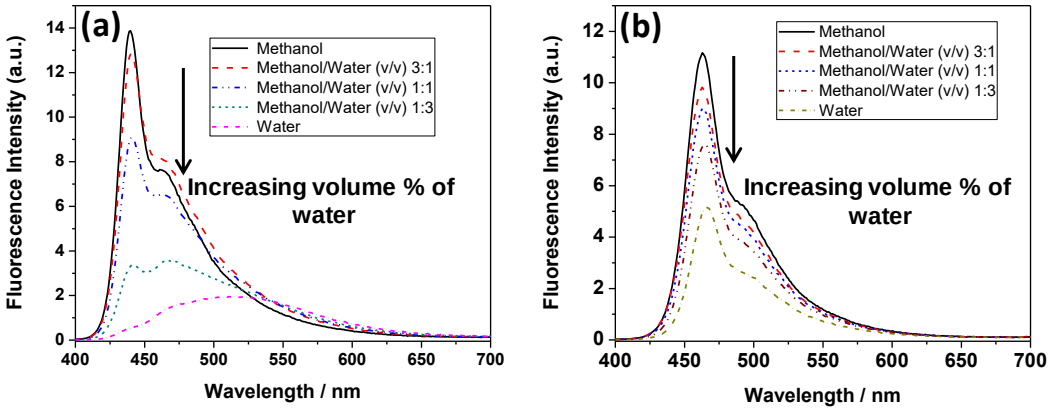

Figure 8.9: Fluorescence spectra of (a) PIM-2, and (b) PIM-4 in a mixture of methanol and water.

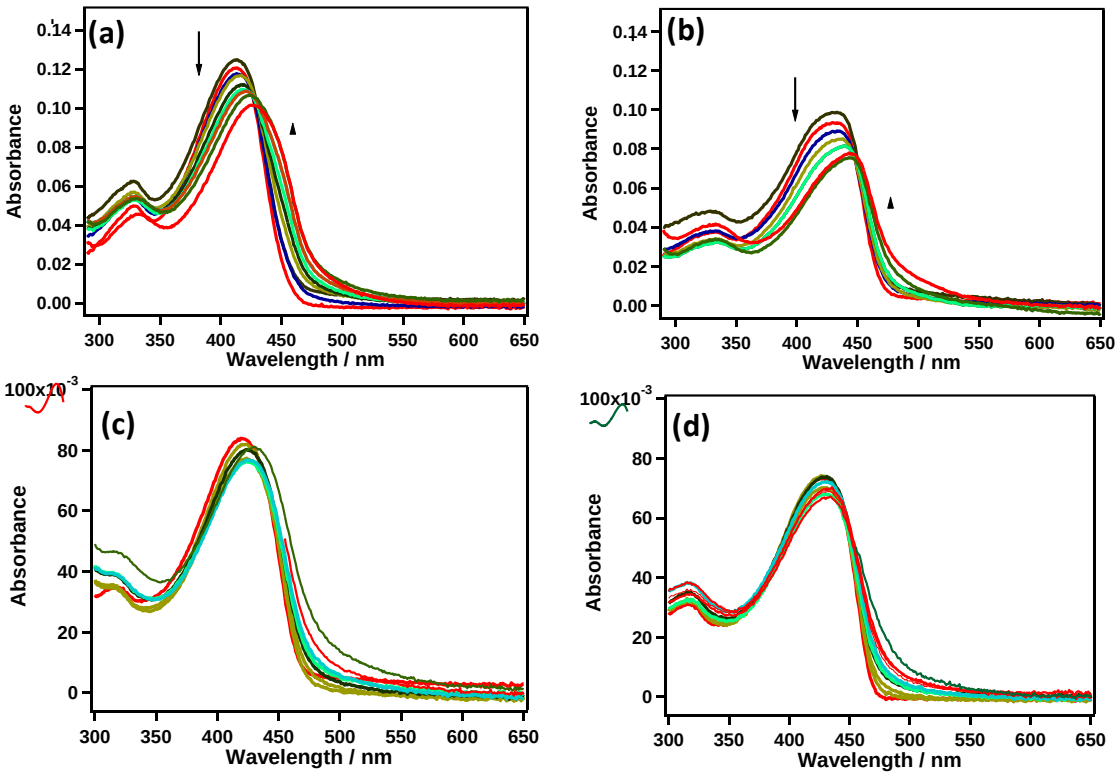

Figure 8.10: UV-Absorption spectra of PIM-2 and PIM-4 with added AQS. [PIM-2] = [PIM-4] = 10 μM in all cases. (a) PIM-2 in methanol ([AQS] = 0.09 to 1.1 μM), (b) PIM-

2 in water ([AQS] = 0.09 to 1.1 μM), (c) PIM-4 in methanol ([AQS] = 0.09 to 1.4 μM), and (d) PIM-4 in water ([AQS] = 0.09 to 1.4 μM).

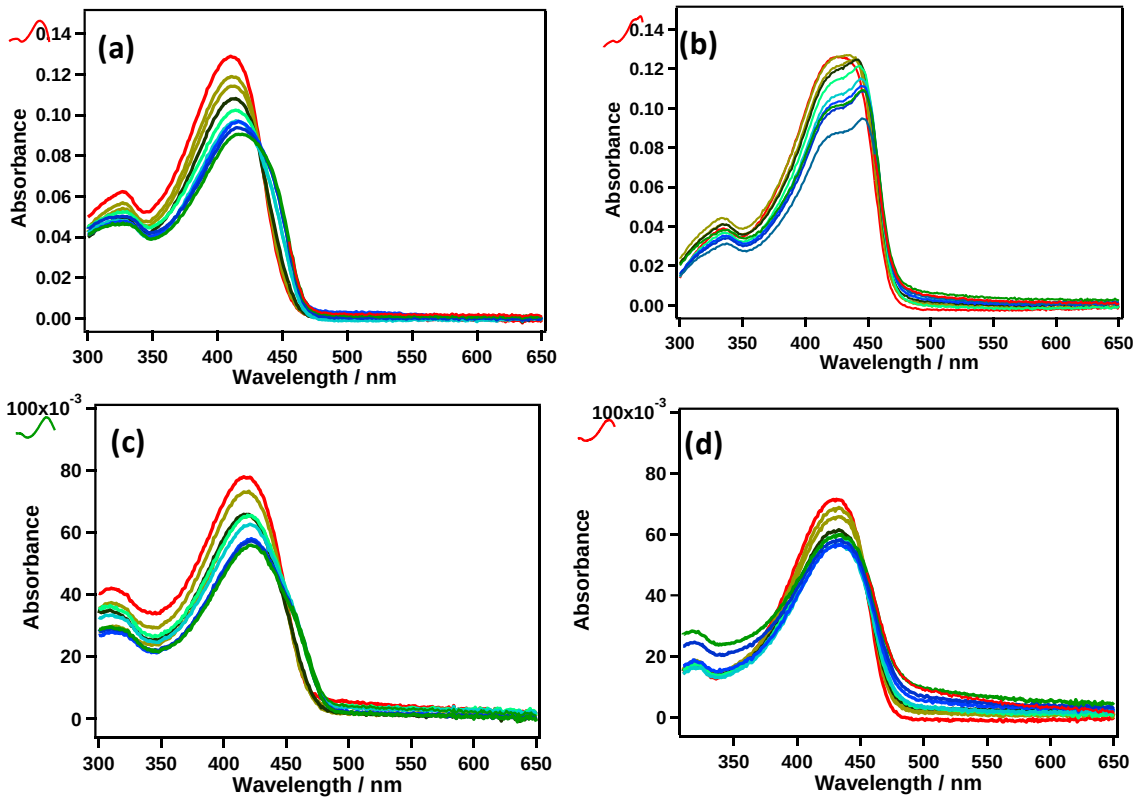

Figure 8.11: UV-Absorption spectra of PIM-2 and PIM-4 with added PPi. [PIM-2]= [PIM-4] = 10 μM in all cases. (a) PIM-2 in methanol ([PPi] = 0.1 to 2.1 μM), (b) PIM-2 in water ([PPi] = 0.4 to 9.5 μM), (c) PIM-4 in methanol ([PPi] = 0.4 to 6 μM), and (d) PIM-4 in water ([PPi] = 1.2 to 13.7 μM).

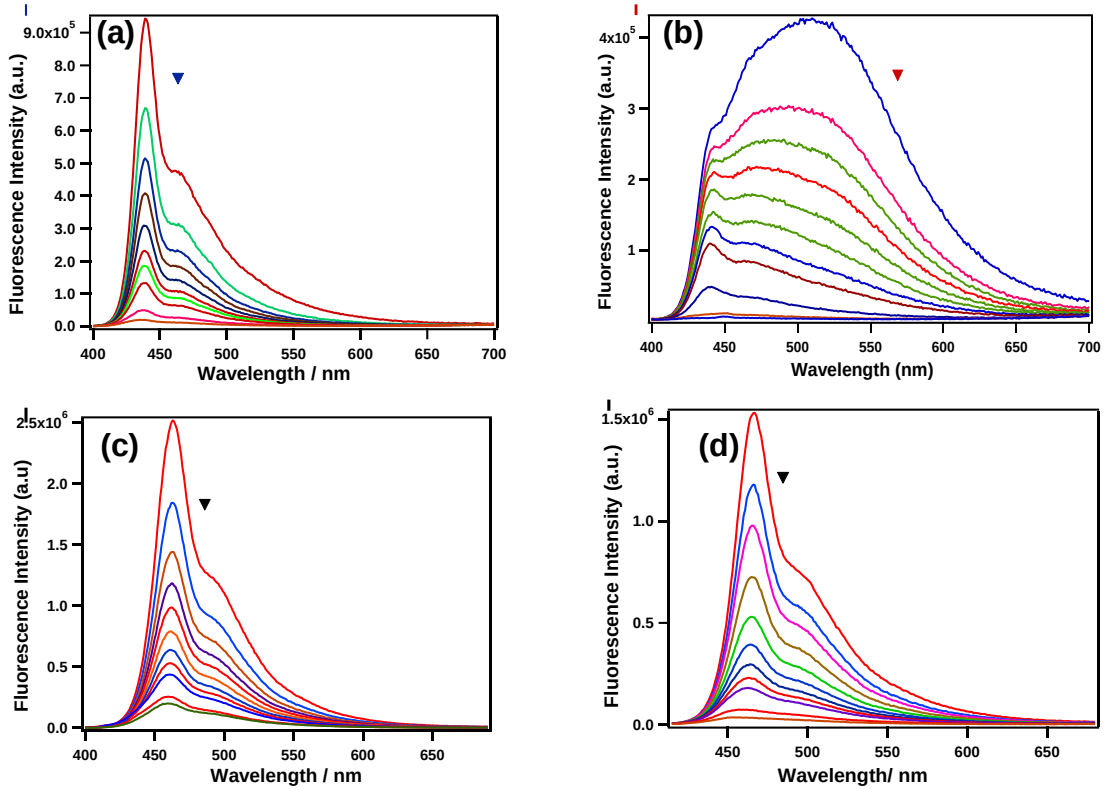

Figure 8.12: Fluorescence spectra of PIM-2 and PIM-4 with added AQS. [PIM-2]= [PIM-4] = 10 μM in all cases. (a) PIM-2 in methanol ([AQS] = 0.09 to 1.1 μM), (b) PIM-2 in water ([AQS] = 0.09 to 1.1 μM), (c) PIM-4 in methanol ([AQS] = 0.09 to 1.4 μM), and (d) PIM-4 in water ([AQS] = 0.09 to 1.4 μM).

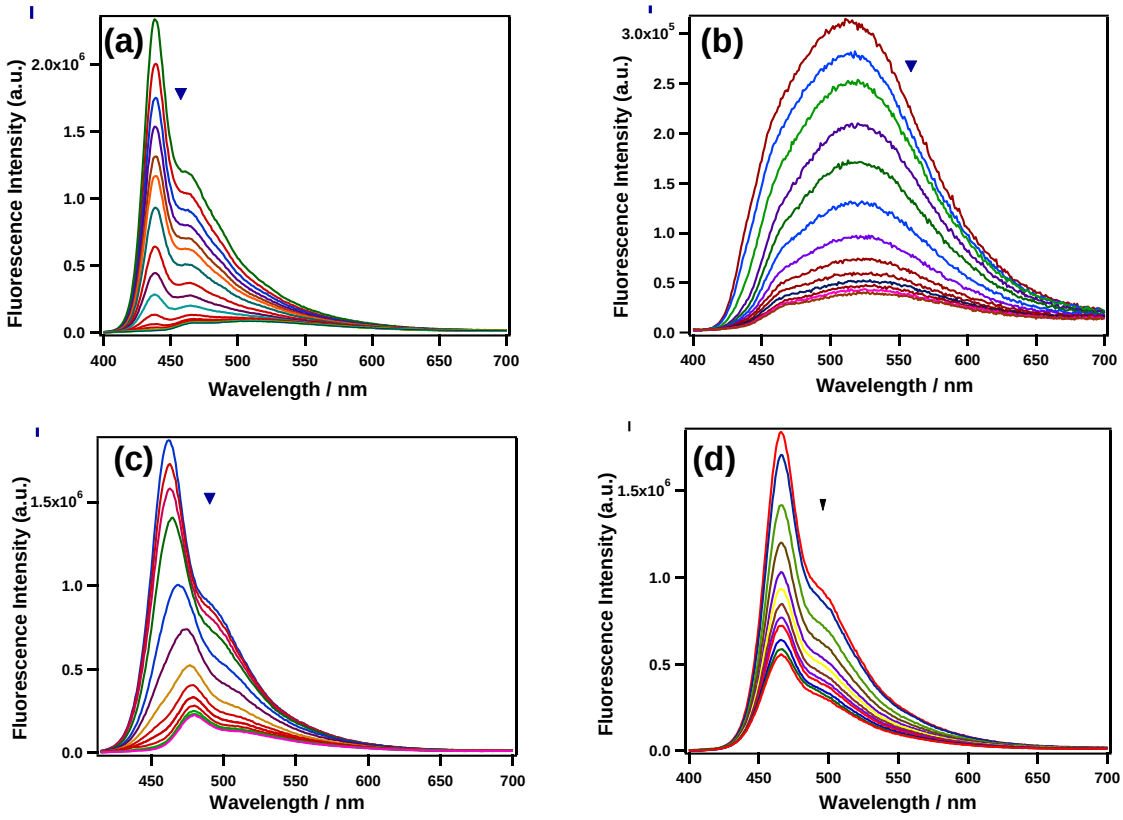

Figure 8.13: Fluorescence spectra of PIM-2 and PIM-4 with added PPi. [PIM-2]= [PIM-4] = 10 μM in all cases. (a) PIM-2 in methanol ([PPi] = 0.1 to 2.1 μM), (b) PIM-2 in water ([PPi] = 0.4 to 9.5 μM), (c) PIM-4 in methanol ([PPi] = 0.4 to 6 μM), and (d) PIM-4 in water ([PPi] = 1.2 to 13.7 μM).

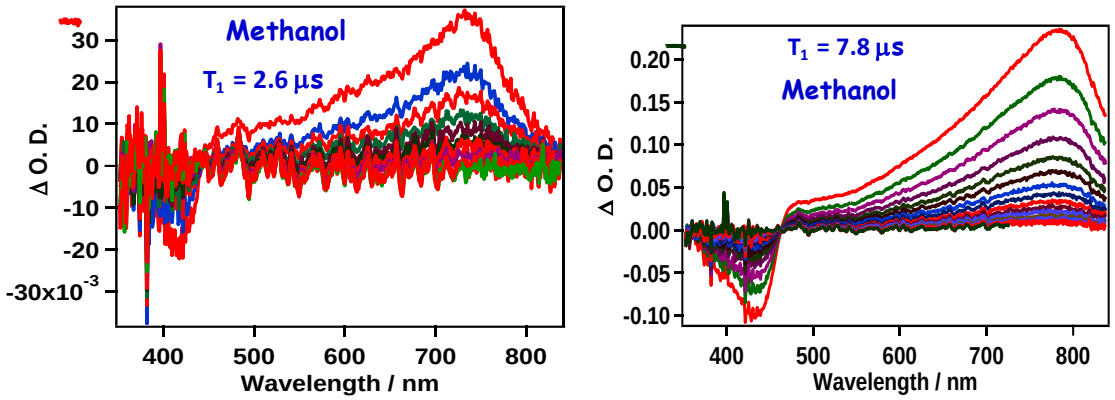

Figure 8.14: Transient absorption difference spectra of PIM-2 (left) and PIM-4 (right) in methanol (initial delay = 65 ns, subsequent delay increment = 1 µs); OD ~ 0.7 at 355 nm and excited with the laser energy of ~7 mJ.

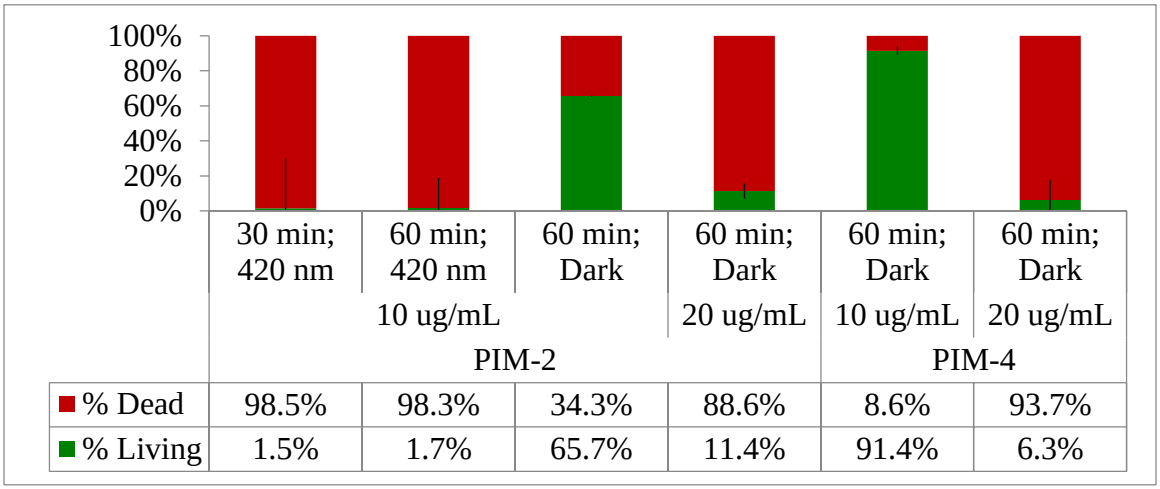

	30 min; 420 nm	60 min; 420 nm	60 min; Dark	60 min; Dark	60 min; Dark	60 min; Dark
	10 ug/mL			20 ug/mL	10 ug/mL	20 ug/mL
	PIM-2				PIM-4	
% Dead	98.5%	98.3%	34.3%	88.6%	8.6%	93.7%
% Living	1.5%	1.7%	65.7%	11.4%	91.4%	6.3%

Figure 8.15: Biocidal activity of PIM-2 and PIM-4 against Gram-negative *E. coli*, relative to 60 minute UVA Negative Control. Data obtained via standard plating techniques on nutrient agar.

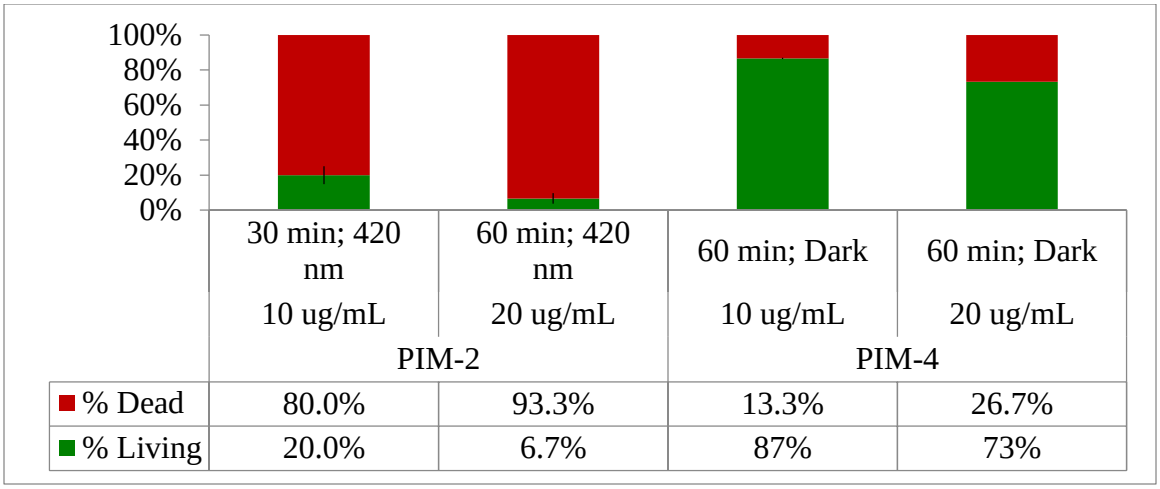

	30 min; 420 nm 10 ug/mL	60 min; 420 nm 20 ug/mL	60 min; Dark 10 ug/mL	60 min; Dark 20 ug/mL
	PIM-2		PIM-4	
% Dead	80.0%	93.3%	13.3%	26.7%
% Living	20.0%	6.7%	87%	73%

Figure 8.16: Biocidal activity of PIM-2 and PIM-4 against Gram-positive *S. aureus*, relative to 60 minute UVA negative Control. Data obtained via standard plating techniques on nutrient agar.

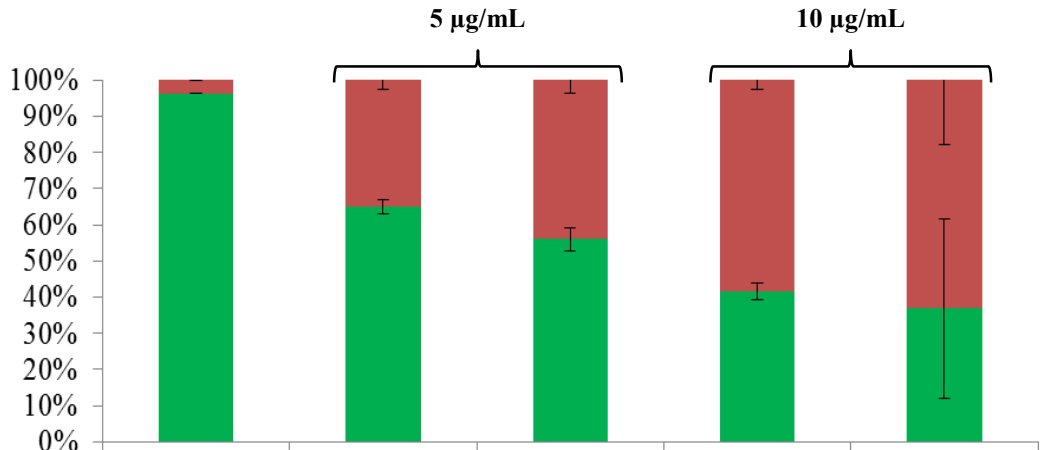

	420 nm NC	30 min; 420 nm	60 min; 420 nm	30 min; 420 nm	60 min; 420 nm
% Dead	3.63	34.99	43.96	58.44	63.10
% Living	96.37	65.01	56.04	41.56	36.90

Figure 8.17: Biocidal Activity of PPE-DABCO against *E. coli*. Data obtained via flow cytometry live/dead analysis.

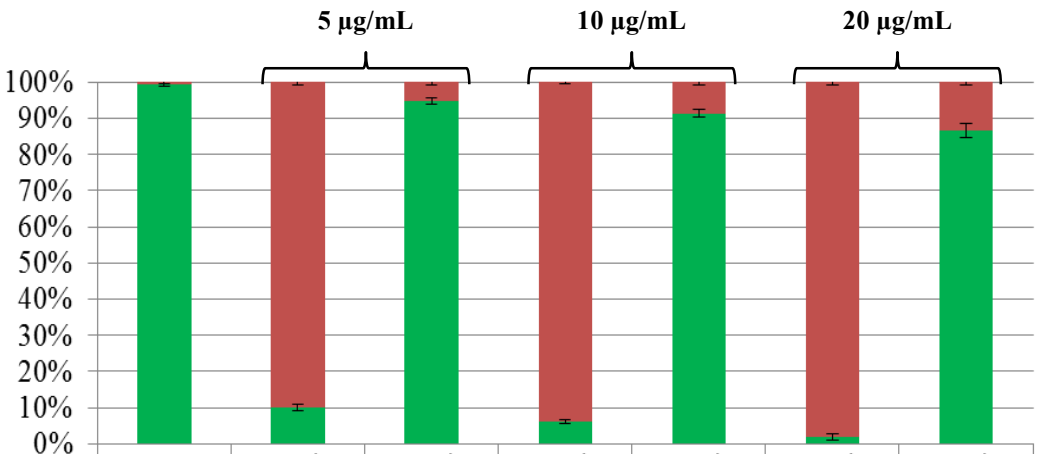

	420 nm NC	60 min; 420 nm	60 min; Dark	60 min; 420 nm	60 min; Dark	60 min; 420 nm	60 min; Dark
% Dead	0.46	89.85	5.29	93.96	8.68	98.19	13.40
% Living	99.54	10.15	94.71	6.04	91.32	1.81	86.60

Figure 8.18: Biocidal activity of PPE-DABCO against *S. aureus*. Data obtained via flow cytometry live/dead analysis.

8.15 Growth and Preparation of *Bacillus atrophaeus* spores

Bacillus atrophaeus (ATCC #9372) spores were obtained from 20% glycerol-suspended spore stock stored at -70 °C. A working batch of *B. atrophaeus* spores was obtained by induced germination and subsequent sporulation on sporulation agar. Using a sterile inoculation loop, spore colonies were scraped off the sporulation agar, suspended in sterile DI water, and filtered through glass wool as described by Gaillard *et al.*[240]. Spores were then washed three times via centrifugation (15 minutes, 4.4k RPM), with the pellet being suspended in 50% ethanol, and stored at 4 °C for 12 hours to provide time for vegetative cell death. Spores were then washed another three times via centrifugation and suspended in sterile DI water. Spores were then aliquoted into glass vials and stored at 4 °C until use. Concentration of these aliquots was determined with a hemocytometer.

8.16 Growth and Preparation of *Bacillus atrophaeus* vegetative cells

Bacillus atrophaeus vegetative cells were obtained by adding 1 mL of prepared spore aliquot to 50 mL Bacto tryptic soy broth (TSB; Becton Dickinson), which was then incubated for 18 hours at 30 °C with shaking (250 RPM). Vegetative cells were prepared for analysis by a triple-wash step consisting of three centrifugations of 4.4k RPM for 15 minutes each; with pellets suspended in 0.85% NaCl (physiological saline solution). The resulting cell concentrations were determined with a hemocytometer.

8.17 *Bacillus atrophaeus* viability testing

Viability testing was carried out at concentrations of 10^7 bacteria/mL in 0.85% NaCl. OPE concentrations of 10 μg/mL and 20 μg/mL were used to target *B. atrophaeus* vegetative cells and spores, respectively. Samples were prepared at volumes of 1 mL in 0.5-dram glass vials (VWR; Radnor, PA), and exposed to light or dark conditions for varying time periods. Light experiments were carried out in a 10-lamp LZC-ORG photoreactor (Luzchem Research; Ontario, Canada) fitted with UVA lamps (Hitachi FL8BL-B) exhibiting a power density of 0.975 mW/cm^2, over a wavelength range of 316-400 nm (centered at 350 nm). Samples were loaded into a rotating carousel in the center of the photoreactor to ensure uniform light exposure. Following light exposure, samples were stained with a membrane-permeable stain, SYTO 21 (Life Technologies; Carlsbad, CA), and a membrane-impermeable stain, propidium iodide (PI; Life Technologies). Membrane-permeable nucleic acid dyes such as SYTO 21 stain nucleic acids throughout a bacterium, independent of membrane damage. On the other hand,

membrane-impermeable stains such as propidium iodide selectively stain nucleic acids in bacteria with compromised membranes. Vegetative cell samples were permitted 15 minutes to stain at room temperature (in the dark), while spores were allowed 45 minutes to stain at room temperature (also in the dark). Staining of spores with hydrophilic nucleic acid stains, such as propidium iodide[241], takes longer than that of vegetative cells due to the fact that a spore's DNA is supercoiled within the inner membrane, which is inherently impermeable to hydrophilic molecules.[242]

Stained samples were then evaluated with an Accuri C6 (Becton Dickinson) flow cytometer equipped with a 488 nm, 50 mW laser. SYTO 21 fluorescence was quantified with the FL1 detector at 530 ± 15 nm; PI fluorescence was quantified with the FL3 detector at wavelengths exceeding 670 nm.

Two thresholds were used in viability analysis; the first was a forward scatter (FSC) threshold that ensured that only events exceeding 50,000 FSC units were included in the data sets. Lowering the forward scatter threshold to 50,000 helps ensure that small *Bacillus* spores aren't omitted as events. The second threshold was specific to the FL1 detector, and ensured that only events exhibiting some degree of SYTO 21 uptake (at least 250 fluorescence units) were included as data points. Bacteria were analyzed at a nominal flow rate of 14 μL/min, with a stream core diameter of 10 μm. All samples were evaluated until at least 10,000 events had been recorded. Using *B. atrophaeus* vegetative cells, the live gate was based on untreated negative controls, while the dead gate was based on positive controls exposed to 70% ethanol for 60 minutes. An additional gate was obtained to denote the fluorescence regions of viable, untreated spores.

This is not the first instance of flow cytometry being demonstrated to monitor progressive germination of *Bacillus* spores; in some cases, a single fluorescence reporter was used,[169] while other studies—such as those described herein—utilize a pair of complementary fluorescence stains[243].

8.18 SEM of *Bacillus atrophaeus* vegetative cells and spores

Spores exposed to EO-OPE (Th, C2), or simply 0.85% NaCl as a negative control, were examined by scanning electron spectroscopy (SEM) (Quanta 250 FEG SEM; FEI; Hillsboro, OR). Samples were fixed in 2.5% glutaraldehyde overnight at room temperature, rinsed in phosphate-buffered saline (PBS), and subsequently dehydrated in ethanol. Dehydrated samples were sputtercoated in approximately 12 nm of gold and palladium under vacuum and subsequently analyzed by SEM.

8.19 Growth and Preparation of *Bacillus anthracis* Sterne

BSL2 agent *B. anthracis* Sterne was not permitted for use in flow cytometry facilities and thus was prepared and evaluated independently of the aforementioned *B. atrophaeus*. *B. anthracis* Sterne spore stocks were prepared as previously described.[244] Briefly, spores were prepared in phage assay broth[245,246]; sporulation was subsequently confirmed with phase-contrast microscopy, and any remaining vegetative cells were killed with a 40 minute, 68 °C heat treatment. Bacteria were then washed and suspended in Dulbecco's phosphate-buffered saline (DPBS; Gibco), tittered, aliquoted, and stored at -80 °C. Colony growth of aliquots was evaluated before and after heat treatment (40 minutes at 68 °C) to ensure the absence of vegetative cells.

B. anthracis Sterne vegetative cells were prepared exclusively for the experiments described herein. *B. anthracis* Sterne spores were removed from frozen storage and thawed at room temperature before 20 μL of suspension was streaked onto a tryptic soy agar (TSA) plate. TSA plates were incubated for 16 hours at 37 °C. A sterile inoculation loop was then used to transfer 2 colonies from the TSA plate into 40 mL of brain heart infusion (BHI), along with 200 μL of glycerol. The flask was then aerobically incubated for 16 hours at 37 °C with 250 RPM shaking. To ensure sterility of BHI a second flask was aerobically incubated with 10 mL BHI. Following verification of sterility, 200 μL of the inoculated BHI was added to 800 μL sterile BHI, vortexed, and subsequently transferred to a disposable cuvette. The absorbance of the cuvette was measured at 600 nm relative to sterile BHI. A subculture was then prepared at an OD of 0.1 and aerobically incubated at 37 °C with shaking until the subculture's OD reached 1.0—indicating a vegetative cell concentration of 2×10^7 CFU/mL (confirmed by colony growth on TSA).

Saline-washed *B. anthracis* Sterne vegetative cells were exposed to 10 μg/mL EO-OPE (Th,C2) in light and dark conditions for varying time durations, diluted, and streaked onto TSA plates. TSA plates were incubated at 37 °C for 18 hours and the colonies counted to estimate viability. *B. anthracis* Sterne spores were evaluated by a similar technique, albeit with the implementation of heat treatment. In this case, samples were diluted, plated, and subsequently heat-treated to kill vegetative cells. Heat treatment is applied via a 68 °C water bath for 30 minutes, such that *B. atrophaeus* vegetative cells are killed; presumably, any resulting colony growth would result from spores and not vegetative cells. Heat-treated samples were also diluted and plated—the

difference of colony growth between the heat-treated and non-heat treated samples was used to gauge the percentage of sample which was vegetative cells. Negative controls contained no OPE, while heat treatment consisted of submersion in a 68 °C water bath for 30 minutes. Equations 1-3 were used to infer sample populations based on colony growth.

Equation 1

$$\%\ \text{of CFUs that are Viable Vegetative Cells} = 100\ \times \frac{CFU - CFU_{HT}}{CFU}$$

Equation 2

$$\%\ \text{of CFUs that are Viable Spores} = 100\ \times \frac{CFU_{HT}}{CFU}$$

Equation 3

$$\%\ \text{of CFUs that are nonviable relative to negative control} = 100\ \times \frac{CFU_{NC} - CFU}{CFU_{NC}}$$

CFUs are defined as the number of colony forming units on TSA prior to Heat Treatment, CFU_{HT} is the number of colony forming units on TSA after Heat Treatment, and CFU_{NC} is the number of colony forming units on TSA in the negative control (no heat treatment). These equations are implemented in Figure 5.6 as a means to monitor viability and germination, under the assumption that heat treated vegetative cells lose their ability to form colonies. All *B. anthracis* Sterne experiments (Figure 5.5 and Figure 5.6) were conducted in triplicate.

8.20 Fungal Culture

Candida albicans (ATCC, #MYA-2876), *C. parapsilosis* (ATCC, #22019), and *C. glabrata* (ATCC, #2001) were grown from glycerol stocks, stored at -80 °C. Said stock was transferred to 5 mL filter-sterilized yeast extract-peptone-dextrose (YPD) medium (Becton Dickinson), and grown for 16 h at 30 °C, with a shaking speed of 300 RPM. Such growth conditions yielded yeast at the late log phase [247].

Following a 10-minute centrifugation at 2,900 rcf, the supernatant was replaced with sterile phosphate-buffered saline (PBS), and subsequently vortexed. This washing step is repeated a second time to mitigate cell debris. Cell concentration was then determined using a disposable hemocytometer (INCYTO C-Chip; Fisher Scientific).

8.21 Derivation of Clinical Isolate Strains of *C. albicans*

Patient specimens (peripheral blood or catheter tips) were processed by Tricore Reference Laboratories (Albuquerque, NM) and identified as *C. albicans* using a Bruker Biotyper MALDI-TOF system (MS ID score > 2.0). Clonal isolates so identified were subcultured on Sabouraud agar slants and provided to the investigators as unique strains. Isolate strains were provided in completely deidentified form according to procedures approved by the University of New Mexico School of Medicine Human Research Protections Office. For biocidal assays, clinical isolates were grown in YPD broth as described above.

8.22 Biocidal Testing of Yeast Cells

All biocidal experiments were carried out in either translucent or opaque 1.5 mL microcentrifuge tubes, at cell concentrations of 5 x 10^6/mL in PBS. Two cationic compounds were tested, both based on the p-phenylene ethynylene backbone, with quaternized diazabicyclo[2,2,2]octane (DABCO)-functionalities. EO-OPE-DABCO and PPE-DABCO stocks were prepared in sterile deionized water (18.2 MΩ·cm at 25 °C), and contained 0.47% dimethyl sulfoxide (by volume) to improve solubility and minimize aggregate formation. Negative controls contained equal amounts of dimethyl sulfoxide.

Samples were exposed to controlled amounts of light using a 14-lamp photoreactor (LZC-4V; Luzchem Research; Ottawa, Ontario). A rotating carousel ensured that all samples receive equivalent levels of light exposure; ventilation kept the photoreactor below 30 °C. EO-OPE-DABCO absorbs in the ultraviolet region [166], warranting the use of UVA lamps (350 nm emission peak; 4.46 ± 2.41 mW/cm^2) to optimize singlet oxygen yields. Conversely, 420 nm blue-light lamps (6.62 ± 2.93 mW/cm^2) were used in PPE-DABCO tests; unlike its oligomeric counterpart, polymeric PPE-DABCO absorbs in the near-visible range [52]. Power density output was measured at the peak excitation wavelength for both lighting configurations. Data shown is an aggregation of two independent replicate experiments.

Samples were then stained with 5 µM membrane-permeable SYTO 9 (Invitrogen, S34854) and 1 µM membrane-impermeable TO-PRO-3 (Invitrogen, T3605), both of which are nucleic acid stains. After 30 min, samples were evaluated by flow cytometry (FACSCalibur; Becton Dickinson). At least 10,000 events were evaluated in each trial.

A heat-killed sample (70 °C for 30 min) was used to identify the fluorescence characteristics of dead cells.

15 min dark-activity assays were carried out in a somewhat different manner. Samples were prepared and stained with SYTO 9 and TO-PRO-3, albeit in the absence of any biocide. After a 30 min staining duration, EO-OPE-DABCO was added (10 µg/mL final concentration); the sample was then vortexed and analyzed by flow cytometry. Every minute, viability data was collected (again, 10,000 events/sample), for a total of 15 minutes. It is important to note that EO-OPE-DABCO was added one sample at a time, so that, in each case, flow cytometry readings could begin within 1 min of the biocide's introduction.

8.23 Spectroscopy of β-Glucan Interactions

Stocks of *S. cerevisiae* β-(1,3)-glucan (high, medium or low MW; gift of Biothera, Eagan, MN), PPE-DABCO, and EO-OPE-DABCO were mixed with 10 mM pH 7.4 phosphate buffer to a final concentration of 2 µg/mL in PPE-DABCO or EO-OPE-DABCO and 100 µg/mL in β-glucan. 200 µL solutions were transferred to a 160 µL nominal volume fused quartz fluorimetry cuvette, and read on a PTI QuantaMax 40 steady-state fluorescence spectrophotometer (HORIBA Scientific, Edison, NJ) with PMT detection. Emission spectra were obtained using an excitation wavelength of 350 nm for EO-OPE-DABCO and 420 nm for PPE-DABCO, and excitation spectra were obtained with the corresponding maximum emission wavelength.

8.24 Interactions of PPE-DABCO with Glucan Microparticles

Glucan microparticles were prepared from *C. albicans* SC5314 yeast cells using the extraction techniques described in Lowman *et al* [248]. Glucan microparticles were then suspended in PBS at a concentration of 1×10^5 mL^{-1}. Microparticles were sonicated for 10 min, and subsequently vortexed for another 5 min. PPE-DABCO was then added at a concentration of 2 µg/mL, and incubated at room temperature for 1 h. No PPE-DABCO was added to the negative control. 500 µL of each sample was transferred to petri dishes for examination by confocal microscopy. 405 nm excitation was used to induce fluorescence of PPE-DABCO.

8.25 Surface Exposure of β-Glucan

C. albicans yeast cells were treated in a similar manner to that of the previously described biocidal experiments. In effort to maintain a consistent degree of cell death across samples, OPE-DABCO exposure in UVA light was limited to just 10 min. A thermal positive control was also implemented, which entailed heating samples to 100 °C for 30 min. Following the appropriate treatment and removal from the photoreactor, samples were blocked with 1% (w/v) bovine serum albumin (BSA) for 30 min at room temperature. The samples were then treated with a primary antibody, anti β-glucan IgG (Biosupplies, 400-2), at a final concentration of 10 µg/mL, for an additional 30 min. Negative controls contained 10 µg/mL isotype-matched murine IgG in place of anti β-glucan IgG. A secondary antibody with Alexa Fluor 647 dye (Invitrogen, A21235) was then added (1 µg/ml in PBS+1% BSA), along with 5 µM SYTO 9 were simultaneously

added and allowed to stain cells for 30 minutes at 25 °C prior to analysis by flow cytometry. Data shown is an aggregation of two independent replicate experiments.

8.26 Tissue Culture & Transfection

HEK-293 cells (ATCC, #CRL-1573) were cultured in DMEM supplemented with 10% CS, 1% Penicillin/Streptomycin, 2mM L-glutamine, and 1mM sodium pyruvate at 37°C, 5% CO_2. Cells were then plated in 6 well plate at $1x10^5$ cell per well. mApple-human Dectin1A-C-10 (gift of Michael Davidson, Addgene #54883) was transfected into cells by following standard protocols using Fugene 6 (Promega, #E2691). Cell cultures were used for further experimentation at 24 h post-transfection with growth in normal medium, as described above.

8.27 Phagocytosis Assay

C. albicans yeast cells were subjected to the same treatment conditions as in the aforementioned β-glucan exposure study, before being spun down and washed in PBS. Following the last wash step the *C. albicans* were stained with 7.5μM of SYTO 9 (Invitrogen, #S-34854) and 75μM of CypHer5E NHS-ester (GE Healthcare, #PA15401) for one hour at 25°C. After staining the *C. albicans* were added to live, Dectin-1A-C-10 transfected HEK-293 cells for one hour. Next ice cold PBS was used to lift the HEK-293 cells off of the plate. The controls with *C. albicans* or HEK-293 alone or the above samples with a mixture of *C. albicans* and HEK-293 cells were analyzed using an LSR Fortessa flow cytometer (Becton Dickinson) and FlowJo software (FlowJo, Ashland, OR). At least 10,000 side scatter (SSC)-positive events are evaluated in each trial.

CypHer 5, SYTO 9, and mApple fluorescence was observed at emission wavelengths of 660 nm (670/14), 525 nm (505 LP, 530/30), and 578 nm (582/15), respectively. Data shown is an aggregation of two independent replicate experiments.

Chapter 9: Appendix

9.1 OPE-SDS Complexation

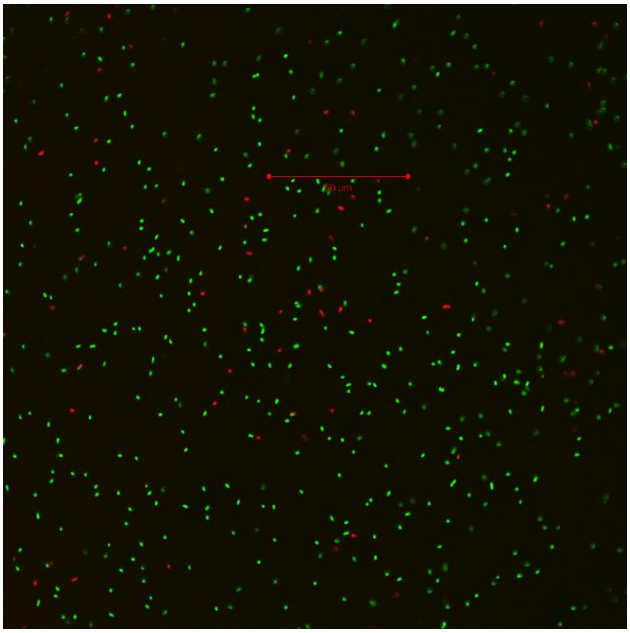

Figure 9.1: Confocal Fluorescence Microscopy images of *E. coli* exposed to 2 hour pre-irradiated EO-OPE (C2)**.**

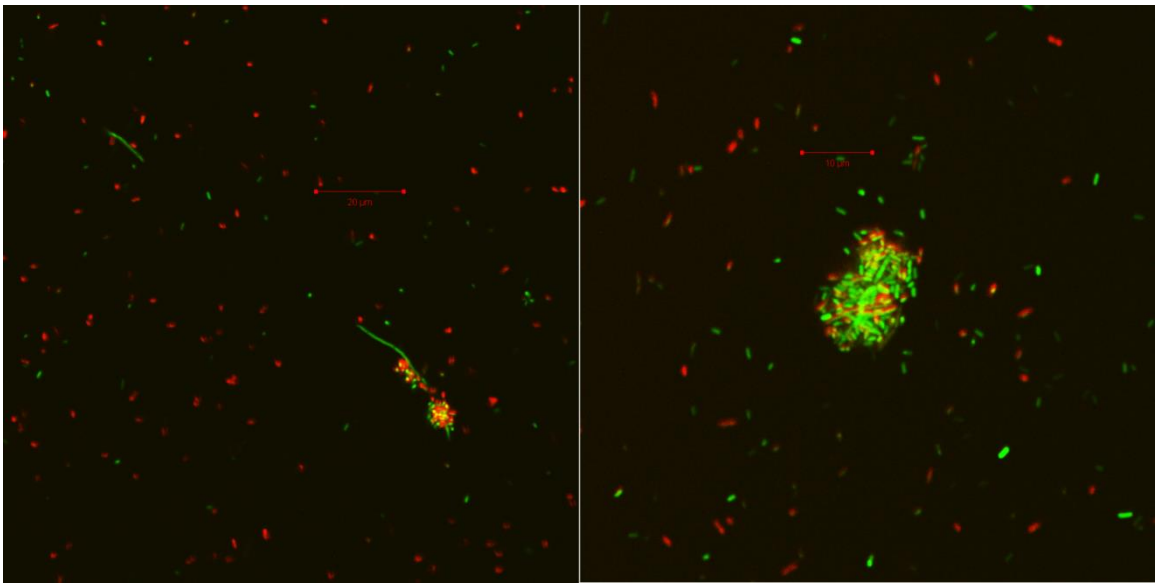

Figure 9.2: Confocal Fluorescence Microscopy images of *E. coli* exposed to 2 hour pre-irradiated OPE-SDS.

9.2 OPE-TTAB Complexation

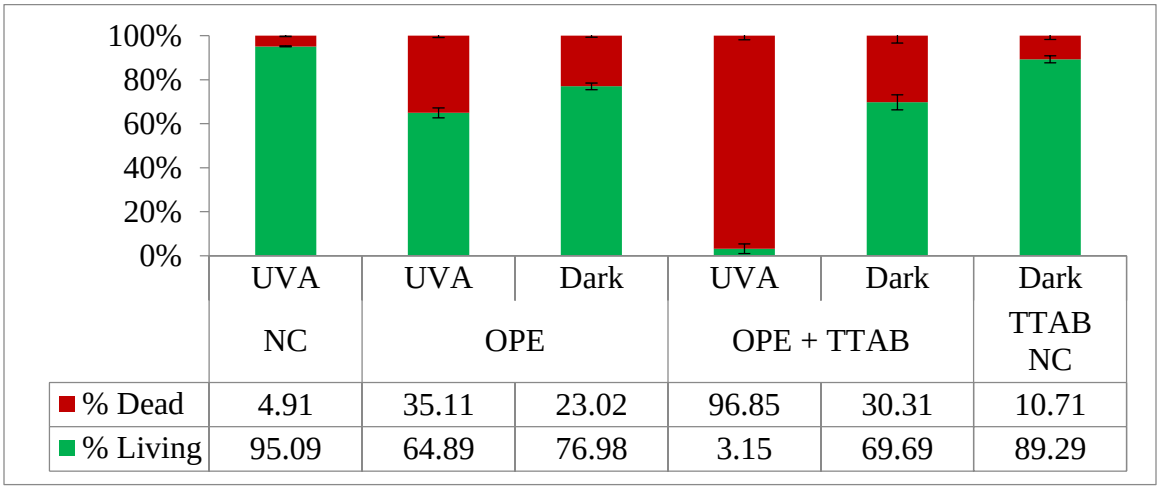

	UVA NC	UVA OPE	Dark OPE	UVA OPE + TTAB	Dark OPE + TTAB	Dark TTAB NC
% Dead	4.91	35.11	23.02	96.85	30.31	10.71
% Living	95.09	64.89	76.98	3.15	69.69	89.29

Figure 9.3: Flow cytometry-reported biocidal activity of OPE and OPE-TTAB complex against Gram-positive *S. aureus* after 1 hour of exposure in the light or dark.

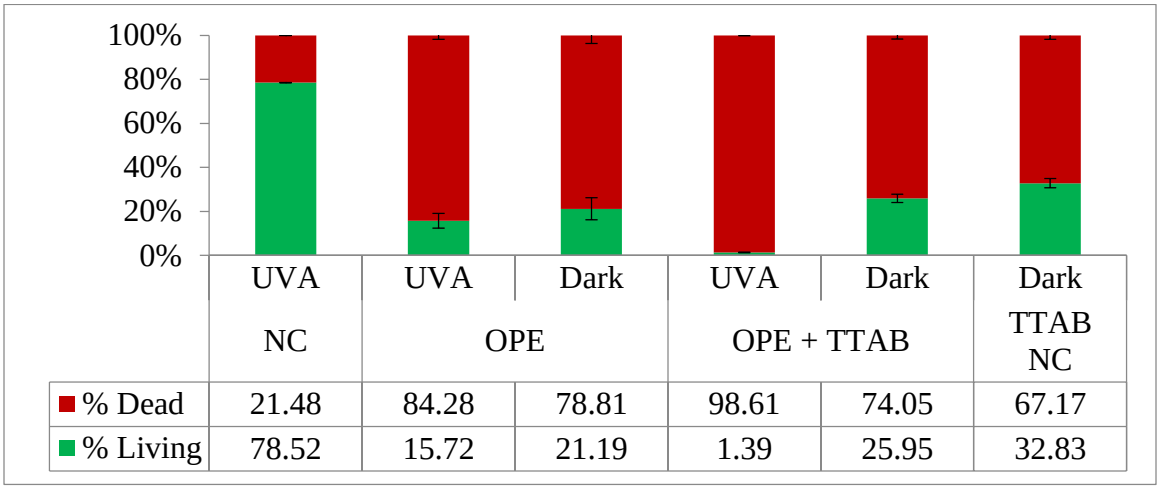

	UVA NC	UVA OPE	Dark OPE	UVA OPE + TTAB	Dark OPE + TTAB	Dark TTAB NC
% Dead	21.48	84.28	78.81	98.61	74.05	67.17
% Living	78.52	15.72	21.19	1.39	25.95	32.83

Figure 9.4: Flow cytometry-reported biocidal activity of OPE and OPE-TTAB complex against Gram-negative *E. coli* after 1 hour of exposure in the light or dark.

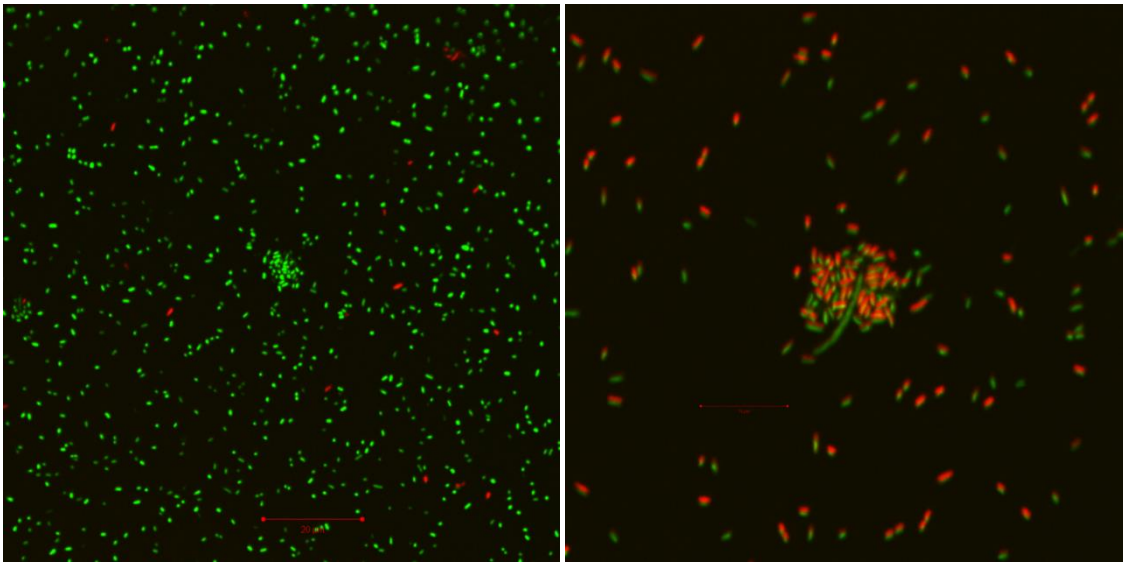

Figure 9.5: Confocal fluorescence microscope image of *E. coli* negative control (left) and following exposure to the OPE-TTAB complex for 1 hr in UVA light. The "live" stain is SYTO9 in green, and the "dead" stain is propidium iodide in red. The scale bar indicates 20 µm.

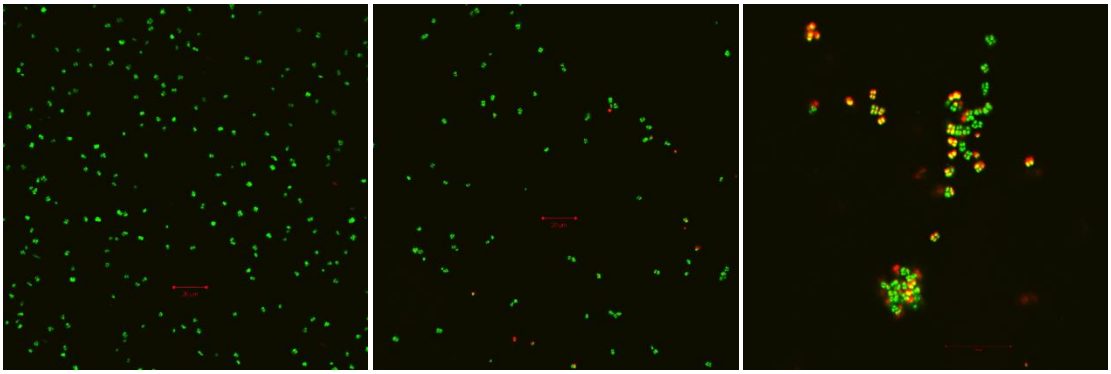

Figure 9.6: Confocal fluorescence microscope image of *S. aureus* negative control (left), following exposure to 40 µM TTAB for 1 hr in UVA light (middle), and following exposure to the OPE-TTAB complex for 1 hr in UVA light. The "live" stain is SYTO 9 in green, and the "dead" stain is propidium iodide in red. The scale bar indicates 20 µm.

9.3 Developing an Anti-Biofouling Surface

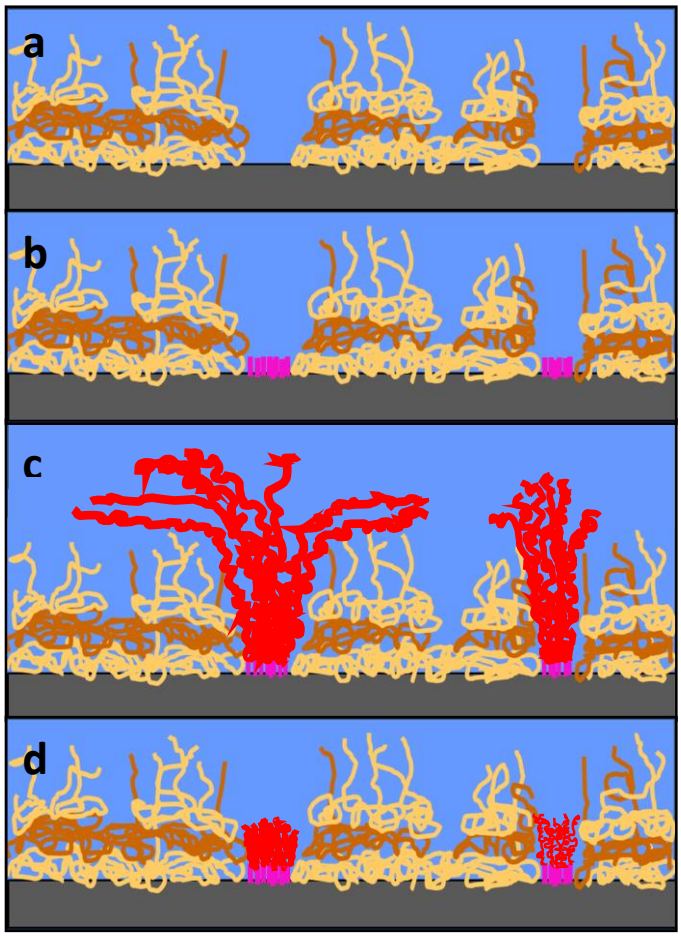

Figure 9.7: Structure of the random mixed CPE and PNIPAAm surfaces. (a) Layer-by-layer film formed from PPE-DABCO (light brown) and PPE-SO_3 (orange) on a glass surface (gray). (b) 3 layer CPE surface with silane linkers (pink) attached to the glass substrate via gaps in the CPE coverage. PNIPAAm (red) polymerized from the silane linkers at 4 °C (c) and 37 °C (d). The PNIPAAm extends beyond the CPE layers to create the plumes and surface coverage observed in the AFM images.

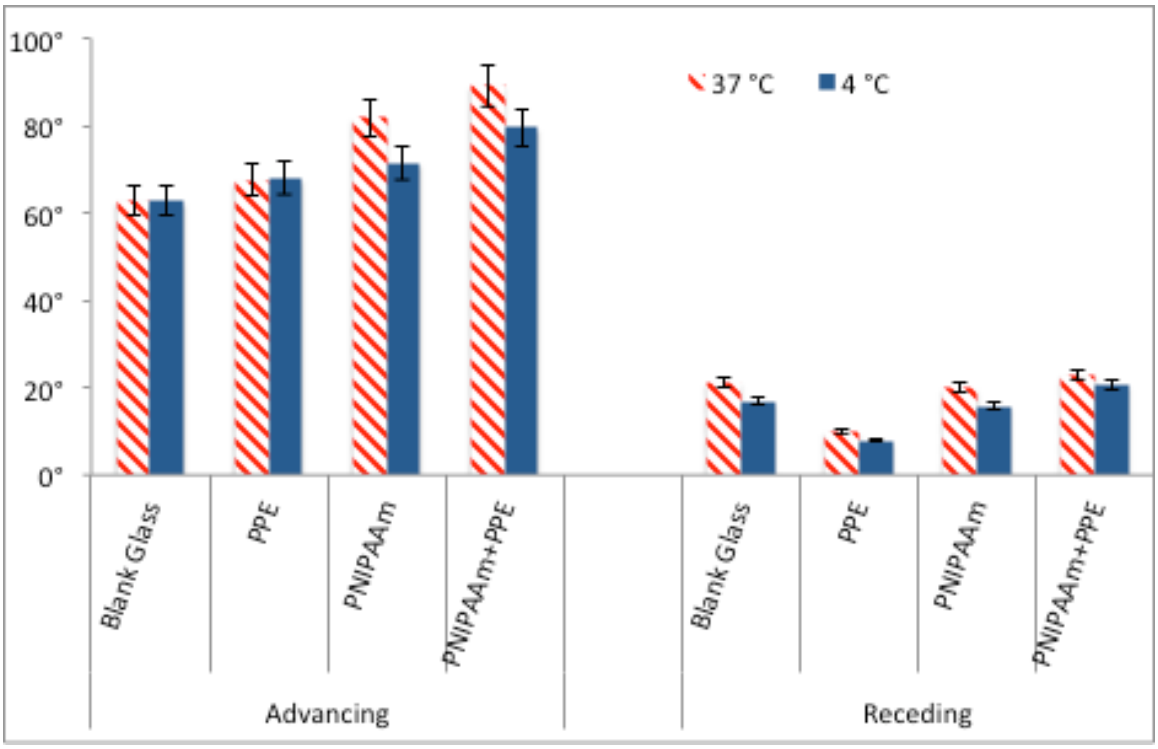

Figure 9.8: Advancing and Receding Cover Slip Contact Angles as a function of substrate and water temperature. Rinsing the cover slips with cold water resulted in a ~10° decrease of advancing contact angle, which presumably increased the surface hydrophobicity and facilitated bacterial release in the presence of rinse-induced shear stress.

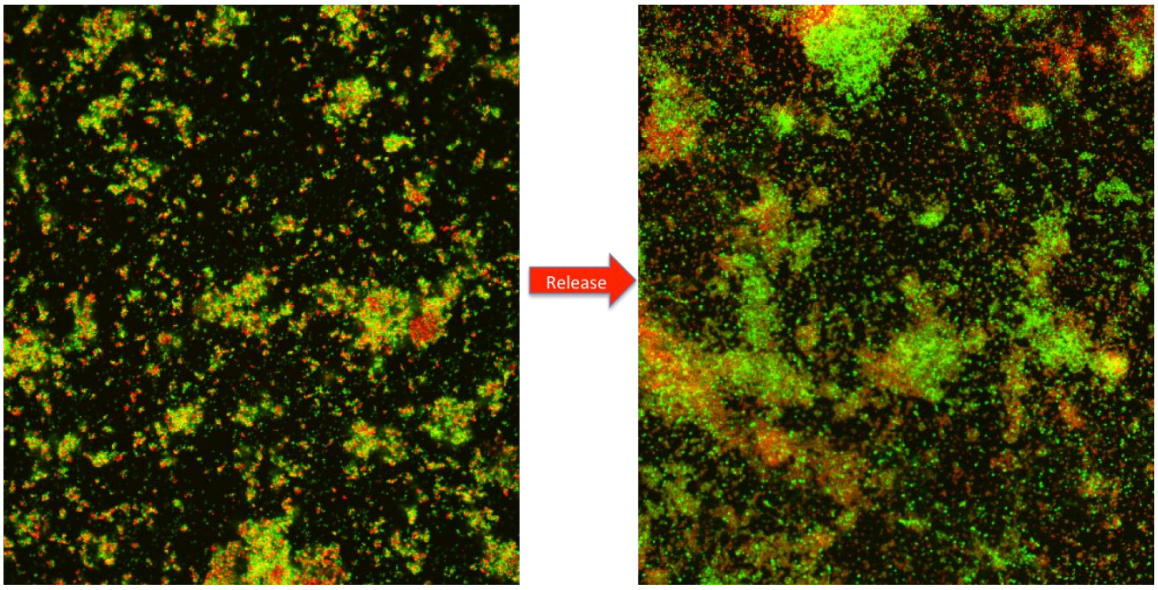

Figure 9.9: Confocal Microscopy illustrates minimal release of *S. aureus* from glass cover slip coated with PNIPAAm on CPE. Left column: Before Induced Cell Release; Right: After substrate rinsed with warm water (37 °C). These confocal images illustrate minimal release of Gram-positive *S. aureus* following a warm-water rinse. While significant release was observed upon rinsing the treated substrate with cold water, a failure to bring the substrate temperature below PNIPAAm's lower critical solution temperature (LCST) failed to induce cell release. These images also indicate that the shear stress caused by the water rinse was insufficient to cause cell release; that is, the changing temperature of the substrate caused by the cold water rinse was far more effective at inducing cell release than the force caused by the water rinse, itself.

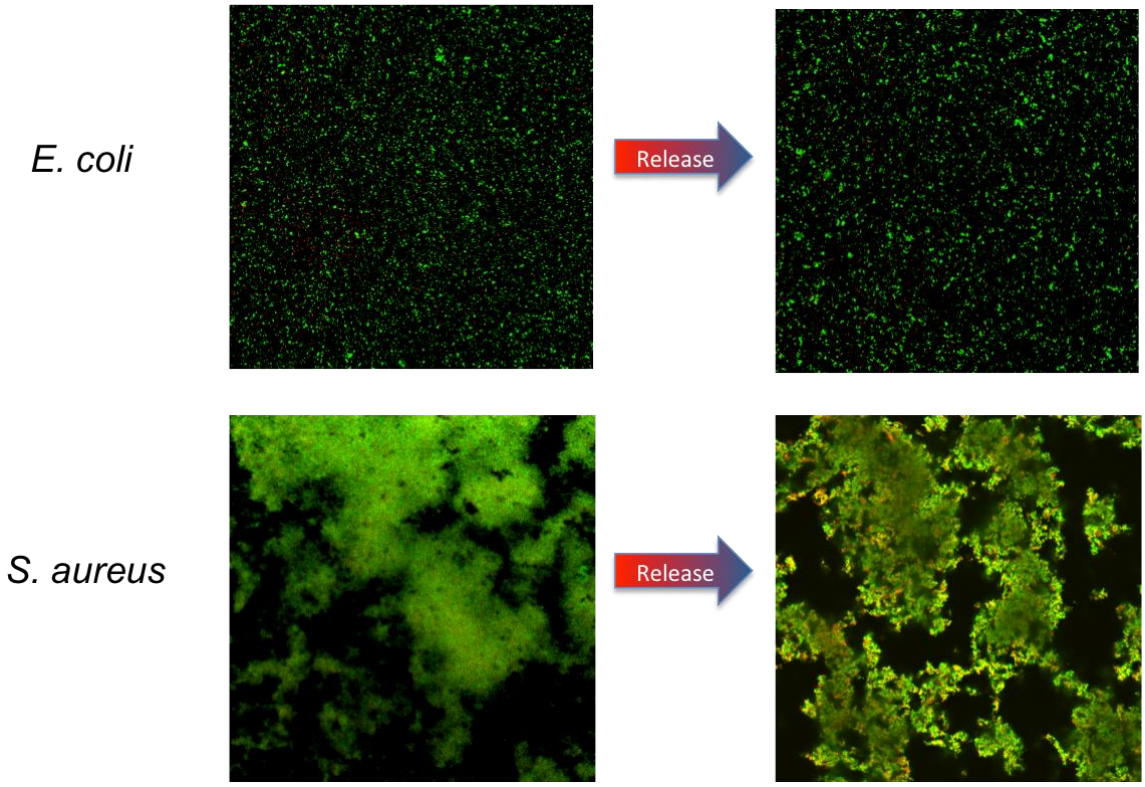

Figure 9.10: Confocal Microscopy illustrates minimal release of bacteria from glass cover slip coated with just CPE. Left column: Before Induced Cell Release; Right: After substrate rinsed with cold water. Cells were added at a concentration of 1 x 10^7 bacteria/mL. These confocal microscopy images illustrate minimal release of bacteria following a cold-water rinse. The absence of PNIPAAm did not affect the quantity of bacteria that initially attached to the surface; however, just 10% of cells were ejected from the CPE surface upon being rinsed with cold water. This indicates that the addition of PNIPAAm is critical in achieving bacterial-release with decreasing temperature. In particular, the absence of PNIPAAm prevents large clusters of *S. aureus* from being released from the surface. Initial levels of attachment (prior to rinsing) appear unaffected by the absence of PNIPAAm.

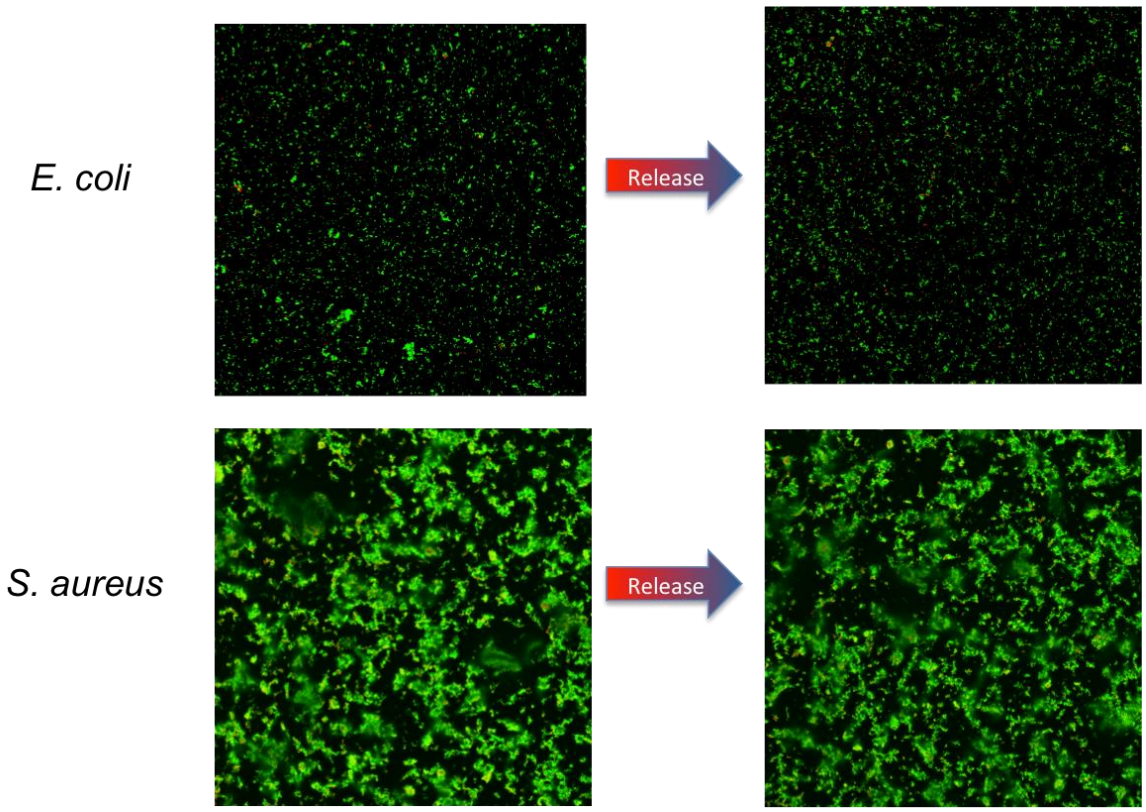

Figure 9.11: Confocal Microscopy illustrates minimal release of bacteria from piranha-cleaned glass cover slip. Left column: Before Induced Cell Release; Right: After substrate rinsed with cold water. Cells were added at a concentration of 1 x 10^7 bacteria/mL. Similarly to Figure 9.10, cell release from piranha-cleaned cover slips was not induced with a cold-water rinse. It is interesting to note, however, that in the absence of CPE, *S. aureus* clusters are smaller.

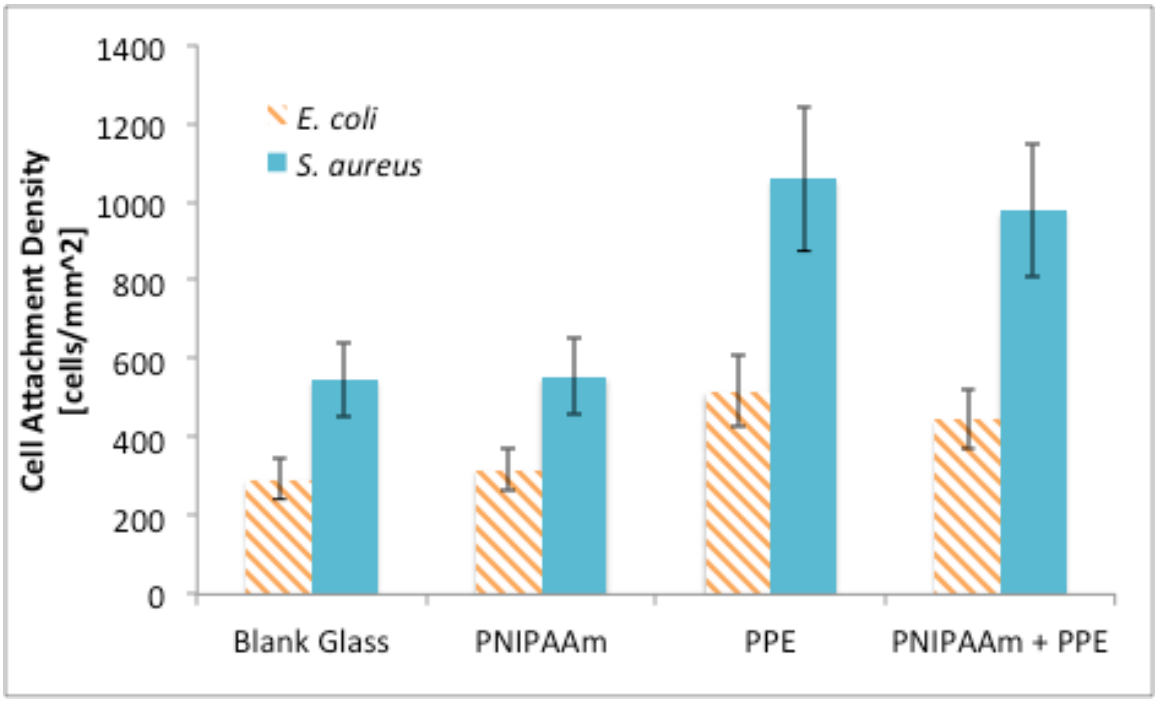

Figure 9.12: Cell adhesion was quantified as a function of substrate-treatment. Cells were added at a concentration of 1 x 10^5 bacteria/mL. This data shows that the presence of PNIPAAm did not increase the likelihood of bacterial attachment to the cover slips. CPE, on the other hand, doubled the number of cells bound to the substrate following an exposure period of 1 hr. Furthermore, grafting PNIPAAm on top of CPE mitigated cell attachment to some degree, although this change was not significant. Increased attachment of cells onto CPE-grafted samples is attributed to the net cationic charge of PPE-DABCO.

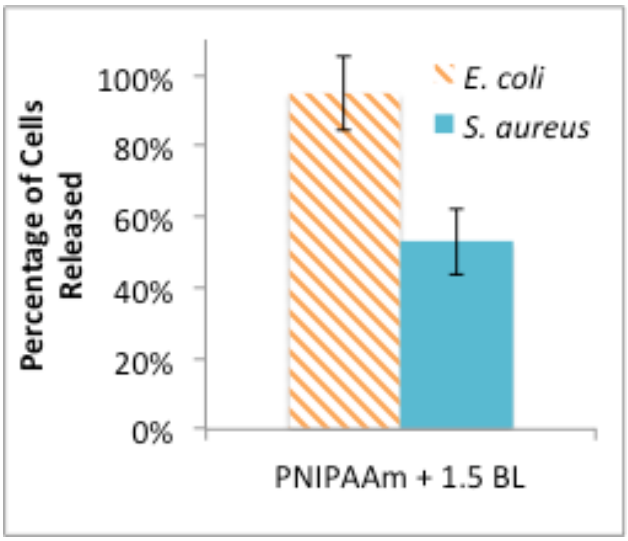

Figure 9.13: Cell release induced by a cold-water rinse varied as a function of initial seeding concentration of bacterial cells. Cells were added at a concentration of 1 x 10^5 cells/mL. This data shows that the efficiency by which *E. coli* was released from the CPE/PNIPAAm surface increased if fewer cells were initially added. In other words, seeding the substrate with a lower concentration

of *E. coli* (1 x 10^5 cells/mL, as opposed to 1x 10^7 cells/mL) actually increased the efficiency by which cells were released upon exposure to cold water. Conversely, the release of *S. aureus* did not appear to be affected by the starting cell concentration.

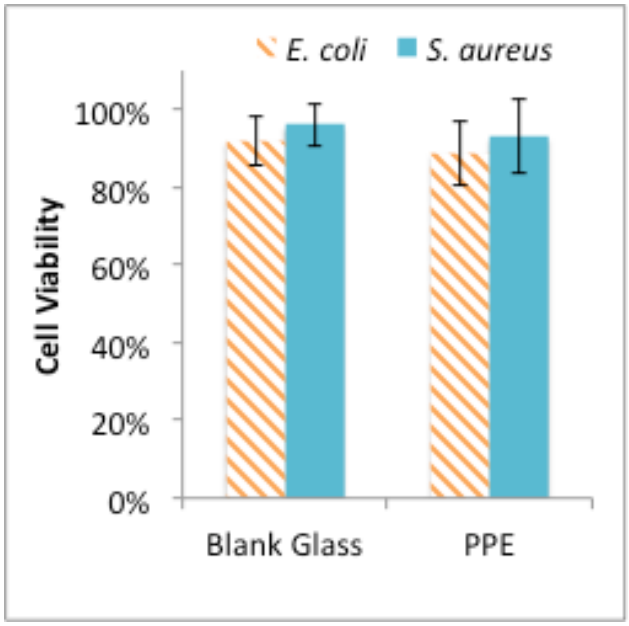

Figure 9.14: Viability of substrate-bound cells following 1 hr exposure in the dark. Cells were added at a concentration of 1 x 10^5 cells/mL. In the absence of 420 nm near-visible light, killing of both *E. coli* and *S. aureus* is significantly decreased. Generally speaking, when suspended in saline buffer, PPE-DABCO is highly biocidal against bacterial cells—even in the dark. However, upon being grafted to glass cover slips, the biocidal polymer is no longer able to diffuse to and into cell membranes, severely mitigating damage incurred by bacteria. As a result, killing is hypothesized to be largely dependent on the polymer's capacity to sensitize the production of singlet oxygen, which may subsequently generate ROS upon interacting with lipids in the cell membrane.

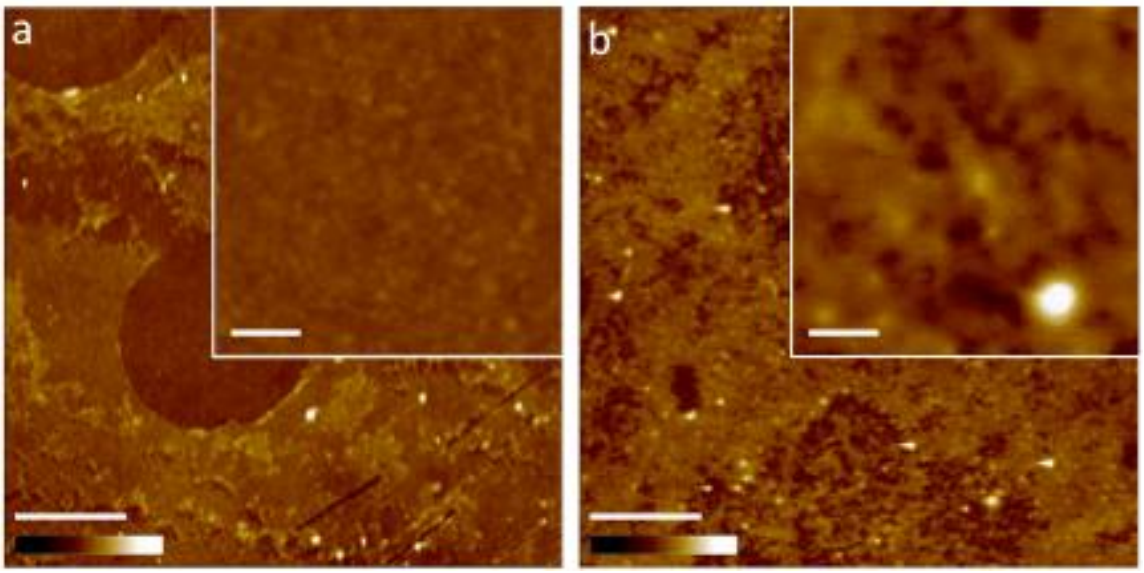

Figure 9.15: AFM tapping mode height images of active films: a) LbL CPE film with the structure: substrate//PPE-DABCO//PPE-SO_3//PPE-DABCO. The main image is 5 μm x 5 μm (scale bar 1 μm). The inset image is 500 nm x 500 nm (scale bar 100 nm). Height scale color bar is 25 nm from black to white. b) Mixed CPE/PNIPAAm film created by forming the LbL layers in (a), followed by surface polymerization of PNIPAAm. Scale and color bars as in (a).

9.4 Synthesis and Characterization of the Conjugated Polyelectrolytes

The effect of solvent on the fluorescence of the CPEs is reinforced by more detailed study of the fluorescence through measurement of the fluorescence quantum yields and lifetimes (ϕ_f and τ_f, Table 1). As can be seen, for both CPEs in methanol the quantum yields are comparatively large and the decays are single exponential, with $\tau \sim 0.5$ ns. These characteristics are typical of PPE-type polymers that are molecularly dissolved, where the emission emanates from an interchain exciton state [54]. By contrast, for both PIM-2 and PIM-4, the fluorescence quantum yields are lower in water, but the effect is more pronounced for the former. In addition, the fluorescence decays become multi-exponential, and the behavior is more pronounced for PIM-2, where the emission lifetime displays a pronounced component with $\tau \sim 3$ ns. The fluorescence parameters are consistent with the model outlined above, where both CPEs are molecularly dissolved in methanol, whereas in water PIM-2 is aggregated but PIM-4 appears to be mainly molecularly dissolved.

Table 1: Photophysical data for PIM-2 and PIM-4

	λ_{max}^{ab} (nm)	ε_{max} (M^{-1} cm^{-1})	λ_{max}^{FI} (nm)	$\phi_f{}^a$	τ_f (ns)
PIM-2/ methanol	410	27900	440	0.25 ± 0.02	0.49
PIM-2/ water	426	25100	512	0.12 ± 0.02	0.21 (20%), 1.1 (31%), 3.6 (49%)
PIM-4/ methanol	418	15400	465	0.56 ± 0.03	0.59
PIM-4/ water	430	14200	466	0.34 ± 0.03	0.41 (92%), 0.95 (8%)

[a]Measured using quinine sulfate in 0.1 M sulfuric acid (Φ_F = 0.54) as the actinometer.

9.5 Fluorescence Quenching

The fluorescence quenching of CPEs by two different anionic quenchers, namely sodium anthraquinone-2,6-disulfonate (AQS) and pyrophosphate (PPi) were studied. Quenching generally results from formation of ion-pair complexes between CPE chains and oppositely charged quencher ions [48]. It is known that AQS quenches the fluorescence of electron donors by a photoinduced electron transfer mechanism [249]. We anticipated that the electron-rich CPE backbone would be quenched by AQS by a similar mechanism while the pendant imidazolium moiety would facilitate ion-pairing between polymer/quencher driven by electrostatic interaction. Conversely, it was speculated that anionic PPi could induce fluorescence quenching by an aggregation induced-quenching mechanism [57,250].

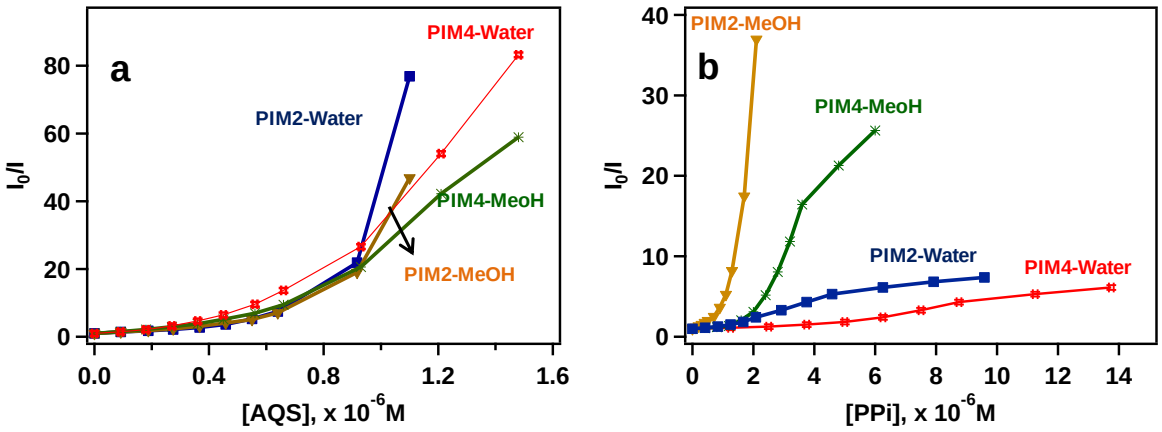

Figure 9.16: Stern-Volmer plots of PIM-2 and PIM-4 with (a) AQS and, (b) PPi as quenchers. (Polymer concentration = 10 μM in all cases).

A series of Stern-Volmer fluorescence quenching studies of PIM-2 and PIM-4 with AQS or PPi were conducted in both methanol and water to compare the quenching behavior of the polymers. The Stern-Volmer plots are shown in Figure 9.16, and the full absorption and fluorescence spectra are shown in Supporting Information. A general trend with increasing quencher concentration is that the absorption spectra of the polymers exhibit a 5-10 nm spectral shift with concomitant band broadening (Figure 8.10 and Figure 8.11). Such spectral characteristics suggest conformational changes in the polymeric backbone due to the formation of polymer/quencher complex driven by ion-pairing. In general, the Stern-Volmer plots exhibit upward curvature, but Stern-Volmer constants K_{SV} were computed from the slopes extrapolated at low quencher concentration and the values are summarized in Table 2. Comparison of the K_{SV} for quenching by AQS in methanol and water reveals several clear trends. First, the Stern-Volmer plot is linear at lower quencher concentrations and shows an upward curvature as the concentration of the quencher is increased (Figure 9.16). Secondly, the K_{SV} is on the order of ~10^6 M^{-1} in both methanol and water, for both CPEs. These very large K_{SV} values clearly indicate that amplified quenching occurs. Note that the homopolymer, PIM-4, shows slightly larger K_{SV} values for AQS in comparison to the copolymer, PIM-2, in both methanol and water; this is quite likely due to the increase in charge density on the PIM-4 backbone [251,252].

Table 2: Stern-Volmer constants for the fluorescence quenching of PIM-2 and PIM-4

	K_{SV} (M^{-1})			
	PIM-2[a]		PIM-4[a]	
	methanol	water	methanol	water
AQS	3.8×10^6	4.5×10^6	7.7×10^6	9.8×10^6
PPi	1.6×10^6	3.1×10^5	2.7×10^5	1.3×10^5

[a] K_{SV} was calculated at low concentrations (<0.4 μM for AQS and <2 μM for PPi) of the quencher where the plot was linear.

Another quencher that was employed in the study was pyrophosphate (PPi). PPi is an important ion in biological chemistry [250], and it is a potent mineralization inhibitor with a strong affinity for divalent metal ions. We previously demonstrated a CPE-based fluorescence sensor for alkaline phosphatase, with PPi as the substrate, by exploiting its binding affinity with Cu^{2+} [253]. Previous studies have shown that PPi complexes with imidazolium units, and the interaction has been used as the basis for a PPi fluorescence sensor in non-aqueous solution [254]. In the present study, it was anticipated that PP_i would associate with the imidazolium cationic units, possibly inducing aggregation of the CPE chains, resulting in fluorescence quenching. To test this, fluorescence quenching studies of PIM-2 and PIM-4 were carried out in methanol and water.

Stern-Volmer plots for the PPi quenching are shown in Figure 9.16b, and the full spectra are illustrated in Figure 8.13. The Stern-Volmer plots show that the quenching response for PIM-2 and PIM-4 is much greater in methanol than in aqueous solution, with PIM-2 showing the greatest response, with 90% quenching at ~1 μM for PIM-2 and 3 μM for PIM-4. The quenching efficiency is less in water solution; however, significant quenching is still observed, with both CPEs exhibiting K_{SV} values > 10^5 M^{-1}. The quenching in all cases is likely due to PPi-induced aggregation of the CPEs. The enhanced efficiency in methanol is likely due to the fact that the PPi--imidazole association is stronger in methanol and this leads to greater effective efficiency in inducing aggregation of the chains in this medium. Perusal of the quenching spectral data in the Supporting Information augments the premise that PPi induces aggregation (Figure 8.13). Spectral shifts in the emission spectra are quite evident upon addition of PPi to the solutions of the CPEs in methanol, where the chains are believed to be molecularly dissolved prior to addition of PPi.

9.6 Transient Absorption and Singlet Oxygen Sensitization

Recent findings from our labs demonstrate the light-activated antibacterial properties of cationic CPEs [22]. This work has established that PPE-type CPEs are able to sensitize singlet oxygen, and this process is believed to play a major role to play in the light-activated biocidal activity [24,29,255,256]. Since the triplet excited state of CPEs plays a central role in the singlet oxygen sensitization process, we utilized transient absorption (TA) spectroscopy to monitor the triplet-triplet absorption of PIM-2 and PIM-4 in methanol and water.

As shown in Figure 9.17 (PIM-4 in water) and Figure 8.14 (PIM-2 and PIM-4 in methanol), nanosecond pulsed excitation of the CPEs results in the formation of a broad transient absorption in the visible region and extending into the near-infrared. The transients have lifetimes in the 1-4 μs range, and they are efficiently quenched by O_2, confirming they are the triplet excited state [22]. Although we have not determined absolute triplet yields, previous studies have established that for similar polymers the intensity of the triplet-triplet absorption is proportional to the triplet yield. Thus, it is of interest that for this series it is found that the triplet-triplet intensities vary in the sequence PIM-4 (methanol) > PIM-4 (water) > PIM-2 (methanol) >> PIM-2 (water), while in the latter system very little TA signal was observed. These results parallel the fluorescence yields, and suggest that the triplet yield is comparatively high for PIM-4 in both methanol and water, and it is lower for PIM-2 in both media. The trend in the triplet yield is likely due to the quenching of the singlet exciton by aggregation, as discussed above. Further information regarding the triplet state and the relative yields comes from measuring the singlet oxygen yields by the PIM-2 and PIM-4 (these experiments can only be done in methanol-*d*). As expected based on the transient absorption results, PIM-4 is somewhat more efficient in sensitizing the formation of singlet oxygen (Φ_Δ = 0.13± 0.02) in comparison to PIM-2 (Φ_Δ = 0.08± 0.02).

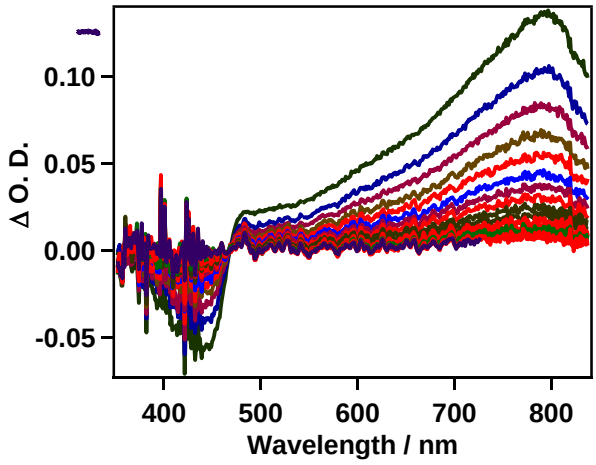

Figure 9.17: Transient absorption difference spectra of PIM-4 (OD ~ 0.7 at 355 nm and excited with the laser energy of ~7 mJ) in water (initial delay = 65 ns, subsequent delay increment = 6.5 μs, triplet lifetime = 28.6 μs).

9.7 Interactions of an OPE with *Bacillus* spores

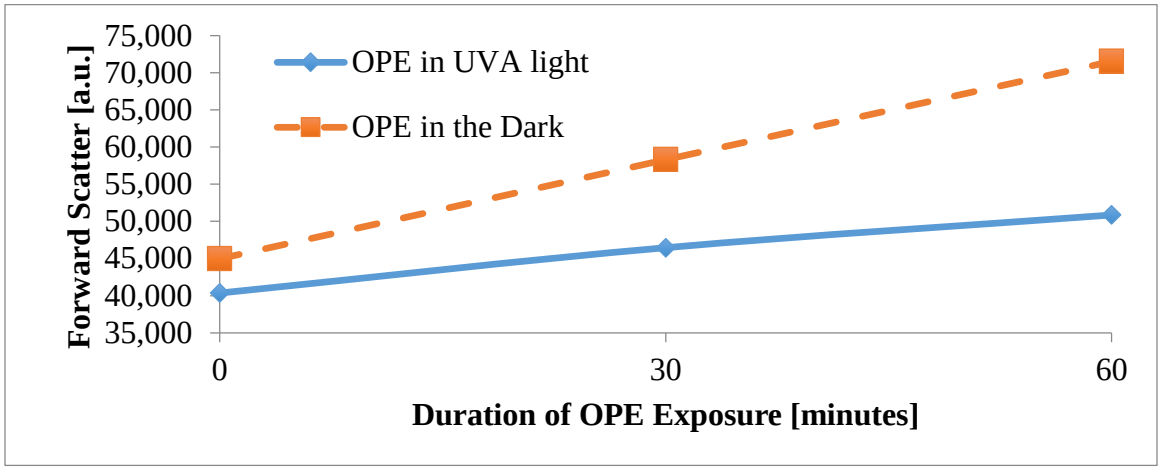

Figure 9.18: Flow cytometry-reported forward scatter of germinating *B. atrophaeus* spores as a function duration of exposure to 20 μg/mL EO-OPE (Th,C2).

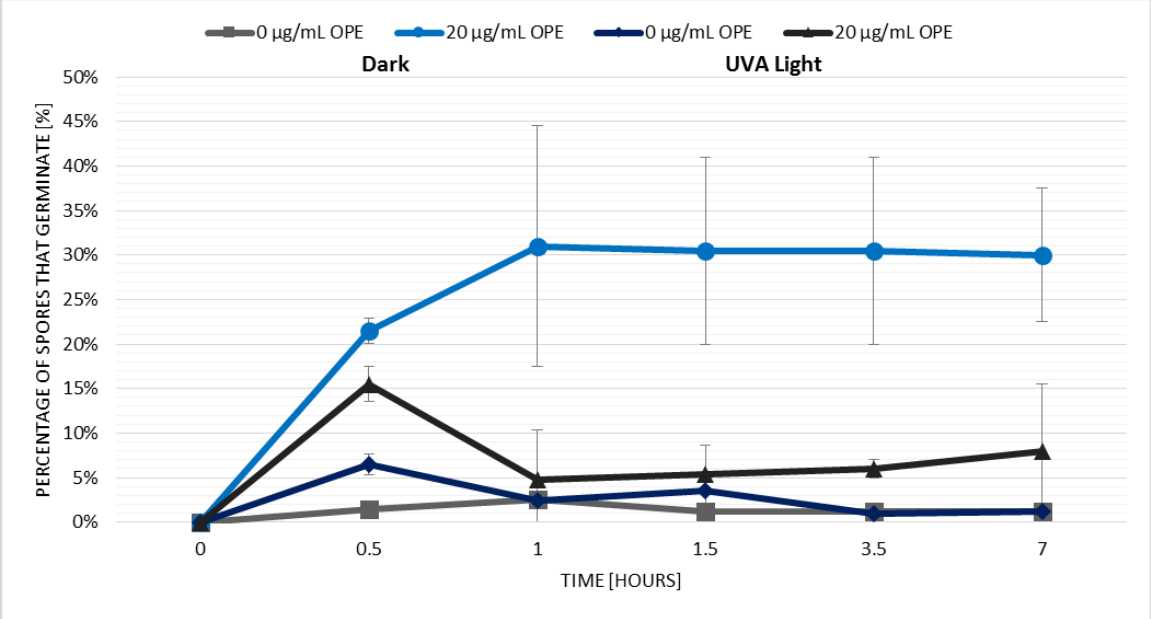

Figure 9.19: Percentage of *B. atrophaeus* spores induced to germinate by EO-OPE (Th,C2) in the absence and presence of UVA light. FCS Express (De Novo Software) was used to quantify the fraction of all spores that germinate upon exposure to UVA light and/or oligomer, according to the florescence gates defined in Figure 5.2 and Figure 5.3. Error bars illustrate standard deviations of three experimental trials.

Table 3: Supplements Figure 5.6. *B. anthracis* Sterne spore and germinated vegetative cell viability as a function of starting concentration. OPE exposed to varying spore concentrations for 90-min durations in the absence (A) and presence (B) of UVA light. Viability was inferred based on the spore's capacity to grow colonies on TSA before and after heat treatment, as described by Equations 1-3.

	Viable Spores	Viable Vegetative Cells	Dead Cells
1E7 spores	5.4 ± 5.8%	0.6 ± 0.7%	94.0 ± 15.4%
1E6 spores	22.5 ± 5.5%	0.5 ± 0.6%	76.9 ± 12.3%
1E5 spores	5.2 ± 6.0%	0.6 0.7%	94.2 ± 18.4%
1E4 spores	3.4 ± 6.8%	0.0 ± 0.0%	96.6 ± 14.9%
1E3 spores	1.3 ± 6.7%	0.0 ± 0.0%	98.7 ± 9.6%

9.8 *Candida* Studies

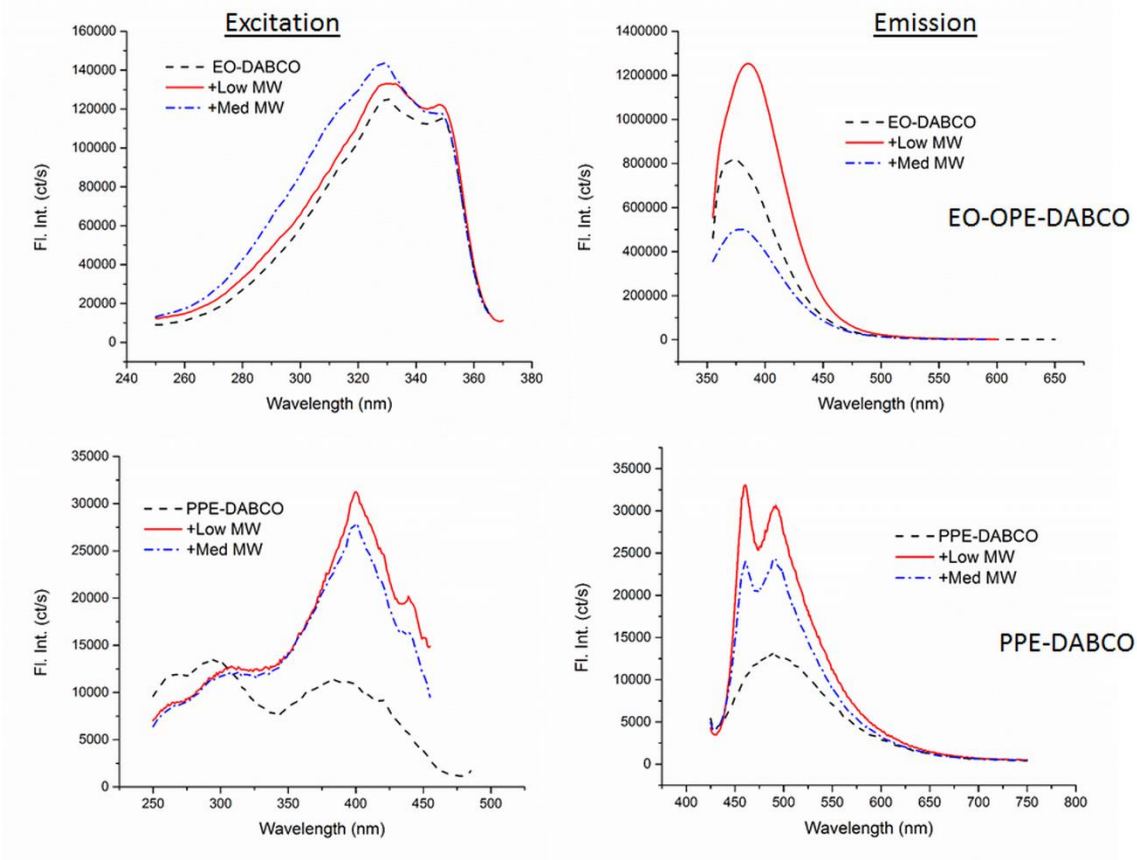

Figure 9.20: Spectroscopy of low and medium molecular weight β-glucan.

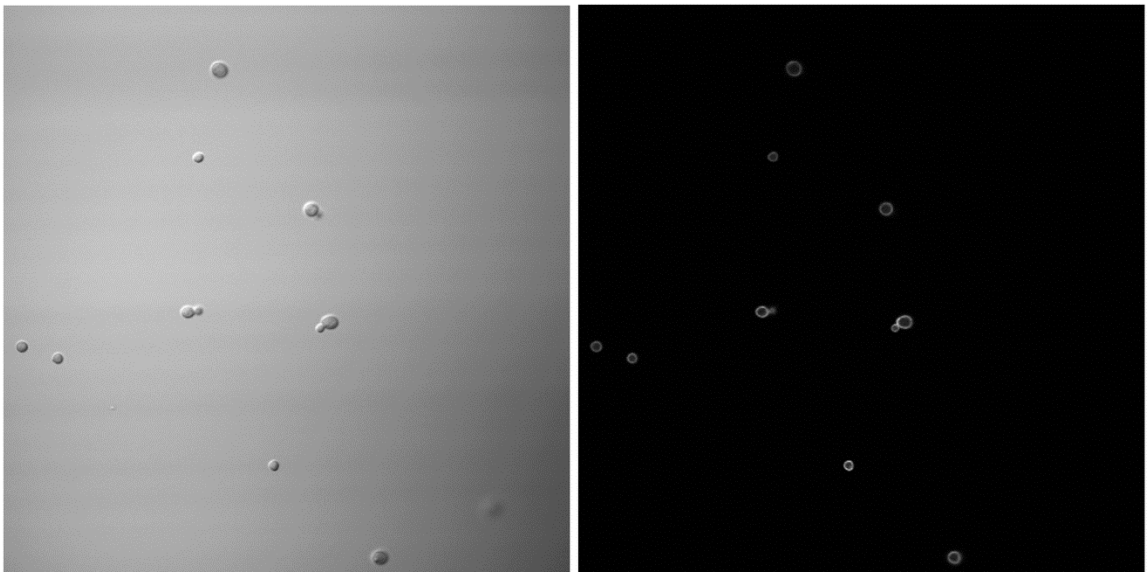

Figure 9.21: Confocal microscopy images illustrate the presence of PPE-DABCO on the cell wall of *C. albicans* yeast cells. A transmitted light image (left) and reflected light image are shown (right) 405 nm excitation was used to generate fluorescence of bound PPE-DABCO.

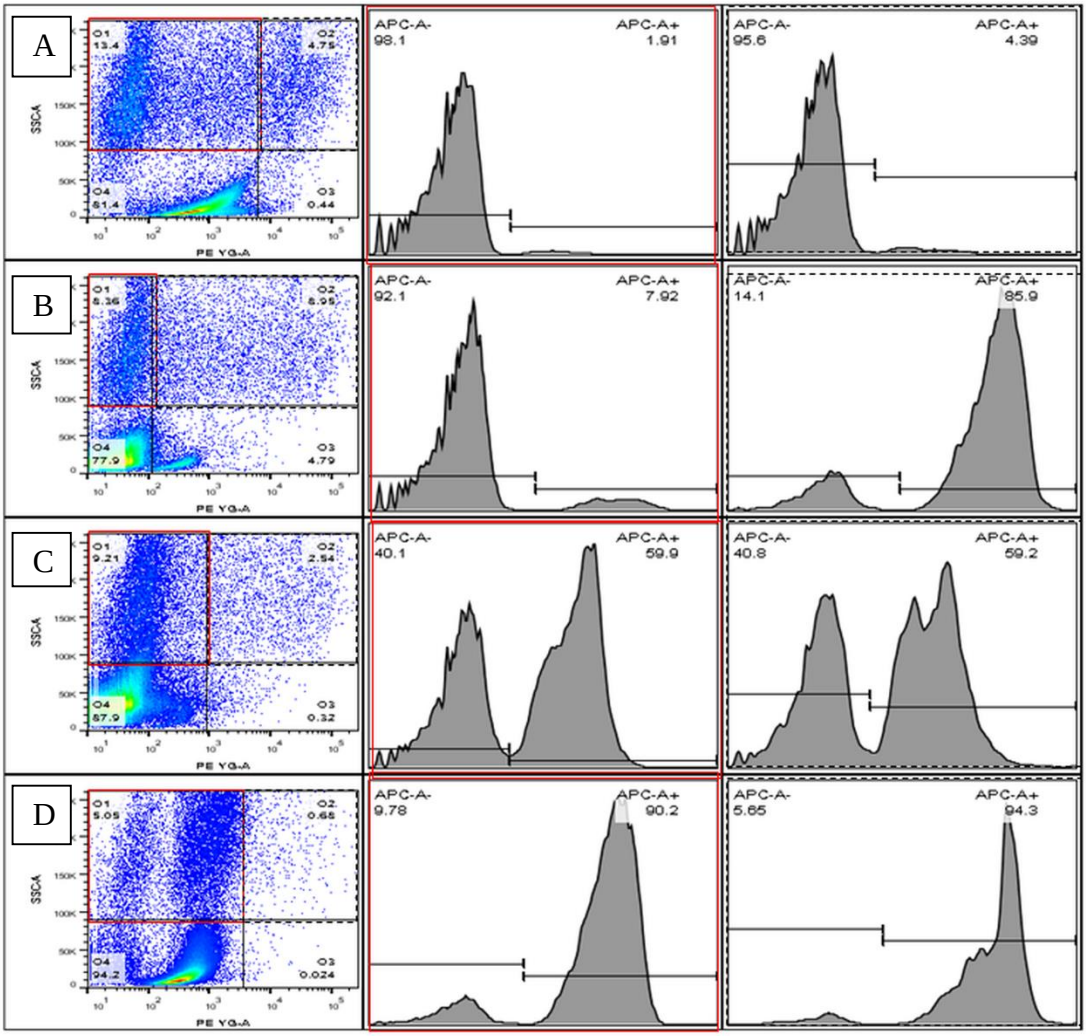

Figure 9.22: Gating scheme used to quantify yeast cell interaction with a HEK-293 cell, as well as internalization. Row A: Light NC; Row B: Heat PC; Row C: PPE-Dark; Row D: PPE-Light. Red Gate encompasses events that are SSC+ and mApple-, and represent all HEK-293 cells that were not successfully transfected, and therefore do not express Dectin-1. The Green Gate encompasses events that are SSC+ and mApple+, and represent all HEK-293 cells that were successfully transfected, and therefore do express Dectin-1. Of all events falling under the red or green gates, those that are CypHer 5- are assumed to be non-transfected HEK cells that are not interacting with a *C. albicans* yeast cell; those that are CypHer 5+ are interacting with at least one *C. albicans* yeast cell.

Chapter 10: References

(1) Klevens, R. M., Edwards, J. R., Richards, C. L., Horan, T. C., Gaynes, R. P., Pollock, D. A., and Cardo, D. M. Estimating health care-associated infections and deaths in U.S. hospitals, 2002. *Public Health Rep. 122*, 160–6.

(2) Fleming, A. (2001) On the antibacterial action of cultures of a penicillium, with special reference to their use in the isolation of B. influenzae. 1929. *Bull. World Health Organ. 79*, 780–90.

(3) Kardos, N., and Demain, A. L. (2011) Penicillin: the medicine with the greatest impact on therapeutic outcomes. *Appl. Microbiol. Biotechnol. 92*, 677–87.

(4) Schatz, A., Bugie, E., and Waksman, S. A. (2005) Streptomycin, a substance exhibiting antibiotic activity against gram-positive and gram-negative bacteria. 1944. *Clin. Orthop. Relat. Res.* 3–6.

(5) Tacconelli, E., De Angelis, G., Cataldo, M. A., Pozzi, E., and Cauda, R. (2008) Does antibiotic exposure increase the risk of methicillin-resistant Staphylococcus aureus (MRSA) isolation? A systematic review and meta-analysis. *J. Antimicrob. Chemother. 61*, 26–38.

(6) Cooper, B. S., Medley, G. F., Stone, S. P., Kibbler, C. C., Cookson, B. D., Roberts, J. A., Duckworth, G., Lai, R., and Ebrahim, S. (2004) Methicillin-resistant Staphylococcus aureus in hospitals and the community: stealth dynamics and control catastrophes. *Proc. Natl. Acad. Sci. U. S. A. 101*, 10223–8.

(7) Chamchod, F., and Ruan, S. (2012) Modeling methicillin-resistant Staphylococcus aureus in hospitals: transmission dynamics, antibiotic usage and its history. *Theor. Biol. Med. Model. 9*, 25.

(8) Nickerson, E. K., West, T. E., Day, N. P., and Peacock, S. J. (2009) Staphylococcus aureus disease and drug resistance in resource-limited

countries in south and east Asia. *Lancet. Infect. Dis. 9*, 130–5.

(9) Gorwitz, R., Fridkin, S. K., and Workowski, K. A. (2008) More challenges in the prevention and management of community-associated, methicillin-resistant Staphylococcus aureus skin disease. *Ann. Intern. Med. 148*, 310–2.

(10) Wilson, M. (2003) Light-Activated Antimicrobial Coating for the Continuous Disinfection of Surfaces. *Infect. Control Hosp. Epidemiol. 24*, 782–784.

(11) Noimark, S., Dunnill, C. W., Wilson, M., and Parkin, I. P. (2009) The role of surfaces in catheter-associated infections. *Chem. Soc. Rev. 38*, 3435–48.

(12) Lu, L., Rininsland, F. H., Wittenburg, S. K., Achyuthan, K. E., McBranch, D. W., and Whitten, D. G. (2005) Biocidal Activity of a Light-Absorbing Fluorescent Conjugated Polyelectrolyte. *Langmuir 21*, 10154–10159.

(13) Bozja, J., Sherrill, J., Michielsen, S., and Stojiljkovic, I. (2003) Porphyrin-based, light-activated antimicrobial materials. *J. Polym. Sci. Part A Polym. Chem. 41*, 2297–2303.

(14) Perni, S., Piccirillo, C., Pratten, J., Prokopovich, P., Chrzanowski, W., Parkin, I. P., and Wilson, M. (2009) The antimicrobial properties of light-activated polymers containing methylene blue and gold nanoparticles. *Biomaterials 30*, 89–93.

(15) Lu, Z., Dai, T., Huang, L., Kurup, D. B., Tegos, G. P., Jahnke, A., Wharton, T., and Hamblin, M. R. (2010) Photodynamic therapy with a cationic functionalized fullerene rescues mice from fatal wound infections. *Nanomedicine (Lond). 5*, 1525–1533.

(16) Giuliani, F., Martinelli, M., Cocchi, A., Arbia, D., Fantetti, L., and Roncucci, G. (2010) In vitro resistance selection studies of RLP068/Cl, a

new Zn(II) phthalocyanine suitable for antimicrobial photodynamic therapy. *Antimicrob. Agents Chemother. 54*, 637–642.

(17) Pagonis, T. C., Chen, J., Fontana, C. R., Devalapally, H., Ruggiero, K., Song, X., Foschi, F., Dunham, J., Skobe, Z., Yamazaki, H., Kent, R., Tanner, A. C. R., Amiji, M. M., and Soukos, N. S. (2010) Nanoparticle-based Endodontic Antimicrobial Photodynamic Therapy. *J. Endod. 36*, 322–328.

(18) Zhou, Z., Corbitt, T. S., Parthasarathy, A., Tang, Y., Ista, L. K., Schanze, K. S., and Whitten, D. G. (2010) "End-Only" Functionalized Oligo(phenylene ethynylene)s: Synthesis, Photophysical and Biocidal Activity. *J. Phys. Chem. Lett. 1*, 3207–3212.

(19) Banerjee, I., Mehta, K. K., Dordick, J. S., and Kane, R. S. (2012) Light-activated porphyrin-based formulations to inactivate bacterial spores. *J. Appl. Microbiol. 113*, 1461–7.

(20) Chemburu, S., Corbitt, T. S., Ista, L. K., Ji, E., Fulghum, J., Lopez, G. P., Ogawa, K., Schanze, K. S., and Whitten, D. G. (2008) Light-induced biocidal action of conjugated polyelectrolytes supported on colloids. *Langmuir 24*, 11053–11062.

(21) Corbitt, T. S., Sommer, J. R., Chemburu, S., Ogawa, K., Ista, L. K., Lopez, G. P., Whitten, D. G., and Schanze, K. S. (2009) Conjugated polyelectrolyte capsules: light-activated antimicrobial micro "Roach Motels". *ACS Appl. Mater. Interfaces 1*, 48–52.

(22) Ji, E., Corbitt, T. S., Parthasarathy, A., Schanze, K. S., and Whitten, D. G. (2011) Light and dark-activated biocidal activity of conjugated polyelectrolytes. *ACS Appl. Mater. Interfaces 3*, 2820–9.

(23) Wang, Y., Jones, E. M., Tang, Y., Ji, E., Lopez, G. P., Chi, E. Y., Schanze, K. S., and Whitten, D. G. (2011) Effect of Polymer Chain Length on Membrane Perturbation Activity of Cationic Phenylene Ethynylene Oligomers and Polymers. *Langmuir 27*, 10770–10775.

(24) Corbitt, T. S., Ding, L., Ji, E., Ista, L. K., Ogawa, K., Lopez, G. P., Schanze, K. S., and Whitten, D. G. (2009) Light and dark biocidal activity of cationic poly(arylene ethynylene) conjugated polyelectrolytes. *Photochem. Photobiol. Sci. 8*, 998–1005.

(25) Ding, L., Chi, E. Y., Chemburu, S., Ji, E., Schanze, K. S., Lopez, G. P., and Whitten, D. G. (2009) Insight into the mechanism of antimicrobial poly(phenylene ethynylene) polyelectrolytes: interactions with phosphatidylglycerol lipid membranes. *Langmuir 25*, 13742–51.

(26) Ding, L., Chi, E. Y., Schanze, K. S., Lopez, G. P., and Whitten, D. G. (2010) Insight into the mechanism of antimicrobial conjugated polyelectrolytes: lipid headgroup charge and membrane fluidity effects. *Langmuir 26*, 5544–50.

(27) Wang, Y., Jett, S. D., Crum, J., Schanze, K. S., Chi, E. Y., and Whitten, D. G. (2013) Understanding the dark and light-enhanced bactericidal action of cationic conjugated polyelectrolytes and oligomers. *Langmuir 29*, 781–92.

(28) Hill, E. H., Whitten, D. G., and Evans, D. G. (2014) Computational study of bacterial membrane disruption by cationic biocides: structural basis for water pore formation. *J. Phys. Chem. B 118*, 9722–32.

(29) Hill, E. H., Stratton, K., Whitten, D. G., and Evans, D. G. (2012) Molecular dynamics simulation study of the interaction of cationic biocides with lipid bilayers: aggregation effects and bilayer damage. *Langmuir 28*, 14849–54.

(30) Oren, Z., and Shai, Y. (1998) Mode of action of linear amphipathic alpha-helical antimicrobial peptides. *Biopolymers 47*, 451–63.

(31) Brogden, K. A. (2005) Antimicrobial peptides: pore formers or metabolic inhibitors in bacteria? *Nat. Rev. Microbiol. 3*, 238–50.

(32) Tang, Y., Corbitt, T. S., Parthasarathy, A., Zhou, Z., Schanze, K. S.,

and Whitten, D. G. (2011) Light-induced antibacterial activity of symmetrical and asymmetrical oligophenylene ethynylenes. *Langmuir 27*, 4956–62.

(33) Pappas, H. C., Lovchik, J. A., and Whitten, D. G. (2015) Assessing the Sporicidal Activity of Oligo-p-phenylene Ethynylenes and Their Role as Bacillus Germinants. *Langmuir 31*, 4481–9.

(34) Wang, Y., Canady, T. T. D., Zhou, Z., Tang, Y., Price, D. N., Bear, D. G., Chi, E. Y., Schanze, K. S., and Whitten, D. G. (2011) Cationic Phenylene Ethynylene Polymers and Oligomers Exhibit Efficient Antiviral Activity. *ACS Appl. Mater. Interfaces 3*, 2209–14.

(35) Wang, Y., Schanze, K., Chi, E., and Whitten, D. (2013) When worlds collide: Interactions at the interface between biological systems and synthetic cationic conjugated polyelectrolytes and oligomers. *Langmuir 8*, 1–30.

(36) Ista, L. K., Dascier, D., Ji, E., Parthasarathy, A., Corbitt, T. S., Schanze, K. S., and Whitten, D. G. (2011) Conjugated-polyelectrolyte-grafted cotton fibers act as "micro flypaper" for the removal and destruction of bacteria. *ACS Appl. Mater. Interfaces 3*, 2932–7.

(37) Pappas, H. C., Phan, S., Yoon, S., Edens, L. E., Meng, X., Schanze, K. S., Whitten, D. G., and Keller, D. J. (2015) Self-Sterilizing, Self-Cleaning Mixed Polymeric Multifunctional Antimicrobial Surfaces. *ACS Appl. Mater. Interfaces* acsami.5b06852.

(38) Chen, L., McBranch, D. W., Wang, H.-L., Helgeson, R., Wudl, F., and Whitten, D. G. (1999) Highly sensitive biological and chemical sensors based on reversible fluorescence quenching in a conjugated polymer. *Proc. Natl. Acad. Sci. 96*, 12287–12292.

(39) Pinto, M. R., and Schanze, K. S. (2004) Amplified fluorescence sensing of protease activity with conjugated polyelectrolytes. *Proc. Natl. Acad. Sci. U. S. A. 101*, 7505–10.

(40) Liu, B., and Bazan, G. C. (2004) Homogeneous Fluorescence-Based DNA Detection with Water-Soluble Conjugated Polymers. *Chem. Mater. 16*, 4467–4476.

(41) Jiang, H., Taranekar, P., Reynolds, J. R., and Schanze, K. S. (2009) Conjugated polyelectrolytes: synthesis, photophysics, and applications. *Angew. Chem. Int. Ed. Engl. 48*, 4300–16.

(42) Duan, X., Liu, L., Feng, F., and Wang, S. (2010) Cationic conjugated polymers for optical detection of DNA methylation, lesions, and single nucleotide polymorphisms. *Acc. Chem. Res. 43*, 260–70.

(43) Duarte, A., Pu, K.-Y., Liu, B., and Bazan, G. C. (2011) Recent Advances in Conjugated Polyelectrolytes for Emerging Optoelectronic Applications †. *Chem. Mater. 23*, 501–515.

(44) Liu, B., and Bazan, G. C. (2013) Conjugated Polyelectrolytes.

(45) Rochat, S., and Swager, T. M. (2013) Conjugated amplifying polymers for optical sensing applications. *ACS Appl. Mater. Interfaces 5*, 4488–502.

(46) Child, A. D., and Reynolds, J. R. (1994) Water-Soluble Rigid-Rod Polyelectrolytes: A New Self-Doped, Electroactive Sulfonatoalkoxy-Substituted Poly(p-phenylene). *Macromolecules 27*, 1975–1977.

(47) Brookins, R. N., Schanze, K. S., and Reynolds, J. R. (2007) Base-Free Suzuki Polymerization for the Synthesis of Polyfluorenes Functionalized with Carboxylic Acids. *Macromolecules 40*, 3524–3526.

(48) Tan, C., Pinto, M. R., and Schanze, K. S. (2002) Photophysics, aggregation and amplified quenching of a water-soluble poly(phenylene ethynylene). *Chem. Commun. (Camb).* 446–7.

(49) Nelson, J. C., Saven, J. G., Moore, J. S., and Wolynes, P. G. (1997) Solvophobically driven folding of nonbiological oligomers. *Science 277*,

1793–6.

(50) Zhou, Q., and Swager, T. M. (1995) Fluorescent Chemosensors Based on Energy Migration in Conjugated Polymers: The Molecular Wire Approach to Increased Sensitivity. *J. Am. Chem. Soc. 117*, 12593–12602.

(51) Liu, Y., Ogawa, K., and Schanze, K. S. (2009) Conjugated polyelectrolytes as fluorescent sensors. *J. Photochem. Photobiol. C Photochem. Rev. 10*, 173–190.

(52) Zhao, X., Pinto, M. R., Hardison, L. M., Mwaura, J., Müller, J., Jiang, H., Witker, D., Kleiman, V. D., Reynolds, J. R., and Schanze, K. S. (2006) Variable band gap poly(arylene ethynylene) conjugated polyelectrolytes. *Macromolecules 39*, 6355–6366.

(53) Pinto, M. R., Kristal, B. M., and Schanze, K. S. (2003) A Water-Soluble Poly(phenylene ethynylene) with Pendant Phosphonate Groups. Synthesis, Photophysics, and Layer-by-Layer Self-Assembled Films †. *Langmuir 19*, 6523–6533.

(54) Koenen, J.-M., Zhu, X., Pan, Z., Feng, F., Yang, J., and Schanze, K. S. (2014) Enhanced Fluorescence Properties of Poly(phenylene ethynylene)-Conjugated Polyelectrolytes Designed to Avoid Aggregation. *ACS Macro Lett. 3*, 405–409.

(55) Zhao, X., and Schanze, K. S. (2010) Fluorescent ratiometric sensing of pyrophosphate via induced aggregation of a conjugated polyelectrolyte. *Chem. Commun. (Camb). 46*, 6075–7.

(56) Yang, J., Wu, D., Xie, D., Feng, F., and Schanze, K. S. (2013) Ion-Induced Aggregation of Conjugated Polyelectrolytes Studied by Fluorescence Correlation Spectroscopy. *J. Phys. Chem. B 117*, 16314–16324.

(57) Zhu, X., Yang, J., and Schanze, K. S. (2014) Conjugated polyelectrolytes with guanidinium side groups. Synthesis, photophysics and

pyrophosphate sensing. *Photochem. Photobiol. Sci. 13*, 293–300.

(58) Donabedian, P. L., Pham, T. K., Whitten, D. G., and Chi, E. Y. (2015) Oligo(p-phenylene ethynylene) Electrolytes: A Novel Molecular Scaffold for Optical Tracking of Amyloids. *ACS Chem. Neurosci. 6*, 1526–35.

(59) Rambaran, R. N., and Serpell, L. C. Amyloid fibrils: abnormal protein assembly. *Prion 2*, 112–7.

(60) Knowles, T. P. J., Vendruscolo, M., and Dobson, C. M. (2014) The amyloid state and its association with protein misfolding diseases. *Nat. Rev. Mol. Cell Biol. 15*, 384–96.

(61) Ittner, L. M., and Götz, J. (2011) Amyloid-β and tau--a toxic pas de deux in Alzheimer's disease. *Nat. Rev. Neurosci. 12*, 65–72.

(62) Westermark, P., Andersson, A., and Westermark, G. T. (2011) Islet amyloid polypeptide, islet amyloid, and diabetes mellitus. *Physiol. Rev. 91*, 795–826.

(63) Barnhart, M. M., and Chapman, M. R. (2006) Curli biogenesis and function. *Annu. Rev. Microbiol. 60*, 131–47.

(64) Nilsson, K. P. R. (2009) Small organic probes as amyloid specific ligands--past and recent molecular scaffolds. *FEBS Lett. 583*, 2593–9.

(65) Skeby, K. K., Sørensen, J., and Schiøtt, B. (2013) Identification of a common binding mode for imaging agents to amyloid fibrils from molecular dynamics simulations. *J. Am. Chem. Soc. 135*, 15114–28.

(66) Swaminathan, R., Ravi, V. K., Kumar, S., Kumar, M. V. S., and Chandra, N. (2011) Lysozyme: a model protein for amyloid research. *Adv. Protein Chem. Struct. Biol. 84*, 63–111.

(67) Hill, S. E., Robinson, J., Matthews, G., and Muschol, M. (2009)

Amyloid protofibrils of lysozyme nucleate and grow via oligomer fusion. *Biophys. J. 96*, 3781–90.

(68) Hill, E. H., Evans, D. G., and Whitten, D. G. (2013) Photochemistry of "end-only" oligo-p-phenylene ethynylenes: Complexation with sodium dodecyl sulfate reduces solvent accessibility. *Langmuir 29*, 9712–9720.

(69) Hill, E. H., Goswami, S., Evans, D. G., Schanze, K. S., and Whitten, D. G. (2012) Photochemistry of a Model Cationic p-Phenylene Ethynylene in Water. *J. Phys. Chem. Lett. 3*, 1363–8.

(70) Hill, E. H., Pappas, H. C., Evans, D. G., and Whitten, D. G. (2014) Cationic oligo-p-phenylene ethynylenes form complexes with surfactants for long-term light-activated biocidal applications. *Photochem. Photobiol. Sci. 13*, 247–53.

(71) Turro, N. J., and Yekta, A. (1978) Luminescent probes for detergent solutions. A simple procedure for determination of the mean aggregation number of micelles. *J. Am. Chem. Soc. 100*, 5951–5952.

(72) Ron, E. Z., and Davis, B. D. (1971) Growth rate of Escherichia coli at elevated temperatures: limitation by methionine. *J. Bacteriol. 107*, 391–6.

(73) Rolinson, G. (1998) Forty years of beta-lactam research. *J. Antimicrob. Chemother. 41*, 589–603.

(74) Burton, P., and Holland, I. B. (1983) Two pathways of division inhibition in UV-irradiated E. coli. *Mol. Gen. Genet. 190*, 128–32.

(75) Storz, G., and Imlay, J. A. (1999, February 19) Oxidative stress. *Curr. Opin. Microbiol.*

(76) Cabiscol, E., Tamarit, J., and Ros, J. (2010) Oxidative stress in bacteria and protein damage by reactive oxygen species. *Int. Microbiol.* 3–8.

(77) Jones, T. H. H. (2012) Response of Escherichia coli to environmental stress, in *Stress response of foodborne microorganisms*, pp 293–330.

(78) Lock, R. L., and Harry, E. J. (2008) Cell-division inhibitors: new insights for future antibiotics. *Nat. Rev. Drug Discov. 7*, 324–38.

(79) Addinall, S., Cao, C., and Lutkenhaus, J. (1997) Temperature shift experiments with an ftsZ84 (Ts) strain reveal rapid dynamics of FtsZ localization and indicate that the Z ring is required throughout septation and. *J. Bacteriol. 179*, 4277–4284.

(80) Stricker, J., Maddox, P., Salmon, E. D., and Erickson, H. P. (2002) Rapid assembly dynamics of the Escherichia coli FtsZ-ring demonstrated by fluorescence recovery after photobleaching. *Proc. Natl. Acad. Sci. U. S. A. 99*, 3171–3175.

(81) Romberg, L., and Levin, P. A. (2003) Assembly dynamics of the bacterial cell division protein FTSZ: poised at the edge of stability. *Annu. Rev. Microbiol. 57*, 125–54.

(82) Anderson, D. E., Gueiros-Filho, F. J., and Erickson, H. P. (2004) Assembly dynamics of FtsZ rings in Bacillus subtilis and Escherichia coli and effects of FtsZ-regulating proteins. *J. Bacteriol. 186*, 5775–81.

(83) Goehring, N. W., and Beckwith, J. (2005) Diverse paths to midcell: Assembly of the bacterial cell division machinery. *Curr. Biol.*

(84) Rico, A. I., García-Ovalle, M., Palacios, P., Casanova, M., and Vicente, M. (2010) Role of Escherichia coli FtsN protein in the assembly and stability of the cell division ring. *Mol. Microbiol. 76*, 760–71.

(85) Ma, X., Ehrhardt, D. W., and Margolin, W. (1996) Colocalization of cell division proteins FtsZ and FtsA to cytoskeletal structures in living Escherichia coli cells by using green fluorescent protein. *Proc. Natl. Acad. Sci. U. S. A. 93*, 12998–3003.

(86) Kruse, T., Møeller-Jensen, J., Løbner-Olesen, A., and Gerdes, K. (2003) Dysfunctional MreB inhibits chromosome segregation in Escherichia coli. *EMBO J. 22*, 5283–5292.

(87) Maciag-Dorszyńska, M., Ignatowska, M., Jannière, L., Wegrzyn, G., and Szalewska-Pałasz, A. (2012) Mutations in central carbon metabolism genes suppress defects in nucleoid position and cell division of replication mutants in Escherichia coli. *Gene 503*, 31–35.

(88) Boeneman, K., Fossum, S., Yang, Y., Fingland, N., Skarstad, K., and Crooke, E. (2009) Escherichia coli DnaA forms helical structures along the longitudinal cell axis distinct from MreB filaments. *Mol. Microbiol. 72*, 645–657.

(89) Teitzel, G. M., and Parsek, M. R. (2003) Heavy Metal Resistance of Biofilm and Planktonic Pseudomonas aeruginosa. *Appl. Environ. Microbiol. 69*, 2313–2320.

(90) McNeill, K., and Hamilton, I. . (2003) Acid tolerance response of biofilm cells of Streptococcus mutans. *FEMS Microbiol. Lett. 221*, 25–30.

(91) Magrex-Debar, E. Le, and Lemoine, J. (2000) Evaluation of biohazards in dehydrated biofilms on foodstuff packaging. *Int. J. … 55*, 239–243.

(92) Leid, J. G., Shirtliff, M. E., Costerton, J. W., and Stoodley, a. P. (2002) Human Leukocytes Adhere to, Penetrate, and Respond to Staphylococcus aureus Biofilms. *Infect. Immun. 70*, 6339–6345.

(93) Stewart, P. S., and William Costerton, J. (2001) Antibiotic resistance of bacteria in biofilms. *Lancet 358*, 135–138.

(94) Gilbert, P., Allison, D. G., and McBain, A. J. (2002) Biofilms in vitro and in vivo: do singular mechanisms imply cross-resistance? *J. Appl. … 92*, 98S–110S.

(95) Mah, T.-F. C., and O'Toole, G. a. (2001) Mechanisms of biofilm resistance to antimicrobial agents. *Trends Microbiol. 9*, 34–39.

(96) Hall-Stoodley, L., Costerton, J. W., and Stoodley, P. (2004) Bacterial biofilms: from the natural environment to infectious diseases. *Nat. Rev. Microbiol. 2*, 95–108.

(97) Shanks, R. M. Q., Donegan, N. P., Graber, M. L., Buckingham, S. E., Zegans, M. E., Cheung, A. L., and O'Toole, G. a. (2005) Heparin stimulates Staphylococcus aureus biofilm formation. *Infect. Immun. 73*, 4596–606.

(98) Mann, E. E., Rice, K. C., Boles, B. R., Endres, J. L., Ranjit, D., Chandramohan, L., Tsang, L. H., Smeltzer, M. S., Horswill, A. R., and Bayles, K. W. (2009) Modulation of eDNA release and degradation affects Staphylococcus aureus biofilm maturation. *PLoS One 4*, e5822.

(99) Rice, K. C., Mann, E. E., Endres, J. L., Weiss, E. C., Cassat, J. E., Smeltzer, M. S., and Bayles, K. W. (2007) The cidA murein hydrolase regulator contributes to DNA release and biofilm development in Staphylococcus aureus. *Proc. Natl. Acad. Sci. U. S. A. 104*, 8113–8.

(100) Cramton, S., and Gerke, C. (1999) The intercellular adhesion (ica) locus is present in Staphylococcus aureus and is required for biofilm formation. *Infect. … 67*, 5427–33.

(101) Flemming, H.-C., and Wingender, J. (2010) The biofilm matrix. *Nat. Rev. Microbiol. 8*, 623–33.

(102) Wang, Y., Tang, Y., Zhou, Z., Ji, E., Lopez, G. P., Chi, E. Y., Schanze, K. S., and Whitten, D. G. (2010) Membrane perturbation activity of cationic phenylene ethynylene oligomers and polymers: selectivity against model bacterial and mammalian membranes. *Langmuir 26*, 12509–14.

(103) Malik, Z., Hanania, J., and Nitzan, Y. (1990) New trends in photobiology bactericidal effects of photoactivated porphyrins — An

alternative approach to antimicrobial drugs. *J. Photochem. Photobiol. B Biol. 5*, 281–293.

(104) Hill, E. H., Sanchez, D., Evans, D. G., and Whitten, D. G. (2013) Structural basis for aggregation mode of oligo-p-phenylene ethynylenes with ionic surfactants. *Langmuir 29*, 15732–7.

(105) Buffet-Bataillon, S., Tattevin, P., Bonnaure-Mallet, M., and Jolivet-Gougeon, A. (2012) Emergence of resistance to antibacterial agents: the role of quaternary ammonium compounds--a critical review. *Int. J. Antimicrob. Agents 39*, 381–9.

(106) Evans, D. F., Allen, M., Ninham, B. W., and Fouda, A. (1984) Critical micelle concentrations for alkyltrimethylammonium bromides in water from 25 to 160 C. *J. Solution Chem. 13*, 87–101.

(107) Lindig, B. A., Rodgers, M. A. J., and Schaap, A. P. (1980) Determination of the lifetime of singlet oxygen in water-d2 using 9,10-anthracenedipropionic acid, a water-soluble probe. *J. Am. Chem. Soc. 102*, 5590–5593.

(108) Neuhaus, F. C., and Baddiley, J. (2003) A continuum of anionic charge: structures and functions of D-alanyl-teichoic acids in gram-positive bacteria. *Microbiol. Mol. Biol. Rev. 67*, 686–723.

(109) Nikaido, H. (1996) Outer Membrane, in *Escherichia coli and Salmonella typhimurium: cellular and molecular biology, 2nd ed.*, pp 29–47.

(110) Träuble, H., and Overath, P. (1973) The structure of Escherichia coli membranes studied by fluorescence measurements of lipid phase transitions. *Biochim. Biophys. Acta 307*, 491–512.

(111) Vollmer, W., Blanot, D., and de Pedro, M. A. (2008) Peptidoglycan structure and architecture. *FEMS Microbiol. Rev. 32*, 149–67.

(112) Lawrence, M. J., and Rees, G. D. (2012) Microemulsion-based media as novel drug delivery systems. *Adv. Drug Deliv. Rev. 64*, 175–193.

(113) Rabinow, B. E. (2004) Nanosuspensions in drug delivery. *Nat. Rev. Drug Discov. 3*, 785–96.

(114) Gursoy, R. N., and Benita, S. (2004) Self-emulsifying drug delivery systems (SEDDS) for improved oral delivery of lipophilic drugs. *Biomed. Pharmacother. = Biomédecine pharmacothérapie 58*, 173–82.

(115) Müllertz, A., Ogbonna, A., Ren, S., and Rades, T. (2010) New perspectives on lipid and surfactant based drug delivery systems for oral delivery of poorly soluble drugs. *J. Pharm. Pharmacol. 62*, 1622–1636.

(116) Williams, A. C., and Barry, B. W. (2012) Penetration enhancers. *Adv. Drug Deliv. Rev. 64*, 128–137.

(117) Gelperina, S., Maksimenko, O., Khalansky, A., Vanchugova, L., Shipulo, E., Abbasova, K., Berdiev, R., Wohlfart, S., Chepurnova, N., and Kreuter, J. (2010) Drug delivery to the brain using surfactant-coated poly(lactide-co-glycolide) nanoparticles: Influence of the formulation parameters. *Eur. J. Pharm. Biopharm. 74*, 157–163.

(118) Onaizi, S. A., and Leong, S. S. J. Tethering antimicrobial peptides: current status and potential challenges. *Biotechnol. Adv. 29*, 67–74.

(119) Muñoz-Bonilla, A., and Fernández-García, M. (2012) Polymeric materials with antimicrobial activity. *Prog. Polym. Sci. 37*, 281–339.

(120) Kugel, Alex, Shane Stafslien, and B. J. C. (2011) Antimicrobial coatings produced by “tethering” biocides to the coating matrix: A comprehensive review. *Prog. Org. Coatings 72*, 222–252.

(121) Salwiczek, M., Qu, Y., Gardiner, J., Strugnell, R. A., Lithgow, T., McLean, K. M., and Thissen, H. (2014) Emerging rules for effective

antimicrobial coatings. *Trends Biotechnol.*

(122) Yang, W. J., Cai, T., Neoh, K. G., Kang, E. T., Dickinson, G. H., Teo, S. L. M., and Rittschof, D. (2011) Biomimetic anchors for antifouling and antibacterial polymer brushes on stainless steel. *Langmuir 27*, 7065–7076.

(123) Muszanska, A. K., Busscher, H. J., Herrmann, A., Van der Mei, H. C., and Norde, W. (2011) Pluronic-lysozyme conjugates as anti-adhesive and antibacterial bifunctional polymers for surface coating. *Biomaterials 32*, 6333–6341.

(124) Yuan, S., Yin, J., Jiang, W., Liang, B., Pehkonen, S. O., and Choong, C. (2013) Enhancing antibacterial activity of surface-grafted chitosan with immobilized lysozyme on bioinspired stainless steel substrates. *Colloids Surfaces B Biointerfaces 106*, 11–21.

(125) Wang, L., Chen, J., Shi, L., Shi, Z., Ren, L., and Wang, Y. (2014) The promotion of antimicrobial activity on silicon substrates using a “click” immobilized short peptide. *Chem. Commun. (Camb). 50*, 975–7.

(126) Lim, K., Chua, R. R. Y., Saravanan, R., Basu, A., Mishra, B., Tambyah, P. A., Ho, B., and Leong, S. S. J. (2013) Immobilization studies of an engineered arginine-tryptophan-rich peptide on a silicone surface with antimicrobial and antibiofilm activity. *ACS Appl. Mater. Interfaces 5*, 6412–6422.

(127) Tiller, J. C., Liao, C. J., Lewis, K., and Klibanov, A. M. (2001) Designing surfaces that kill bacteria on contact. *Proc. Natl. Acad. Sci. U. S. A. 98*, 5981–5985.

(128) Lee, S. B., Koepsel, R. R., Morley, S. W., Matyjaszewski, K., Sun, Y., and Russell, A. J. (2004) Permanent, nonleaching antibacterial surfaces, 1. Synthesis by atom transfer radical polymerization. *Biomacromolecules 5*, 877–882.

(129) Gottenbos, B., Van Der Mei, H. C., Klatter, F., Nieuwenhuis, P., and

Busscher, H. J. (2002) In vitro and in vivo antimicrobial activity of covalently coupled quaternary ammonium silane coatings on silicone rubber. *Biomaterials 23*, 1417–1423.

(130) Oosterhof, J. J. H., Buijssen, K. J. D. A., Busscher, H. J., Van Der Laan, B. F. A. M., and Van Der Mei, H. C. (2006) Effects of quaternary ammonium silane coatings on mixed fungal and bacterial biofilms on tracheoesophageal shunt prostheses. *Appl. Environ. Microbiol. 72*, 3673–3677.

(131) Poverenov, E., Shemesh, M., Gulino, A., Cristaldi, D. A., Zakin, V., Yefremov, T., and Granit, R. (2013) Durable contact active antimicrobial materials formed by a one-step covalent modification of polyvinyl alcohol, cellulose and glass surfaces. *Colloids Surfaces B Biointerfaces 112*, 356–361.

(132) Shivapooja, P., Ista, L. K., Canavan, H. E., and Lopez, G. P. (2012) ARGET-ATRP synthesis and characterization of PNIPAAm brushes for quantitative cell detachment studies. *Biointerphases 7*, 1–9.

(133) Sidorenko, A., Krupenkin, T., Taylor, A., Fratzl, P., and Aizenberg, J. (2007) Reversible switching of hydrogel-actuated nanostructures into complex micropatterns. *Science 315*, 487–490.

(134) Sidorenko, A., Krupenkin, T., and Aizenberg, J. (2008) Controlled switching of the wetting behavior of biomimetic surfaces with hydrogel-supported nanostructures. *J. Mater. Chem. 18*, 3841–3846.

(135) Alexander Sidorenko, Sergiy Minko, Karin Schenk-Meuser, Heinz Duschner, and M. S. (1999) Switching of Polymer Brushes. *Langmuir 15*, 8349–8355.

(136) Lemieux, M., Usov, D., Minko, S., Stamm, M., Shulha, H., and Tsukruk, V. V. (2003) Reorganization of binary polymer brushes: Reversible switching of surface microstructures and nanomechanical properties. *Macromolecules 36*, 7244–7255.

(137) Vyas, M. K., Nandan, B., Schneider, K., and Stamm, M. (2008) Nanowear studies in reversibly switchable polystyrene-poly(acrylic acid) mixed brushes. *J. Colloid Interface Sci. 328*, 58–66.

(138) Yu, Q., Ge, W., Atewologun, A., Stiff-Roberts, A. D., and López, G. P. (2015) Antimicrobial and bacteria-releasing multifunctional surfaces: Oligo (p-phenylene-ethynylene)/poly (N-isopropylacrylamide) films deposited by RIR-MAPLE. *Colloids Surfaces B Biointerfaces 126*, 328–334.

(139) Ista, L. K., Pérez-Luna, V. H., and López, G. P. (1999) Surface-grafted, environmentally sensitive polymers for biofilm release. *Appl. Environ. Microbiol. 65*, 1603–1609.

(140) D. Dunliffe, C.A. Smart, J. Tsibouklis, S. Young, C. Alexander, E. N. V. (2000) Bacterial adsorption to thermoresponsive polymer surfaces. *Biotechnol. Lett. 22*, 141–145.

(141) David Cunliffe, Carolina de las Heras Alarcon, Vanessa Peters, James R. Smith, C. A. (2003) Thermoresponsive Surface-Grafted Poly(N−isopropylacrylamide) Copolymers: Effect of Phase Transitions on Protein and Bacterial Attachment. *Langmuir 19*, 2888–2899.

(142) Ista, L. K., Mendez, S., and Lopez, G. P. (2010) Attachment and detachment of bacteria on surfaces with tunable and switchable wettability. *Biofouling 26*, 111–118.

(143) Plunkett, K. N., Zhu, X., Moore, J. S., and Leckband, D. E. (2006) PNIPAM chain collapse depends on the molecular weight and grafting density. *Langmuir 22*, 4259–66.

(144) Young, K. D. (2006) The selective value of bacterial shape. *Microbiol. Mol. Biol. Rev. 70*, 660–703.

(145) Beveridge, T. J. (1988) The bacterial surface: general considerations towards design and function. *Can. J. Microbiol. 34*, 363–372.

(146) Parthasarathy, A., Pappas, H. C., Hill, E. H., Huang, Y., Whitten, D. G., and Schanze, K. S. (2015) Conjugated Polyelectrolytes with Imidazolium Solubilizing Groups. Properties and Application to Photodynamic Inactivation of Bacteria. *ACS Appl. Mater. Interfaces 7*, 28027–28034.

(147) Patil, A. O., Ikenoue, Y., Wudl, F., and Heeger, A. J. (1987) Water soluble conducting polymers. *J. Am. Chem. Soc. 109*, 1858–1859.

(148) Shi, S., and Wudl, F. (1990) Synthesis and characterization of a water-soluble poly(p-phenylenevinylene) derivative. *Macromolecules 23*, 2119–2124.

(149) Ho, H.-A., Béra-Abérem, M., and Leclerc, M. (2005) Optical sensors based on hybrid DNA/conjugated polymer complexes. *Chemistry 11*, 1718–24.

(150) Zeng, Q., Cai, P., Li, Z., Qin, J., and Tang, B. Z. (2008) An imidazole-functionalized polyacetylene: convenient synthesis and selective chemosensor for metal ions and cyanide. *Chem. Commun.* 1094.

(151) Liu, L., Huang, Y., Riduan, S. N., Gao, S., Yang, Y., Fan, W., and Zhang, Y. (2012) Main-chain imidazolium oligomer material as a selective biomimetic antimicrobial agent. *Biomaterials 33*, 8625–8631.

(152) Riduan, S. N., and Zhang, Y. (2013) Imidazolium salts and their polymeric materials for biological applications. *Chem. Soc. Rev. 42*, 9055–70.

(153) Bakken, L. R. (1997) Culturable and nonculturable bacteria in soil, in *Modern Soil Microbiology* (van Elsas, J. dirk, Ed.), pp 47–61. CRC Press.

(154) Balaban, N. Q., Merrin, J., Chait, R., Kowalik, L., and Leibler, S. (2004) Bacterial persistence as a phenotypic switch. *Science 305*, 1622–5.

(155) Setlow, B., Melly, E., and Setlow, P. (2001) Properties of spores of Bacillus subtilis blocked at an intermediate stage in spore germination. *J. Bacteriol. 183*, 4894–9.

(156) Titball, R. W., Turnbull, P. C., and Hutson, R. A. (1991) The monitoring and detection of Bacillus anthracis in the environment. *Soc. Appl. Bacteriol. Symp. Ser. 20*, 9S–18S.

(157) Williams, R. (1986) Bacillus anthracis and other aerobic spore-forming bacilli.

(158) Gould, G. W. (1969) Germination, in *The Bacterial Spore* (Gould, G. W., and Hurst, A., Eds.), pp 397–444.

(159) Pandey, R., Ter Beek, A., Vischer, N. O. E., Smelt, J. P. P. M., Brul, S., and Manders, E. M. M. (2013) Live cell imaging of germination and outgrowth of individual bacillus subtilis spores; the effect of heat stress quantitatively analyzed with SporeTracker. *PLoS One 8*, e58972.

(160) Setlow, P. (2003) Spore germination. *Curr. Opin. Microbiol. 6*, 550–556.

(161) Young, S. B., and Setlow, P. (2003) Mechanisms of killing of Bacillus subtilis spores by hypochlorite and chlorine dioxide. *J. Appl. Microbiol. 95*, 54–67.

(162) Wang, Y., Zhou, Z., Zhu, J., Tang, Y., Canady, T. D., Chi, E. Y., Schanze, K. S., and Whitten, D. G. (2011) Dark Antimicrobial Mechanisms of Cationic Phenylene Ethynylene Polymers and Oligomers against Escherichia coli. *Polymers (Basel). 3*, 1199–1214.

(163) Wang, Y., Schanze, K. S. K., Chi, E. Y. E., and Whitten, D. G. D. (2013) When worlds collide: interactions at the interface between biological systems and synthetic cationic conjugated polyelectrolytes and oligomers. *Langmuir 29*, 10635–47.

(164) Wilde, K. N. K., Whitten, D. G. D., and Canavan, H. E. (2013) In vitro cytotoxicity of antimicrobial conjugated electrolytes: interactions with mammalian cells. *ACS Appl. Mater. Interfaces 5*, 9305–11.

(165) Schuch, R., Nelson, D., and Fischetti, V. (2002) A bacteriolytic agent that detects and kills Bacillus anthracis. *Nature 418*, 440–445.

(166) Dascier, D., Ji, E., Parthasarathy, A., Schanze, K. S., and Whitten, D. G. (2012) Efficacy of end-only-functionalized oligo(arylene-ethynylene)s in killing bacterial biofilms. *Langmuir 28*, 11286–90.

(167) Stratis-Cullum, D. N., Griffin, G. D., Mobley, J., Vass, A. A., and Vo-Dinh, T. (2003) A miniature biochip system for detection of aerosolized Bacillus globigii spores. *Anal. Chem. 75*, 275–80.

(168) Turnbough, C. L. (2003) Discovery of phage display peptide ligands for species-specific detection of Bacillus spores. *J. Microbiol. Methods 53*, 263–71.

(169) Kong, L., Zhang, P., Yu, J., Setlow, P., and Li, Y. (2010) Monitoring the kinetics of uptake of a nucleic acid dye during the germination of single spores of Bacillus species. *Anal. Chem. 82*, 8717–8724.

(170) Fiester, S. E., Helfinstine, S. L., Redfearn, J. C., Uribe, R. M., and Woolverton, C. J. (2012) Electron beam irradiation dose dependently damages the bacillus spore coat and spore membrane. *Int. J. Microbiol. 2012*, 579593.

(171) Setlow, P. (2000) Resistance of Bacterial Spores, in *Bacterial Stress Responses* (Storz, G., and Hengge-Aronis, R., Eds.), pp 217–230. American Society for Microbiology, Washington DC.

(172) Russell, A. (1990) Bacterial spores and chemical sporicidal agents. *Clin. Microbiol. Rev. 3*, 99–119.

(173) Nerandzic, M. M., and Donskey, C. J. (2010) Triggering germination represents a novel strategy to enhance killing of Clostridium difficile spores. *PLoS One 5*, e12285.

(174) Inglesby, T., and Henderson, D. (1999) Anthrax as a biological weapon: medical and public health management. *Jama 281*, 1735–1746.

(175) Dragon, D., and Rennie, R. (1995) The ecology of anthrax spores: tough but not invincible. *Can. Vet. J. 36*.

(176) Genest, P. C., Setlow, B., Melly, E., and Setlow, P. (2002) Killing of spores of Bacillus subtilis by peroxynitrite appears to be caused by membrane damage. *Microbiology 148*, 307–14.

(177) Loshon, C. A., Melly, E., Setlow, B., and Setlow, P. (2001) Analysis of the killing of spores of Bacillus subtilis by a new disinfectant, Sterilox. *J. Appl. Microbiol. 91*, 1051–8.

(178) Melly, E., Cowan, a. E., and Setlow, P. (2002) Studies on the mechanism of killing of Bacillus subtilis spores by hydrogen peroxide. *J. Appl. Microbiol. 93*, 316–325.

(179) Caipo, M. L., Duffy, S., Zhao, L., and Schaffner, D. W. (2002) Bacillus megaterium spore germination is influenced by inoculum size. *J. Appl. Microbiol. 92*, 879–884.

(180) Harry, E., and Lewis, P. (2003) Early targeting of Min proteins to the cell poles in germinated spores of Bacillus subtilis: evidence for division apparatus-independent recruitment of Min. *Mol. Microbiol. 47*, 37–48.

(181) Zhang, P., Garner, W., Yi, X., Yu, J., Li, Y., and Setlow, P. (2010) Factors affecting variability in time between addition of nutrient germinants and rapid dipicolinic acid release during germination of spores of Bacillus species. *J. Bacteriol. 192*, 3608–19.

(182) Maki, D. G., Kluger, D. M., and Crnich, C. J. (2006) The Risk of Bloodstream Infection in Adults With Different Intravascular Devices: A Systematic Review of 200 Published Prospective Studies. *Mayo Clin. Proc. 81*, 1159–1171.

(183) Wisplinghoff, H., Bischoff, T., Tallent, S. M., Seifert, H., Wenzel, R. P., and Edmond, M. B. (2004) Nosocomial bloodstream infections in US hospitals: analysis of 24,179 cases from a prospective nationwide surveillance study. *Clin. Infect. Dis. 39*, 309–317.

(184) Snydman DR, Gorbea HF, Pober BR, Majka JA, Murray SA, P. L. (1982) Predictive value of surveillance skin cultures in total-parenteral-nutrition-related infection. *Lancet 320*, 1385–1388.

(185) Bjornson, H. S., Colley, R., Bower, R. H., Duty, V. P., Schwartz-Fulton, J. T., & Fischer, J. E. (1982) Association between microorganism growth at the catheter insertion site and colonization of the catheter in patients receiving total parenteral nutrition. *Surgery 92*, 720–727.

(186) Cooper, G.L. and Hopkins, C. . (1985) Rapid diagnosis of intravascular catheter-associated infection by direct Gram staining of catheter segments. *N. Engl. J. Med. 312*, 1142–1147.

(187) Raad, I., Costerton, W., Sabharwal, U., Sadlowski, M., Anaissie, E. and Bodey, G. P. (1993) Ultrastructural analysis of indwelling vascular catheters: a quantitative relationship between luminal colonization and duration of placement. *J. Infect. Dis. 168*, 400–407.

(188) Edmond, M. B., Wallace, S. E., McClish, D. K., Pfaller, M. A., Jones, R. N., and Wenzel, R. P. (1999) Nosocomial bloodstream infections in United States hospitals: A three-year analysis. *Clin. Infect. Dis. 29*, 239–244.

(189) Wingard, J. R. (1995) Importance of Candida species other than C. albicans as pathogens in oncology patients. *Clin. Infect. Dis. 20*, 115–125.

(190) Giri, S., & Kindo, A. J. (2012) Review of Candida species causing

blood stream infection. *Indian J. Med. Microbiol. 30*, 270.

(191) Ruiz-Herrera, J., Elorza, M. V., Valentín, E., and Sentandreu, R. (2006) Molecular organization of the cell wall of Candida albicans and its relation to pathogenicity. *FEMS Yeast Res. 6*, 14–29.

(192) Klis, F. M., Groot, P. D. E., and Hellingwerf, K. (2001) Molecular organization of the cell wall of Candida albicans 1–8.

(193) Netea, M. G., Gow, N. A. R., Munro, C. a., Bates, S., Collins, C., Ferwerda, G., Hobson, R. P., Bertram, G., Hughes, H. B., Jansen, T., Jacobs, L., Buurman, E. T., Gijzen, K., Williams, D. L., Torensma, R., McKinnon, A., MacCallum, D. M., Odds, F. C., Van Der Meer, J. W. M., Brown, A. J. P., and Kullberg, B. J. (2006) Immune sensing of Candida albicans requires cooperative recognition of mannans and glucans by lectin and Toll-like receptors. *J. Clin. Invest. 116*, 1642–50.

(194) Kojic, E. M., and Darouiche, R. O. (2004) *Candida* Infections of Medical Devices. *Clin. Microbiol. Revi 17*, 255–267.

(195) Nett, J. E., and Andes, D. R. (2015) Fungal Biofilms: In Vivo Models for Discovery of Anti-Biofilm Drugs. *Microbiol. Spectr. 3*.

(196) Mitchell, K. F., Taff, H. T., Cuevas, M. A., Reinicke, E. L., Sanchez, H., and Andes, D. R. (2013) Role of matrix β-1,3 glucan in antifungal resistance of non-albicans Candida biofilms. *Antimicrob. Agents Chemother. 57*, 1918–20.

(197) Brun-Buisson, C., Doyon, F., Sollet, J.-P., Cochard, J.-F., Cohen, Y., and Nitenberg, G. (2004) Prevention of intravascular catheter-related infection with newer chlorhexidine-silver sulfadiazine-coated catheters: a randomized controlled trial. *Intensive Care Med. 30*, 837–43.

(198) Ramritu, P., Halton, K., Collignon, P., Cook, D., Fraenkel, D., Battistutta, D., Whitby, M., and Graves, N. (2008) A systematic review comparing the relative effectiveness of antimicrobial-coated catheters

in intensive care units. *Am. J. Infect. Control 36*, 104–117.

(199) Kalfon, P., De Vaumas, C., Samba, D., Boulet, E., Lefrant, J.Y., Eyraud, D., Lherm, T., Santoli, F., Naija, W. and Riou, B. (2007) Comparison of silver-impregnated with standard multi-lumen central venous catheters in critically ill patients*. *Crit. Care Med. 35*, 1032–1039.

(200) Groeger JS. Lucas AB. Coit D. LaQuaglia M. Brown AE. Turnbull A. Exelby P. (1993) A prospective, randomized evaluation of the effect of silver impregnated subcutaneous cuffs for preventing tunneled chronic venous. *Ann. Surg. 218*, 206–210.

(201) Perfect, J. R. (2004) Antifungal resistance: the clinical front. *Oncology (Williston Park). 18*, 15–22.

(202) Wang, Y., Chi, E. Y., Natvig, D. O., Schanze, K. S., and Whitten, D. G. (2013) Antimicrobial activity of cationic conjugated polyelectrolytes and oligomers against Saccharomyces cerevisiae vegetative cells and ascospores. *ACS Appl. Mater. Interfaces 5*, 4555–61.

(203) Moran, G., Coleman, D., Sullivan, D., Butler, G., Hoyer, L. L., Romani, L., Netea, M. G., Gow, N. A. R., Spellberg, B., Fu, Y., Ibrahim, A. S., Jang, W. S., Edgerton, M., Murno, C., Richard, M. L., Brown, A. J. P., Haynes, K., Quinn, J., Zordan, R., Cormack, B., Vylkova, S., Lorenz, M. C., Deepu, A., Calderone, R., Li, D., Pfaller, M. A., and Diekema, D. J. (2012) Candida and Candidiasis (Calderone, R. A., and Clancy, C. J., Eds.) 2nd ed. ASM Press, Washington DC.

(204) Brown, J. A., and Catley, B. J. (1992) Monitoring polysaccharide synthesis in Candida albicans. *Carbohydr. Res. 227*, 195–202.

(205) Hong, Y., Lam, J. W. Y., and Tang, B. Z. (2011) Aggregation-induced emission. *Chem. Soc. Rev. 40*, 5361–88.

(206) Fitzpatrick, D. A., Logue, M. E., Stajich, J. E., and Butler, G. (2006) A fungal phylogeny based on 42 complete genomes derived from supertree and

combined gene analysis. *BMC Evol. Biol. 6*, 99.

(207) Tsoni, S. V., and Brown, G. D. (2008) β-Glucans and Dectin-1. *Ann. N. Y. Acad. Sci. 1143*, 45–60.

(208) Carrion, S. d. J., Leal, S. M., Ghannoum, M. A., Aimanianda, V., Latge, J.-P., and Pearlman, E. (2013) The RodA Hydrophobin on Aspergillus fumigatus Spores Masks Dectin-1- and Dectin-2-Dependent Responses and Enhances Fungal Survival In Vivo. *J. Immunol. 191*, 2581–2588.

(209) Rappleye, C. A., Eissenberg, L. G., and Goldman, W. E. (2007) Histoplasma capsulatum alpha-(1,3)-glucan blocks innate immune recognition by the beta-glucan receptor. *Proc. Natl. Acad. Sci. U. S. A. 104*, 1366–70.

(210) Wheeler, R. T., Kombe, D., Agarwala, S. D., and Fink, G. R. (2008) Dynamic, Morphotype-Specific Candida albicans β-Glucan Exposure during Infection and Drug Treatment. *PLoS Pathog.* (Mitchell, A. P., Ed.) *4*, e1000227.

(211) Wheeler, R. T., and Fink, G. R. (2006) A Drug-Sensitive Genetic Network Masks Fungi from the Immune System. *PLoS Pathog. 2*, e35.

(212) Underhill, D. M., Rossnagle, E., Lowell, C. A., and Simmons, R. M. (2005) Dectin-1 activates Syk tyrosine kinase in a dynamic subset of macrophages for reactive oxygen production. *Blood 106*, 2543–50.

(213) Adie, E. J., Kalinka, S., Smith, L., Francis, M. J., Marenghi, A., Cooper, M. E., Briggs, M., Michael, N. P., Milligan, G., and Game, S. (2002) A pH-sensitive fluor, CypHer 5, used to monitor agonist-induced G protein-coupled receptor internalization in live cells. *Biotechniques 33*, 1152–4, 1156–7.

(214) Adie, E. J., Francis, M. J., Davies, J., Smith, L., Marenghi, A., Hather, C., Hadingham, K., Michael, N. P., Milligan, G., and Game, S. (2003)

CypHer 5: a generic approach for measuring the activation and trafficking of G protein-coupled receptors in live cells. *Assay Drug Dev. Technol. 1*, 251–9.

(215) Jamieson, D. J., Stephen, D. W., and Terrière, E. C. (1996) Analysis of the adaptive oxidative stress response of Candida albicans. *FEMS Microbiol. Lett. 138*, 83–8.

(216) Nikolaou, E., Agrafioti, I., Stumpf, M., Quinn, J., Stansfield, I., and Brown, A. J. P. (2009) Phylogenetic diversity of stress signalling pathways in fungi. *BMC Evol. Biol. 9*, 44.

(217) Kaloriti, D., Jacobsen, M., Yin, Z., Patterson, M., Tillmann, A., Smith, D. a, Cook, E., You, T., Grimm, M. J., Bohovych, I., Grebogi, C., Segal, B. H., Gow, N. a R., Haynes, K., Quinn, J., and Brown, A. J. P. (2014) Mechanisms Underlying the Exquisite Sensitivity of Candida albicans to Combinatorial Cationic and Oxidative Stress That Enhances the Potent Fungicidal Activity of Phagocytes. *MBio 5*, 1–11.

(218) Sasada, M., and Johnston, R. B. (1980) Macrophage microbicidal activity. Correlation between phagocytosis-associated oxidative metabolism and the killing of Candida by macrophages. *J. Exp. Med. 152*, 85–98.

(219) Miramón, P., Kasper, L., and Hube, B. (2013) Thriving within the host: Candida spp. interactions with phagocytic cells. *Med. Microbiol. Immunol. 202*, 183–95.

(220) Bahmed, K., Bonaly, R., and Coulon, J. (2003) Relation between cell wall chitin content and susceptibility to amphotericin B in Kluyveromyces, Candida and Schizosaccharomyces species. *Res. Microbiol. 154*, 215–22.

(221) Mesa-Arango, A. C., Rueda, C., Román, E., Quintin, J., Terrón, M. C., Luque, D., Netea, M. G., Pla, J., and Zaragoza, O. (2016) Cell wall changes in AmB-resistant strains from Candida tropicalis and relationship with the immune responses elicited by the host. *Antimicrob. Agents Chemother.*

(222) Mochon, A. B., and Liu, H. (2008) The antimicrobial peptide histatin-5 causes a spatially restricted disruption on the Candida albicans surface, allowing rapid entry of the peptide into the cytoplasm. *PLoS Pathog. 4*, e1000190.

(223) Nikawa, H., Jin, C., Fukushima, H., Makihira, S., and Hamada, T. (2001) Antifungal activity of histatin-5 against non-albicans Candida species. *Oral Microbiol. Immunol. 16*, 250–2.

(224) Helmerhorst, E. J., Venuleo, C., Beri, A., and Oppenheim, F. G. (2005) Candida glabrata is unusual with respect to its resistance to cationic antifungal proteins. *Yeast 22*, 705–14.

(225) Raman, N., Lee, M.-R., Lynn, D. M., and Palecek, S. P. (2015) Antifungal Activity of 14-Helical β-Peptides against Planktonic Cells and Biofilms of Candida Species. *Pharmaceuticals (Basel). 8*, 483–503.

(226) Briones-Martin-del-Campo, M., Orta-Zavalza, E., Cañas-Villamar, I., Gutiérrez-Escobedo, G., Juárez-Cepeda, J., Robledo-Márquez, K., Arroyo-Helguera, O., Castaño, I., and De Las Peñas, A. (2015) The superoxide dismutases of Candida glabrata protect against oxidative damage and are required for lysine biosynthesis, DNA integrity and chronological life survival. *Microbiology 161*, 300–10.

(227) Kasper, L., Seider, K., and Hube, B. (2015) Intracellular survival of Candida glabrata in macrophages: immune evasion and persistence. *FEMS Yeast Res. 15*, fov042.

(228) Lowman, D., Ensley, H., and Williams, D. (2005) Introduction to the Chemistry and Immunobiology of Beta-Glucans, in *Toxicology of 1 - 3-Beta-Glucans*, pp 1–34. Informa Healthcare.

(229) Young, S. H., Dong, W. J., and Jacobs, R. R. (2000) Observation of a partially opened triple-helix conformation in 1-->3-beta-glucan by fluorescence resonance energy transfer spectroscopy. *J. Biol. Chem. 275*, 11874–9.

(230) Horisberger, M., and Clerc, M. F. (1988) Ultrastructural localization of anionic sites on the surface of yeast, hyphal and germ-tube forming cells of Candida albicans. *Eur. J. Cell Biol. 46*, 444–52.

(231) Cutler, J. E. (2001) N-glycosylation of yeast, with emphasis on Candida albicans. *Med. Mycol. 39 Suppl 1*, 75–86.

(232) Hall, R. A., and Gow, N. A. R. (2013) Mannosylation in Candida albicans: role in cell wall function and immune recognition. *Mol. Microbiol. 90*, 1147–61.

(233) Whitesides, G. M. (2015) Reinventing chemistry. *Angew. Chem. Int. Ed. Engl. 54*, 3196–209.

(234) Corbitt, T. S., Zhou, Z., Tang, Y., Graves, S. W., and Whitten, D. G. (2011) Rapid evaluation of the antibacterial activity of arylene-ethynylene compounds. *ACS Appl. Mater. Interfaces 3*, 2938–43.

(235) Schulze, K., López, D. a, Tillich, U. M., and Frohme, M. (2011) A simple viability analysis for unicellular cyanobacteria using a new autofluorescence assay, automated microscopy, and ImageJ. *BMC Biotechnol. 11*, 118.

(236) McQuade, D. T., Hegedus, A. H., and Swager, T. M. (2000) Signal Amplification of a "Turn-On" Sensor: Harvesting the Light Captured by a Conjugated Polymer. *J. Am. Chem. Soc. 122*, 12389–12390.

(237) Ji, E., Whitten, D. G., and Schanze, K. S. (2011) pH-dependent optical properties of a poly(phenylene ethynylene) conjugated polyampholyte. *Langmuir 27*, 1565–8.

(238) Farley, R. T. (2007) No Title. University of Florida.

(239) Parthasarathy, A., Goswami, S., Corbitt, T. S., Ji, E., Dascier, D., Whitten, D. G., and Schanze, K. S. (2013) Photophysics and light-activated

biocidal activity of visible-light-absorbing conjugated oligomers. *ACS Appl. Mater. Interfaces 5*, 4516–20.

(240) Gaillard, S., Leguérinel, I., and Mafart, P. (1998) Modelling combined effects of temperature and pH on the heat resistance of spores of Bacillus cereus. *Food Microbiol.* 625–630.

(241) Jain, J. P., and Kumar, N. (2010) Self assembly of amphiphilic (PEG)(3)-PLA copolymer as polymersomes: preparation, characterization, and their evaluation as drug carrier. *Biomacromolecules 11*, 1027–35.

(242) Gerhardt, P., Scherrer, R., and Black, S. (1972) Molecular Sieving by Dormant Spore Structures, in *Spores V*, pp 68–74. American Society for Microbiology, Washington DC.

(243) Sislian, P. R., Rau, J., Zhang, X., Pham, D., Li, M., Mädler, L., and Christofides, P. D. (2010) Bacterial aerosol neutralization by aerodynamic shocks using an impactor system: Experimental results for B. atropheus spores. *Chem. Eng. Sci. 65*, 4803–4815.

(244) Lovchik, J. A., Drysdale, M., Koehler, T. M., Hutt, J. A., and Lyons, C. R. (2012) Expression of either lethal toxin or edema toxin by Bacillus anthracis is sufficient for virulence in a rabbit model of inhalational anthrax. *Infect. Immun. 80*, 2414–25.

(245) Chand, H. S., Drysdale, M., Lovchik, J., Koehler, T. M., Lipscomb, M. F., and Lyons, C. R. (2009) Discriminating virulence mechanisms among Bacillus anthracis strains by using a murine subcutaneous infection model. *Infect. Immun. 77*, 429–35.

(246) Heninger, S., Drysdale, M., Lovchik, J., Hutt, J., Lipscomb, M. F., Koehler, T. M., and Lyons, C. R. (2006) Toxin-deficient mutants of Bacillus anthracis are lethal in a murine model for pulmonary anthrax. *Infect. Immun. 74*, 6067–74.

(247) King, R. D., Lee, J. C., and Morris, A. L. (1980) Adherence of

Candida albicans and other Candida species to mucosal epithelial cells. *Infect. Immun. 27*, 667–74.

(248) Lowman, D. W., Greene, R. R., Bearden, D. W., Kruppa, M. D., Pottier, M., Monteiro, M. A., Soldatov, D. V, Ensley, H. E., Cheng, S.-C., Netea, M. G., and Williams, D. L. (2014) Novel structural features in Candida albicans hyphal glucan provide a basis for differential innate immune recognition of hyphae versus yeast. *J. Biol. Chem. 289*, 3432–43.

(249) Pinto, M. R., Tan, C., Ramey, M. B., Reynolds, J. R., Bergstedt, T. S., Whitten, D. G., and Schanze, K. S. (2007) Amplified fluorescence quenching and biosensor application of a poly (para-phenylene) cationic polyelectrolyte. *Res. Chem. Intermed. 33*, 79–90.

(250) Kim, S. K., Lee, D. H., Hong, J.-I., and Yoon, J. (2009) Chemosensors for pyrophosphate. *Acc. Chem. Res. 42*, 23–31.

(251) Feng, F., Yang, J., Xie, D., McCarley, T. D., and Schanze, K. S. (2013) Remarkable Photophysics and Amplified Quenching of Conjugated Polyelectrolyte Oligomers. *J. Phys. Chem. Lett. 4*, 1410–1414.

(252) Feng, F., Lee, S. H., Cho, S. W., Kömürlü, S., McCarley, T. D., Roitberg, A., Kleiman, V. D., and Schanze, K. S. (2012) Conjugated Polyelectrolyte Dendrimers: Aggregation, Photophysics, and Amplified Quenching. *Langmuir 28*, 16679–16691.

(253) Liu, Y., and Schanze, K. S. (2008) Conjugated Polyelectrolyte-Based Real-Time Fluorescence Assay for Alkaline Phosphatase with Pyrophosphate as Substrate. *Anal. Chem. 80*, 8605–8612.

(254) Kim, S. K., Singh, N. J., Kwon, J., Hwang, I.-C., Park, S. J., Kim, K. S., and Yoon, J. (2006) Fluorescent imidazolium receptors for the recognition of pyrophosphate. *Tetrahedron 62*, 6065–6072.

(255) Kilger, R., Maier, M., Szeimies, R.-M., and Bäumler, W. (2001) Bidirectional energy transfer between the triplet T1 state of photofrin and

singlet oxygen in deuterium oxide. *Chem. Phys. Lett. 343*, 543–548.

(256) Maisch, T., Baier, J., Franz, B., Maier, M., Landthaler, M., Szeimies, R.-M., and Baumler, W. (2007) The role of singlet oxygen and oxygen concentration in photodynamic inactivation of bacteria. *Proc. Natl. Acad. Sci. 104*, 7223–7228.